

Crystallisation of Oxidic Gasifier Slags

Jan Peter Schupsky

Energie & Umwelt / Energy & Environment

Band / Volume 514

ISBN 978-3-95806-506-2

Forschungszentrum Jülich GmbH
Institut für Energie- und Klimaforschung
Werkstoffstruktur und -eigenschaften (IEK-2)

Crystallisation of Oxidic Gasifier Slags

Jan Peter Schupsky

Schriften des Forschungszentrums Jülich
Reihe Energie & Umwelt / Energy & Environment

Band / Volume 514

ISSN 1866-1793

ISBN 978-3-95806-506-2

Bibliografische Information der Deutschen Nationalbibliothek.
Die Deutsche Nationalbibliothek verzeichnet diese Publikation in der
Deutschen Nationalbibliografie; detaillierte Bibliografische Daten
sind im Internet über <http://dnb.d-nb.de> abrufbar.

Herausgeber und Vertrieb: Forschungszentrum Jülich GmbH
Zentralbibliothek, Verlag
52425 Jülich
Tel.: +49 2461 61-5368
Fax: +49 2461 61-6103
zb-publikation@fz-juelich.de
www.fz-juelich.de/zb

Umschlaggestaltung: Grafische Medien, Forschungszentrum Jülich GmbH

Druck: Grafische Medien, Forschungszentrum Jülich GmbH

Copyright: Forschungszentrum Jülich 2020

Schriften des Forschungszentrums Jülich
Reihe Energie & Umwelt / Energy & Environment, Band / Volume 514

D 82 (Diss. RWTH Aachen University, 2020)

ISSN 1866-1793
ISBN 978-3-95806-506-2

Vollständig frei verfügbar über das Publikationsportal des Forschungszentrums Jülich (JuSER)
unter www.fz-juelich.de/zb/openaccess.



This is an Open Access publication distributed under the terms of the [Creative Commons Attribution License 4.0](https://creativecommons.org/licenses/by/4.0/), which permits unrestricted use, distribution, and reproduction in any medium, provided the original work is properly cited.

Kurzfassung

Brennstoffvergasung ist eine flexible Technologie, die das Potential hat, die Wende von der Nutzung fossiler Brennstoffe hin zu regenerativen Energieträgern zu unterstützen. Während der Vergasung fallen oxidische Rückstände in einem Vergaser an, die als Schlacke bezeichnet werden. Der Schlackeabfluss muss kontinuierlich gewährleistet werden um den Vergaserbetrieb aufrecht zu erhalten. Eine hohe Schlackeviskosität verschlechtert jedoch die Fließeigenschaften. Kristallisation kann eine solche Viskositätserhöhung verursachen, die bisher nicht ausreichend untersucht worden ist. Die Schlackeviskosität kann zwar durch Modelle berechnet werden, es existieren allerdings keine Modelle für (teil-)kristalline Schlacken. Um den Einfluss der Kristalle korrekt zu modellieren, sind detaillierte Kristallmorphologiedaten erforderlich.

Im Rahmen dieser Arbeit wurden die Kristallisationseigenschaften von vier synthetischen Vergaserschlacken untersucht (ST-D-2, HKT, SOM-1 und HKR). Ihre Zusammensetzungen basieren mehrheitlich auf echten Schlacken, wurden allerdings aus Oxiden synthetisiert. Die Schlacken wurden auf ihr Schmelz- und Erstarrungsverhalten hin untersucht, um die erforderlichen Temperaturparameter für die anschließenden Experimente zu definieren. Thermodynamische Gleichgewichtsberechnungen wurden mit dem FactSage Equilib Programm durchgeführt, um eine erste Einschätzung der Liquidus- und Solidustemperatur sowie der zu kristallisierenden Phasen zu gewinnen. Zunächst wurde die Viskosität der Schlacken mit einem Hochtemperaturviskosimeter gemessen. ST-D-2 und HKT zeigten ein hochviskoses, HKR ein niedrigviskoses und SOM-1 ein intermediärviskoses Verhalten. Ebenfalls setzte teilweise nicht-Newton'sches Fließverhalten sowie Kristallisation in den Schlacken ein, weshalb sie anschließend mittels eines Abschreckversuchs und CLSM (konfokale Laser-Scanning-Mikroskopie) weiter untersucht wurden. Die experimentell untersuchten Proben wurden anschließend aufbereitet und für die Analyse durch Mikroskopie, Röntgenbeugung und REM (Rasterelektronenmikroskopie) präpariert. Es konnte festgestellt werden, dass die ST-D-2, HKT und SOM-1 Schlacken großflächiges Wachstum von Anorthit ($\text{CaAl}_2\text{Si}_2\text{O}_8$) zeigten. Begleitet wurde diese Phase durch die Kristallisation von Cristobalit (SiO_2), Klinopyroxen ($(\text{Ca},\text{Mg},\text{Fe})(\text{Si},\text{Al})_2\text{O}_6$) und Olivin ($(\text{Ca},\text{Mg},\text{Fe})_2\text{SiO}_4$). In der HKR Schlacke wurde Melilith ($(\text{Ca},\text{Mg},\text{Fe})_2\text{SiO}_4$) als häufigste Phase neben Olivin und Spinell ($(\text{Mg},\text{Fe})\text{AlO}_4$) nachgewiesen. Die hochviskosen Schlacken zeigten Inkubationszeiten von einzelnen Stunden, die SOM-1 Schlacke von wenigen Stunden bis hin zu Zehnerminuten und die HKR Schlacke kristallisierte schließlich bereits im Abkühlprozess und konnte nie zur vollständigen Verglasung kontrolliert abgekühlt werden. Diese Ergebnisse wurden in sogenannten Zeit-Temperatur-Umwandlungsdiagrammen (ZTU) dargestellt.

Die Analyse der Proben erlaubte die Definition von allgemeingültigen Morphologien für Anorthit, Spinell, Olivin und Melilith. Anorthit wurde als tetragonales Prisma, Spinell als Oktaeder, Olivin als längliche, gleichseitige Bipyramide und Melilith als rechteckige Bipyramide definiert. Um Morphologiedaten zu generieren, wurden insgesamt 1022 Kristalle aller Phasen auf ihre Länge und Breite hin vermessen. Es konnte der allgemeine Trend nachvollzogen werden, dass höhere Temperaturen zum Wachstum größerer Kristalle führen, wie es die Kristallisationstheorie beschreibt. Diese Daten wurden mit dem Kristallwachstum in einer realen Schlacke aus dem Testreaktor PiTER (TU München, HotVeGas-Projekt) verglichen. In ihr konnten ebenfalls Anorthite und Spinell mit exakt gleicher Morphologie festgestellt werden. Nicht zuletzt wegen dieser Übereinstimmung mit der realen Schlacke werden die Ergebnisse als vertrauenswürdig und reproduzierbar angesehen. Sie können daher in einem zukünftigen Viskositätsmodell für teilkristalline Schlacken angewandt werden.

Abstract

Gasification is a flexible technology that has the potential to support the transition from a fossil fuelled to decarbonised energy supply system. During gasification, an oxidic residue is produced that is named as slag. Slag flow needs to be constant in a gasifier, but a high viscosity impairs the flow behaviour. The phenomenon of crystallisation has such effect, yet is only barely understood. Viscosity of slag can be modelled and therefore predicted. However, no sufficient model exists to calculate the viscosity of partly crystallised slags. A sufficient data source of crystal morphology data is required to enable the application of an improved viscosity model for partly crystallised slags.

In this study, the crystallisation characteristics of four synthetic gasifier slags (ST-D-2, HKT, SOM-1, and HKR) have been investigated. Initially, the synthetic slag systems have been blended from high purity compounds. Their compositions are mostly based on real coal slags that have been investigated in previous studies. The slag systems were analysed on their melting and solidification behaviour and so, the temperature parameters for the following experiments were set. Equilibrium calculations were conducted with FactSage Equilib programme to predict solidus and liquidus temperatures, as well as the crystallised phases. As a first experiment, high temperature viscosimetry was performed on the four slag systems. ST-D-2 and HKT slags were identified as high viscous, HKR as a low viscous and SOM-1 as an intermediately viscous slag. Viscosity measurements revealed non-Newtonian behaviour and the presence of crystals in the slag. The evolution of crystallisation was analysed by quenching and CLSM (confocal laser scanning microscopy) experiments. The resulting slag samples were analysed via microscopy, X-ray diffraction and SEM (scanning electron microscopy). ST-D-2, HKT, and SOM-1 slag displayed significant growth of anorthite ($\text{CaAl}_2\text{Si}_2\text{O}_8$) crystals. Several more phases crystallised in these slags, such as cristobalite (SiO_2), clinopyroxene ($(\text{Ca},\text{Mg},\text{Fe})(\text{Si},\text{Al})_2\text{O}_6$), and olivine ($(\text{Ca},\text{Mg},\text{Fe})_2\text{SiO}_4$). In the HKR slag, melilite ($\text{Ca}_2(\text{Al},\text{Mg})(\text{Si},\text{Al})_2\text{O}_7$) was the dominating crystal phase, followed by olivine and spinel ($(\text{Mg},\text{Fe})\text{AlO}_4$). For the high viscous slags, time-temperature-transformation (TTT) diagrams indicated an incubation time of single hours. SOM-1 slags incubation time varied between double digit minutes to single hours and lastly HKR slag displayed very rapid, partly instant crystallisation.

The crystal morphologies of anorthite, spinel, olivine, and melilite could be defined based on the sample analysis of quenching and CLSM experiments. Anorthite was defined as a tetragonal prism with variation in the elongation, spinel formed idiomorphic octahedrons, olivine crystallised as elongated, equiaxed bipyramids and melilite formed large rectangular bipyramids. To gather relevant morphology data, the crystals were measured on their length and width to quantify their presence with respect to the applied temperature. In total, 1022 individual crystals were measured for the quantification. Generally, the crystals tend to grow larger at higher temperatures, which is in agreement with the crystallisation theory. The morphology was compared with crystallisation of real slag samples from PiTER reactor (TU Munich, HotVeGas project). Anorthite and spinel were found in PiTER slag with identical morphologies, as provided for the synthetic slag samples. This accordance is an application-related proof that the investigations on crystal morphologies performed in this study are reproducible and realistically display crystallisation processes in gasifiers. Therefore, they are highly applicable in viscosity models for partly crystallised slags.

Publications

- 1. J.P. Schupsky, O.Saar, G. Wu, M. Dohrn, M. Müller**
Viscosity and crystal morphology data of anorthite bearing synthetic coal slag systems
Fuel, 280 (2020), <https://doi.org/10.1016/j.fuel.2020.118663>
- 2. J.P. Schupsky, G. Wu, M. Guo, M. Müller**
Crystallisation characteristics and crystal phase quantification of a synthetic lignite gasifier slag system
Fuel Processing Technology, 201 (2020), <https://doi.org/10.1016/j.fuproc.2020.106345>
- 3. J.P. Schupsky, M. Guo, B. Blanpain, M. Müller**
Investigations on Crystallization Processes of Three Oxidic Gasifier Slag Systems
Journal of Energy Resources Technology, 142 (2020), <https://doi.org/10.1115/1.4046145>
- 4. J.P. Schupsky, M. Guo, B. Blanpain, M. Müller**
The Impact of Sample Homogeneity, Crucible Material, and Oxygen Partial Pressure on the Crystallization of Fe-Rich Oxidic Slag in CLSM Experiments
Journal of Sustainable Metallurgy, (2020), <https://doi.org/10.1007/s40831-020-00262-x>
- 5. J.P. Schupsky, M. Guo, M. Müller**
Investigations on Crystallization Processes of Three Oxidic Gasifier Slag Systems
Proceedings of the 44th International Technical Conference on Clean Energy, Clearwater, U.S. (2019)
- 6. J.P. Schupsky, M. Guo, B. Blanpain, M. Müller**
Influence of Parameters on the Crystallisation Behaviour of Oxidic Slag Systems Determined by CLSM Investigation
Proceedings of the 6th International Slag Valorisation Symposium, Belgium (2019)

Table of Content

Table of Content	I
1 Introduction	1
2 Fundamentals	4
2.1 Gasification Fuels	4
2.2 Gasification.....	7
2.2.1 Entrained Flow Gasification and Combined Cycles.....	7
2.2.2 Slag Formation	10
2.3 Rheology of Slags	11
2.3.1 Rheology Fundamentals.....	12
2.3.2 Network Theory and Basicity	14
2.3.3 Modelling of Slag Viscosity	16
2.4 Crystallisation	19
2.4.1 Fundamentals of mineralogy and crystallography	20
2.4.2 Nucleation, crystal growth and kinetics.....	23
2.4.3 Multicrystalline systems	27
2.4.4 Recent findings on oxidic gasifier slag crystallisation	29
3 Methods and Experiments	33
3.1 Slag Characterisation.....	33
3.1.1 Selection of Samples and Preparation	33
3.1.2 Hot Stage microscopy	34
3.1.3 Differential Thermal Analysis.....	35
3.1.4 Thermochemical Equilibrium calculations.....	37
3.2 Viscosimetry	37
3.2.1 Fundamentals and Sample Preparation	38
3.2.2 Set up and Measuring Campaign	38
3.3 Quenching Experiment.....	40
3.3.1 Sample Preparation and Setup	40
3.3.2 Experimental Parameters	42
3.4 Confocal Laser Scanning Microscope (CLSM)	43
3.4.1 Set up, Parameters and Procedures	43

3.4.2	Assessment of Experimental Parameters	44
3.5	Analytics	46
3.5.1	Analytical Preparation.....	46
3.5.2	Digital Microscopy.....	46
3.5.3	X-Ray Diffraction (XRD)	47
3.5.4	Scanning Electron Microscopy (SEM)	49
3.5.5	Measuring of Crystal Shapes.....	51
4	Results and Discussion	52
4.1	Slag Characterisation.....	52
4.1.1	Melt and Solidification Behaviour.....	53
4.1.2	Phase Predictions by Equilibrium Calculations	55
4.2	Viscosity of Slags	58
4.2.1	Viscosity measurement data.....	59
4.2.2	Isothermal crystallisation.....	62
4.3	Crystallisation Characteristics	66
4.3.1	Macroscopic Investigations.....	66
4.3.2	Structural Phase Determination	71
4.3.3	Chemical Phase Determination.....	74
4.3.1	Crystallisation Kinetics	81
4.4	Crystal Phase Quantification	87
4.4.1	Anorthite – ST-D-2, HKT, and SOM-1 Slag Systems	87
4.4.2	Spinel – HKR Slag System	93
4.4.3	Olivine – HKR Slag System.....	96
4.4.4	Melilite – HKR Slag System.....	99
4.5	Crystallisation in PiTER Slags	103
4.5.1	PiTER setup and Slag Origin	103
4.5.2	Crystallisation Characterisation and Comparison.....	104
5	General Discussion	108
5.1.1	Accordance of the Applied Methods and Experiments	108
5.1.2	Application of Crystallisation Results.....	111
5.1.3	Approach of model implementation	115
6	Summary and Outlook	117

Literature120
Index of Figures I
Index of Tables IX
Appendix XI
Appreciation XXII

1 Introduction

Our modern and globalised society is aware of the fact that anthropogenic CO₂ emissions have an accelerating effect on global warming. In regular global climate conferences, representatives discuss actions that could reduce the CO₂ emissions to weaken global warming. In 2015, 195 participating countries of the annual climate conference in Paris found consensus and ratified the so called Paris Agreement [1]. The long-term aim of the agreement is to hold the global temperature rise below 2 °C compared to the pre-industrial state. Even major emitters such as China, USA, India, Russia, Canada, Australia and the European Union ratified the Paris Agreement [1] and so induced a wave of optimism that the long-term aim can be achieved. Subsequently, however, a step backwards was marked by the USA withdrawing from the agreement in 2017, as announced by President Donald J. Trump [2]:

“As President, I can put no other consideration before the wellbeing of American citizens. The Paris Climate Accord is simply the latest example of Washington entering into an agreement that disadvantages the United States to the exclusive benefit of other countries, leaving American workers — who I love — and taxpayers to absorb the cost in terms of lost jobs, lower wages, shuttered factories, and vastly diminished economic production.”

This change of heart is a symbol of the accompanying conflicts that are associated with modern climate protection efforts. The purpose of implementing CO₂ poor or free technologies affords vast investments that cannot compete with the conventional techniques and it could possibly lead to lower employment rates. In terms of the energy sector, the fossil fuels: coal, oil and natural gas have been used since decades and respectively centuries, are widely implemented and a lot of experience has been gathered during their operation. Also the investments of those conventional fuel conversion techniques were depreciated and they generate profits any time. For such reasons, other countries such as Germany failed to achieve their own set milestones e.g. in the field of CO₂ neutral mobility [3]. Accordingly, the euphoria of the 2015 Paris Agreement was followed by disillusionment and disappointment among the societies. Based on such developments, dissatisfaction spread and protest movements aroused. Organisations and activist groups such as “Fridays for Future” were founded and created a platform that should convince politics, industry, and society to improve the climate protection efforts. As a summary, it must be accepted that the implementation of climate protection efforts is a tough challenge that will be dealt with for upcoming decades.

In the energy supply sector, a reduction of CO₂ emissions can be adjusted from two different perspectives. Firstly, the emitted amount of CO₂/kWh can be reduced due to an efficiency increase in the conversion of fossil fuels and due to the expansion of renewable energies. Secondly, the overall energy demand can be reduced, also by an efficiency increase and by an overall reduction of the electric demand.

The development of the European-28 energy supply will be used as an example to display the recent changes in the energy supply sector (Fig. 1.1). The traditionally strong contribution of fossil fuels is indicated by the supply distribution of 1990. Coal has the highest electric generation with 1050 TWh, followed by nuclear with 794 TWh. Renewables played only a minor role with a proportion of approx. 13% (333 TWh) [4]. The maximum energy generation was reached in the 2010s with approx. 3350 TWh. It can be summarised that the overall proportion of fossil fuels remained almost unchanged, since its share declined marginally from 56.5% in 1990 to 54.3% in 2005. While there was less coal converted, natural gas compensated the existing gap sufficiently (Fig. 1.1). However, after 2005 the increase of renewable energy sources can be noted for the recent years. On the one hand, the proportion of fossil fuels declined to 43% by 2015, while on the other hand, renewables rose to 30.5% [4]. Regarding the proceeding expansion of renewable energies, the European contribution of the global CO₂ emissions will likely decline further in the upcoming years. Even though Europe initiated its change to renewables, the overall electric supply remains at a high level and a serious reduction of the fossil energy sources seems not be likely for the near future (Fig. 1.1).

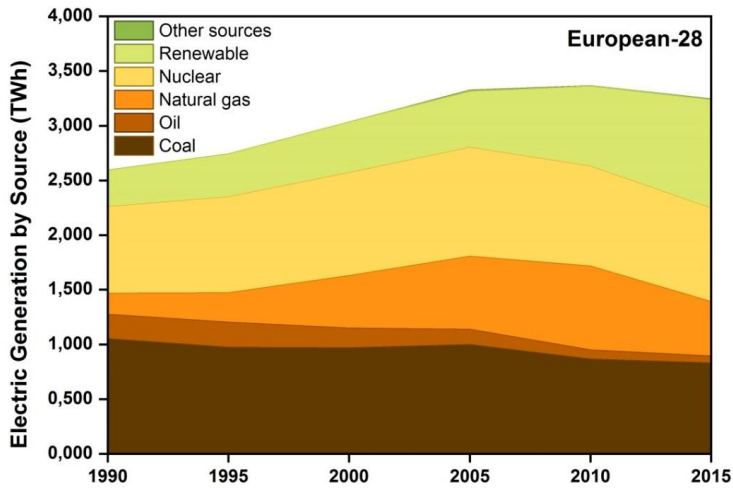


Fig. 1.1: Electric generation by source of the European-28. Data provided by the International Energy Agency [4].

Since trends in the global energy demand directly influence the CO₂ emissions, the global energy demand is displayed in Fig. 1.2. In the year 1990, the annual global energy consumption was about 73 PWh and rose to approx. 110 PWh in the year 2015. In the observed time period of 25 years, the global consumption increased by 50.3% [4]. This significant increase was not based on the growing economic strength of the industrialised countries, as can be seen e.g. by the energy supply increase of European countries by 25% and the USA by 38%. Moreover, the emerging countries such as India (+470%) and China (+943%) contributed majorly to the global rise of energy request [4]. Since China and India are the most populous and two of the most rapidly growing economies [5], they were chosen as representatives.

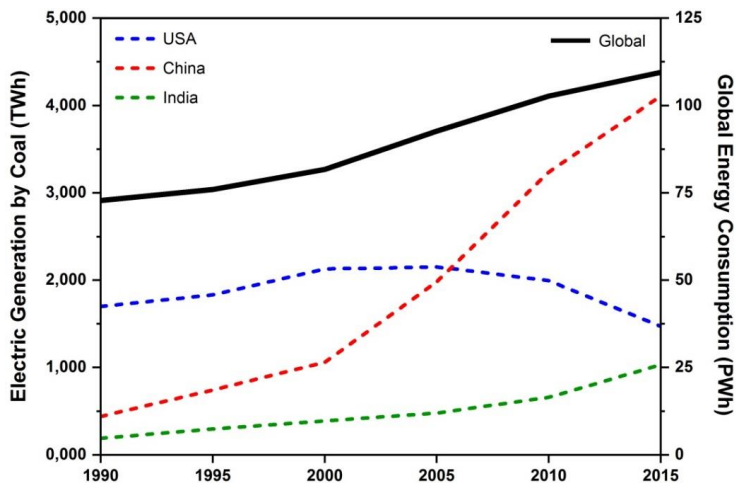


Fig. 1.2: Electric generation by coal of the countries China, the USA and India in TWh (left Y-axis) and the global energy consumption in PWh (right Y-axis). Data provided by the International Energy Agency [4]

The tremendous growth rates of India and China were carried by the vast use of fossil fuels as can be seen by the example of coal (Fig. 1.2). China increased its electric generation by the factor of nine in the observed 25 years' time period. India's electric generation also rose remarkably by the factor of 5 in the same time period [4]. China and India mined the most and fourth-most amount of coal globally [6]. Since they have generous national coal reserves it is a probable scenario that both countries will further expand their conversion of coal for strategic and economic reasons [5, 7]. India's estimated energy requirements are supposed to increase by a factor of four or five, drawing the same level as today's China [8], while China's demand could further increase by roughly 30% or even stagnate [5]. The coal fired industry is the working horse in China's energy supply system nowadays and a reduction with benefit of renewable energies is not expected [9]. Since the coal fired industry accounted for approx. 80% (2012) of China's total energy supply, pollutants such as CO, SO₂, O₃ and NO_x are emitted [10]. As a result, the air and life quality is reduced, especially during the winter and spring period in (north-) east China [10]. The transition to renewable energies could help to reduce environmental damage. Nonetheless, China's coal fire industry has a long tradition, decades of technical experience and has built new power plants whose lifetimes will not be surpassed in the following decade [6]. Accordingly, the implementation of renewable energy sources is not feasible for China. However, the importance of renewable energy sources is generally accepted, e.g. Wang et al., 2019 suggested to replace outdated coal fire facilities with state-of-the-art techniques to further use coal as the main energy source [9].

It can be summarised that the political will and the awareness of society for an active CO₂ reduction is present, though its practical implementation lags behind the expectations. While industrialised countries recently executed their transition to renewables, the emerging countries, especially India and China, pursue their economic growth on the basis of fossil fuels (i.e. coal). Since fossil fuel technologies are feasible for such countries, a rapid transition to renewable energy sources is very improbable. In contrast, bridge-building techniques could potentially be in focus of such countries. A technology is requested that uses the benefits of the numerous fossil fuel reserves on the one hand and on the other hand, helps the implementation of CO₂-neutral technologies or at least has a higher efficiency than conventional power plants. At the beginning of the 2020s, we still have to accept that further anthropogenic CO₂ emissions cannot be avoided in the following decades, that progress can only be made in small steps, and that the fight against global warming is a generation task we have to face.

Gasification is a flexible technology that has the potential to support the transition from a fossil fuelled to decarbonised energy supply system. During gasification, an oxidic residue is produced that is named as slag. Slag flow needs to be constant in a gasifier, but a high viscosity impairs the flow behaviour. The phenomenon of crystallisation has such effect, yet is only barely understood. Viscosity of slag can be modelled and therefore predicted. However, no sufficient model exists to calculate the viscosity of partly crystallised slags. A sufficient data source of crystal morphology data is required to enable the application of an improved viscosity model for partly crystallised slags.

Therefore, the aim of this work was to investigate the crystallisation of oxidic gasifier slags. Special focus was set on the characterisation of individual phases growing in the slag. Their crystal morphologies were defined based on the results of performed SEM and CLSM investigations. These morphologies are in agreement with the individual crystallographic properties of the crystals and accordingly, represent the crystals nature at best. The crystals dimensions were quantified with respect to the applied temperature. As a result, morphology datasets of the crystallised phases: anorthite, spinel, olivine, and melilite were gathered in this study that can be applied in an improved viscosity model for partly crystallised slags.

2 Fundamentals

To understand the importance of research on slag crystallisation, a broad understanding of crystallisation, slag rheology, gasification, and fuels is required, firstly. Thus, this section provides fundamental knowledge about these individual topics. It will be started with a brief description of fuels, as their residues form the slag in gasifiers. To understand the procedure and the parameters of gasification, the process of (entrained-flow) gasification is explained in the following. As a next step, rheological fundamentals will be provided as they enable the judgement if a slag flow is sufficient or fails due to a high viscosity. Lastly, the crystallisation process is described from several perspectives since it is of a complex nature.

2.1 Gasification Fuels

As concluded in the introduction, the transition from fossil fuels to renewable energy sources is a long-term process that requires bridge-building techniques. While the advantages of solar thermal, photovoltaic, wind and water are known, their implementation has to face the comparable cheap fossil fuels. Therefore, coal as a major energy source (Fig. 1.1) will be used in combination with CO₂ neutral fuels, such as biomass and in combination with new power generation techniques. Ultimately, this chapter will focus on the fuels coal and biomass, as well as on new techniques besides conventional power plants.

Coal is a natural resource that was formed by geological processes over millions of years [11]. The starting substance of coal was basically the organic matter of diverse lifeforms that inhabited our planet in the Palaeozoic. In detail, various today's coal reserves are based on the early ecosystems of the Carboniferous and Permian [12, 13], as well as more recent Tertiary deposits [14]. In the Carboniferous, flat lands and swampy regions were covered with forests accompanied by an already diverse fauna. Those lifeforms died eventually and were deposited by sediments (mainly fluvial) and debris [13, 15]. Under regular conditions, bacteria would use organic matter as their feedstock, but in numerous regions, anaerobic conditions were present that prevented such disintegration. The early state of coal can be compared with recent peat fields. Those organic deposits were further deposited with sediments until they reached sufficient depths where diagenesis influenced the properties of the organic matter. Generally it can be stated that with an increase of depth, the physical parameters: pressure and temperature increased [16]. This process leads to a release of volatile compounds such as CO₂ and N₂ as well as to the formation of CH₄ [17]. The moisture content also declines from 70% (peat) to approx. 15% in the end product anthracite. In between peat and anthracite, there are several forms defined, the superordinate categories are lignite and bituminous coal [17]. Since the amount of volatiles and water is higher, while the carbon content is lower in lignite, the calorific value is in favour of bituminous coal [17].

Since coal consists of organic matter in sedimentary rocks, there is also mineral matter included in the deposited coal seams (Table 2.1). Since the Palaeozoic organic matter was covered by sediments under fluvial or marine influence, the associated mineral phases are reasonable. Clay minerals derived from any fine grained sediments, carbonates form as part of the evaporate series or are recycled marine rocks [18] and quartz is the ultimate remaining product of eroded continental rocks due to its comparable high hardness. It can be summarised that the main mineral content in a generalised coal consists of the following elements: Si, Al, Ca, Mg, Fe, K, S, O, and H.

Table 2.1: Generalised mineral phases included in coal. Data based on [19], modified after [17].

Classification	Mineral phase	Chemical formula	Fraction (wt%)
Clay minerals	kaolinite	$\text{Al}_2\text{Si}_2\text{O}_5(\text{OH})_4$	< 50
	illite	$(\text{K},\text{H}_3\text{O})\text{Al}_2(\text{Si}_3\text{Al})\text{O}_{10}(\text{H}_2\text{O},\text{OH})_2$	
Carbonates	calcite	CaCO_3	< 20
	dolomite	$\text{CaMg}(\text{CO}_3)_2$	
	siderite	FeCO_3	
Oxides	quartz (incl. modifications)	SiO_2	1- 15
Sulphides	pyrite	FeS_2	< 20
Accessory minerals	plagioclase (feldspar)	$(\text{K},\text{Na})\text{AlSi}_3\text{O}_8$	< 1
	hematite	Fe_2O_3	
	apatite	$\text{Ca}_5\text{F}(\text{PO}_4)_3$	
	halite	NaCl	
	rutile	TiO_2	

In contrast to coal, biomass is a CO_2 neutral fuel, as it is defined as “*non-fossilized and biodegradable organic material originating from plants, animals and micro-organisms*” [20]. Biomass is formed by the flora and fauna that interacts with H_2O , CO_2 , Air, soil, and sunlight [21]. For the case that the flora and fauna dies, its compounds are broken down by microorganisms and potential energy is lost. Nonetheless, since the former lifeform accumulated all of its potential energy and CO_2 during its lifetime, biomass is called greenhouse gas neutral [21] or simplified: CO_2 neutral. As indicated by the aforementioned definition of biomass, it is a heterogeneous fuel and can be divided in the following categories [21]: agricultural (straw, bagasse, nutshells, etc.), forest (trees, wood waste, mill scrap, etc.), municipal (sewage sludge, food waste, yard clippings, etc.), energy crops (switchgrass, alfalfa, canola and other oil plants), and biological (animal waste, aquatic species, biological waste). Since biomass sources are various, the description of its chemical character helps to estimate its suitability as a fuel. As an example, the generalised composition of dried plant biomass is shown in Table 2.2 .

Table 2.2: Ten most abundant elements in a generalised dried plant biomass. Data provided by Kaltschmitt et al., 2016 [22].

Element	C	O	H	N	K	Ca	Si	Mg	Cl	S
(wt%)	42-47	40-44	6	1-5	0.3-5	0.3-5	0.05-3	0.05-1	0.02-1	0.05-0.8

Approximately 90% of the dried plant biomass is build up on carbon and oxygen [22]. Hydrogen is produced through hydrolysis out of the absorbed water. The elements N, K and Ca are the major plants’ macronutrients, while Si is deposited in the cells to increase the growth stability [22]. When biomass is converted into energy, biomass loses its amount of carbon (since it is converted), as well as the volatile compounds and remaining humidity. As the mineral compounds have low portions of “waste” residues. Regarding coal, a particle could lose up to 70-80% of its weight (release of humidity, volatiles, tars, and other organic compounds) during the conversion [16]. The comparison of coal mineral elements (Table 2.1) with the dried plant composition (Table 2.2) shows, that there is an accordance of several major elements that will remain in both fuels after the conversion: Si, Al, Ca, Mg, K, S, and O (in mineral matter). Also, minor elements such as Fe, Na, Ti, and Mn can be found in the residues [23, 24].

To compare both fuels in terms of their suitability for thermal conversion to produce energy, several properties need to be considered, exemplary the energy density, volatile content and the ash content will be described briefly [16, 25]. The energy density (MJ/kg) of coal is generally higher compared to biomass, since it experienced a diagenesis (and metamorphosis) and therefore lost

moisture and volatile compounds. The content of volatiles diverges strongly between biomass and coal. In wood and torrefied wood, the volatile content lies in the range of 55-80%, while in charcoal and bituminous coal only 10-45% volatiles are included [21]. Further classification of both fuels is made by the van Krevelen diagram [26, 27]. In general, higher values of carbon, lead to improved heating values of the fuel [21]. As can be seen in Fig. 2.1, the H/C and O/C ratio is in favour of peat and biomass respectively, while lignite, coal and anthracite have lower values. Accordingly, the fossil fuels have improved heating values compared with biomass. This finding is reasonable, due to the lower amounts of moisture and volatiles since coal-based fuels have experienced a diagenesis [16, 21].

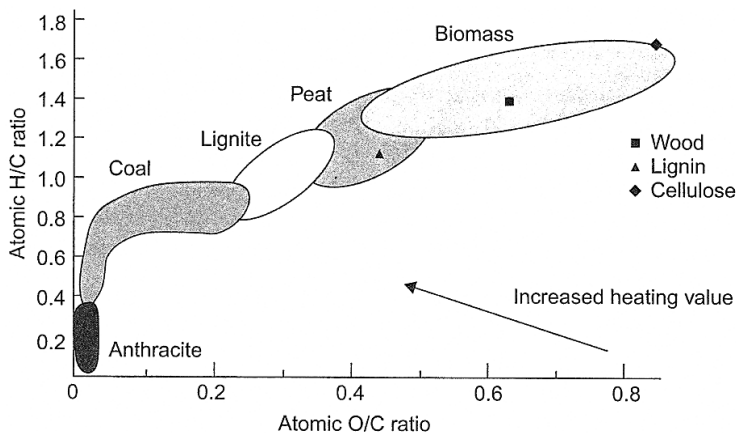


Fig. 2.1: Classification of coal-based and biomass fuels, regarding the H/C and O/C ratio. Data provided by [28], as seen in [21].

The assessment whether coal or biomass play the major role in the latest and future energy supply industry is clearly out in the favour of coal. Coal conversion generates 41% of the global electric supply (2015 [29]) and therefore, the vast used fuel today. Also, its world market price is stable and low compared to oil and natural gas [29]. Furthermore, the world reserves are estimated to last for more than 100 years [30]. In contrast, the global role of biomass is minor. The current portion of biomass to the primary energy consumption is 10.6% [17]. Since biomass has a lower content of carbon and therefore less heat yield, more volumetric biomass is needed. The majority of nowadays biomass is based on wood and by-products from the wood industry. However, the amount of wood that can be recultivated is limited and other sources of biomass such as energy crops compete with food crops for agricultural land. Biomass has a maximum technical potential of approx. 100 EJ/year and could therefore be accountable for 22% of the global primary energy consumption of 2006 levels [17].

Finally, it can be stated that coal and biomass are two sides of the same coin, separated by their age and the conditions they have experienced. Both are based on organic matter of former lifeforms. Since coal has experienced diagenesis and metamorphism, it is enriched in carbon and depleted in e.g. volatiles and humidity. The remaining mineral compounds (after the conversion) are mainly equal, though their distribution differs. Since the availability of biomass has certain limitations, coal will very likely be in favour for the energy supply industry.

2.2 Gasification

It was concluded that the significance of fossil fuels (i.e. coal) will not vanish in the industrialised countries in the near future and will very likely increase in the emerging countries. Conventional coal power plants have the ability to convert a large amount of fuel and thus produce large amounts of electricity. However, in the industrialised countries, most of such power plants have been built decades ago, have limited efficiency and are no longer state of the art. Based on their design and their high conversion rates, a load flexible operation can cause serious issues e.g. by the fouling behaviour [16, 31]. Since the renewable energy sources are not fully extended yet, conventional coal power plants have to close the gaps in the energy supply sector. In contrast to power plants, gasifiers can be operated in load flexible operation [17, 32]. Furthermore, the starting times of a gasifier are shorter, that gives another advantage to gasification technology [17]. Additionally, an operation with both, coal and biomass in the same facility can be realised [17, 22]. Also, gasifier plants can reach efficiencies of 50%, which is higher compared to conventional power plants [15, 33]. As a result, gasifier technology enables reduced CO₂ emissions that can support the transition to CO₂ neutral energy supply systems. All in all, gasifiers have several benefits compared to conventional (coal) power plants that can be applied successfully in the modern energy supply sector.

2.2.1 Entrained Flow Gasification and Combined Cycles

Gasifiers can be divided into three types of functions: fixed bed, fluidised bed and entrained flow gasification (or: pulverised bed gasification) [17]. Fixed bed systems are based on a solid, stationary fuel bed. Air is blown in from the bottom, feeding the combustion process and generating the highest heat load in those bottom regions. This heat is consumed by devolatilization processes and gasification reactions in the upper part. As the fuel is fully converted, the remaining residues fall through a grate and the next layer of fuel respectively coke can be converted. The process maintains, as long as the process is fed by fresh air (bottom) and fuel (top) [17]. A fluidised bed system has comparable fundamentals. The reactor is filled with fuel from the top and air (or oxygen and steam) is blown in from the bottom regions. However, due to high gas flow rates, the bed becomes fluidised. The fuel-air suspension starts to circulate, floats and behaves like a fluid. Produced ash has to be removed and new fuel to be injected. In both gasifier types, the fuel residence time is noticeably longer compared with the gas flow [17]. Since entrained flow gasification is of higher relevance for the energy supply sector and also potentially for the chemical industry [15, 17], entrained flow gasification will be described in detail.

Fig. 2.2 displays the basic design of a Siemens SFG (Siemens Fuel Gasification) gasifier. The process was developed in the 1970s in Freiberg (Germany) to gasify lignite and was further enhanced in 1991 to gasify also waste materials and liquid residues [15]. The SFG gasifier concept is based on a vertical reactor, where gas, oxygen and fuel are injected through a burner at the top (Fig. 2.2) [34]. There are three advantages of the SFG design: reduced equipment cost due to axisymmetrical construction, reduction to only three controllable flows (oxygen, steam, coal) and hot gas and ash residues leave the reactor together, which reduces the probability of blockages [15]. Based on the SFG concept, different variations can be designed that apply to the individual fuel used. The reactor shown in Fig. 2.2 includes an actively cooled screen that is in contact with the remaining residues [35]. According to the relatively intense cooling performance, this type is used for fuels with ash contents higher than 3% [36]. Fuels with lower ash contents (<2%) can be converted in a SFG gasifier with simple cooling walls, since less fuel residues are produced [36]. In the late 2010s, five SFG reactors (500 MWh power each) were produced for a Chinese project, to generate chemicals out of coal [37].

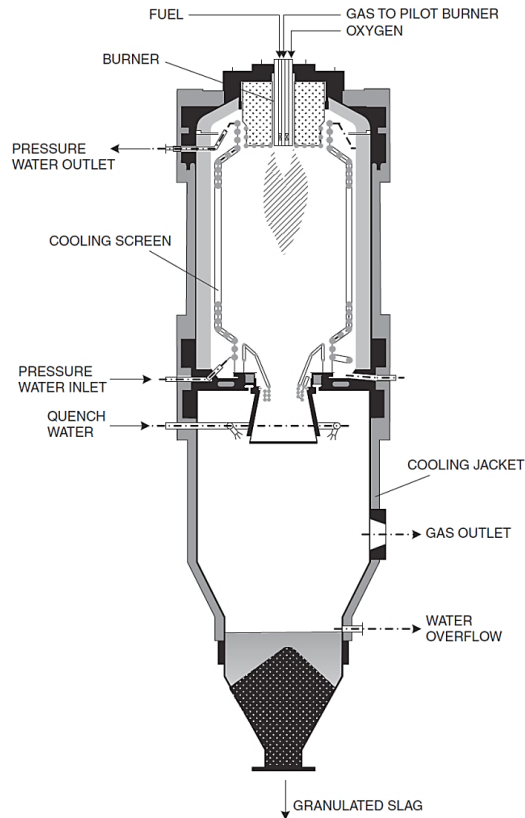


Fig. 2.2: Sketch of the Siemens SFG Gasifier with cooling screen, as shown in [15].

Besides, the use of gasifier technology enables further use-cases next to power generation. Gasifiers can be operated as a single reactor only for power generation, like it is the case for conventional coal power plants. However, since the fuel is not simply combusted but converted instead, a syngas is produced that serves as a resource for further application [7, 17, 38, 39]. The syngas consists of compounds such as H_2 , and CO [39, 40] that are released from the fuel char particles. This process will be described at the end of this chapter in more detail. The syngas is treated in a gas processing unit that can separate several gas phases from the syngas, depending on the facility design. As a last step, the remaining syngas is used to run a combined cycle power plant for power generation. The overall process, including gasification, syngas treatment/separation and combined cycle power plant is described by the integrated gasification combined cycle (IGCC). In 2008 the global cumulative gasification power was about 70 GWth, indicating that IGCC technology is already applied with certain extend [15, 17].

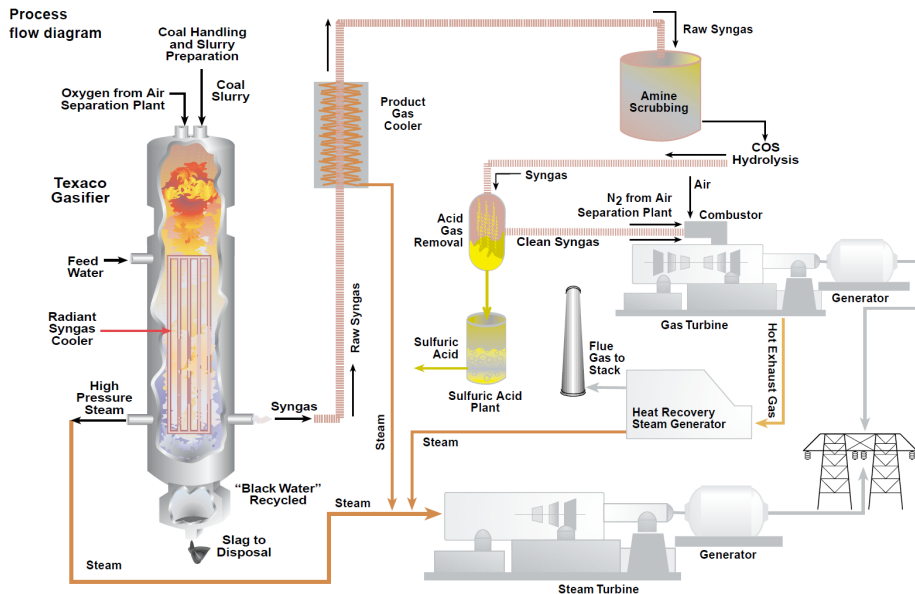


Fig. 2.3: Simplified flow diagram of the Polk Power Station process (Tampa Electric, USA) [41], as an example for an IGCC plant.

Polk Power Station (PPS, Tampa Electric, Florida, USA) will be briefly explained as an example for the IGCC process (Fig. 2.3). PPS unit 1 produces approx. 250 MW (netto) of electrical power and was put into operation in 1996 [41, 42]. In ideal operation, the gasifier produces between 2200- 2500 t/d of syngas out of the applied fuels: hard coal, petroleum coke and biomass [41, 42]. The molten fuel residues flow in a quenching unit where they solidify. Excess syngas heat is recovered in a cooler and the syngas surpasses an amine scrubbing unit afterwards (Fig. 2.3). Subsequently, COS is converted into H_2S in a hydrolysis reactor [41]. The produced hydrogen sulphide (acid gas) is removed by scrubbing with amine solvent. Finally, the clean syngas is combusted in a gas turbine for electric power generation, in addition to the extracted gasifier steam beforehand (Fig. 2.3). The abovementioned desulphurisation is one utilisation of the byproducts in the syngas, e.g. also applied in the IGCC plant in Buggenum (Belgium)[43]. However, since there are also hydro carbonates included in the syngas, CH_4 , CO and H_2 can be valorised as well [15, 17]. Customised (dual-phase) membranes can be implemented in the syngas separation unit to separate H_2 by water-gas-shift reactions [44, 45], or to separate CO_2 by e.g. carbonate-ceramic membranes [46].

As mentioned above, fuel and feeding gas are injected at the top of the entrained flow gasifier. The fuel is converted on a millisecond time frame. That high reaction kinetics can only be achieved by several steps of fuel treatment and reactions: drying, pyrolysis, ignition, conversion of volatiles and residual char [15, 39, 47, 48]. Initially, the char particles experience a preheating of a few hundred degrees Celsius (Fig. 2.4), which is sufficient to release adsorbed (pore) water [17]. Pyrolysis describes the process of the decomposition of organic coal substance, resulting in the formation of gaseous products [17, 49, 50]. In the temperature range between 300 and 600 °C, the char particle releases tars and other light hydrocarbons such as CO_2 and CH_4 and it begins to soften and to swell, due to this inner gas and tar formation [17, 51]. Regarding the limited particles size (<100 μm), drying and pyrolysis are completed in less than 0.1 seconds and approx. half of the carbon is burned out (Fig. 2.4) [17]. The remaining carbon is converted into syngas in the "burnout" zone. Since the carbon was converted, fly ash with particle sizes of less than 10 μm remains from the gasification process (Fig. 2.4). Depending on the ash properties and on the gasification temperature, the ash is present in a solid or in a liquid state. If the slag is in a liquid state, it is named as slag.

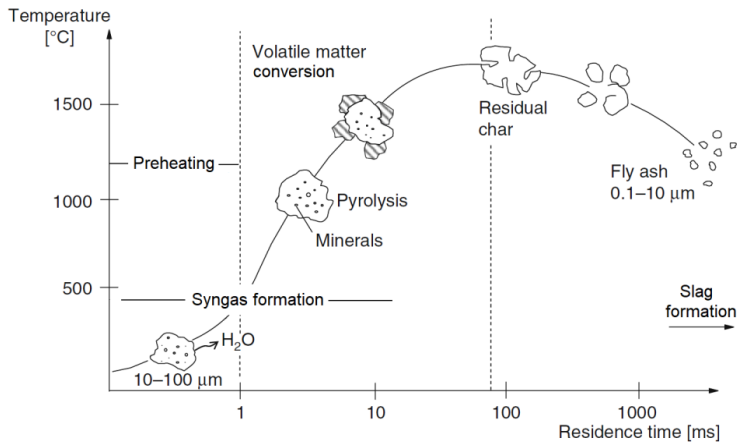


Fig. 2.4: Schematic drawing of the gasification process in entrained flow gasification, modified after [17].

2.2.2 Slag Formation

The phenomenon of slagging is common in entrained flow gasifiers. The aforementioned SFG Gasifier and the Gasifier at PPS are also slagging gasifiers (Fig. 2.4, Fig. 2.3). In contrast, if the fuel residues would be in a solid state, the process would rather be named as fouling [17]. Both, fouling and slagging influence the gasification process in several kinds, so their behaviour needs to be considered by the design of a gasifier. Entrained flow gasifiers are high temperature gasifiers and therefore produce molten ash, respectively slag [15, 17]. Since the crystallisation of fuel residues requires a liquid state, this chapter will focus on the slag state of fuel ash.

Slag formation itself is an inevitable process that is strongly related to the composition of the fuel and the gasification temperature [17]. Since carbon was converted and water and volatiles are released to form the syngas, the mineral matter remains as the non-convertible species in the slag (as seen in chapter 2.1). Accordingly, the composition of the mineral matter strongly corresponds with the slag composition. If the mineral matter contains high amounts of silica, the ash has high melting points and high viscosities [52]. In contrast, alkalis such as K and Na, reduce the melting point and the viscosity, as long as they are present in small amounts [53, 54]. Nonetheless, it must be noted that the mineral matter does not always liquefy. Minerals with high melting points, especially quartz (SiO_2) tend to withstand the melting procedure and so form solid artefacts in the liquid slag [55]. As a result, the melting behaviour of fuel ash is of high importance for the gasifier operation.

The slag formation in a(n) (entrained flow) gasifier serves both, advantages and disadvantages during the operation. The major advantage of slagging is the formation of a slag layer on the cooling screen or refractory walls. Since the fuel is injected with high velocities in the gasifier and turbulence is generated by the downstream and the conversion, slag droplets get deposited on the walls and form a layer of liquid slag [17]. The slag down-flow is called slag tapping and will not break off, since there is new slag deposited frequently. Especially for biomass slags, notable amounts of sulphur and chlorine are released during the gasification [15, 22]. During the conversion, they can form alkali sulfides and alkali chlorides that can condensate on the refractory or cooling screens. If comparably low amounts of sulphur are present, KCl and NaCl are forming, that leads to serious high temperature corrosion [22]. In a slagging gasifier however, a produced slag layer covers the cooling screen or refractory walls. Due to the reduced temperatures at these reactor lining or refractory materials, a solidified slag layer forms. The solid slag layer is covered with new liquid slag, due to the constantly ongoing slag production (Fig. 2.5). The solidified slag layer ultimately prevents the lining

from chloride condensation and so, corrosion incidents become less relevant [15]. Higman & van der Burgt (2008) report further that the slag layer is a self-healing layer that allows a wall service life of 8-10 years and overall lifetimes of about 20 years [15].

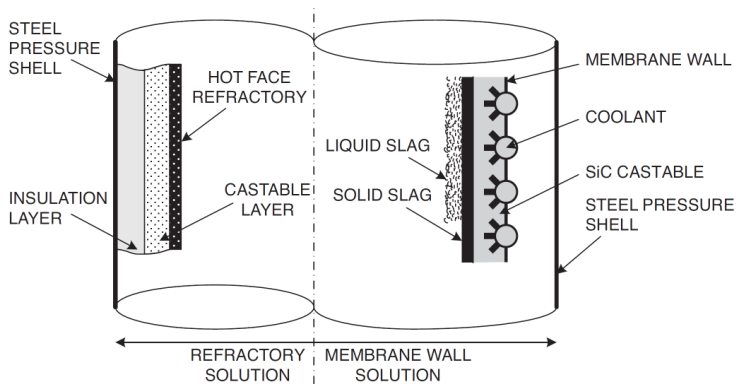


Fig. 2.5: Sketch of refractory lining (left) and membrane walls (right) covered with slag, as shown in [15], source [56].

Accordingly, the permanent presence of solid and liquid slag layers is a useful side product against corrosion on the one hand, but on the other hand a blockage of the slag tap can cause serious incidents. For example, if the flow behaviour of the liquid slag is not sufficient, more and more slag becomes stationary and the slag tapping process comes to succumb [57]. As a result, the heat absorption of the refractory walls as well as the efficiency is reduced. In a worst-case-scenario, an existing slag blockage has to be removed in the sense of maintenance duty. Such incidents reduce the feasibility of gasifier plants, since a gasifier shut down is obligatory for the maintenance and so, no power or syngas can be produced [58]. It can be summarised that slag layers on the inner reactor lining serve as protectives against syngas corrosion, yet include the risk of slag tapping blockage. Because of that the flow behaviour of slag and the influencing parameters are discussed in the following section.

2.3 Rheology of Slags

The flow behaviour of gasifier slag is an important parameter that needs to be considered for a successful gasifier operation. The flow behaviour is generally described by the viscosity η (Pa·s) [32, 53, 54]. In case of the previously described slag formation in entrained flow gasifiers, the investigation and the prediction of the viscosity is in the research scope. General findings, such as a constantly required slag viscosity of less than 25 Pa·s is generally accepted and guarantees a successful gasifier operation [15, 17]. However, the slags' rheology is almost never constant and influenced by several factors such as: temperature, composition, crystallisation and the partial pressure of oxygen [32]. The combination of all factors not only varies between different gasifiers types, but may also change in the same reactor over time, by the spatial position, and the operation parameters. To summarize, the slag viscosity is an important and complex research field, whose understanding is of great importance for gasifier plant designers and operators. Vargas et al., (1999) [53] and Liu et al., (2018) [60] created extensive summaries of the fundamental rheological properties of coal slags and silicate melts that will be mainly referred to in this section.

2.3.1 Rheology Fundamentals

The rheological behaviour of fluids basically describes the flow of materials. Therefore, rheology accounts for solid materials as well as for liquids. The investigation of gasifier slag flow behaviour is only one application area among others. For example, in the field of metallurgy, the flow behaviour of silicate slags is essential when it comes to the removal of slag during steel casting [53]. Another use case compared to gasifier slags can be found in the field of geology. The flow of mantle rock or magmas is an important process in endogenous fields such as: plate tectonics, geochemistry and volcanology. Earth mantle rock is based on silicate minerals and is therefore comparable with the gasifier slag systems [53]. To clarify the analogy between gasifier slag systems and endogenous systems a natural example was chosen (chapter 2.4.3) to state those similarities.

Viscosity is the mainly investigated property of materials in the abovementioned disciplines. The viscosity of a material describes the materials resistance towards an applied external motion due to internal friction of the material [53]. The viscosity can be explained by a simplified model concept that is commonly used to illustrate the physically background (Fig. 2.6).

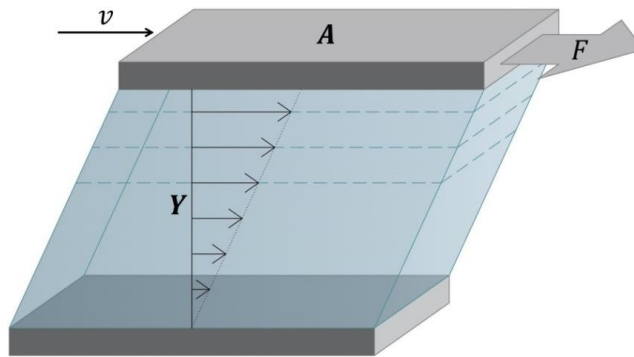


Fig. 2.6: Conceptual illustration of the viscosity. A represents the surface area of the plates; Y the distance between both plates; v represents the upper plates velocity and F the applied force on the upper plates.

In the above figure, a fluid is located between two parallel orientated plates, having the similar surface area. While the bottom plate is fixed, the upper plate is moved in a certain direction with a specific velocity v and a specific force F (Fig. 2.6). The fluid is sheared between the plates with linear distribution, assuming that the fluid flow is not turbulent [53]. The viscosity can be described as the applied force F (N) divided by the unit area A (m^2) of the plate per velocity gradient (s^{-1}) (Eqs. 1, 3) [53]. For further continuity, the unit Pa·s will be used to determine the viscosity, since it is based on the SI-unit systematic. The viscosity was firstly described by Newton, as the ratio between shear stress τ (kg/s^2m) and the shear rate $\dot{\gamma}$ (s^{-1}) (Eq. 2) [61, 62].

$$\eta = \frac{F}{A} \cdot \frac{Y}{v} \quad (1)$$

$$\eta \equiv \frac{\tau}{\dot{\gamma}} \quad (2)$$

$$1 \text{ Pa} \cdot \text{s} = 10 \text{ P}(\text{poise}) = \frac{N \cdot s}{m^2} = \frac{kg}{m \cdot s} \quad (3)$$

With an increase of the viscosity value, a certain medium behaves tenacious towards deformation (shearing). Vice versa, the lower the viscosity value the runnier behaves a medium. Some examples for everyday liquids are given: water = 0.001 Pa·s, machine oil = 0.1 Pa·s, glycerol = 10 Pa·s, olive oil =

100 Pa·s [53]. The described fundamental equations were used to determine the viscosity of the analysed slag systems from viscosity measurements. The applied methodology for viscosity measurements will be described in chapter 3.2.

A Newtonian fluid is marked by a linear relationship between the shear stress and the applied strain rate. Therefore, the relationship displayed in Eq. 2 is constant [32, 62]. Also, Newtonian fluids do not show a change of the rheological character by time [53]. Natural examples of Newtonian fluids are water, air and oils. Though, if the linear relationship between shear stress and strain rate is invalid, the fluid is described as non-Newtonian. Non-Newtonian behaviour describes several flow type characteristics [53, 60-62]. Two flow categories are displayed in Fig. 2.7, shear thickening and shear thinning behaviour.

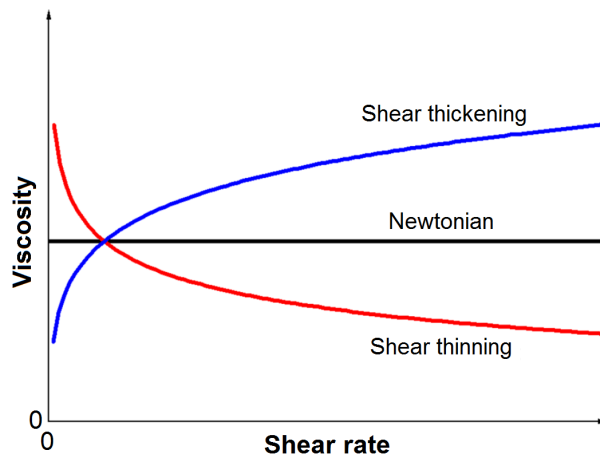


Fig. 2.7: Rheological characteristics of liquids and materials with shear thickening and shear thinning behaviour, compared with a Newtonian behaviour. Modified after [60].

Shear thickening behaviour describes a positive correlation of the viscosity with the applied shear rate, which means that a fluid behaves more tenacious. Shear thickening is often observed in suspension with high concentrations of solid particles with uniform size distributions that form clusters at high shear rates [32, 53, 60]. However, for silicate systems, such as gasifier slags, the contrary flow behaviour is more relevant – shear thinning.

Shear thinning describes the process of a reduced viscosity at higher shear rates. By applying the example of grown crystals in a gasifier slag, high viscosity is observed at low shear rates, due to the physical resistance of the crystal particles in the liquid [53, 60]. The individual resistance varies, depending on the amount, size and morphology of the crystal phase. However, as the shear rate is increased, the shear stress drags on the particles and they begin to rotate and align parallel to the direction of the applied shear stress [60]. Accordingly, the crystal orientation results in a viscosity decrease, as their hydrodynamic character has improved. As gasifier slags are liquids dominated by silicates, shear thinning behaviour is also expected without the presence of crystals. Van der Waals force allows silicate molecules to arrange in a cluster or network structure that generates a certain resistance in the fluid. If the shear rate exceeds a specific value, those structures were ripped apart and the lack of resistance leads to a decrease of the silicate melts' viscosity [53, 60]. Though, the impact of a solid fraction (e.g. crystals) on the viscosity of silicate melts is more significant, the effect of cluster and network formation is a basic property that needs to be considered. For this reason, the fundamentals of network formation are briefly described in the following chapter.

2.3.2 Network Theory and Basicity

Gasifier slags and silicate melts can be seen as liquid glass. Though liquid glass is a fluid, it has an internal structure in contrast to other fluids, e.g. water. In a liquid medium, a completely random distribution of atoms or molecules is assumed, there is no inner structure existing. However, glass bearing melts show a certain internal arrangement of its silicate compounds on a very small scale, even though such melts have no structure on a larger scale [53]. An ancient theory of Frankenheim (1985) describes very small crystallites that build up a glass structure. The crystallites are arranged randomly, resulting in an amorphous macrostructure [63]. For multicomponent systems, different crystallites shall form in the liquid glass. In contrast, the modern interpretation of the inner glass structure differs, based on X-ray analysis of glasses [64]. It was proposed that silicon is mainly responsible for the inner structure formation as it is tetrahedrally surrounded by oxygen atoms [53]. As a result, a SiO_4 tetrahedron is formed that is defined as the smallest structural unit in a silicate glass. This fundamental concept is generally accepted and was extended in recent decades [53]. Since the SiO_4 tetrahedron is described as the smallest unit, it is capable of forming larger units of higher order that overall build up the so called network structure.

The coordination of the silicate tetrahedra is strongly influenced by the content of SiO_2 in the melt. Bockris et al. (1955) postulated several silicate ions (Fig. 2.8) that increase in dimension with a rising content of SiO_2 [65]. While having a 50% SiO_2 content in the melt, the $(\text{Si}_3\text{O}_9)^{6-}$ ion is present. Instead, a $(\text{Si}_9\text{O}_{21})^{6-}$ ion requires SiO_2 contents of 75% [65]. However, it is assumed that equilibrium mixtures exist, though the content of SiO_2 may stay constant [65]. Fig. 2.8 indicates that the length of silicate ions increases, as the SiO_2 content rises as well. In terms of the viscosity, silicate-rich melts have a higher viscosity, since the larger ion structures build up the silicate network and therefore generate more resistance to shear stress.

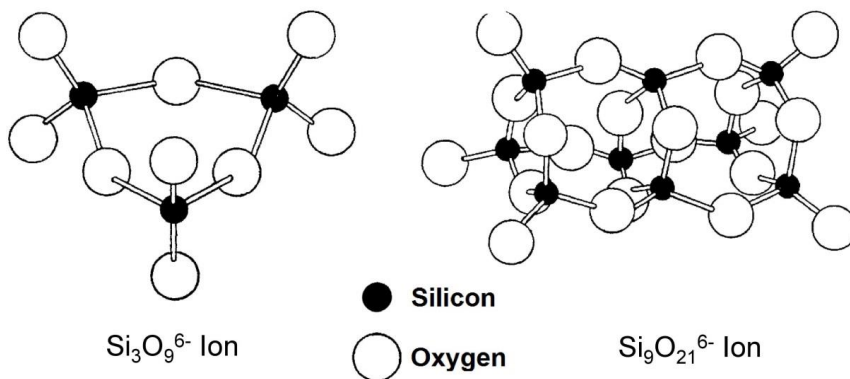


Fig. 2.8: Two suggested structural ions in silicate melts, modified after [65].

As can be seen in Fig. 2.8, the silicate ions form three dimensional structures, which include gaps in between the oxygen atoms. Those gaps are often occupied by positive metallic or alkali atoms that can be stabilised in the silicate structures due to their polar bondings [53]. An analogy on a molecule basis is found in the field of mineralogy. Silicate minerals are divided into silicate groups, based on the complexity of the Si-O bonds [66, 67]. In between the SiO_4 tetrahedra, also metallic and alkali atoms are settled. The structural and chemical similarities of oxidic gasifier slags and magmatic melts are causal for the network theory application in both fields.

It can be summarised that the presence of a network structure accounts for a viscous behaviour of silicate melts. Hence, the network structure relies on Si^{4+} , it is named a network former [53, 68]. Next to Si^{4+} there are only two further (transition) metals occupying the same function: Ge^{4+} and Ti^{4+} [53]. Accordingly, slags and silicate melts consist of further compounds, which have a different impact on

the network structure due to their varying oxidation state and atom radius. Hence, cations are divided into three different groups: network formers, amphoteric and network modifiers (Table 2.3).

Table 2.3: Network forming, amphoteric, and modifying cations in silicate melts [53].

Function	Cations	Effect on network structure
network formers	$\text{Si}^{4+}, \text{Ge}^{4+}, \text{Ti}^{4+}$	strengthen
amphoterics	$\text{Al}^{3+}, \text{Fe}^{3+}, \text{B}^{3+}, \text{Zn}^{3+}$	dependency on composition
network modifiers	$\text{Na}^+, \text{K}^+, \text{Mg}^{2+}, \text{Ca}^{2+}, \text{Fe}^{2+}, \text{Cr}^{3+}, \text{V}^{5+}, \text{Ba}^{2+}, \text{Sr}^{2+}$	weaken

In contrast to the network formers, network modifiers disturb the network structure and are able to reduce the viscosity of the silicate melt [54, 69]. Based on their abundance, Ca^{2+} , Fe^{2+} , Mg^{2+} , Na^+ , and K^+ are the most relevant cations for gasifier slags. Amphoteric cations have a more diverse character, since they can act as network formers or modifiers [53, 54, 69]. Their function depends on the charge balance by the available network modifiers and they can form metal-oxygen anion complexes [53]. Due to the presence of this complex, amphoteric species such as Al^{3+} can substitute Si^{4+} cations and support the network. The charge compensation phenomenon is described for such substitution by the presence of Na^+ cations [70]. Al^{3+} and Na^+ form the $(\text{NaAl})^{4+}$ species that is capable of substituting the silicon cation. However, if the formation of such complexes fails due to a lack of modifiers, amphoteric species behave as modifiers and distort the network [53]. Fig. 2.9 displays a two-dimensional random network of an oxide glass. The network forming species are connected with covalent bonds, generating viscous behaviour in the dashed regions [69]. However, network modifiers disrupt the network, by breaking up the covalent bonds. The bonding forces henceforth consist of weaker ionic ones. As a result, percolation channels exist in the oxide glass that represent low viscous pathways (Fig. 2.9) [69].

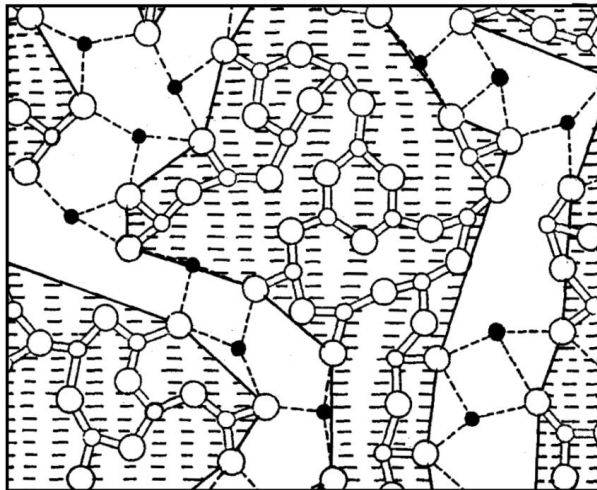


Fig. 2.9: Sketch of a two-dimensional modified random network of an oxide glass. White circles = network former, black dots = network modifiers, solid lines = covalent bonds, connecting dashed lines = ionic bonds. Modified after [69]

Since the cations are now clearly associated with certain functions in silicate melts/slags, the concept of basicity i.e. the base/acid-ratio can be introduced. The oxide species of the abovementioned cations can be divided into acidic and basic species. While oxides with a supporting role for the network are the acidic species and oxides with disruptive properties on the network account as the

basic species [53]. Since the role of amphoteric species depends on the presence of modifiers, the transition between both categories starts to vanish. The common basic concept of basicity was described by Nowok et al. (1994) [71]:

$$\frac{\text{Base}}{\text{Acid}} = \frac{Na_2O+K_2O+CaO+MgO+FeO}{SiO_2+Al_2O_3+Fe_2O_3+TiO_2} \quad (4)$$

Based on the abovementioned definition of the basicity, further precise definitions have been made. Another concept of basicity was described by Senior & Srinvasachar (1995) [72]. The authors included the binding properties of oxygen. In brief, binding oxygen (BO) creates further connection between silicate tetrahedra structures and strengthens the network, respectively. In contrast, non-binding oxygen (NBO) weakens the network, due to the lack of tetrahedra linking [53]. Fe is the most common representative of such species, occupying different functions. The oxidation state of iron determines, if it accounts as a network modifier or an amphoteric (Eq. 4). So, the presence of FeO and Fe₂O₃ may influence the basicity, the network structure and therefore the viscosity in a different manner [73]. In oxidic gasifier slags, a change of the oxidation state of iron is realised by the available amount of oxygen. Low partial pressures (reducing conditions) may reduce Fe³⁺ species to Fe²⁺ species and so, influence the rheology of the present slag [73]. If entrained flow gasifiers are operated under (strong) reducing conditions, Fe²⁺ is presumably present and the slag behaves runnier [53].

The concept of basicity incorporates the fluctuations that may occur due to the different functions of amphoteric species. In the case of iron, the influence of reducing atmosphere on the basicity of silicate melts/slugs becomes a non-negligible factor that needs to be considered for viscosity measurements and predictions [73]. Finally, it must be summarised, since the individual species do not influence the silicate network uniformly and since the function of amphoteric species change, no quantitative statement can be made by singly determining the basicity of a certain system. [32]. Gasifier slags and silicate melts can merely be categorised and compared with each other, using the basicity i.e. the base/acid ratio. It can only be assumed, if a system tends to have a high or low viscosity.

2.3.3 Modelling of Slag Viscosity

Afterward the properties of silicate melts and gasifier slags as well as the emergence of the viscosity have been explained, this chapter will focus on different approaches of viscosity modelling. Several reviews about the viscosity of high temperature melts of vast extent exist, including the works of Vargas et al. (2001) and Liu et al. (2018) [53, 60], which have already been referred to several times in this work. Starting with the Arrhenius model in 1887 [53], numerous model enhancements and new model approaches have been proposed ever since then. However, since this work deals with the investigation of crystallisation in oxidic gasifier slags, only a brief selection of models is presented in this chapter. This chapter scopes to explain the assumptions, boundary conditions and simplifications that are inevitable to fail in recent models and how the data of slag crystallisation generated in this study may give serious contribution to improve such models.

Firstly, the model of Wu (2015) [54] will be briefly introduced as an example for a viscosity model for Newtonian fluids and since it was used to calculate the viscosity of the slag systems investigated in this study (chapter 4.2). Fundamentally, the viscosity is described as a function of temperature, composition and oxygen partial pressure that influence the melt molecule structure [73]. The viscosity is correlated with such molecule structure that is based on associate species [73]. The associate species were applied to quantify the Gibbs energy of oxide melts and each one represents a certain structural unit of the melt [73]. The structural unit distribution of oxide species is calculated, using a thermodynamic database [74-76] regarding parameters: temperature, composition, and oxygen partial pressure [54]. An overview of relevant pure oxide associate species is given: (Table 2.4)

Table 2.4: Selection of some associate species, relevant for this study [54].

Compounds	Associate species	Structural units
SiO ₂	Si ₂ O ₄	SiO
Al ₂ O ₃	Al ₂ O ₃	AlO _{1.5}
CaO	Ca ₂ O ₂	CaO
MgO	Mg ₂ O ₂	MgO

Accordingly, the model of Wu (2015) [54] is capable of calculating the viscosity for oxidic slags, as long as the viscosity is influenced only by the distribution of oxide species units. However, in partial crystalline melts, the physical impact of the crystallised phase cannot be considered. Recent work of Seebold (2017) [32] had a different approach for viscosity modelling. In the course of that work, the viscosity of several oxidic slag systems has been investigated by high temperature viscosity measurements. Based on the generated viscosity data, the model incorporates thermodynamic, kinetic and physical functions and the crystallised slag is treated as homogeneous fluid [32]. Basically, the overall viscosity of the defined homogeneous liquid consists of individual slag viscosities: supercooled slag and slag in crystallisation equilibrium. The approach of the supercooled slag viscosity is valid for Newtonian behaviour and therefore similar to the one of Wu (2015) [54]; the viscosity is modelled, based on the melt structure of the oxidic compounds. In the non-Newtonian regime, solid phase formation has various influences on the flow behaviour. As seen in Fig. 2.10, a small amount of particles increase the fluids resistance to shear by still displaying Newtonian behaviour. However, if the amount of particles exceeds a certain amount, the fluid behaves non-Newtonian. For the case of solid or crystal formation, equilibrium between the remaining slag and the crystal phase is reached [32].

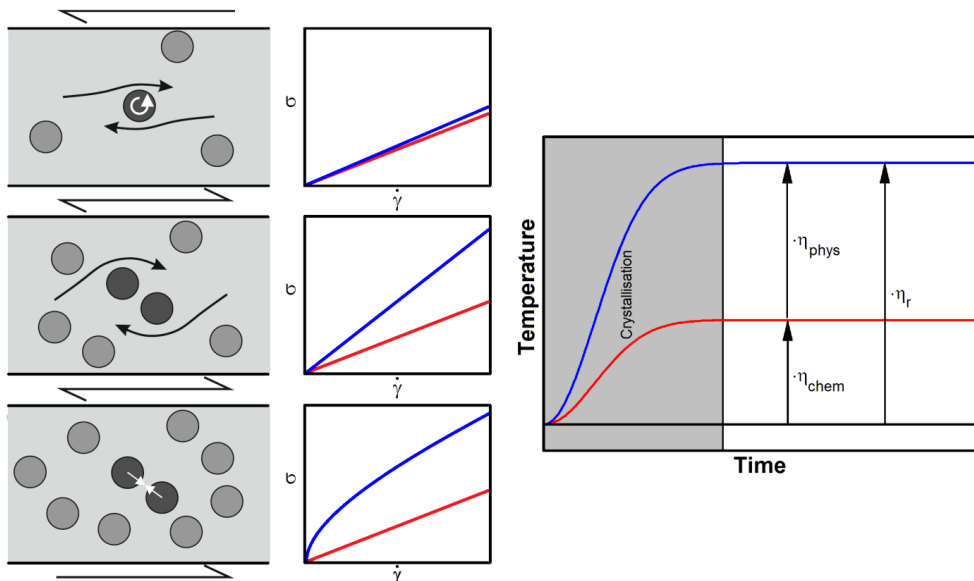


Fig. 2.10: Rheological behaviour of a partial liquid with increasing amount of solid particles (left). Concept of the relative viscosity η_r (right). Modified after Seebold (2017) [32].

The equilibrium is built up of a chemical and a physical viscosity (Fig. 2.10). The chemical viscosity represents the viscosity of the remaining liquid slag. The remaining slag is depleted, due to the incorporation of specific oxides during the crystallisation. Since the composition of the depleted slag differs from the initial bulk composition, the viscosity differs as well. According to the amount and

composition of the crystallised phases, the composition i.e. the viscosity of the depleted slag can face high fluctuations. Lastly, the physical viscosity represents the impact of the solid phase i.e. crystals on the viscosity [32]. The crystals are determined by the sphericity and the volume fraction they occupy in the depleted slag. The combination of chemical and physical viscosity is defined as the relative viscosity (Fig. 2.10) [32]:

$$\eta_r = \eta_{chem} * \eta_{phys} \quad (5)$$

By introducing the concept of chemical and physical viscosity, the model of Seebold (2017) [32] includes a very reasonable approach to calculate the viscosity of partially liquid slags. However, since the solid i.e. crystal phase is defined by the sphericity (and the volume fraction), the diversity of real crystal morphologies is not represented quiet well. Certain generalisations of the crystal morphology are necessary for a successful model implementation. Studies of Mueller et al. (2010, 2011) [62, 77] investigated the influence on viscosity of a Newtonian liquid (silicon oil), incorporating differently shaped particles. The particles were chosen, based on their dissimilar aspect ratios, representing particles with oblate, spherical, angular and prolate shapes (Fig. 2.11) [62].

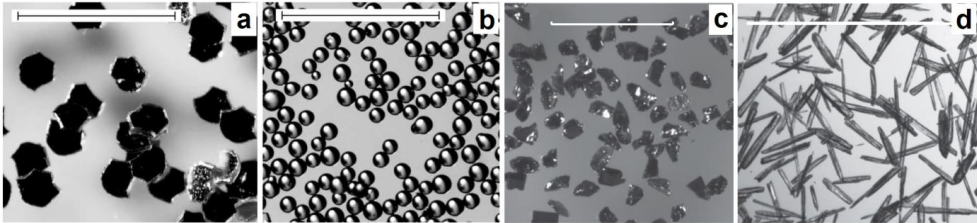


Fig. 2.11: Investigated particle shapes by Mueller et al. (2009, 2011). An oblate polyacrylic glitter, b spherical glass beads (both scale bars = 1 mm), c angular silicon carbide grit (scale bar = 500 μm), d high aspect ratio wollastonite (scale bar = 1 mm). Modified after [62, 77].

The viscosity of the suspensions was ascertained using a rotational rheometer with a parallel plate set up [62]. Based on the experimental rheology data, viscosity calculations of different models were conducted. The best accordance with the experimental data were achieved by applying the Maron & Pierce model for data fitting [78]. The relative viscosity (η_r) of the suspensions was determined by relating the packing density (ϕ) with the maximum packing density (ϕ_m) regarding the individual particle shape (Eq. 6).

$$\eta_r = \left(1 - \frac{\phi}{\phi_m}\right)^{-2} \quad (6)$$

Mueller et al. (2009, 2011) determined a clear dependency of the particle shape on the viscosity i.e. the maximum packing density. Spherical particles display the highest maximum packing density, regarding their aspect ratio of 1. If a particle deviates from the spherical shape, the maximum packing density declines. As an example, investigated biotite flakes (oblate particles) displayed a mean aspect ratio of $r_p^a = 0.04$ and a maximum packing density of $\phi_m^c = 0.22$ while glass spheres (Fig. 2.11b) occupy a maximum packing density of $\phi_m^c = 0.633$ [77]. On the other hand, wollastonite crystals (prolate particles, Fig. 2.11d) with a mean aspect ratio of $r_p^a = 9.17$ reached a maximum packing density of $\phi_m^c = 0.339$ [62]. It was furthermore concluded that the relative consistency K_r (analogy to viscosity) increases compared to spherical particles with the same particle density (Fig. 2.12). For the case of intense of strong oblate biotite, the consistency significantly increases even at low particle fractions (Fig. 2.12). However, in case of the oblate glitter particles with higher aspect ratios ($r_p^a = 0.14, 0.16$), the maximum packing fraction of $\phi_m^c = 0.54$ and 0.55 displays only minor deviations compared to the spherical particles (Fig. 2.12). Accordingly, the individual particle shape,

determined by the aspect ratio, can have significant influence on the relative viscosity of a liquid suspension.

It can be summarised that several approaches are published, which scoped to quantify the influence of crystals in a liquid suspension [53, 60]. The introduced examples of viscosity models by Seebold (2017) and Mueller (2009, 2011), display latest approaches to incorporate the influence of solid particles i.e. crystals on the viscosity of liquid suspensions [32, 62, 77]. The individual shape of crystals, defined by the aspect ratio, lead to partly significant viscosity increases. Therefore, the investigation of crystal morphologies is of great importance to estimate their influence on the viscosity of a liquid suspension i.e. a partly crystallised slag.

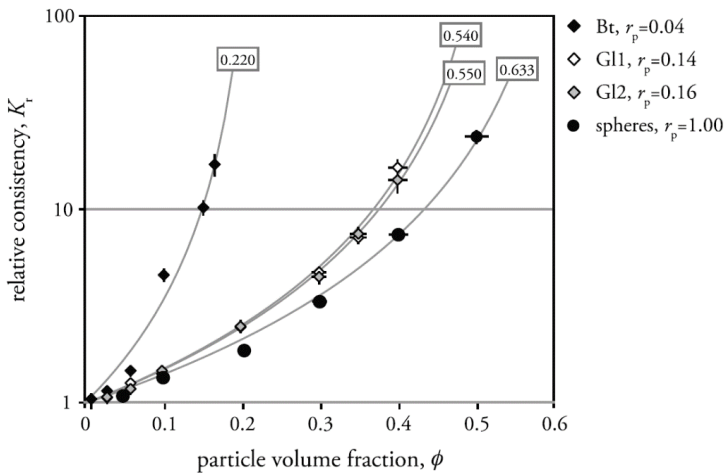


Fig. 2.12: Relative consistency K_r versus the particle volume fraction ϕ of oblate particles. Bt = biotite, Gl1,2 = glitter, modified after [62].

2.4 Crystallisation

In the previous section, the influence of solid particles on the viscosity of a liquid suspension was explained. Herewith, the volume fraction and the individual crystal shape are key parameters to determine the rheological influence of the solid particles. Nonetheless, the previously introduced studies define the crystal morphology as distorted spheres or as objects with a primitive three-dimensional morphology [32, 60, 62]. However, the fields of mineralogy and crystallography fundamentally explain crystallisation processes, kinetics as well as the underlying crystallographic systems and individual crystal shapes [66, 67, 79]. Both sciences are sub-fields of geosciences, which can rely on centuries of experience of observing and quantifying such natural phenomena.

The fundamental processes of crystallisation will be explained in this section. Furthermore, the mineralogical properties of a selection of relevant crystal phases will be described in brief. Since the crystallisation in natural systems and the one in oxidic gasifier slags share many similarities, such analogy will be used to create a deep consciousness of crystallisation.

2.4.1 Fundamentals of mineralogy and crystallography

Geosciences are strongly based on findings of observations and investigations of nature and natural processes. Mineralogy and crystallography are settled in the field of geosciences and strongly focus on the smallest geological units – minerals. Though, the term “mineral” seems quite common, its scientific definition provides a valuable insight into the processes that are relevant for crystallisation, as defined by Klein & Dutrow (2008) [79]:

“A mineral is a naturally occurring solid with a highly ordered atomic arrangement and a definite (but not necessarily fixed), homogeneous chemical composition. Minerals are usually formed by inorganic processes.”

Regarding the abovementioned definition, crucial properties of minerals are their highly ordered atomic arrangement and the definite homogeneous composition. The combination of structure and composition makes each mineral unique and allow one to identify and characterise them. However, it must be noted that the crystallisation in gasifier slags is not countable as a natural process. Though, the crystals grown inside the slag shall not be defined as minerals, their mineralogical properties are expected to be identical. Accordingly, this study aims to apply the unique properties of natural minerals on the crystallised phases in gasifiers. Since natural minerals shall be used as a blueprint, the systematic of minerals needs to be considered.

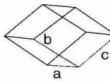
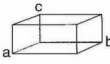
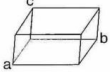
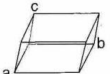
<p>Cubic</p>  <p>$a = b = c$ $\alpha = \beta = \gamma = 90^\circ$</p>	<p>Tetragonal</p>  <p>$a = b \neq c$ $\alpha = \beta = \gamma = 90^\circ$</p>
<p>Hexagonal</p>  <p>$a = b \neq c$ $\alpha = \beta = 90^\circ, \gamma = 120^\circ$</p>	<p>Trigonal</p>  <p>$a = b = c$ $\alpha = \beta = \gamma \neq 90^\circ$</p>
<p>Orthorhombic</p>  <p>$a \neq b \neq c$ $\alpha = \beta = \gamma = 90^\circ$</p>	<p>Monoclinic</p>  <p>$a \neq b \neq c$ $\alpha = \gamma = 90^\circ, \beta \neq 90^\circ$</p>
<p>Triclinic</p>  <p>$a \neq b \neq c$ $\alpha \neq \beta \neq \gamma \neq 90^\circ$</p>	

Fig. 2.13: Crystallographic systems and their parameters, modified after Markl (2008) [80].

Minerals are divided into categories such as: sulphides, oxides, carbonates, and silicates, based on their chemical composition [66, 79, 80]. As the oxidic slags have high contents of silica their crystallisation products are associated with the silicates. Besides those categories, there is a structural systematic that divides minerals based on the crystal lattice structure. It is differentiated between seven crystallographic systems: cubic, tetragonal, hexagonal, trigonal, orthorhombic, monoclinic, and triclinic (Fig. 2.13) [79, 81, 82]. The cubic crystallographic system occupies the highest symmetries. In contrast, the triclinic crystallographic system has the lowest symmetries (Fig. 2.13) [66, 82]. The crystallographic parameters describe the spatial expansion of the crystals primitive cell: its edge lengths are described by a , b , and c and their orientation relative to each other with α , β , and γ . The primitive cell represents the smallest spatial unit on an atom scale, which builds up minerals throughout the succession of the primitive cells [80].

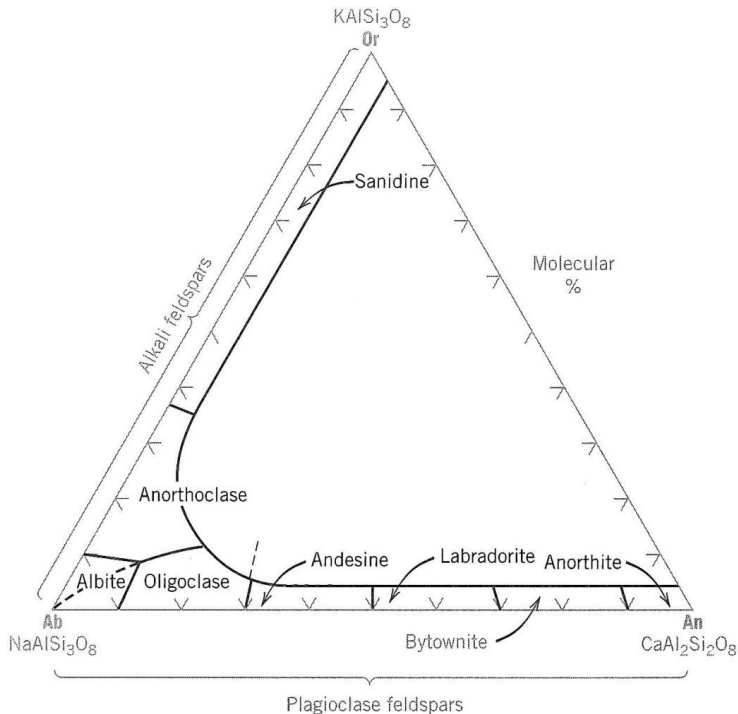


Fig. 2.14: Systematic of the plagioclase and the alkali feldspar series in natural systems, as shown in Klein & Dutrow (2008) [79].

Regarding the aforementioned definition of a mineral, the structure and the chemical composition are crucial properties to define a mineral and both properties influence each other. The feldspar group can be used as an example to state the dependency between both, structure and composition (Fig. 2.14). Feldspar minerals can be categorised in the ternary system of anorthite ($\text{CaAl}_2\text{Si}_2\text{O}_8$) – albite ($\text{NaAlSi}_3\text{O}_8$) – orthoclase (KAlSi_3O_8) [12, 66, 79]. Due to the varying coordination of Ca^{2+} , Na^+ , and K^+ the ratio to Al is modified and the composition is changed. Since the cations also vary in their atom sizes, the crystal structures are unequal, resulting in anorthite being triclinic and orthoclase being monoclinic [66, 79]. The miscibility between those end members is covered with eight individual minerals (Fig. 2.14), which diverge only slightly in their composition and crystal structure. This brief digression displays the variety of minerals in nature that are numbered to be approx. 4000 [79].

Regarding the vast amount of mineral phases, one might conclude that such a large variety of minerals requires an equal number of crystal morphology data for a potential slag model. Fortunately, there are two main reasons that reduce the amount of potential crystal morphologies significantly. Firstly, not all mineral phases have the potential to grow in gasifier slags, since the required elements for crystal growth are not present in coal or biomass slags. Further examples will be given in section 2.4.4. Secondly, the limitations of the crystallographic systems only allow certain morphologies, based on the crystallographic parameters, as can be seen exemplarily in the appendix in Fig. A.1. So, different crystals share similar i.e. highly comparable morphologies that can be used for a viscosity model.

When it comes to the morphological description of a crystal, the overall shape is categorised by two different terms: (crystal) habit and (crystal) “tracht” [66, 80]. The term “tracht” (germ.: dress, costume) is not defined in English reference literature. Therefore, the German term “tracht” will be used further on in this study. As displayed in Fig. 2.15 (a), the left and the middle crystal share the

similar crystal habit, as indicated by their overall rough shapes. However, the arrangement of the crystal surfaces is completely different. The crystal surface arrangement of the middle crystal however, is similar to the crystal on the right – both crystals share the same tracht (Fig. 2.15 (a)). Additional examples are given in Fig. 2.15 (b): the tetragonal prism and the cube have the same tracht in common, though their habit diverges, as the prism is clearly elongated and the cube is not. In contrast, the tetragonal bipyramid and the octahedron occupy the similar tracht, although the bipyramid and the prism, share the similar habit (Fig. 2.15). Accordingly, the combination of crystal habit and tracht leads to the existence of various forms of crystal shapes.

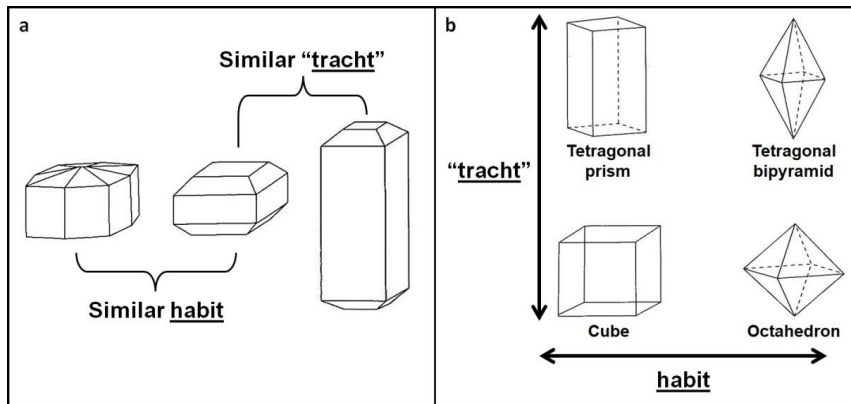


Fig. 2.15: a) Sketches of crystals occupying the similar crystal habit and crystal "tracht". b) Examples of four three-dimensional crystal shapes that have similar habit and similar tracht. Modified after Markl (2008) [80].

The precise quantification of crystals regarding their habit and tracht would serve a high degree of scientific data accuracy. Regarding the scope of defining crystal morphology data for a viscosity model for partial crystalline slags, such approach is not recommended, since it requires absolute accuracy for crystal growth and the followed analysis methodology. As will be described in the methods and experiment section, the morphology data will be gained by SEM analysis of two-dimensional cross sections. Also, very early studies of Goldschmidt (1916, 1920, 1922) [83-85] undoubtedly display the large variety of shapes that crystals of the same mineral may occupy Fig. A.2 (appendix). It must be noted that crystals do not always grow properly idiomorphic since not all boundary conditions remain constant. Ultimately, a high three-dimensional resolution, as theoretically provided by the crystal tracht, cannot be determined by that methodology. The examples of the olivine and feldspar group give evidence that the combination of both: crystal habit and tracht results in very complex overall morphologies (Fig. A.2). In contrast, a promising approach is the utilization of specified crystal habits (Fig. 2.16, Fig. A.3, appendix). For high symmetric crystals, several distinct geometries can be differentiated from each other and geometrically described. Some natural examples are given in Fig. 2.16. Pyrite (FeS_2) and fluorite (CaF_2) crystallise in the cubic crystallographic system and form highly symmetric cubes. For low symmetric crystallographic systems such as triclinic and monoclinic, the definition of a uniform shape is very challenging, as can be seen by the examples of Fig. A.1 and Fig. A.2 (appendix). Such crystals are often described as tabular due to the lack of higher symmetric shapes. The aforementioned systematic of the feldspars (Fig. 2.14) represents such low symmetric crystals that are broadly deposited in bedrocks. Idiomorphic examples of tabular shaped alkali feldspars are given in Fig. 2.16a.

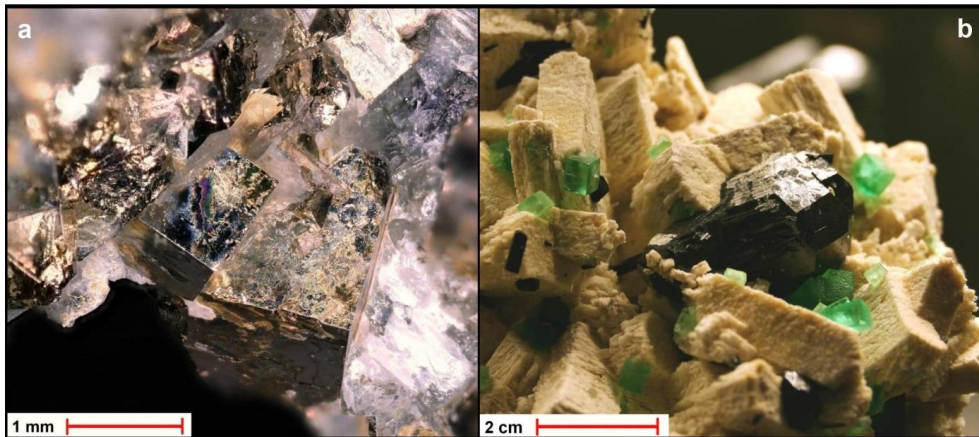


Fig. 2.16: Examples of idiomorphic crystals: (a) cubic goldish pyrite (FeS_2) crystals on silicate bedrock, Ardino, Bulgaria, personal collection; (b) cubic greenish fluorite (CaF_2) and hexagonal blackish foitite ($\text{Na}_{0.5}(\text{Fe}^{2+}, \text{Al}, \text{Mn}^{2+}, \text{Li})_3\text{Al}_6[(\text{OH})_4 | (\text{BO}_3)_3 | \text{Si}_6\text{O}_{18}]$) on tabular beige alkali feldspar ($(\text{Na}, \text{K})\text{AlSi}_3\text{O}_8$), Erongo mountains, Namibia, terra mineralia (Freiberg).

It can be summarised that crystals are distinct units of minerals with a specific atomic structure and chemical composition, which may include miscibility. Crystal shapes underlie the boundary conditions of the corresponding crystallographic systems and therefore cannot be of a random nature. Crystal shapes can be generalised by geometric habits. The crystal tracht incorporates high detailed information on the crystal surface arrangement, but is inappropriate for a crystal morphology parametrisation. The crystal habit is bridge-building however, since it complies sufficient crystallographic accuracy to satisfy the actual morphology of crystals in gasifier slags and simultaneously provides enough broadness to neglect eventual crystal shape imperfections and so allows the creation of a generalised crystal morphology.

2.4.2 Nucleation, crystal growth and kinetics

The mineralogical and crystallographic fundamentals of crystals, including their morphologies were briefly described in the previous chapter. This section however, constitutes with nucleation, crystal growth, and the impact of kinetics. Though, all stages of homogeneous crystallisation can be described and quantified highly detailed, the crystallisation process is influenced by numerous interactions. The crystallisation process can be described from several points of views. In this section, crystallisation will be described qualitatively from a mineralogical point of view. The following explanations shall provide an insight view on nucleation and growth of a single crystal. This approach is the most suitable one to understand crystallisation in multicrystalline systems, which will be described subsequently in chapter 2.4.3 and is often under-represented by the physicochemical narrative.

The homogeneous crystallisation process is divided into two subprocesses [67, 79]. Nucleation represents the first of both stages and crystal growth the second one that can only build up on the nucleation [67, 79-81]. The variable that judges about the stability of minerals (and chemical reactions in general) is the Gibbs free energy G and its unit is given in joule or calories [81]. The stability of chemical reactions can be described as the following:

$$\Delta G_{\text{reaction}} = \Delta G_{\text{products}} - \Delta G_{\text{reactants}} \quad (7)$$

Therefore, the free energy of a reaction is defined as the difference between the free energy of the products and the reactants [81]. According to defined temperature (and pressure) conditions, $\Delta G_{reaction} < 0$ results in higher stability of the products, so the reaction takes place. Vice versa, if $\Delta G_{reaction} > 0$, the reactants are stable and the reaction cannot not be realised [81]. In terms of the nucleation, the nuclei (embryos) will not grow, if the crystal has a higher Gibbs free energy compared to the elements in the melt.

In the field of geology, the formation of igneous rocks from molten magmas corresponds to the crystal formation in gasifier slags. If a magma chamber ascends from the earth's mantle into the crust, the magma chamber cools down due to the geothermal gradient [12, 79]. In the supercooled magma two competing processes determine the nucleation. Firstly, attractive forces aggregate atoms into a nucleus and secondly, thermal vibrations pull and drag at the ordered nucleus [79, 81]. The atoms in the liquid magma have a randomly disordered distribution. During nucleus formation, the constituent atoms of a crystal must be at the same position simultaneously to form an ordered pattern, which is characteristic for the particular crystal [79, 81]. The nucleus (or: embryo) formation occurs, when the ordered state of the atoms represents a lower energy configuration, compared to the disordered state in the liquid slag [79, 81]. Therefore, the nucleus represents the first and smallest structural pattern of the crystal, which can be extended by the process of crystal growth (Fig. 2.17(a)). The transition from a melt to a crystalline configuration with the volume v is therefore described as:

$$\Delta G_v = (\Delta G_{f(cryst)} - \Delta G_{f(melt)})v \quad (8)$$

$\Delta G_{f(cryst)}$ is the free energy of the formation of the crystal and $\Delta G_{f(melt)}$ is the free energy of the melt, expressed in the units of joule or calories per crystal volume [81]. The following term describes the surface energy, while γ represents the surface energy per unit area and a is the overall surface area of the crystal or the nucleus [81]:

$$\Delta G_s = \gamma a \quad (9)$$

Regarding the crystallographic systems described in chapter 2.4.1, the equation (9) can be adapted with specific geometrical information. For the example of a cubic crystal, the edges would have the length c , the surface area $6c^2$, and the volume c^3 . Lastly, the free energy for the formation of a crystal is represented by the following equation:

$$\begin{aligned} \Delta G &= \Delta G_v + \Delta G_s \\ &= (\Delta G_{f(cryst)} - \Delta G_{f(melt)})c^3 + \gamma 6c^2 \end{aligned} \quad (10)$$

The relation between the Gibbs free energy and the nucleus i.e. embryo radius for isothermal conditions is displayed in Fig. 2.17(b). The critical radius r_c represents the radius that a nucleus needs to exceed to successfully grow [81]. However, as mentioned before in the example of the rising magma chamber, the liquid systems experience proceeding cooling conditions, resulting in higher degrees of supercooling. Accordingly, an example of three supercooling conditions is given in Fig. 2.17(c), with an increasing degree of supercooling $T_1 < T_2 < T_3$. Due to the higher degree of supercooling, the atom mobility of the liquid reduces, resulting in weaker forces that disrupt the initial nuclei. As a result, a higher degree of supercooling shifts the critical radius of nuclei to lower values and smaller crystals may form in the supercooled liquid Fig. 2.17(c).

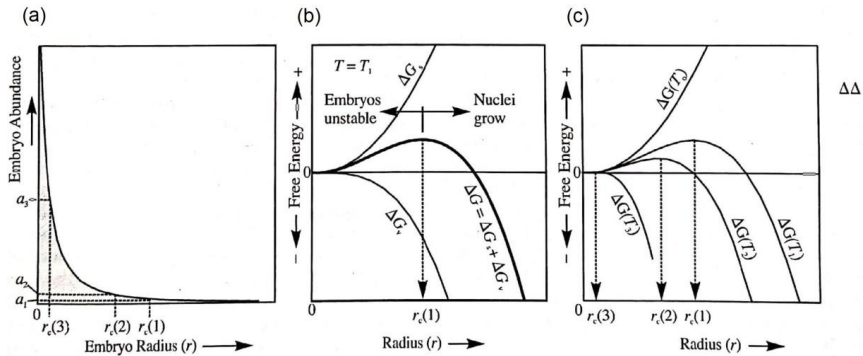


Fig. 2.17: Free energy of formation of crystal nuclei from a melt as a function of size. (a) Abundance of different size crystal embryos in melt. (b) Gibbs free energy of formation ΔG of crystal nuclei for isothermal conditions. (c) Critical growth radius for different degrees of undercooling. As seen in Nesse (2009) [81].

Since the nucleation is sufficiently explained, the subsequently following process of crystal growth requires a brief explanation. After the nucleus formed and exceeded its critical radius, further atoms must be added on the crystal surfaces [79, 81, 82]. Examples for crystal growth on an atomic scale are given in Fig. 2.18. The addition of an atom unit on the nucleus surface also faces energetic hurdles [79]. The addition of a unit on the planar surface (Fig. 2.18(a)) is energetically the most difficult, as the unit has only stabilising bonds at one of the six faces [79, 81]. Accordingly, atoms from the surrounding liquid may use the remaining five faces to drag the unit apart from the nucleus. The example of Fig. 2.18(b) represents an attachment on an edge of a new crystal surface layer that is energetically preferred, due to two bonding atom unit faces [81]. By progressing this principle, it can be concluded that crystal growth of a nucleus follows an energetically determined order: 1. A comparable high amount of energy is required to add the first unit on the nucleus face. 2. The following units attach on the faces of the first unit, as the free energy reduced. 3. The forming layer is filled up, row by row. 4. The process restarts as the layer is completed. Since the crystal growth is also affected by the competition of attaching and dragging mechanisms, (especially by starting a new layer), crystal growth for a single crystal underlies probabilities and cannot be predicted.

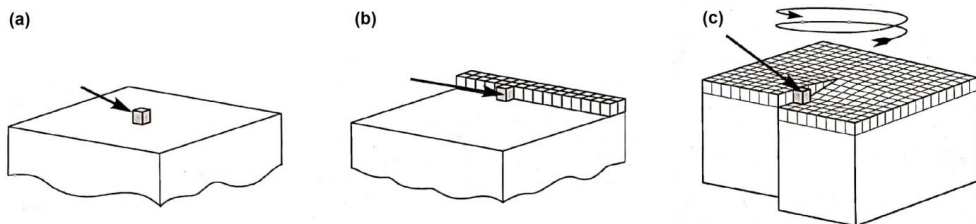


Fig. 2.18: Growth on a crystal face for a cubic nucleus. (a) Adding a crystal unit on a planar crystal face. (b) Adding a crystal unit on the edges or partially completed crystal layer. (c) Growth of a unit on a screw dislocation. Modified after Nesse (2009) [81].

The overall growth characteristic of a crystal is described by the crystallisation theory (Fig. 2.19) [86, 87]. As explained, the processes of nucleation and crystal growth are related with the corresponding temperature i.e. degree of supercooling. As mentioned before, a higher degree of supercooling reduces the diffusion in the supercooled liquid and therefore reduces the dragging forces that apply on the early stage of a nucleus [80]. This results in a higher probability for the nucleus to exceed its

critical radius. Accordingly, the rate of nucleation is higher in regions with comparable low temperatures i.e. high degree of supercooling, as indicated by the red zone in Fig. 2.19 [87]. The crystal growth however, has a contrary behaviour. Since the critical radius of the nucleus is exceeded, the pace of crystal growth relies on the ability to attach new atom units on the crystal faces. Higher temperatures increase the diffusion and therefore the rate of units attaching on the crystal faces (blue zone, Fig. 2.19) [87]. Though, both processes prefer different degrees of supercooling, there is an intersection where they converge [86, 87]. In this temperature region, a supercooled liquid has the capability to crystallise.

As summarised by Fig. 2.19, the temperature is a key parameter for the crystallisation. Nonetheless, from a fundamental point of view, the temperature dependency of crystallisation reveals another crucial parameter – time. Since the combination of constituent atoms (nucleus formation) and the attachment of units (crystal growth) depend on atom collisions, a sense of probabilities is an inevitable parameter. The more time passes at a specific degree of supercooling, the likelier the nucleation and subsequent growth will occur in the liquid system. This consciousness stands in a direct conflict with thermodynamics, as time is not a variable.

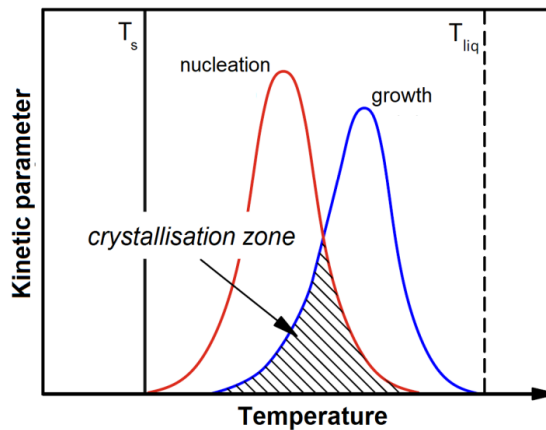


Fig. 2.19: Sketch of the relationship of nucleation and growth for a supercooled liquid. T_s is the solidus temperature, T_{liq} is the liquidus temperature. Modified after [32].

Thermodynamics and kinetics are two sides of the same coin and inseparably connected with each other. Thermodynamic stable crystallised phases can be calculated regarding the law of Gibbs free energy minimisation [81]. The impact of kinetics however, can only be determined by physical evidence i.e. experimental data. Since temperature and time are both crucial parameters for the crystallisation, it is essential to hold one of these parameters constant for investigation of kinetics. As time cannot be hold constant, isothermal investigations are a suitable approach to determine the kinetic influence of slag crystallisation [88-90]. Data of such isothermal investigations are displayed in time-temperature-transformation (TTT) diagrams (Fig. 2.20) [91-93]. The investigated slag is supercooled under its liquidus temperature (metastable), where crystallisation is thermodynamically predicted. With proceeding time, the slag's state adjusts to the thermodynamic state (stable). For distinct temperatures, the progressing slag crystallisation can be ascertained by several time-dependent investigations (Fig. 2.20). The collection of several isothermal crystallisation data reveals the zone where crystallisation occurs for the particular system [58, 94, 95]. Due to its characteristic shape, it is often described as the “crystallisation nose” [32, 95]. Inside that nose, the crystallisation i.e. crystal content is expected to rise with an increase of time (Fig. 2.20).

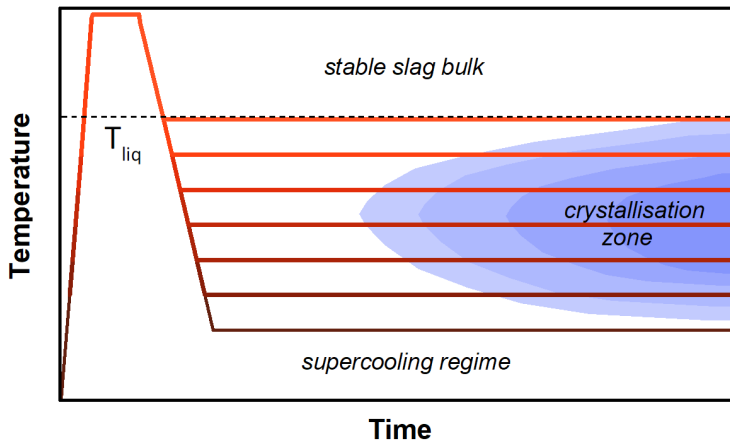


Fig. 2.20: Schematic drawing of a TTT curve and the determined crystallisation zone. T_{liq} is the liquidus temperature of the investigated system.

Finally, it can be concluded that crystallisation of a liquid e.g. a gasifier slag is based on nucleation and crystal growth and depends on temperature and time. High degrees of supercooling support the probability to form a nucleus with a critical radius. However, lower degrees of supercooling accelerate the crystal growth, due to higher atom mobility. The intersection of both processes allows crystallisation. Those processes require a certain time period before an equilibrium is reached, which is represented by kinetics (metastable state). As soon as every atom of the system is equilibrated, the slag is thermodynamically stable. The stable thermodynamic state can be predicted i.e. calculated, the metastable kinetics must be determined. One approach is the analysis of slag with respect to time under isothermal conditions (TTT-diagram).

2.4.3 Multicrystalline systems

The crystallisation process of a single crystal was sufficiently described in the previous chapter. Since the crystallisation in gasifier slags involves several crystalline phases, it is beneficial to explain the processes of multicrystalline crystallisation. Once more, a natural example from the field of geology serves as a comparable analogy to the crystallisation of oxidic gasifier slags – magmatic differentiation [79-81]. Since gasifier slags consist of the non-convertible oxidic compounds from coal or biomass (Table 2.1, Table 2.2), they could also be described as silicate-melts and are therefore related with natural magmatic melts.

A magma chamber is a residue of igneous rocks with earth mantle composition that has a liquid state and intrudes into the earth's crust. Regarding the geothermal gradient [12, 81], the magma chamber incorporates more heat compared to the surrounding crustal rocks. Therefore, the chamber will release its heat and cool down, leading to supercooled conditions of the magma. With respect to long holding times (approx. thousand to millions of years), crystallisation occurs in the magma chamber. Concerning the composition of the magma chamber, various minerals crystallise out of the liquid bulk, ultimately [12]. The systematic of the multiphase crystallisation is described by the term magmatic differentiation (Fig. 2.21) [79-81]. Magmatic differentiation is a crystallisation process where kinetics is highly involved. If the stability of the magma chamber, below the liquidus temperature, would be described from a thermodynamic point of view, several crystallised phases may be in a potential equilibrium state with the remaining magma. However, thermodynamics cannot provide information about the growth speed and more importantly the overall crystallisation order of the crystals. In the case of oxidic gasifier slags, a critical crystal fraction regarding their

morphology (Fig. 2.12) is required, to result in a slag tapping failure [96, 97]. If this fraction is reached before the slag is in equilibrium, individual thermodynamic calculations are insufficient to support viscosity models for partially crystallised slags.

To understand the impact of kinetics during cooling of magma chambers, geologists made several attempts to verify the processes of differentiation [12]. Artificial magmas were heated and supercooled and their crystallisation products were investigated. The main conclusion was summarised as: the magma displays a discrete crystallisation order, rather than simultaneous crystallisation of several phases; the last crystallising phase is the first one to melt during heating; the crystallisation order corresponds with the melting point of the mineral phase [12]. Fig. 2.21 displays an example of a supercooled multicrystalline magma chamber with mafic composition. A mafic composition represents the typical composition of the earth's mantle and is enriched in Fe^{2+} and Mg^{2+} . As the magma is supercooled below the liquidus, olivine crystallises as the first phase, subsequently followed by pyroxene (Fig. 2.21(a,b)). Both phases form due to the supersaturation of Fe^{2+} and Mg^{2+} , which are relatively enriched in both minerals. When the slag bulk is strongly depleted in Fe^{2+} and Mg^{2+} , other cations such as K^+ , Al^{3+} and Ca^{2+} become enriched until (kali-)feldspar crystallises from the magma chamber (Fig. 2.21 (d)) [12, 98].

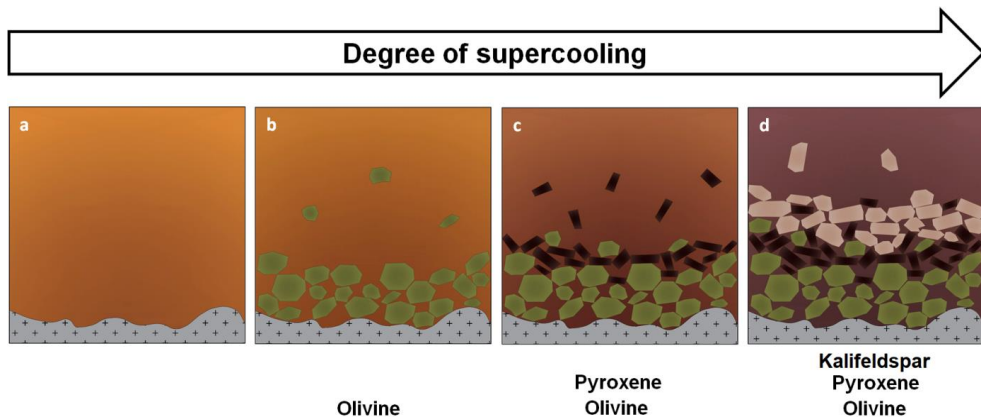


Fig. 2.21: Example of magmatic mafic differentiation based on the Bowen's reaction series [98]. (a) Stable magma bulk above T_{liq} . (b) Slightly supercooled magma with crystallising olivine (green). (c) Moderate supercooled magma with crystallising pyroxene (brown) and precipitated olivine. (d) Intense supercooled magma with crystallising kalifeldspar (pink) and precipitated olivine and pyroxene.

It is generally assumed that the crystallisation order is strongly influenced by the change in the composition of the magma bulk [12]. Since the initial growing phase incorporates only specific elements of the magma, the remaining bulk changes its composition [12, 81, 99]. The abovementioned example is based on the Bowen's reaction series [98-100]. It describes crystallisation orders for continuous (felsic, Ca^{2+} -rich) and discontinuous (mafic, Fe^{2+} -, Mg^{2+} -rich) series that are separately described due to their diverging composition [12, 99]. For the continuous felsic series the order is the following: Ca-rich feldspar (anorthite), solid solutions (Fig. 2.14), and Na-rich feldspar (albite). On the other hand, the order for the discontinuous mafic series is: olivine, pyroxene, amphibole, and biotite [12, 98]. Regarding the principle that the mineral phase crystallises, whose composition is highly comparable with the composition of the magma bulk, the depleted mafic and felsic magmas compositions approach each other [99]. Accordingly, both share the similar remaining crystallisation path, occupied by kalifeldspar, muscovite and quartz [12, 99].

The aforementioned natural example of multi-phase crystallisation, gives valuable insight into the crystallisation of oxidic gasifier slags. Though, the composition of magma and gasifier slags is not

identical, some key fundamentals can be concluded that apply for both systems: in supercooled magmas, the phase with the highest melting point and/or the most similar composition (with the initial bulk) crystallises firstly; a simultaneous growth of different phases is unlikely; the initially crystallised phase changes the composition of the bulk, resulting in the crystallisation of the second phase due to the enrichment of required elements and so forth.

2.4.4 Recent findings on oxidic gasifier slag crystallisation

Since a fundamental understanding of mineral crystallisation for natural processes was provided, the following section closely focusses on the crystallisation processes in gasifier slags. As already implied, the composition of magmatic systems is comparable with oxidic gasifier slags. Accordingly, the crystallisation processes, parameters (excluding pressure) and most importantly, the crystallised phases could share similarities. Thus, an assessment of typical gasifier slags needs to be executed to determine the variety of potential crystal phases.

In previous works of Melchior (2011) and Seebold (2017), gasifier slags were investigated on their rheological behaviour [32, 101]. Numerous coal and biomass slags from Germany, as well as from international origins, were investigated on their surface tension and their viscosity. A selection of ten gasifier ashes and slags was chosen to determine their variety of potential crystal phases (Table 2.5). Their individual composition can be seen in Table A.1 (appendix). The slags were randomly chosen to cover typical slag compositions at best and can be characterised as: S1-3, ST-ZAF-2, and ST-D-6 enriched in Al_2O_3 , Fe_2O_3 , SiO_2 ; K3-1 strongly enriched in SiO_2 ; ST-D-1/-2, ST-N-1, and BK-D-1 enriched in SiO_2 with intermediate fractions of Al_2O_3 and CaO ; HTC and HKS enriched in CaO and SiO_2 (Table A.1). Since the ashes were generated after an annealing procedure, the composition of the ashes and the resulting slags is expected to be identical. Based on their compositions, FactSage Equilib calculations (v7.2, GTox database) have been performed to predict the crystallised phases for a reduced atmosphere at equilibrium conditions (Table 2.5).

Table 2.5: Crystallising phases of ten ash or slag samples as predicted by FactSage Equilib (v7.2 with GTox database). The applied atmosphere was set to $p(\text{O}_2) = 10^{-12}$ atm. The basicity was calculated using Eq (4).

Author	Sample ID	Basicity	Calculated crystal phases (FactSage)
Melchior (2011) [102]	S1-3	0.07	mullite, cordierite, anorthite, SiO_2 , spinel, feldspar
Seebold (2017) [32]	ST-ZAF-2	0.08	cordierite, sapphire, anorthite, olivine
Melchior (2011) [102]	ST-D-6	0.10	mullite, corundum, spinel, anorthite, cordierite
Melchior (2011) [102]	K3-1	0.14	SiO_2 , clinopyroxene, olivine, anorthite, feldspar, spinel
Seebold (2017) [32]	ST-D-1	0.14	cordierite, anorthite, SiO_2 , feldspar, spinel
Seebold (2017) [32]	ST-D-2	0.29	anorthite, SiO_2 , clinopyroxene, cordierite, feldspar, spinel
Melchior (2011) [102]	ST-N-1	0.31	anorthite, olivine, clinopyroxene, spinel, feldspar
Seebold (2017) [32]	BK-D-1	0.40	SiO_2 , anorthite, wollastonite, clinopyroxene, albite
Seebold (2017) [32]	HTC	1.02	calcio-olivine, $\text{Ca}_3\text{MgSi}_2\text{O}_8$, rankinite, melilite, olivine,
Melchior (2011) [102]	HKS	1.44	calcio-olivine, $\text{Ca}_3\text{MgSi}_2\text{O}_8$, $\text{Na}_2\text{CaSiO}_4$, melilite,

For the Al_2O_3 - and Fe_2O_3 -enriched slags S1-3, ST-ZAF-2 and ST-D-6, it can be summarised that the crystallised phases are strongly dominated by mullite (Al_2O_3 - SiO_2 phase, with solubility for FeO_x), cordierite (ternary Al_2O_3 - MgO - SiO_2 , Al_2O_3 - MnO - SiO_2 , Al_2O_3 - FeO - SiO_2 phase) and anorthite ($\text{CaAl}_2\text{Si}_2\text{O}_8$) (Table 2.5). Regarding their composition, a high fraction of aluminosilicates with solubility of FeO seems to be a reasonable prediction. The K3-1 slag system is dominated by SiO_2 crystallisation due to the high SiO_2 fraction of 68.2 wt.-% (Table A.1). Anorthite, SiO_2 , and clinopyroxene ($(\text{Na,Ca,Mg,Fe})_2\text{Si}_2\text{O}_6$) are abundantly present in the slag systems of ST-D-1/-2, ST-N-1, and BK-D-1 (Table 2.5). Their fractions of SiO_2 , Al_2O_3 , and CaO (>85% of the whole individual slag systems) lead to the formation of anorthite and SiO_2 , as the slag is comparably saturated with the required compounds for crystal growth. In contrast, clinopyroxene incorporates the remaining compounds MgO and Fe_2O_3 , as they become enriched due to the anorthite and SiO_2 crystallisation. Lastly, the basic slags HTC and HKS display diverging major crystallisation products: calcio-olivine (Ca_2SiO_4), $\text{Ca}_3\text{MgSi}_2\text{O}_8$, and melilite ($(\text{Ca,Na})_2(\text{Al,Mg,Fe}^{2+})(\text{Si,Al})_2\text{O}_7$). This is based on the comparably low contents of silica, but high contents of CaO , compared to the previous slags.

Finally, it can be summarised that in total 51 crystallised phases are predicted for the selected slag systems (Table 2.5). Anorthite has by far the highest occurrence in oxidic gasifier slags, followed by cordierite, spinel and feldspars (which also include anorthite, Fig. 2.14). Further relevant species are: SiO_2 , olivine and clinopyroxene. In total, 17 different phases crystallise in the oxidic slags of which only 11 occurred at least twice in the slag systems (by separating calcio-olivine from olivine), giving them some sort of relevance. According to the estimated amount of approx. 4000 minerals present in nature, as explained before (chapter 2.4.1, [79]), the amount of relevant phases for oxidic gasifier slag crystallisation seems manageable.

Nonetheless, this study investigates the crystallisation phenomenon in gasifier slags from a completely new point of view, other recent studies investigated crystallisation in gasifier slags with similar motivation, though diverging intentions. Numerous studies were performed on the influence of crystallisation on the viscosity of oxidic slags by viscosity measurements [32, 60, 77, 103, 104]. These studies measured the viscosity, detected non-Newtonian behaviour and developed models to determine the influence of crystals. Though, the studies especially from Seebold (2017) and Liu (2018) provided beneficial approaches, the investigation of crystal phases and their morphologies were not in the scope. The studies of Mueller (2010) as seen in chapter 2.3.3, discovered the dependency of a viscosity increase regarding the solid fraction and the associated individual shape of the solids [62]. However, the solid shapes were not associated with specific crystal phases, relevant for gasifiers. So, the applicability for oxidic slag systems remains unclear. The review publication of Liu [60] summarises recent approaches on slag viscosity modelling very adequately. With reference to that review publication [60] and the findings already mentioned in chapter 2.3.3, this section will focus on recent studies that investigated the crystallisation phenomenon directly.

Song et al., (2010) expounded that a solid fraction of 10% is already sufficient to generate non-Newtonian flow behaviour, which is supported by the findings of Mueller (2010) and Zhou for elongated particles [60, 62, 105]. For spherical particles, an influence on the viscosity was measured in the range of 20-30% crystal fraction [62, 105]. Referring to the previously described crystallisation order by Bowen [106] these findings conclude that the crystallisation of the first phase(s) of an oxidic slag system might already be sufficient to reach a non-Newtonian regime. Accordingly, the crystallisation kinetics is crucial to determine the importance of certain crystallising phases.

Several studies utilised special experimental setups that serve a high time resolution of sampling and so, give insight into the crystallisation kinetics: single/double hot thermocouple (SHTT, DHTT) and confocal laser scanning microscopy (CLSM) [107-114]. Both setups have in common that supercooled slag is observed in-situ, resulting in live-documentation of crystallisation. Especially Xuan et al., published several articles using the SHTT-method to investigate slag crystallisation [90, 108, 115-117]. These studies will be used exemplarily to outline the content of typical research in the field of slag crystallisation, as they are of a representative character.

The research interest is set on the dependency of the crystallisation temperature towards certain compound ratios (preferably $\text{SiO}_2/\text{Al}_2\text{O}_3$), as well as the influence of Fe_2O_3 [110, 115, 117]. For an application related background such an approach is reasonable. However, there are several issues

that need to be considered to explain the fundamentals of slag crystallisation. Firstly, the crystallised phases were identified by equilibrium calculations and not determined from the investigated samples. Secondly, the crystal shapes are described briefly, without crystal morphology parametrisation and without addressing them to the corresponding phases. Lastly, since no correlation with specific phases was made, the results are unique and therefore cannot be transferred to slag systems with diverging composition.

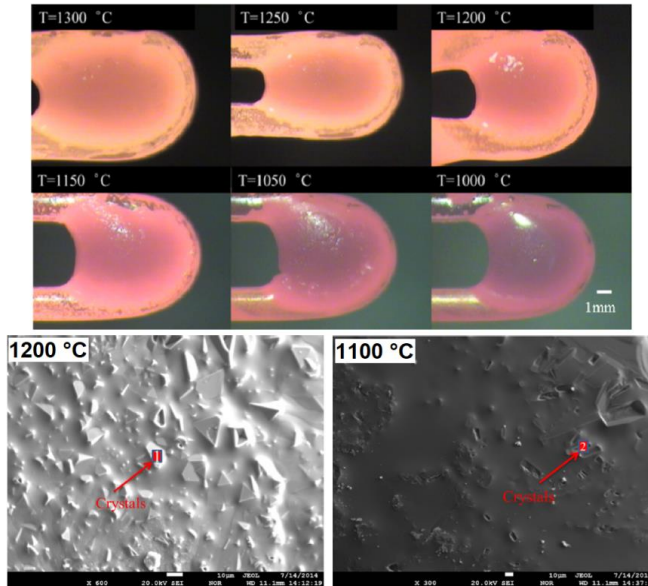


Fig. 2.22: Crystallization images of the SHTT experiment for different temperatures. SEM BSE images of the sample surfaces displaying crystal morphologies. Modified after [118].

However, a recent study of Xuan et al., (2016) [118] serves more valuable information on the crystallised slags (Fig. 2.22). Afterward the SHTT experiments, the slag droplets were investigated via SEM-EDX and XRD. The phases were determined to be spinel and melilite [118]. The documented triangular crystals (Fig. 2.22(a)) display an Al-Mg-Fe-rich composition and were associated with spinels. As a conclusion, it can be summarised that application-related studies often focus strongly on the slag composition. The crystallised phases were neither analysed deeply, nor were they correlated with the in-situ observations. Accordingly, no specific crystal morphology data were quantified, as well as no specific kinetic data of the crystallised phases were provided.

However, the results of some recent studies can be used nonetheless, to gather indirect information on the impact of kinetics on the crystallising phases. A brief review of a selection of studies, investigating coal slag crystallisation, is given in Table 2.6. The studies were firstly compared based on the chosen samples. Secondly, the crystallised phases predicted also by equilibrium calculations were listed. Ultimately, the crystallised phases determined from the experimental results were enumerated. By condensing all solid solutions together as a main phase, thermodynamic calculations indicated the presence of 15 phases in total. The most calculated phases are: anorthite, melilite, spinel and clinopyroxene. Only 10 out of the 15 phases were calculated more than once in the studies. However, during the performed experiments, only 9 different crystal phases were observed in the slag samples by the authors (Table 2.6). From these 9 phases only 5 phases were determined more than in one study. Anorthite and melilite are by far the most relevant phases. Accordingly, from initially calculated 15 phases only 5 phases are of practical relevance as proven by experimental data.

Table 2.6: Overview of investigated crystal bearing slag systems as presented by different authors.

Author	Coal sample	Calculated crystal phases (FactSage)	Determined crystal phases
Kong et al., 2014 [119]	YL (Yinli) GP (Gaoping) 50/50 blending	mullite, anorthite, cordierite, quartz, clinopyroxene	anorthite
Schwitalla et al., 2017 [103]	slag 3	melilite (>1300 °C)	melilite (>1300 °C)
Shen et al., 2016 [120]	Chinese bituminous coal	hematite, anorthite andradite, gehlenite (melilite), melilite	gehlenite (melilite)
Xuan et al., 2017 [121]	synthetic slag #5	spinel, melilite, merwinite, Ca ₂ SiO ₄	åkermanite (melilite), Mg-Fe-spinel, merwinite
Yuan et al., 2012 [104]	Shenfu	anorthite, wollastonite, gehlenite (melilite), melilite, Fe-spinel, wustite	anorthite, wollastonite, iron silicon oxide
Ren et al., 2018 [111]	BF slag with fly ash F - 2	melilite, anorthite, clinopyroxene, spinel	åkermanite, gehlenite (melilite), clinopyroxene, anorthite
Xuan et al., 2016 [118]	Chinese coal Kuangou	spinel, melilite, olivine, nepheline	Fe-spinel, gehlenite (melilite), Mg-Fe-spinel
Xuan et al., 2019 [122]	real gasifier slag GS	anorthite, feldspar, andradite, clinopyroxene, nepheline, wollastonite	anorthite, diopside (clinopyroxene), quartz (SiO ₂)
Jiang et al., 2015 [68]	CVS	mullite, anorthite, cordierite, SiO ₂ , spinel	anorthite, cristobalite (SiO ₂), hematite

It can be concluded that experimental studies that display real gasifier conditions indicate a fewer number of crystallised phases. The most likely reason is that the slag is not reaching a thermodynamic equilibrium, as predicted by the calculations. Furthermore, it is proven that crystallisation experiments with application-related parameters lead to crystallisation of a reduced number, but mostly similar phases. It can be assumed that equilibrium conditions were not reached during the experiments, resulting in the differing crystal phase occurrences. These findings justify the conduction of crystallisation experiments, since a kinetic influence on gasifier slag crystallisation is undeniable and thus cannot be predicted with the existing calculation tools. Accordingly, the approach performed in this study is additionally supported, since the amount of relevant crystallising phases is actually lower compared to the pure equilibrium calculation results. Combining the findings of Table 2.5 and Table 2.6, the real amount of crystal phases that need to be quantified to serve sufficient morphology data is vanishingly small (compared to the numerous occurring natural minerals), legitimising the approach provided in this study.

3 Methods and Experiments

The following chapter will describe the methods and experiments that were applied in this study. The investigated slag samples and their preparation will be described, firstly. Investigations on the slags melt and solidification behaviour subsequently follow. The first experiment is the high temperature viscosimetry, which was used to determine slags rheological behaviour. For the investigation of slag crystallisation, numerous quenching experiments were performed. A detailed view on rapidly crystallising slags was gathered by confocal laser scanning microscopy (CLSM). The generated samples were prepared to be analysed by digital optical microscopy to identify crystallisation in the slag. If slag crystallisation was present, relevant samples were analysed via SEM and SEM-EDX as well as XRD to determine the crystallised phases and the crystal structures. Crystal morphology data were determined by measuring the crystals dimensions, based on microscopic and SEM images.

3.1 Slag Characterisation

3.1.1 Selection of Samples and Preparation

In this study, four oxidic gasifier slags were investigated. These slag samples (Table 3.1) were selected, based on previous results of the HotVeGas project [123] by Melchior (2011), Seebold (2017), as well as Saar (2019), who also investigated oxidic gasifier slags [32, 101, 124]. The slag samples were chosen to cover a variety of potential slag systems, as their composition and basicity varies. Synthetic ST-D-2 slag represents a highly viscous slag. Detailed viscosity and few crystallisation results are already described for the real slag [32]. Synthetic ST-D-2 composition was reduced to four compounds to determine the difference in viscosity and crystallisation behaviour, compared to the real ST-D-2 slag (Table 3.1) [32]. The synthetic HKT slag consists of five oxidic compounds and is based on the real HKT slag [102]. It has a lower content of silica and a higher basicity, though it is expected to be a high viscous slag as well (Table 3.1). The composition of the synthetic HKT slag represents 95% of the real slag's composition and is expected to be highly comparable with the real slag. Due to the further decreasing silica content, the SOM-1 slag is expected to have an intermediate viscosity (Table 3.1). This synthetic slag sample was defined, based on the predicted crystallising phases (FactSage Equilib). A detailed presentation of the SOM-1 slag was performed by Saar (2019) [124]. Lastly, synthetic HKR slag represents the basic slag of this selection (Table 3.1). Due to its diverging composition, it was chosen as it possibly produces different crystallising phases. Similar with the synthetic HKT slag, HKR slag represents 95% of its real slag composition. It must be noted that synthetic ST-D-2, HKT and HKR slag were fully investigated in this study. SOM-1 slag however was investigated on viscosity in this study. Further experiments concerning slag crystallisation were performed in the study of Saar (2019) [124]. As mentioned before, the slags consist of five, respectively four oxidic compounds (Table 3.1). The decision of utilising synthetic samples was made on purpose, to remove alkali compounds out. Due to their low partial pressure, intense reactions and volatilisation were expected otherwise by the alkali compounds. As open crucibles were used, a potential volatilisation could not have been prevented. Therefore, the generalisation to the five compounds $\text{SiO}_2\text{-Al}_2\text{O}_3\text{-CaO-Fe}_2\text{O}_3\text{-MgO}$ was made, as explained in the publication of Schupsky et al. (2020) [125].

Table 3.1: The compositions of the investigated slag samples (wt%). Samples were synthetically produced, based on real coal ash samples. SOM-1 slag was partly investigated in the originating study by Saar (2019) [124].

Samples	Reference	SiO ₂	Al ₂ O ₃	CaO	Fe ₂ O ₃	MgO	Basicity
ST-D-2	Seebold (2017) [32]	60.9	21.6	10.6	6.9	-	0.12
HKT	Melchior (2011) [102]	54.7	22.3	14.6	2.6	5.8	0.26
SOM-1	Saar (2019) [124]	47.6	19.2	14.4	9.2	9.6	0.32
HKR	Melchior (2011) [102]	34.8	12.0	27.4	14.5	11.4	0.94

The synthetic slag samples were produced on the basis of different reagents with high purity (Alfa Aesar, Massachusetts, U.S. and Merck, Darmstadt, Germany). Initially, the five analytical reagents were balanced, mixed together, and dried subsequently at 100 °C for 10 hours to remove potential humidity. To ensure sample homogeneity, the oxide powders were blended for 24 hours on a roll bank. To further increase the homogenisation and to prevent the agglomeration of oxides, Al₂O₃ milling balls were added to the oxide powders.

Evaluation of the precise composition of the synthetic slag samples has been performed by elemental analysis. The analysis was outsourced to the Central Institute of Engineering and Analytics at the Forschungszentrum Jülich GmbH. The elements Si, Al, Ca, Mg, and Fe were quantified via inductively coupled plasma optical emission spectroscopy (ICP-OES). To dissolve the oxidic compounds, the samples were treated beforehand with lithium metaborate and heated. Regarding analysis errors and inaccuracies, a relative error of up to 20% needs to be mentioned. Henceforth, the term “synthetic slag samples” will be substituted by the term “slag samples” to improve the readability of this study.

3.1.2 Hot Stage microscopy

As mentioned in chapter 2.4.2, nucleation is the first step of crystallisation. To ensure homogeneous crystallisation in the slag samples, all oxidic compounds need to be completely molten. To determine the adequate temperatures for initial oxidic slag powder melting, hot stage microscopy (HSM) was performed with the slag samples. HSM is a commonly used method to determine the melt behaviour of coal ashes or slags [16, 32, 126, 127] and is described in the industry standard DIN 51730.

The fundamental principle of HSM is the optical observation of a sample with defined dimensions under high temperature treatment (Fig. 3.1). Beforehand, the samples were prepared by pressing several spatula tips of oxidic slag powder into a cylindrical pellet shape with an edge height of 5 mm. Therefore, a manually operated press was utilised to apply a compensating force of prox. 10 kN on the sample. Afterwards, the pellet was placed on an Al₂O₃ sample boat in a horizontal high temperature furnace (Rubotherm EB04/30, Bochum, Germany). On the rear side of the furnace, a glass window including flange is installed. A conventional lamp is located in front of the rear flange to serve as a light source enabling the initial sample positioning. On the front side, the furnace chamber is sealed with a glass window containing flange that allows the sample observation (Fig. 3.1). Different atmospheres can be applied on the installed experimental setup [101]. The cylindrical sample pellet is observed by a CCD camera that is protected by an additional infrared filter to prevent the camera from damaging heat radiation. The CCD camera is connected with a computer and a customised LabView programme (National Instruments, Austin, U.S.) [16] is used to operate the experimental set up (Fig. 3.1).

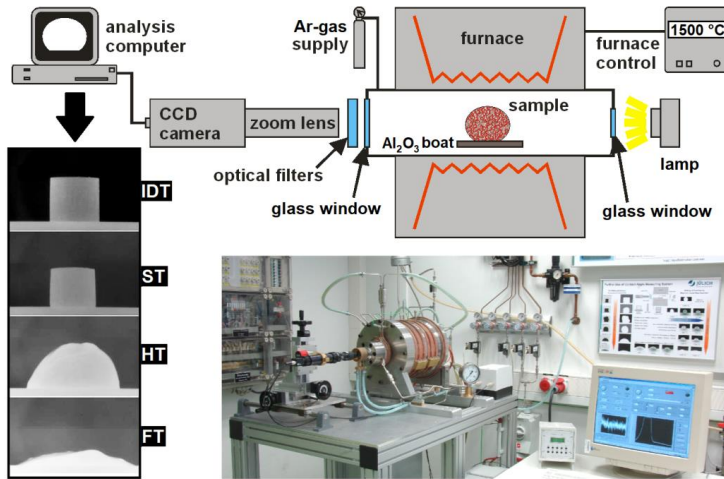


Fig. 3.1: Schematic sketch of the hot stage microscope setup used in this study. Including modified content of Dohrn (2018) [16].

In this study, Ar gas was used to create an inert atmosphere during the measurements (Fig. 3.1). The heating profile was set to a heating slope with +5 K/min. Throughout the heating procedure, the pellet experienced a sequence of stages, typically representing the melting behaviour: initial deformation temperature (IDT), softening temperature (ST), hemispherical temperature (HT), and flow temperature (FT), which are defined by the sample geometry (Fig. 3.1) [31, 68, 94]. Firstly, the sample slightly shrinks as it reaches the ST. With an increase in temperature, the melting intensifies and the sample reaches a spherical shape, followed by a hemispherical shape (HT). The majority of the sample pellet is now molten. However, only as the flow temperature FT is reached, it can be assumed that the sample is in an almost liquid state. The flow temperature was therefore used as the least required temperature to ensure a complete slag melting for creating homogeneous slag bulks.

3.1.3 Differential Thermal Analysis

In the field of fuel conversion residues, the liquid and the solid state as well as the transition between these two are of certain interest. This transition indicates an enthalpy change since crystallisation and melting are exo- and endothermic reactions, respectively [128]. Fluctuations in the heat content of a sample, due to such state changes can be measured thermoanalytically. A commonly used method to determine such heat changes is the differential thermal analysis (DTA), which was also used in this study.

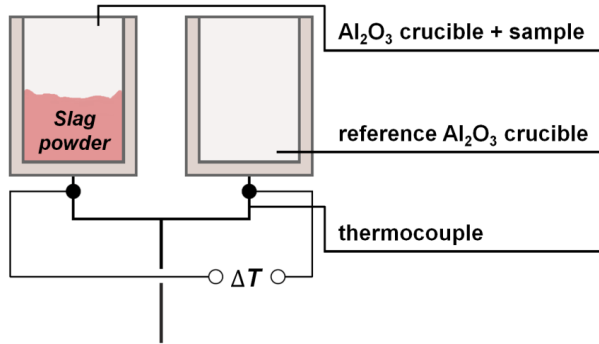


Fig. 3.2: Schematic sketch of the sample holder architecture with relevant components of a DTA device, modified after Seebold (2017) [32].

The differential thermal analysis was performed in a STA 449 F3 Jupiter (Netzsch, Selb, Germany) device. The main characteristic of the device is the sample holder architecture (Fig. 3.2). It consists of two identical Al_2O_3 crucibles that are placed on an Al_2O_3 holding unit. A thermocouple is attached to the holding unit, measuring the temperature directly under both of the crucibles (Fig. 3.2) [128]. One of the crucibles is filled with the sample material (approx. 100 mg), the other one is kept empty to act as a reference. The space around the sample holder is sealed gas tight by a vertical high temperature furnace. The applied device achieves a maximum temperature of 1550 °C. To reconstruct gasification conditions, a slightly reducing atmosphere was generated applying an Ar - Ar/4% H_2 gas mixture with a flow rate of 20 ml/min and 5 ml/min, respectively. Temperature calibrations are made with gold ($T_m = 1064$ °C) and nickel ($T_m = 1455$ °C) standards. When the analysis starts and the furnace chamber heats up, the present temperature at the sample-containing crucible and at the reference crucible is measured and the difference between both temperatures is calculated [32]:

$$\Delta T = T_{\text{sample}} - T_{\text{reference}} \quad (11)$$

As explained before, state change reactions or decomposition reactions are respectively endo- or exothermic, resulting in temperature fluctuations of the sample-containing crucible and so, in a temperature difference of both crucibles [128]. The thermocouple detects the temperature indirectly in form of applied voltage fluctuations, due to the thermoelectric effect. The DTA device is further equipped with a weight unit, determining changes in the sample mass. Accordingly, the DTA results are displayed as thermo-electric voltage per mass of sample (mV/mg) with respect to the applied temperature profile [128]. With regard to these principles, the reference Al_2O_3 crucible remains empty, since neither changes in mass, nor chemical reactions occur in the pure ceramic.

For the analysis of slag samples, a first heating slope of +5 K/min was applied for initial slag powder melting until the maximum temperature of 1500 °C was reached for achieving a homogeneous slag sample bulk. Subsequently, the samples were cooled with a slope of -10 K/min to a target temperature of 800 °C. At this temperature, the slags solidified requiring no further cooling. Subsequently, the slags were heated again to 1500 °C with a slope of +10 K/min. During the heating and cooling slopes, ΔT was constantly measured and crystallisation as well as melting was documented. Ultimately, the procedure was repeated three times since the initial melting from the oxidic compounds may be affected by volatilisation as well as decomposition of impurities and to proof the validation of the single measurements. Initial trials using Pt-crucibles and pure Ar/4% H_2 atmosphere resulted in the formation of pure iron (especially in HKR slag). It was assumed that the applied strong reducing atmosphere combined with the catalytic Pt-crucible triggered the reduction of the Fe_2O_3 species to pure iron. However, since no such pure iron was found in the other experiments, it was decided to choose the minor reducing Ar - Ar/4% H_2 atmosphere mixture in combination with non-catalytic Al_2O_3 crucibles.

3.1.4 Thermochemical Equilibrium calculations

Since the melting and solidification behaviour of the slag samples was sufficiently characterised by the aforementioned techniques, a further characterisation method was used to determine the slag behaviour from a thermodynamic point of view – equilibrium calculations. As previously mentioned in chapter 2.4.4, the crystallising phases can be predicted based on their thermodynamic stability. Though, the relevance of kinetics was already mentioned, equilibrium calculations are beneficial, as an initial crystallisation characterisation can be made. Based on the liquidus and solidus temperature, the experimental parameters can be defined and potentially growing phases can be assumed. For example, the slag system SOM-1 was defined based on the potentially crystallising phases [124] as predicted by initial equilibrium calculations.

Thermochemical equilibrium calculations were performed using the FactSage software package (GTT Technologies, Herzogenrath, Germany) [129]. The software package can be applied for several calculation options, such as the calculation of multi-compound phase diagrams. However, this study used the Equilib software module, as it ascertains the stable phases of a solution with fixed composition and with respect to the temperature. Since the slag compositions were chosen to be constant, due to the exclusion of alkalis, the applied temperatures remain the only variables. The stability of phases is determined by Gibbs free energy G minimisation, while H is the enthalpy, S is the entropy, and T the considered temperature of the system:

$$\Delta G = \Delta H - T\Delta S \quad (12)$$

Thus, the Equilib programme determines phase solidification, dissolution, or transformation under equilibrium conditions, disregarding kinetic effects. The slag characteristics can be predicted with good accordance to the industrial process of gasification, since additionally an atmosphere can be defined (e.g. reduced oxygen partial pressure), which may interact with the slag system. Furthermore, the FactSage software package includes several databases that provide fundamental thermodynamic data for the involved compounds. Such datasets are as essential as the calculation codes. Accordingly, the results strongly rely on the quality of the available datasets. Thermodynamic databases are validated and extended evermore to improve the calculation results [74, 75]. The Equilib module is a method commonly used in both, industry and science to predict crystallised phases in oxidic slag systems [58, 120, 121, 129].

In this study, equilibrium calculations were performed with FactSage version 7.2. As a data source, the latest version of the GTox database was used. GTox is a private database [130], developed by a corporation of the IEK-2 Institute (Institute of Energy and Climate Research – Microstructure and Properties of Materials, Forschungszentrum Jülich GmbH, Germany) and GTT Technologies (Germany). Equilib calculations were performed in the temperature range of 900 °C to 1400 °C with an interval of 10 °C. To represent gasifier conditions, calculations were performed with a reduced oxygen partial pressure of 10^{-12} bar. Since the synthetic systems only contain five, respectively four oxidic compounds, some of the species included in the GTox database have been excluded from the calculations. A summary of the relevant species for FactSage calculations is listed in Table A.2

3.2 Viscosimetry

Initial characterisations of the melting and solidification behaviour as well as the equilibrium calculations are followed by viscosity measurements of the investigated slag systems. The viscosity measurements were performed using a high temperature rheometer. The experimental setup was initially designed for pressurised slag viscosity measurements in previous work of Nentwig (2011) for isobaric conditions [131]. In terms of the work of Seebold (2017) [32], the set up was modified and several optimisations were conducted to improve the reliability of the setup compounds.

3.2.1 Fundamentals and Sample Preparation

There are several methods to determine slag viscosity, e.g. using the pure gravity of a reference object that sinks in the investigated medium or the gravitational flow of the medium itself [32]. However, a rotational rheometer has several advantages compared to such methods. Especially covering a viscosity range between 10^{-2} and 10^4 Pa·s is an advantage, which is relevant for oxidic slag systems [32]. Additionally, a rotational rheometer can determine the viscosity with respect to the shear rate. As already described in chapter 2.3.1, shear rate depending measurements can reveal if the slag displays non-Newtonian behaviour and therefore includes crystallised phases. The viscosity measurement can be performed using varying spindle-crucible designs such as: plate-plate, cone-plate, cylindrical, and double-gap [32]. For the investigated systems, the cylindrical architecture was used. Since the spindle-crucible architecture is identical compared to Seebold (2017) [32], a more detailed description including e.g. the crucible and spindle dimensions are renounced in this study. For the viscosity measurements a slag amount of at least 60 gram was required to ensure a sufficient covering of the spindle. Since the produced synthetic slag powder is voluminous, three annealing steps, using 20 gramm of slag each, were conducted beforehand to produce a homogeneous slag sample. The slag was therefore annealed in a high temperature furnace (HTF 18/8, Carbolite Gero GmbH & Co. KG, Neuhausen, Germany) at 1500 °C including 10 hours of holding time. During the annealing procedure, the slag was already filled in the viscosimetry crucible and subsequently used in the experiment. Molybdenum was used as a crucible and spindle material. Molybdenum has several advantages: high melting point, comparably good availability, sensitive to oxygen under heat treatment (oxygen indicator and oxygen capturing), and no dissolution with oxidic systems. Furthermore, the previous studies of Nentwig (2011) and Seebold (2017) used the same materials, allowing a comparison with the provided data, if it concludes to be reasonable [32, 131].

3.2.2 Set up and Measuring Campaign

The experimental setup is based on a high temperature furnace that was manufactured by Prüfer Ofenbau GmbH (Neuss, Germany) [131]. Initially, the furnace was designed for pressurised measurements (20 bar). To ensure the tightness of the setup, high requirements on the overall design were made that lastly led to an unstable experimental performance as well as numerous component failures during the measurements. In the followed study by Seebold (2017) [32], the set up was simplified and thereby the reliability of the installed compounds was improved. The setup used in this study is identical with one of Mielke (2020) [132]. Since the setup is extensively described in the previous study of Seebold (2017), for more detailed information on the crucible and spindle design as well as their dimensions, it is referred to that study [32].

The utilised setup consists of a high temperature furnace unit, allowing potential viscosity measurements up to 1600 °C [32]. The furnace unit is sealed with water-cooled flanges at the top and at the bottom (Fig. 3.3). Due to the comparably small furnace size (height: 50 cm, diameter: 40 cm), a high heat gradient occurs inside the furnace. The water cooling is required to reduce the temperature on the outer furnace hull. The interior is made up of high temperature Al_2O_3 wool to ensure sufficient temperature isolation. Inside, a vertical Al_2O_3 tube is installed, in which the crucible is located [132]. To ensure tightness, the tube is sealed with rubber o-rings. The atmosphere is injected from the bottom cover through a flange, to constantly flush the inner tube. The crucible is placed on a second Al_2O_3 tube with a reduced diameter, which serves as a stand for the crucible. Inside that tube, a thermocouple type S is installed to measure the temperature right below the slag sample (Fig. 3.3). The inner vertical ceramic tube as well as the crucible is inserted from the bottom of the furnace. The spindle however, is inserted by lowering from the top of the furnace. A fully lowering of the spindle is only possible, if the crucible is heated and the slag is liquid, resulting in a submerged spindle (Fig. 3.3).

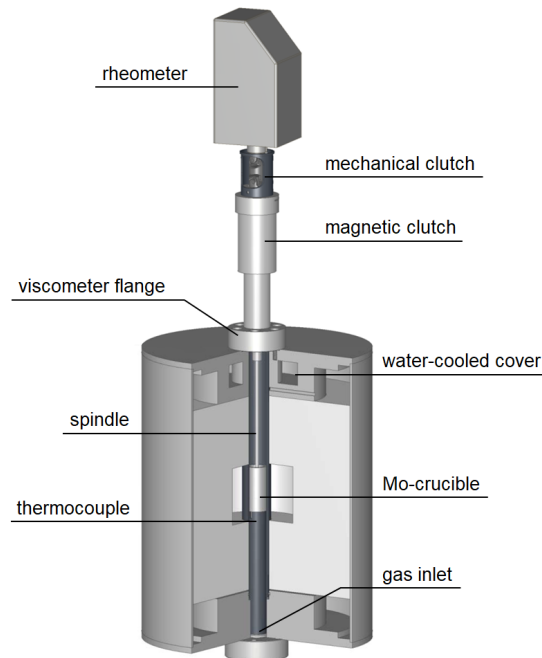


Fig. 3.3: Experimental setup of the high temperature viscosimetry experiment, modified after Seebold (2017) [32].

The spindle is screwed in a cylinder that is connected with a magnetic coupling. In the coupling, a ceramic ball bearing was used to conduct the rotational force from the rheometer to the spindle. Due to recent improvements of the magnetic coupling, the default torque could therefore be reduced to 2 mN·m [32]. The magnetic coupling is followed by a mechanical coupling, which is lastly connected with the rheometer.

A rheometer type RC1 (RheoTec Meßtechnik GmbH, Ottendorf-Okrilla, Germany) was used in the experiment. It can be operated, applying a defined shear rate, as well as applying a fixed torque [131]. The maximum torque is stated as 50 mN·m (milli newtonmeter) and the maximum rotation per minute as 800 rpm [131]. However, for the performed experiments the maximum parameters were set to 40 mN·m and 400 rpm respectively, to create analogue parameters with the recent study of Seebold (2017) [32]. The rheometer is equipped with an electronical interface that was connected with a computer. The rheometer was operated by a customised LabView programme and the data were recorded automatically.

As a first measurement campaign, the slag samples were investigated isothermally in a stepwise manner. Subsequently after the maximum temperature of 1500 °C was reached, the furnace cooled down and started the measurements at 1425 °C. The rheometer measured the required torque, regarding the applied rotation. As soon as the temperature measurement was finished, the furnace cooled down to the subsequent target temperature and the next measurement started. By proceeding with this routine, a temperature profile for every slag was followed in steps of 25 °C. The measurement was intended to end at 900 °C. However, due to high slag viscosity values, the measurement campaigns ended individually, if the maximum required torque of 40 mN·m was reached. For the case of occurring crystallisation, some slags were isothermally measured for several hours at a temperature where crystallisation was expected. It shall be proved, if the slags resistance towards shearing increased i.e. if the slags displayed non-Newtonian behaviour due to the crystallisation. The slag samples that displayed a remarkable viscosity evolution were additionally measured under isothermal conditions. In this case, the target temperature and the time period of

the viscosity measurement was individually chosen. Subsequently after the experiments, the crucibles were removed out of the experimental setup and were investigated on their slag structure, additionally. Since the therefore required preparation techniques and analytical methods are identical with the ones applied for the quenching experiment, a more detailed description will follow in chapter 3.5.1.

3.3 Quenching Experiment

The viscosimetry measurements determine, if a slag behaves Newtonian or non-Newtonian. In case a slag behaves as a non-Newtonian fluid, the growth of crystals is a reasonable assumption. However, the properties of high temperature viscosimetry do not reveal at which time during the measurements which crystals at which fractions were present. Thus, the existing data gap needs to be filled with high resolution crystallisation data with respect to the applied temperature and the required crystallisation time. Therefore, an additional experiment was performed to investigate the evolution of the crystallisation: the quenching experiment.

3.3.1 Sample Preparation and Setup

To examine the crystallisation characteristics of the synthetic $\text{SiO}_2\text{-Al}_2\text{O}_3\text{-CaO-(MgO)-Fe}_2\text{O}_3$ slag systems, quenching experiments with a customised sample holder, setup as well as customised crucibles were performed. To prepare the samples, an amount of approximately 1-1.2 g of slag powder was filled in each molybdenum crucible. The cylindrical Mo-crucibles are 33 mm in height and 10 mm in diameter. In contrast to other crucible materials such as Al_2O_3 , molybdenum was chosen due to a lack of interactions with oxidic melts. To ensure sample homogeneity, the filled crucibles were heat-treated in a high temperature furnace (HTF 18/8, Carbolite Gero GmbH & Co. KG, Neuhausen, Germany). The slag samples were held at 1550 °C for 10 h to generate a homogenous slag bulk. The decision to apply this pre-heating step was made to reduce the retention time of the samples in the quenching experiment for sparing the parts of the sample holder.

The experimental setup is build-up of a vertical high temperature furnace (ERO 7/50 S, Prüfer Ofenbau GmbH, Neuss, Germany). A long vertical Al_2O_3 tube is placed inside the furnace with both endings protruding out of the furnace (Fig. 3.4). Below the furnace, a water basin is located in which the samples are quenched as they are dropped from the hot zone inside the furnace. The vertical tube is set on a tripod inside the water basin. The bottom part of the vertical Al_2O_3 tube was submerged in the water (Fig. 3.4). In other studies [110, 133, 134], furnaces are sealed via flanges to ensure constant atmosphere above the quenching unit. As these flanges are opened for the quenching procedure, air is flooding the furnace and the atmosphere is not constant any longer. In contrast to those studies, the setup used in this study guarantees a constant atmosphere, since the furnace is not "opened" for the quenching. The bottom orifice is also the spot where the atmosphere is injected (Fig. 3.4). Accordingly, potential air is removed through the upper orifice of the vertical tube by the injected atmosphere. The thermocouple and the sample holder hang at stands that are positioned on top of the furnace. The upper orifice is closed with a perforated Al_2O_3 foam plate that allow the remaining parts of the sample holder to stick out of the vertical tube (Fig. 3.4).

Inside the vertical Al_2O_3 tube, the sample holder is placed from the top (Fig. 3.4). The sample holder consists of a main thick Pt-wire that carries all additional parts including the samples. At its end, a perforated Al_2O_3 disc with six drilled holes is fixed. The sample containing crucibles are attached to thin Pt-wires that are wrapped around Al_2O_3 pearls (Fig. 3.4). The pearls are lead through the discs orifices. By now, the samples would simply drop into the underlying water basin, since the pearls are capable of falling through the orifices again. However, additional long Al_2O_3 rods are also placed through the discs orifices from the top, while they protrude out of the upper orifice of the vertical tube. Thus, the crucibles hang on the Al_2O_3 disc, since both, the pearl and the rod cannot pass the

disc simultaneously, as both are too voluminous (Fig. 3.4). With this structure, the samples can be held in the hot zone of the furnace, regarding the applied temperature program and time. To quench a sample at a specific time period, a rod is lifted up, passing through the discs orifice and leaving behind an empty space. Since the Al_2O_3 pearl has now sufficient space, the pearl with the attached crucible falls down and is dropped finally in the underlying water basin to be immediately quenched. As one of the discs orifices can also be used to place the type S thermocouple, five samples can be individually placed and therefore quenched during one experimental run.

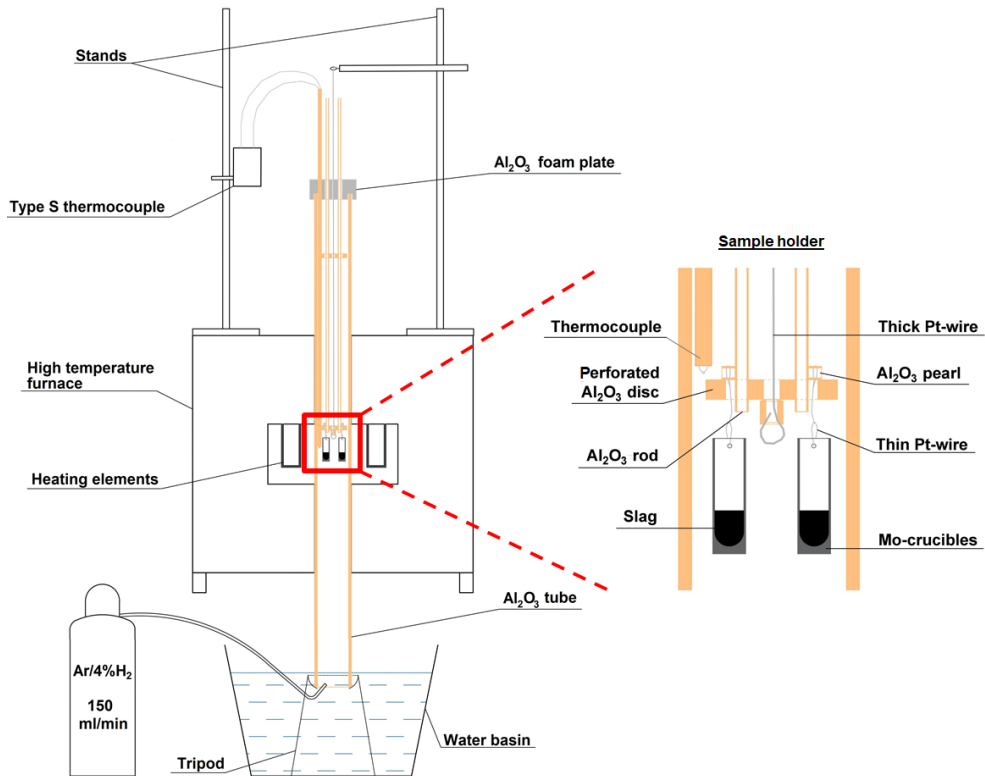


Fig. 3.4: Schematic drawing of the quenching experimental set up and the custom-made sample holder.

The abovementioned design serves several advantages. Firstly, a constant atmosphere can be created, as no air is intruding the vertical tube by the quenching process due to its permanent water-sealing (Fig. 3.4). Secondly, samples can be quenched individually, allowing the operation of isothermal measurement campaigns with respect to the passing time. Thirdly, all samples of the corresponding isothermal conditions have experienced the same time-temperature-atmosphere history and are therefore highly comparable. Lastly, the setup enhances the productivity as one experimental run generates five quenched samples, compared to quenching only one sample with conventional quenching experiment designs [110, 133].

3.3.2 Experimental Parameters

Since the customised sample holder enables the time-dependent quenching of up to five crucibles, isothermal measurements were beneficially conducted. A further important reason for the performance of isothermal measurements was the fact that the target-temperature is fixed and investigations were performed with respect to only one variable: time.

The crystallisation processes under supercooling conditions were investigated by selecting individual isothermal temperature profiles for each slag, regarding the corresponding liquidus and solidus temperature (Fig. 3.5). Firstly, the pre-heated samples were heated to 1450 °C and held for 1 h to generate a homogeneous melt. Afterwards, samples were cooled down with a slope of -7 K/min to the individual isothermal sections. The whole investigations cover a temperature range between 850 and 1300 °C. To provide high sample resolution, profiles were set in 50 °C steps (Fig. 3.5). After reaching a certain isothermal step, samples were quenched time-dependently after 0, 1, 4, 7, and 24 hours of holding time, respectively. For the HKR and SOM-1 slag system, shorter time periods (e.g.: 10, 30, 60 min) were applied, since the crystallisation occurred faster compared to the ST-D-2 and HKT slags. This approach facilitated the examination of crystal evolution over time, including the kinetic influence on crystal growth. The 24 h holding-time-span was chosen to represent conditions close to the equilibrium state. Hereafter, samples were prepared for the subsequently following analysis. Results on the crystallisation evolution could be plotted in time-temperature-transformation diagrams, as already implied in chapter 2.4.2.

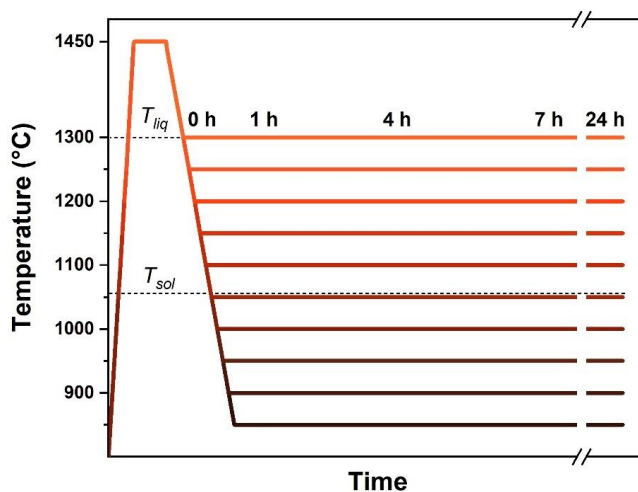


Fig. 3.5: Example of the HKT temperature profile applied in the quenching experimental setup. The number of isothermal steps, as well as the temperature range varies for other slag systems.

The atmosphere of the quenching experiment was set to be reducing, regarding imitate the oxygen partial pressures that are present in real gasification processes. Therefore, an Ar/4% H_2 gas mixture was injected in the vertical tube (Fig. 3.4). As already mentioned for the quenching experiment (chapter 3.2.2), the experimental parameters were set to be equal with the viscosimetry setup to ensure a suitable comparability of results. Accordingly, the crucible material molybdenum was also chosen again. A more detailed description of the influence of atmosphere, the crucible material and the requirement of a pre-heating procedure (state of slag) will be described in chapter 3.4.2.

3.4 Confocal Laser Scanning Microscopy (CLSM)

As an additional experiment, confocal laser scanning microscopy (CLSM) was applied to analyse the evolution of crystallisation for the slag systems. The CLSM is an in-situ experiment, enabling the optical observations of the slag surface. Sample crystallisation as well as melting can be observed in the experiment. Due to the individual properties of the experimental setup, CLSM serves a valuable enhancement to the generated results of the quenching experiment. Two advantages shall be mentioned at this point: covering of initial crystallisation with short incubation times (for basic slags) and in-situ observations of three-dimensional crystal morphologies on the slag surface. In contrast to all other experiments and analysis methods, the CLSM setup used in this study was not located at the Forschungszentrum Jülich GmbH. Instead, the CLSM setup of the Department of Materials Engineering of KU Leuven University (Leuven, Belgium) was used.

3.4.1 Set up, Parameters and Procedures

The CLSM experimental setup can be divided into several units: the high temperature furnace, the laser microscope and computational control unit. The high temperature furnace used in this study was manufactured by Lasertec (Model SVF17SP, Lasertec, Yokohama, Japan). The furnace chamber is comparably small (15-25 cm), oval-shaped (Fig. 3.6), and its inner surface is coated with gold (Fig. 3.7) [135, 136]. The chamber architecture and the coating are necessary for the furnace operation, since the heat is produced by a halogen lamp (Fig. 3.6). The lamp is operated by high voltage to produce heat radiation. The radiation is reflected by the Au coated inner furnace walls. Due to the oval shape, the heat radiation is focused in the upper region of the furnace, where the sample holder is located in the focus point of the heat radiation (Fig. 3.6) [135, 136]. Based on this architecture, high heating and cooling rates of approx. 300 K/min can be achieved in the used set up due to the small furnace volume as well as no use of isolation material that could eventually store heat [135, 136]. On the sample holder, a sample containing crucible can be installed with dimension of a few millimetres. Respectively, the sample amount is of limited extend. The sample holder incorporates a type S thermocouple and the temperature calibration was conducted using the melting points of pure copper and nickel.

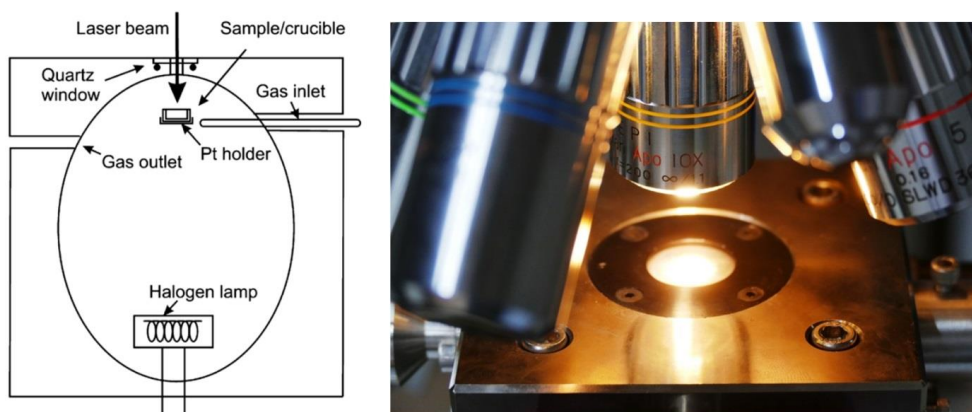


Fig. 3.6: Sketch of the CLSM high temperature furnace, as shown in [135] (left). Image of the ocular lenses on top of the the quartz window containing cover by operation (right).

The furnace is sealed by a quartz glass window containing flange (Fig. 3.6). The quartz glass window enables the observation of the sample by the confocal laser microscope that is located above the furnace unit. The microscope (Model 1LM21H, Lasertec, Yokohama, Japan) is equipped with several

ocular lenses to adjust the magnification (Fig. 3.6) [135]. The furnace and the microscope were computationally controlled using HiTOS software [136]. Images were taken with magnifications of up to x200 and a frame rate of 1/s. The image resolution was set to 960x720 pixels.

Initial experiments were performed to determine the influence of several parameters [137] using different atmospheres: Ar-gas and reduced Ar-gas. Ar-gas was used to display inert atmosphere with an oxygen partial pressure of $p(\text{O}_2) = 10^{-6}$ bar, due to contained oxygen impurities. Comparable partial pressures can be assumed in the early stages of slag formation in gasifiers [17]. To apply such reducing conditions, a Mg-furnace was partly used to reduce the oxygen concentration in the Ar-gas (denominated as reduced Ar-gas) to different magnitudes, based on oxidation reactions of the Mg with the oxygen impurities.

The experiments were performed using initially Pt- and lastly Mo-crucibles. Pt was mainly used for inert atmosphere and Mo was used for the reduced atmosphere, due to intense oxidation behavior of Mo. To monitor the magnitude of reducing conditions, the oxygen partial pressure was additionally measured by an oxygen sensor (rapidox 2100, Cambridge Sensotec, St. Ives, Great Britain) and minimum oxygen partial pressures of down to 10^{-20} bar were detected during individual experiments.

In the CLSM experiment, the samples were investigated mostly isothermally but also under constant cooling conditions. Since HKR slag displayed the fastest crystallisation kinetics, the CLSM experiments were preferably performed for this slag system. The main focus was set to the temperature range between 1100 °C and 1250 °C. The samples were heated up with a rate of 50 K/min to observe the melting of the oxide powder i.e. the annealed slag particles. The heating procedure was continued until a maximum temperature of 1500 °C was reached. To spare the set up components, it was decided to not reach higher temperatures. The samples were hold for 10 minutes at the maximum temperature and were subsequently cooled down to the target temperature of the investigation. Therefore, a high cooling rate of -300 K/min was chosen. After the isothermal treatment, the samples were cooled to room temperature by also applying the cooling rate of -300 K/min. Due to the high applied cooling rates, no influence of the cooling procedure on the crystallization phenomena was observed. However, a few experiments with a constant cooling rate of -6 K/min were additionally performed to simulate slow cooling processes. Furthermore, constant cooling experiments were performed as well to generate additional kinetic data on the crystallisation of the HKR slag.

3.4.2 Assessment of Experimental Parameters

As indicated in the previous chapter, initial CLSM measurements were conducted applying different experimental parameters. With focus on the influence of the sample state, the crucible material, the oxygen partial pressure and a combination of all, an assessment-like study was performed [137]. The main conclusions of this study will be briefly explained in this section to representatively reason the parameter selection made for this whole study. For more detailed information it is considered to check the specific study [137].

CLSM experiments were initially performed utilising Pt-crucibles, inert Ar-gas and slag oxide powder (Fig. 3.7). Though, crystallisation was observed in the slag, subsequent analysis revealed deviations from crystallisation results of the quenching experiment. Heating of oxide slag powder led to heterogeneous melting, resulting in local fluctuations of the bulk slag chemistry. Accordingly, crystalline phases grew heterogeneously in the partially liquid slag. Once the crystals formed, the slag bulk chemistry has changed and the subsequent crystallization is not representative, as also indicated by deviations towards FactSage Equilib calculation results. It was recommended to anneal the slag samples before the experiment at temperatures appropriately above the liquidus temperature. The use of annealed slag particles creates a homogeneous slag bulk, eliminating the probability of heterogeneous nucleation.

Due to the grade of reducing atmosphere, different crystallisation behaviours were observed. Higher O_2 partial pressures led to high-temperature-shifted crystallisation with low growth velocities, while

reduced Ar-gas allowed higher grades of supercooling and, therefore, high crystallization kinetics. It was argued that the O_2 sensitive Fe_2O_3 species was responsible for the observed behaviour. Oxygen partial pressure of 10^{-12} bar reduced Fe_2O_3 to FeO species which is categorized as a network modifier. The formed FeO species resulted in a lower liquidus temperature and so enabled slag cooling to lower temperatures.

Furthermore, it was documented that Pt crucibles in combination with Fe-containing slags form a Pt-Fe-alloy under reducing conditions, also due to the reduction of Fe_2O_3 . This alloy has a low melting point and is responsible for crucible failure. It was advised against the use of Pt crucibles for Fe-rich slags at reducing conditions. To ensure the integrity of the experimental set up and the reproducibility of results, the crucible material Mo was suggested, as it is not forming alloys and has high temperature stability. However, low oxygen partial pressure is required to prevent Mo oxidation. The utilised Mo-crucibles were custom designed and had a round shape (Fig. 3.7). This round shape (in contrast to the rectangular folded Pt-foil, Fig. 3.7) reduced the observed slag surface and also improved the navigation of the microscope. The Mo-crucibles are 8.5 mm in diameter and 6.5 mm in height.

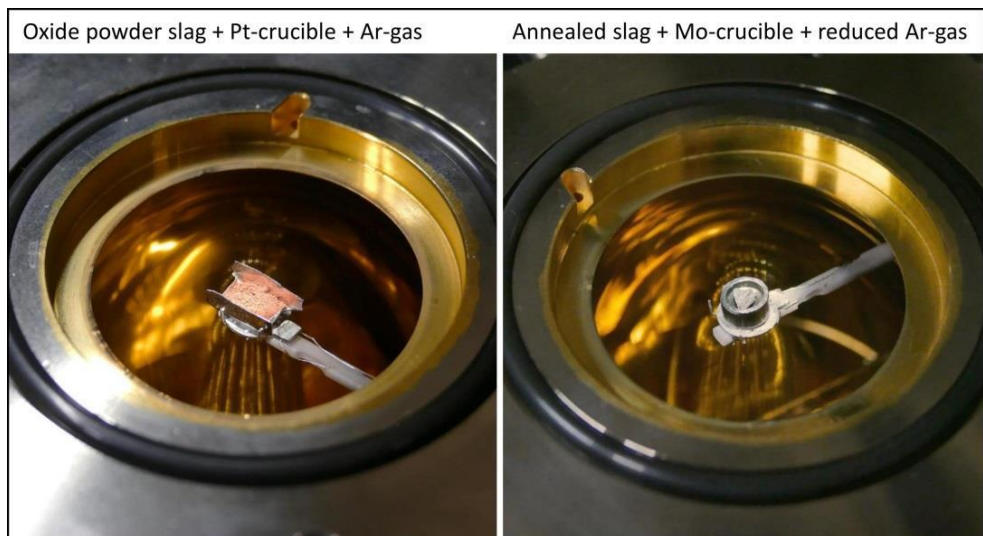


Fig. 3.7: The CLSM high temperature furnace, loaded with synthetic oxide powder in a Pt-crucible (left) and an annealed slag particle in a Mo-crucible (right), as shown in Schupsky et al., (2020) [137].

Lastly, it must be summarised that the decision to utilise annealed slag particles, Mo-crucibles, and reduced Ar-gas resulted in reproducible experimental results, which showed great accordance with the results of the quenching experiment. The comparison with the initial chosen parameters indicates that external factors in general have an unneglectable influence on the performance of experimental studies. The fact that the three experiments (viscosimetry, quenching, and CLSM) used all homogenised pre-annealed slag, (open) Mo-crucibles, as well as reduced atmosphere (Ar/4% H_2 - and reduced Ar-gas), ensures the highest possible comparability. As the result section will further show, the results also display a high accordance. Regarding the motivation of defining crystal morphology datasets for a future viscosity model for partially liquid slags, potential influencing factors on the experimental results need to be identified, evaluated and minimised. In the end, a parameter-assessment as performed in [137] is highly recommended to enable good scientific practice for future studies in this field.

3.5 Analytics

The generated slag samples from the high temperature viscosimetry, the quenching, and the CLSM experiment were analysed post-experimentally on crystallisation. The applied analytic methods are: digital microscopy, X-ray diffraction (XRD) and scanning electron microscopy (SEM). Microscopic and SEM images were utilised to gather crystal morphology data by measuring crystal dimensions using the programme AutoCAD (Autodesk, San Rafael, U.S.). However, before the samples could have been analysed, several preparation steps were required. All preparation steps and applied analytics were realised at the IEK-2 at Forschungszentrum Jülich GmbH.

3.5.1 Analytical Preparation

The following analytical preparation techniques were applied to all sample containing crucibles that were expected to include crystallised slag. Nonetheless the crucible designs and their dimensions varied, the required preparation steps were identical. Since the initial oxidic slag powders were filled into the crucibles and treated inside them, the slag needed to be disclosed, firstly. Therefore, the crucibles were cut into slices (viscosimetry experiment) and into hemispheres (quenching experiment). The viscosimetry crucibles were cut by a manual abrasive cutter due to the comparably large crucible dimensions. The cutting was realised using a diamond containing saw blade. The smaller quenching crucibles were cut in a BRILLIANT 220 (ATM Qness GmbH, Mammelzen, Germany) device. It is equipped with a programmable unit and processes each crucible automatically. The CLSM crucibles were not cut, due to their already small dimensions.

As a next step, the crucibles were embedded into epoxy resin to improve the manageability for subsequently following grinding and polishing. Therefore, Epoxy 2000 resin and Epoxy 2000 hardener (Cloeren Technology GmbH, Wegberg, Germany) cold mounting resin was used. To remove gas bubbles from the resin, the samples were additionally treated in a vacuum chamber. After a time period of two days, the resin hardened. Afterwards, the samples were grinded by using an automatic ATM Sapphir 550.3 (ATM Qness GmbH, Mammelzen, Germany) machine. The samples were grinded in several steps using abrasive paper with varying grain sizes. As the grinding procedure was finished, the sample surfaces were further smoothed by polishing. In the same device also polishing disks with applied diamond paste could be used. Sample polishing was used until a final grain size of 1 μm was reached. It must be mentioned that viscosimetry crucibles were prepared horizontally, meaning that the applied shear forces during the measurements are parallel to the prepared sample surface. So, potential crystals shall be observed best. In the case of the quenching crucibles, the preparation surface was chosen to be vertically orientated. Crystallisation shall be investigated regarding the spatial distribution in the crucible. The CLSM crucibles were both, horizontally and vertically prepared, in some case even both.

3.5.2 Digital Microscopy

First investigations on the slag structure were performed using a KEYENCE VHX-S550E digital microscope (KEYENCE DEUTSCHLAND GmbH, Neu-Isenburg, Germany). The digital microscope is connected with a computer and can be operated with a remote handheld. High resolution images with magnifications up to a factor of 200 have been taken from the samples. In contrast to a conventional microscope, the KEYENCE VHX-S550E is equipped with a coaxial light source and an additional ring-light source. The coaxial light source enables the investigation of the sample surface topography. Contrarily, the ring-light mode has the ability to penetrate inside the slag samples. Since the slag consists of oxidic compounds and shares similarities with a glass, amorphous regions on the slag are vitreous. Accordingly, crystallisation structures below the prepared cross section can be observed. Furthermore, the operating software tool enables the possibility of taking panorama-

images. This imaging mode combines several single images in the planar X- and Y-direction and creates an overall image at the end with comparable high resolution. There is also an advanced 3D mode available that takes images also with respect to the sample depth (Z-direction). Both panorama imaging modes were widely used during this study. The samples were analysed on the abundance of crystals and a selection between pure amorphous and (semi-) crystalline samples was made. The (semi-) crystalline samples were further analysed via X-ray diffraction and scanning electron microscopy.

3.5.3 X-Ray Diffraction (XRD)

X-ray diffraction (XRD) is a vastly used technique to identify crystalline phases in substances. As described in chapter 2.4.1, crystals are defined by a specific and repetitive structure as well as by their chemical composition. XRD represents the analysis of the structural parameters of a crystal phase, while a chemical analysis of a phase can preferably be performed by scanning electron microscopy.

XRD analysis is a comparable old technique, which was used since the beginning of the 19th century [16]. Basically, XRD requires three main components: X-ray tube, rotational sample holder, and a rotational detector [81]. The x-ray tube consists of a filament (cathode) and a copper target (anode) [81]. A high voltage of several tens of kilovolts is applied on the cathode, leading to the emission of high energetic electrons. They are accelerated and penetrate into the copper anode [81]. Thus, the high energetic electrons can produce a continuous and a characteristic spectrum of X-rays. The continuous spectrum is emitted when the electrons have multiple collisions with the copper nuclides, resulting in electromagnetic radiation [81]. However, if an electron collides with an electron in one of the shells of the copper atoms, it gets dislodged and a vacancy is created. Afterwards, an electron from the outer shells drops into the vacancy and emits the excess amount of energy as x-rays. These x-rays have a characteristic energy, since the relevant shell positions are defined. These characteristic x-rays (monochromatic) display a discrete distribution and are called e.g. K_{α} and K_{β} [81]. The applied x-rays in a diffractometer are mostly chosen to be in the range of 1-2 Å and therefore cover typical distances of atoms in crystal lattices.

The X-rays leave the x-ray tube in the direction of the rotational sample holder. The wavelength is in a comparable range to the atom spacing of the most minerals. When the characteristic x-rays collide with the atoms in the crystal structure, they get reflected [81]. Constructive interference of the individual reflected x-rays is possible, if the additional distance that an x-ray penetrates into the sample does not lead to a phase shift. Due to the change in the angle of incidence by rotating the sample, reflected x-rays overlap regarding the crystal atom layer spacing. To improve the recorded peak density, samples get grinded to powder before the analysis. Accordingly, the characteristic crystal lattice structure is defined by the following: the angle of incidence θ , the wavelength of the x-rays λ , and the distance of the atom layer d [79, 81]. The relationship between those three values are set into context by Bragg's Law [79]:

$$n\lambda = 2d \sin(\theta) \tag{13}$$

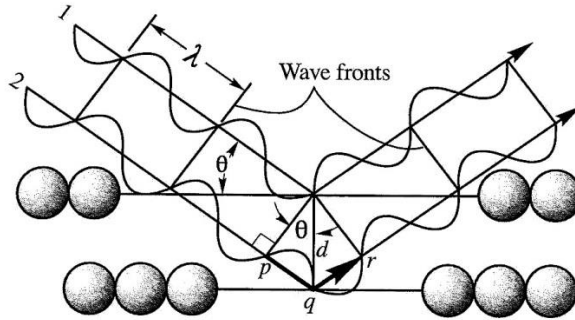


Fig. 3.8: Diffraction from parallel planes of atoms. X-ray 1 and 2 display constructive interference, due to no phase shift of their wavelengths, as seen in [81].

Following the rotational sample holder, a rotational detector is installed. Since the original x-rays are reflected by an elastic collision, the detector must be tilted with a doubled angle of incidence. The detector counts the reflected x-rays and generates a plot of the relative intensity of the x-rays in relation to the angle of incidence [81]. Regarding the individual mineral lattice structures, minerals can be identified due to their individual peak distribution in their XRD spectra [80]. Based on that principle, solid solutions such as olivine, melilite and feldspars occupy similar XRD spectra.

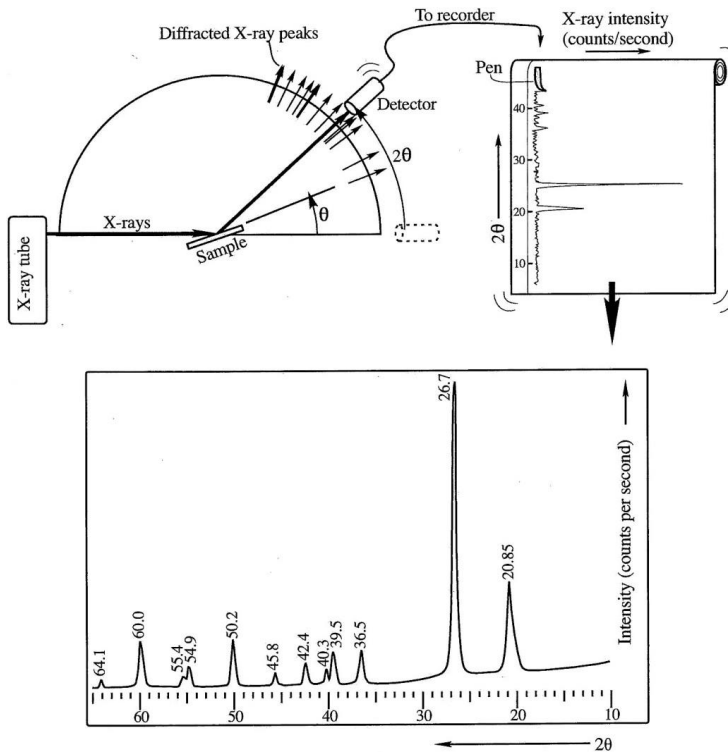


Fig. 3.9: Example of an XRD measurement of a powdered sample. Modified after Nesse (2009) [81].

To determine the crystallised phases structurally, XRD measurements of several representative samples of each slag have been conducted. A copper K_{α} anode (40 kV and 40 mA) was installed during the measurements. A Panalytical EMPYREAN (Malvern Panalytical, Almelo, Netherlands) device was utilized for the μ -XRD sample analysis. This device is located in the IEK-2 institute of the Forschungszentrum Jülich GmbH and was operated by an employee of the Scanning and Analytical Electron Microscopy group. The detected spectra for each slag were compared with datasets from the ICSD (Inorganic Crystal Structure Database, FIZ Karlsruhe, Germany) to determine the crystallised phases in the corresponding sample.

3.5.4 Scanning Electron Microscopy (SEM)

In this study a vast amount of samples was investigated via scanning electron microscopy (SEM). High resolution images with high magnifications can be performed to document the crystal shapes and the crystallisation structures. The chemical composition of samples and areas were determined by additional energy-dispersive x-ray spectroscopy (EDX) analysis. As a further advantage, SEM is a non-destructive analysis, which allows the reuse of a sample after the analysis. To stick to the main scope of this study, the setup and the fundamentals will be described briefly. For a detailed understanding of scanning electron microscopy, it is referred to the works of Erdman et al., (2019) and Schmidt et al., (1994) [138, 139].

Optical investigations via microscopy have been performed since several hundreds of years. Latest optical microscopes have a maximum resolution of 0.2 μm . Unfortunately, the achieved magnification cannot be increased further, since the magnification relies on the wavelength of the applied light [138]. To further increase the magnification, the use of electron beams was considered. Since an electron beam generates a magnetic field, the beam itself can be manipulated by an outer magnetic field. Based on that the use of electron beams enabled the utilisation of electro-magnetic-optical lens systems, resulting in a significantly improved magnification [138]. Driven by that technological improvements the transmission electron microscopy (TEM) was developed, which is capable of displaying atomic lattice structures [67, 80, 138]. Based on the TEM invention, SEM was invented to analyse the surface of samples. Nowadays, SEM is widely used since the analysis results deliver an appropriate magnification for most use cases and since the sample preparation requires far less effort, compared to TEM.

A generalised setup of a SEM device is shown in Fig. 3.10. The electron beam is generated in a Wehnelt cylinder, in which a high voltage (approx. 0.5-30 kV) is applied on a cathode, leading to an emission of the electrons out of the filament [67, 138, 139]. Based on its function, this unit is also often described as the “electron gun”. The electrons are accelerated towards an anode, which has a narrow gap of up to 50 μm in diameter to reduce the spread of the electron beam [139]. However, to additionally focus the beam, condenser lenses are located along the beam path. The focused electron beam surpasses deflection coils, which enable a lateral shift of the electron beam in x and y direction, enabling the scanning function of the beam on the samples surface (Fig. 3.10) [139]. Subsequently, a final arrangement of lenses and an aperture is positioned below the deflection coils to adjust the electron beam after the deflection coils, again. The sample is placed on a rotatable and tiltable sample holder that is located at the bottom of the SEM device (Fig. 3.10). Due to the interaction with the sample, different kinds of (e.g. electron) radiations are produced. To detect those radiations, several detectors are located above and next to the sample holder (Fig. 3.10). To exclude any interactions between the electron beam and molecules in the gas phase, the whole device is set under a vacuum by turbo-molecular pumps [138].

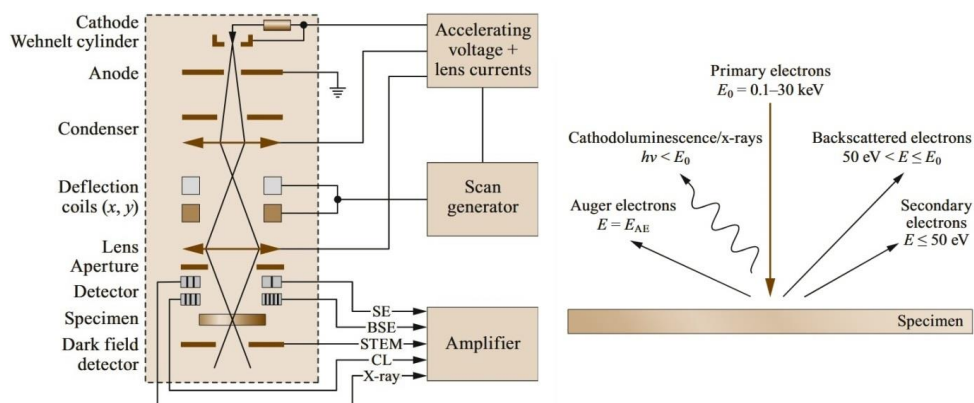


Fig. 3.10: Schematic drawings of a regular SEM setup (left), as well as of the generated signals by impinging electrons on a thin sample. Modified after Erdman et al. (2019) [139].

As the electron beam (primary electrons) impinges on the sample surface, the electrons interact with the sample and the energy of the electrons is converted into several forms of radiation (Fig. 3.10). In case the electrons experience an elastic collision, backscattered electrons (BSE) are emitted. They are comparably energetic and the intensity of the detected BSE per area strongly depends on the atomic number of the individual atom, which was hit. Atoms with a higher atomic number, appear brighter, compared with atoms having a lower atomic number [80]. Secondary electrons (SE) however, are the lower energetic radiation, reflected from the sample. They are produced as the primary electrons interact with the surface in an inelastic manner. As a result, only electrons from the sample surface can be detected, since they cannot cover large distances in the sample. Therefore, SE are commonly used to display the surface topography of a sample. In contrast, BSE can be used as a qualitative metric for the composition of the sample (based on the atomic number). A SEM device can be upgraded by certain modules that e.g. allow the detection of emitted x-rays (Fig. 3.10) [80]. X-rays are produced by inelastic scattering of the electron beam [138, 139]. Primary electrons interact with the atomic nucleus and loose energy that is emitted in the form of x-ray bremsstrahlung [138]. The x-ray analyser module detects the x-ray radiation, resulting in the characteristic spectra, highly comparable to the one in XRD. This method is named as energy-dispersive x-ray spectroscopy (EDX). Since the SEM has the ability to scan a certain area on a sample, such x-ray spectra can be obtained for specific regions and not just a single spot [138, 139]. By focussing on the characteristic peaks of the different elements, element mappings can be generated, displaying the spatial distribution of these elements at the detection area [139]. Based on the gathered chemical information, EDX is a useful enhancement of the regular SEM that was numerously used in this study.

Measurements were carried out by Zeiss Merlin II and Supra 50 VP (Carl Zeiss Microscopy GmbH, Jena, Germany) devices. The samples were prepared, applying an Ir-sputter coating, beforehand. In this manner, the vast majority of all crystallised samples were examined. In addition to taking high resolution images of crystallised phases, single EDX measurements as well as EDX element mappings were performed to gather chemical information. Based on the SEM images, the crystal analysis was applied on the anorthite phase. The length and width of individual anorthite crystals were measured and its aspect ratio (length/width) was calculated. To identify specific trends, a crystal length and the crystal aspect ratio were plotted against quenching temperatures.

3.5.5 Measuring of Crystal Shapes

As a last analysing method, the crystal shapes were measured using AutoCAD software (Autodesk, San Rafael, U.S.). Therefore, a selection of representative microscope and SEM images was made beforehand. The images were loaded in the software and adapted in their image-size with respect to the scale of the initial image. Subsequently afterwards, the crystals were measured using the dimension tool. Regarding the individually defined, generalised crystal morphology (chapter 2.4.1), the crystals were measured in length and width. The crystal size data were extracted into a table and the aspect ratio of the crystals was calculated from difference of the crystal length and the crystal width.

4 Results and Discussion

The analysis of oxidic slag crystallisation behaviour is a complex scope that must be divided into several sub-tasks to sufficiently reveal the crystallisation phenomenon. Since this study represents a basically new and unique approach to investigate slag crystallisation, the contribution of each applied method will be appreciated. At first, the slags need to be characterised on their melting and solidification behaviour by hot stage microscopy (HSM) and differential thermal analysis (DTA). The data of melting and solidification behaviour were used to adjust the experimental parameters for the following experiments. Thermodynamic equilibrium calculations were performed using FactSage Equilib programme as a tool to predict the slag behaviour before the experiments. High temperature viscosimetry is the first experiment to determine the viscosity of the slags. Additionally, it can be proven if non-Newtonian behaviour can be observed, which is expected to indicate crystallisation in the slag. The subsequently following quenching experiment represents the main experiment in this study. More than 250 slag samples were analysed in total, with respect to the applied temperature and the individual holding time under supercooling conditions. The analysis of the corresponding samples via digital microscopy, XRD, and SEM uncovers the evolution of crystallised phases, their growth kinetics, and lastly their morphologies. As an additional experiment, confocal laser scanning microscopy (CLSM) investigations were applied on the slag systems. Due to its in-situ observations, probable crystallisation kinetics can be observed highly detailed. Also, observations of the slags surface can be compared with the cross sections, analysed from the quenching experiment, to improve the consciousness of three-dimensional crystal morphologies. Furthermore, the reproducibility of the quenching methodology can be clarified, if the experimental results display comparable results with the CLSM results.

To enable a proper understanding of the relevant results, each section will display wisely selected data. Since the HKT and the ST-D-2 slag have a comparable composition, as well as are expected to have high viscosities of a similar range, their results will be presented closely related. In contrast, the HKR slag represents a likely low viscous system with diverging composition. Thus, results of the HKR slag will be presented alone-standing. The SOM-1 slag system was partly investigated by Saar (2019) [124], except for the slag viscosity. The results presented in that study are expected to be relevant for the three previously mentioned systems. Results of [124] will be incorporated if it is reasonable. However, it must be noted that a complete insight will only be provided in the originating study of Saar (2019).

Based on the experimental results of the four slag systems, crystal morphologies will be conceptually introduced and subsequently quantified. Based on crystal shape measurements, crystal size distributions of generalised crystal morphologies will be presented. The crystal morphologies will be generated, respecting the fundamentals of mineralogy and crystallography of the corresponding mineral. It is proposed that experimental and natural data show accordance and therefore prove the efficiency of this studies approach.

Finally, the proposed crystal morphology data will be briefly compared with crystallisation of real gasifier slags from the PiTER pilot plant, located at the TU Munich (Bavaria, Germany). In case of coinciding crystal morphologies, the quality of the aforementioned experimental results is additionally strengthened.

4.1 Slag Characterisation

The slag characterisation will be divided into two sub-topics: the melt and solidification behaviour and the crystal phase predictions. Both sub-topics have their unique relevance. HSM and DTA results reveal direct information about the crystallisation and solidification behaviour. These results indicate the least required temperatures that must be ensured in the following experiments to ensure fully slag powder melting. In contrast, phase predictions via FactSage Equilib programme provide an additional outlook on the experimental results based on the crystallised phases. Later on, these

results will be used for a comparison with the experimental quenching and CLSM results for a method validation.

4.1.1 Melt and Solidification Behaviour

Hot stage microscopy (HSM) was applied as the first method to determine the melt behaviour of the slag samples. With respect to the diverging compositions, variations on the melting behaviour of the individual slags were expected. HKT slag will be used in the following as an example to sketch the typical evolution that the pressed slag pellets underwent.

At the beginning of the HSM analysis, the HKT slag displayed a clearly edge shape and planar surfaces, since the slag powder was pressed as a pellet [16]. During the heat treatment, minor fractions of the oxide powder started to melt and pellet softened. Fig. 4.1 displays that the softening temperature (ST) was reached at 1300 °C, especially regarding upper and lower right edges of the pellet where a deformation can be observed. As the heat treatment continues, the pellet further deformed and the pellet-shape started to disintegrate. At 1312 °C, the hemispherical temperature (HT) of the HKT slag was reached (Fig. 4.1). It can be noted that the temperature difference between the ST and the HT is minor, indicating that the majority of the oxide powder fractions melted shortly one after another. Pellet melting proceeded with an increase of the applied temperature. The pellet seemed to be significantly molten at approx. 1330 °C. However, it was observed that the slag droplet melted further and reached its final stage at 1368 °C, as its height reached 1/3 of its initial height. So, 1368 °C represents the flow temperature for the HKT slag system (Fig. 4.1).

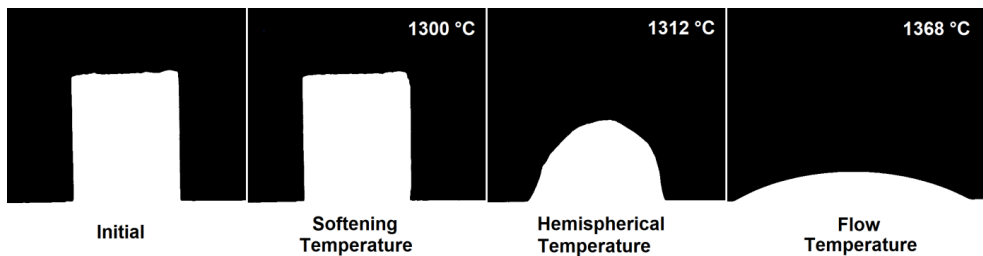


Fig. 4.1: Evolution of the synthetic HKT slag during hot stage microscopy documented by binary images.

The abovementioned HKT slag displayed intermediate melting behaviour, compared with the other slags, as indicated in Table 4.1. Its ST is identical with the ST-D-2 slag for example, but the HT and the FT are settled at significantly lower temperatures, compared to the ST-D-2 slag. In general, ST-D-2 slag displays the highest FT of all four slag systems (Table 4.1). The FT of 1420 °C exceeds the FT of the real ST-D-2 slag by approx. 115 °C [32]. It is believed that the simplified composition of the ST-D-2 slag is reasonable for this finding. By omitting alkali oxides and MgO, the slag composition lacks of network modifiers, resulting in a lower basicity (Table 4.1). Since the amount of SiO₂ is larger than 60%, the shift of the melting behaviour to higher temperatures is reasonable.

On the other hand, SOM-1 and HKR slag displayed melting behaviour at temperatures below 1333 °C. In general, ST, HT and FT of both slags are quite similar (Table 4.1). Regarding the composition of SOM-1 and HKR (Table 3.1) these observations are somehow unexpected, since the basicity of the HKR slag (0.94) is significantly larger than the one of SOM-1 (0.32). HKR slag furthermore melted almost instantly at the HT. Between 1302 °C and 1304 °C the slag pellet fully disintegrated into a droplet and the FT of 1320 °C was finally reached.

Table 4.1: Softening, hemispherical and flow temperature of the four synthetic oxidic slag systems as determined by HSM. SOM-1 data derive from Saar (2019) [124].

Slag Systems	Softening temperature	Hemispherical temperature	Flow temperature	Basicity
ST-D-2	1300 °C	1376 °C	1420 °C	0.12
HKT	1300 °C	1312 °C	1368 °C	0.26
SOM-1	1268 °C	1303 °C	1333 °C	0.32
HKR	1264 °C	1301 °C	1320 °C	0.94

The HSM results give a first insight into the melt behaviour of the investigated slag samples. However, it must be noted that only the initial melting of the pure oxide powders can be investigated by HSM. In contrast, differential thermal analysis (DTA) enables the analysis of a sample for several times by repeating the heating procedure. The solidification (i.e. crystallisation) behaviour is also detected, giving an additional benefit to this method. The DTA results of the HKR slag are displayed in Fig. 4.2.

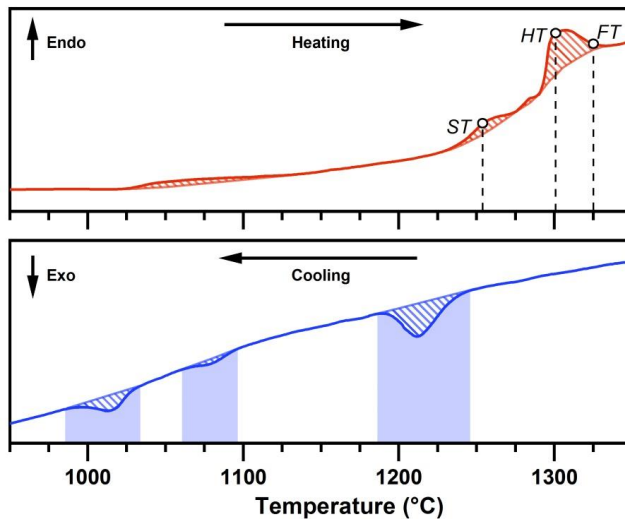


Fig. 4.2: DTA heating (top) and cooling (bottom) graph of the HKR slag. Softening (ST), hemispherical (HT) and flow temperature (FT) were added to the heating graph.

It can be seen that the HKR slag experiences several phases of oxide powder melting. A minor melting signal was detected from 1025-1110 °C, followed by two larger distinct melting signals (Fig. 4.2). The melting signals were compared with the melting stages that the pellet experienced during the HSM experiment. The ST correlates well with the first distinct endothermic signal between 1230 °C and 1275 °C. The subsequently following HT was occupied with a significant melting behaviour. The HT perfectly aligns with the most significant last endothermic signal, which was detected during the DTA measurement. Furthermore, the FT marks the end of the last endothermic signal and so is of great accordance as well (Fig. 4.2). The cooling process includes three exothermic peaks, which indicate solidification and/or crystallisation of the slag. The largest fraction of the slag seems to solidify between 1185 °C and 1245 °C. The final share of the slag however, starts to crystallise at approx. 1030 °C and ends at 985 °C (Fig. 4.2). It can be interpreted that different phases crystallised at each peak, indicating distinct crystal growth processes.

In contrast to the basic HKR slag, the melt and solidification behaviour of the HKT slag will be

described exemplarily for the lower basic slag systems. During the initial heating of HKT slag powder in the DTA device, a vastly distributed endothermic peak was determined (Fig. A.4). The initial melting was documented at 1110 °C and the end of the melting was documented at approx. 1265 °C (Fig. A.4). The comparison of the DTA with the HSM results clarifies, that there is a significant deviation of both experimental results. The temperature range of crystallisation determined by cyclic DTA measurements indicates that crystallisation starts at 1195 °C (Fig. 4.3). The exothermic peaks are vague to identify due to weak peak characteristics. The exothermic behaviour ends at temperatures of about 1000 °C and 980 °C, respectively. Hence, crystallisation in the synthetic HKT slag occurs between 980 °C and 1195 °C (Fig. 4.3). Compared with the real HKT coal ash [58], the crystallisation regime of the synthetic HKT is wider and generally settled at lower temperatures.

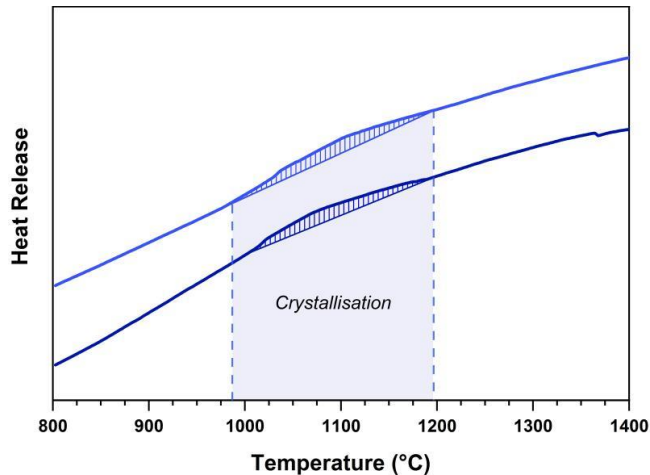


Fig. 4.3: DTA signals of cyclic HKT measurements and curves are shifted on the y-axis to improve the visibility of signals.

The DTA results of both, HKR and HKT slag indicated a shift of the endothermic melting peaks to lower temperatures, compared to the HSM results. The same tendency was observed for the ST-D-2 and the SOM-1 slag [124]. Generally, it can be concluded that HSM and DTA results are not perfectly comparable. Thus, it can be summarised that the DTA results of the individual melting and solidification i.e. crystallisation signals are shifted and do not align well with each other. In comparison with the determined melting temperatures, the crystallisation signals are shifted to lower temperatures. Such observations were also made by Seebold [32], are named as hysteresis and are likely caused by kinetic effects [53]. A certain degree of supercooling is required until the crystallisation is triggered, in contrast to thermodynamic equilibrium conditions, which do not include the influence of kinetics. In general, HSM and DTA measurements are slope measurements and cannot be performed isothermally, especially in the case of the DTA. The meaningfulness of these results must be treated with a certain degree of uncertainty.

4.1.2 Phase Predictions by Equilibrium Calculations

The slag characterisations were additionally supported by thermochemical equilibrium calculations using the FactSage Equilib programme (v.7.2, GTox-database). Thermodynamic equilibrium calculations can also be used to determine the crystallisation temperature of a certain slag system, though without the influence of kinetics, as mentioned before in chapter 3.1.4. As the kinetic influence on the results of HSM and DTA cannot be neglected, pure thermodynamic data are a

reasonable contribution to this study. An additional advantage is given by the fact that equilibrium calculations predict the exact phases that grow in the slag, below the liquidus temperature, regarding their thermodynamic stability.

Firstly, the Equilib results of the ST-D-2 slag will be presented (Fig. 4.4), as it has the most generalised composition. The slags liquidus is predicted to be settled at 1325 °C with an applied reducing atmosphere of 10^{-12} bar of oxygen. The first phase that was predicted to crystallise is anorthite ($\text{CaAl}_2\text{Si}_2\text{O}_8$, end member of the plagioclase solid solution). As a second phase, SiO_2 was predicted to form at 1280 °C in the structural form of cristobalite (Fig. 4.4). Cristobalite is a high-temperature modification of quartz, which is reasonable due to the relatively high crystallisation temperature. Both fractions increase with a decline in temperature. At 1125 °C, almost 75% of the slag is crystallised and the fractions of anorthite increased to approx. 45% and the fraction of cristobalite reached 30%. Below this temperature, cordierite ($(\text{Mg,Fe})_2\text{Al}_4\text{Si}_5\text{O}_{18}$) was predicted to firstly crystallise at 1110 °C. The solidus temperature was reached at 1000 °C and a fourth phase shall form in the slag: olivine ($(\text{Ca,Fe})_2\text{SiO}_4$, Fig. 4.4).

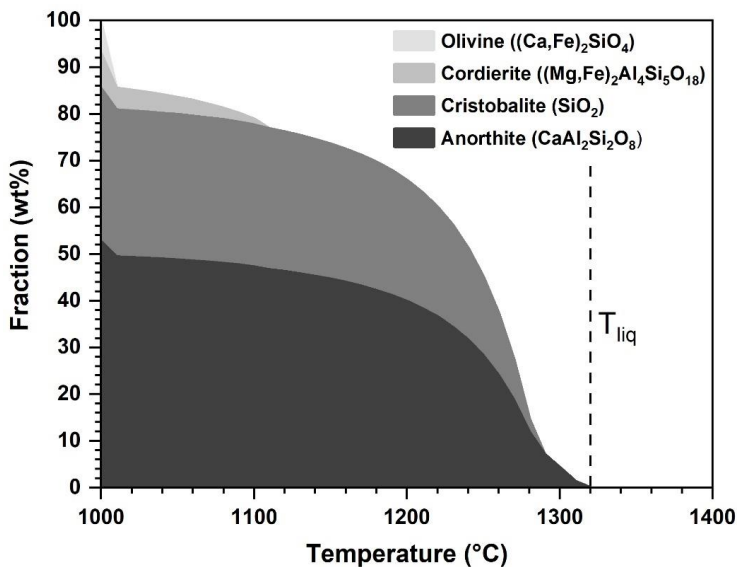


Fig. 4.4: FactSage Equilib prediction of ST-D-2 slag phase formation at an oxygen partial pressure of $p(\text{O}_2) = 10^{-12}$ bar.

FactSage Equilib calculations of the HKT slag system reveal that four phases should form below the liquidus temperature (Fig. 4.5). The predicted liquidus temperature is 1300 °C while the solidus temperature is reached at 1060 °C. These values align well with the experimentally determined flow temperature and temperature range of crystallisation, respectively. Anorthite crystallises as the first phase out of the liquid slag. Its content increases to approximately 47 wt% at 1050 °C. At temperatures of 1260 °C and 1250 °C cordierite and cristobalite (SiO_2) begin to form, respectively. Their fractions increase almost constantly and reach a maximum of about 13 to 14 wt%. Clinopyroxene ($\text{AB}(\text{Si,Al})_2\text{O}_6$) (A = Ca, Mg, Fe(II), B = Ca, Mg, Fe(II), Fe(III)) is the fourth predicted phase to crystallise (Fig. 4.5). Clinopyroxenes are comprised of several mineral phases and are distinguished from orthopyroxenes (orthorhombic) by their monoclinic symmetries. Calculations further reveal that the clinopyroxene phase is comparably enriched in Mg and Ca, but depleted in Fe. Its crystallisation starts at 1140 °C and ends at the solidus temperature with a fraction of 25 wt%. Taking only thermodynamics into account, anorthite represents the dominant crystallising phase in the synthetic HKT slag, especially in the temperature range of 1140-1300 °C (Fig. 4.5).

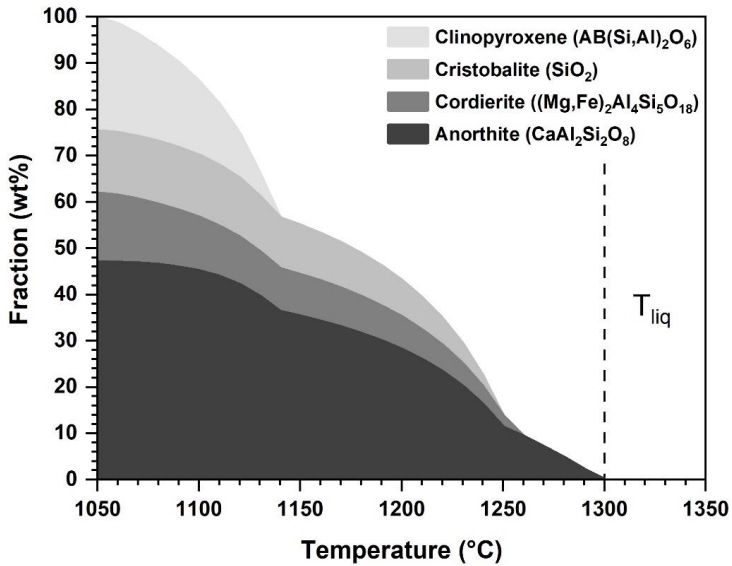


Fig. 4.5: FactSage Equilib prediction of HKT slag phase formation at an oxygen partial pressure of $p(\text{O}_2) = 10^{-12}$ bar.

The crystal phase prediction of the SOM-1 slag system is already described in the work of Saar (2019) [124]. Thus, only a brief summary of the calculation results will be given in this section. The liquidus temperature was predicted at 1250 °C, and the initial crystal phase shall be anorthite. Consequently, SOM-1 is the third slag system, in which anorthite was predicted to grow as the initial and dominant phase (based on the fraction at the solidus temperature). At around 1150 °C, cordierite is the second phase that was expected to grow in the slag. Subsequently following at approx. 1100 °C, clinopyroxene and olivine were ascertained to grow in the slag as the last phases above the solidus temperature. The solidus temperature shall be reached at 1055 °C. In the course of complete crystallisation at the solidus temperature, protopyroxene was predicted as well.

The FactSage Equilib predictions for the crystallisation of the HKR slag system are displayed in Fig. 4.6. Below the liquidus temperature, melilite is the first phase to precipitate. Furthermore, Equilib predicts that melilite miscibility is dominated by åkermanite at temperatures above 1250 °C and dominated by gehlenite at temperatures below 1200 °C (Fig. 4.6). Its overall content fluctuates between 18 and 30 wt%. The second phase to precipitate is supposed to be olivine, starting at 1290 °C (Fig. 4.6). The Olivine content is increasing as the temperature declines, reaching a maximum content of approx. 60 wt% when the slag crystallised completely at 1130 °C. Olivine mainly consists of kirschsteinit (CaFeSiO₄) and monticellite (CaMgSiO₄). The spinel phase is dominated by hercynite and spinel. Spinel phase was present between 1260 and 1150 °C and has the least content of all phases in the slag system (Fig. 4.6). At a high degree of supercooling, below 1150 °C anorthite is also supposed to form, reaching a maximum content of 18 wt% in the HKR slag system. The solidus is reached at 1130 °C. The presence of melilite and spinel in the investigated slag system aligns well with the crystallisation products of aforementioned studies (Table 2.6, [103, 104, 121]).

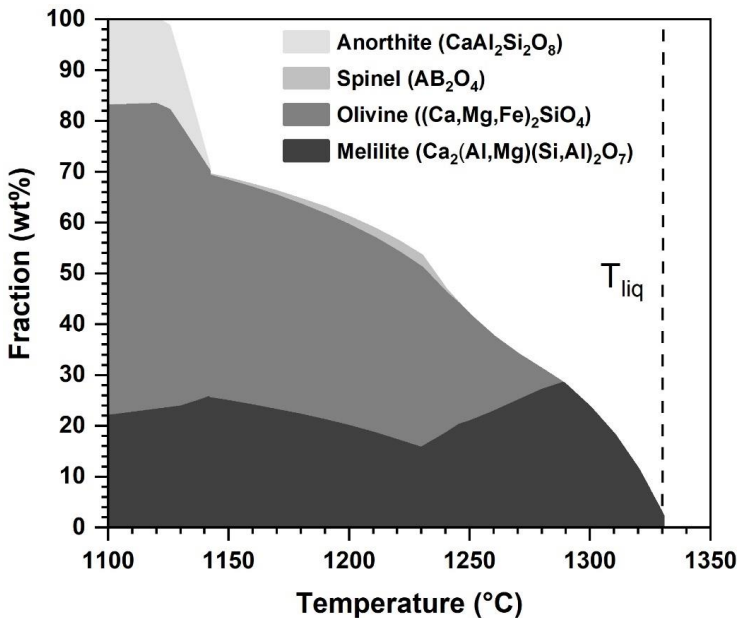


Fig. 4.6: FactSage Equilib prediction of HKR slag phase formation at an oxygen partial pressure of $p(\text{O}_2) = 10^{-12}$ bar.

It can be summarised that the four investigated slag samples were wisely chosen for the intended investigations in this study. ST-D-2, HKT and the SOM-1 system predict a major presence of anorthite and the vast crystallisation of SiO_2 , cordierite and clinopyroxene in the corresponding slag systems. Referring to the brief review of studies on slag crystallisation presented in chapter 2.4.4 (Table 2.6), the aforementioned phases greatly cover the frequently observed phases in real and synthetic slags. The HKR slag system additionally covers the melilite and the olivine phase. Both phases were also summarised to be of relevance for the typically occurring slag systems (Table 2.6). Due to the variations in the slags basicity and therefore the likely variations in the slags viscosities, high viscous (ST-D-2 and HKT), intermediate viscous (SOM-1) and low viscous (HKR) slags, are also satisfactorily covered by the selected slag systems.

4.2 Viscosity of Slags

Since the melting and solidification behaviour of the slag samples was sufficiently determined, the first experimental study on the slag systems could be performed – high temperature viscosimetry. The aforementioned results were considered for the sample preparation, more specifically for the pre-annealing of the oxidic slag powders (chapter 3.2.1). Based on the DTA and HSM results it was decided to choose 1450 °C as the peak temperature in the experimental setup, since all slag samples shall be in a liquid state at this temperature. The viscosity of the slags was measured stepwise at isothermal conditions. Non-Newtonian behaviour was observed, so the crucibles were analysed post-experimentally to determine if crystallisation can be found in the slags.

4.2.1 Viscosity measurement data

The first slags that will be described in this section are the high viscous slag systems ST-D-2 and HKT. The viscosity measurements of both slags were initiated at high temperatures due to their comparably high expected viscosity. At the highest temperature of 1425 °C, ST-D-2 slag displayed a viscosity of 96.5 Pa·s (Fig. 4.7). As indicated by the linear graph, the viscosity increases exponentially until 1275 °C (880 Pa·s), regarding the logarithmic depiction of viscosity values. However, for the lower temperatures of 1225-1250 °C, the viscosity growth is slightly stronger compared to the aforementioned higher temperatures. The overall ST-D-2 measurements could not be proceeded, since the maximum torque-limit of the rheometer was reached. The highest viscosity of the ST-D-2 slag at 1225 °C was determined as 3539 Pa·s (Fig. 4.7). In contrast to the ST-D-2 slag, HKT slag displayed an overall lower viscosity. As indicated in Fig. 4.7, the viscosity of HKT slag was measured as 17.3 Pa·s at 1425 °C. With a decline in the applied temperature, the viscosity increased moderately and reached a value of 76.5 Pa·s at 1300 °C. Accordingly, the viscosity of HKT slag was still lower at 1300 °C, compared to the lowest detected viscosity of the ST-D-2 slag. As already proposed earlier in this study, the viscosity of the ST-D-2 slag was expected to be the highest of the analysed slag systems, which is confirmed by the stated viscosity data (Fig. 4.7). Regarding the compositions of the analysed slag systems, the higher content of network formers and the lower content of network modifiers in the ST-D-2 slag is responsible for that high viscous behaviour.

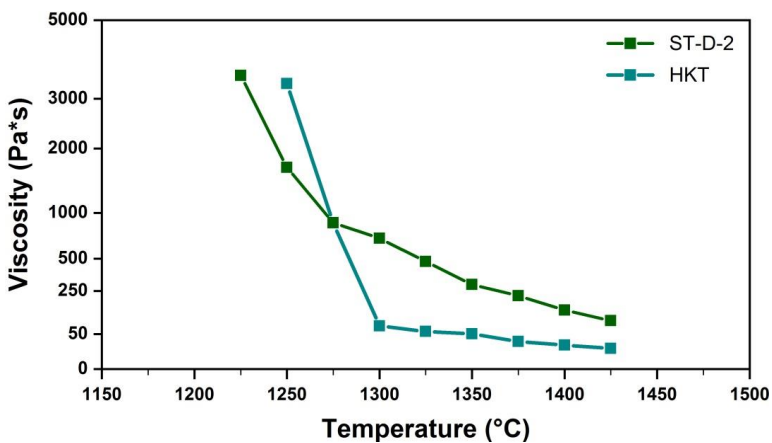


Fig. 4.7: Viscosity data of the high viscous ST-D-2 and HKT slag measured isothermally in steps of 25 °C. The y-axis is logarithmic scaled.

However, the viscosity behaviour of the HKT slag for even lower temperatures (1250-1275 °C), changes drastically (Fig. 4.7). HKT slag experienced a significant rise of the viscosity. From 1300 °C to 1275 °C, the viscosity increased by approx. +1150% (from 76.5 Pa·s to 877 Pa·s). Thus, rheological behaviour of the HKT slag was almost identical with the so far higher viscous ST-D-2 slag. At 1275 °C, the viscosity of HKT slag (3344 Pa·s) even surpassed the viscosity of ST-D-2 slag (1670 Pa·s). The measurements were finished, since HKT slag also reached the torque-limit of the rheometer.

The distinct viscosity increase and the surpassing of the viscosity of ST-D-2 slag stands in conflict with the expected viscosity, based on the basicity of the slags (Table 3.1). In detail, the sharp viscosity increase of HKT slag below 1300 °C cannot be explained by the regular properties of a pure supercooled liquid. The formation of crystals, and therefore the transition from a Newtonian to a non-Newtonian fluid, could be reasonable for the viscosity development. To verify this hypothesis, a comparison between the viscosity measurements and calculations will subsequently follow. Yet, the viscosities of the SOM-1 and the HKR slag will be mentioned before that comparison.

To complete the analysis of the viscosity measurements, the viscosity data of the SOM-1 and HKR

slag will be presented in the following. Based on the fractions of network formers and modifiers, SOM-1 slag was expected to be the slag with an intermediate viscous behaviour of all slags. As Fig. 4.8 indicates, SOM-1 slag has a higher viscosity than the HKR slag and is lower viscous compared to ST-D-2 and HKT slag (Fig. 4.7). The viscosity data reveal an initial viscosity of 16.3 Pa·s at 1400 °C. Herewith, SOM-1 viscosity is highly comparable with the HKT viscosity (23.4 Pa·s). In the temperature regime between 1250-1400 °C, the viscosity raises slightly but remains below 50 Pa·s. HKT slag tended to have a doubled viscosity during that range. However, as already observed in the HKT slag, a sudden viscosity shift to higher viscous behaviour was measured (Fig. 4.8). The rheometer measured a viscosity of 328 Pa·s. Due to too high viscosity values, the measurement could not be resumed further. The observed phenomena strongly coincides with the one observed in the HKT slag. Based on the described data, a fully Newtonian behaviour of the SOM-1 slag is unlikely.

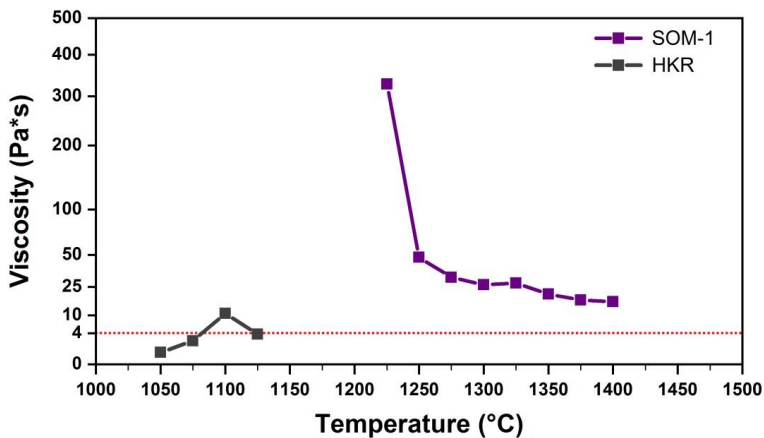


Fig. 4.8: Viscosity data of the intermediate viscous SOM-1 and low viscous HKR slag measured isothermally in steps of 25 °C. The y-axis is logarithmic scaled. The lower measuring tolerance of 4 Pa·s is marked with the red dotted line.

As already mentioned, HKR slag viscosity is lower than the one of the SOM-1 slag and is therefore the lowest viscous system analysed in this study. Fig. 4.8 displays that the HKR viscosity profile consists of only four data points. The overall viscosity range fluctuates between 0.6 Pa·s (1050 °C) and 10.8 Pa·s (1100 °C). Thus, the clear and reasonable trend of a viscosity increase with a reduction of the applied temperature was not found for the HKR slag. The data gap above 1150 °C can be explained by tremendously low viscosity values. The minimum shear resistance, the rheometer is capable of detecting, is given as 4 Pa·s (Fig. 4.8, dotted line). As can be seen, three out of four viscosity values fall below the measuring tolerance, which disqualifies them for a serious evaluation. The measuring campaign was repeated two additional times for the HKR slag, resulting in very similar results. Though, the data gap at higher temperatures can be explained by extreme low viscosities, lower temperatures shall lead to higher viscosities and therefore support the ability to detect a reliable slag viscosity. Nonetheless, the rheometer did not detect any reasonable slag resistance towards shear below 1025 °C and 1050 °C. Probably, the sample analysis presented in the subsequently following chapter enables a reasonable explanation.

As mentioned above, the slag samples displayed suspected non-Newtonian behaviour below a certain temperature (HKT, SOM-1) or unreliable data (HKR). To ensure the trustworthiness of the experimental setup and to exclude methodological faults, a comparison of the viscosity data with viscosity calculations may answer this question. Thus, the viscosity values for the analysed slag systems were determined, applying the latest version of the viscosity model of Wu (2015, 2015, 2019) [73, 140, 141]. The model enables the viscosity calculation of multicomponent systems, including Fe_2O_3 . Self-evidently, only Newtonian behaviour can be modelled and a possible impact of

crystals cannot be mentioned. A comparison of the viscosity measurement data with the model results is given in Fig. 4.9.

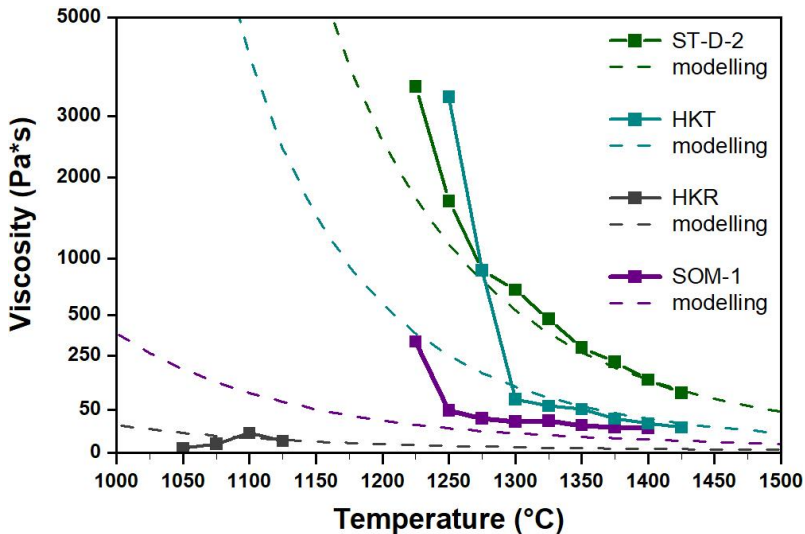


Fig. 4.9: Comparison of the viscosity data of the four slag systems, with the viscosity modelling results executed with the model of Wu et al., (2015, 2015, 2019) [73, 140, 141].

The comparison of the experimental data with the modelling results reveals an overall satisfactory agreement (Fig. 4.9). ST-D-2 slag data align very well with the modelling results. At temperatures below 1350 °C, a tendency of relatively higher viscosities can be identified. For 1250 °C and 1275 °C it can be vaguely argued that the discrepancy is based on non-Newtonian behaviour. The gathered HKT viscosity data are also reasonable, as the comparison with the theoretical modelling results prove (Fig. 4.9). Yet, the accordance accounts only for temperatures above 1275 °C. The previously mentioned drastic viscosity increase at 1275 °C and 1250 °C is clearly not covered by the modelling results. Accordingly, the initial hypothesis of a potential non-Newtonian behaviour is seen to be confirmed. If crystallisation accounted for this phenomenon, the subsequently following slag analysis will uncover the potential presence of crystals in chapter 4.2.2. The SOM-1 slag displays a generally higher viscosity in relation to the calculated values (Fig. 4.9). The measured values exceed relative constantly the model results by approx. 15 Pa·s. By also focussing on the distinct viscosity increase at 1225 °C, the comparison clearly documents that non-Newtonian behaviour of SOM-1 slag was present during the measurements (Fig. 4.9). In the case of the HKR slag, it can be concluded that the low detected viscosities represent the modelled viscosity very well. The fact that even lower viscosities at higher temperatures disabled the collection of data during the measurements is clearly given. Regardless, the viscosity is expected to increase for lower temperatures, which shall generally ensure the successful viscosity measurement in the setup.

Lastly, it can be summarised that the viscosities of three slag systems could be measured (ST-D-2, HKT, SOM-1). The viscosity values show overall a great accordance with the expected viscosities provided by the modelling results [73, 140, 141], in case they behave Newtonian. HKT and SOM-1 clearly display non-Newtonian behaviour below 1300 °C and 1250 °C, respectively. ST-D-2 slag shows a comparable weak viscosity increase at lower temperatures, compared to the other systems. A clear non-Newtonian behaviour could not be argued. Therefore, it is highly likely to expect that crystallisation occurred in the HKT and SOM-1 slag and potentially occurred in the ST-D-2 slag. The HKR slag however, was too low viscous for the available experimental setup. The lack of low temperature viscosity data cannot be explained, as the viscosity values shall be measurable for the experimental setup. Solely based on the viscosity measurements, a reasonable explanation cannot be

provided yet. In the following section, results of isothermal measurements will be provided. They were performed to ascertain the occurring crystallisation during the viscosity measurements. In case of present crystallisation, the deviation of the viscosity data from the calculation results can be explained.

4.2.2 Isothermal crystallisation

As mentioned in the previous chapter, HKT and SOM-1 display non-Newtonian behaviour and ST-D-2 potentially displays non-Newtonian behaviour. HKR slag in contrast, showed non-explainable viscosity behaviour. To reveal, if the slags inner structures were reasonable for the measured data, additional viscosity measurements with subsequent cooling of the crucibles were applied. It was intended to create a “snapshot” of the slag at the very end of the measurement, since the furnace was switched off after an isothermal measurement with a comparable long holding time. The target temperatures and holding times were individually chosen, as higher viscous slags (ST-D-2, HKT) were expected to need a longer incubation time for crystals to grow, compared with the intermediate and lower viscous slags (SOM-1, HKR). The visualisations of the ST-D-2 and SOM-1 sample analysis are settled in the appendix of this study, to keep this section as concise and informative as possible.

Firstly, the viscometer sample of the ST-D-2 slag will be described. ST-D-2 slag was additionally investigated isothermally at 1225 °C, since it represented the likeliest temperature regime in which crystallisation could have been present in the stepwise measurements (Fig. 4.9). The holding time was set to 7 hours, as the high viscosity and therefore low diffusion hinders fast crystallisation kinetics. As can be seen in Fig. A.6, the rheometer was merely able to detect the viscosity of the slag, as no higher rpm as 6 could be reached. It must be noted that the rheometer defines the applied rpm span, based on an initial shear resistance measurement: the higher the resistance, the lesser the maximum rpm. To ensure measurements at isothermal conditions for 7 hours, the rpm-profile was looped for 4 times (Fig. A.6). Regarding the viscosity data, it can be seen that the determined viscosity increases with lower rpm and vice versa. It is based on the silicate network structure of the slag (chapter 2.3.2). Higher rpm disrupt the silicate structure and shear faces occur in the liquid, parallel to the shear stress, resulting in a reduced slag resistance at higher rpm. Since viscosity measurements cover a wide range of rpm, this phenomenon is statistically negligible. Furthermore, it can be seen that the overall detected viscosity increases the more time passed during the overall holding time. The viscosity deviation between the first measurement at 0-105 min and the last at 315-420 min varies between 1-6.5%.

The microscope image of the prepared sample cross section reveals the slag structure afterwards the measurement was completed. ST-D-2 slag contains some Mo-particles (reddish, brownish) that were partially oxidised and/or formed alloys with the contained iron in the slag (Fig. A.6). This finding was determined based on SEM and SEM-EDX analysis of the samples. Accordingly, no grown crystal phase could be identified in the slag sample next to the Mo-particles. Nonetheless, as the microscope image displays, the inner region of the slag has a brighter colour, compared to the outer margin at the crucible walls. As will be seen later on in this study, crystallisation in the investigated slag systems often leads to a clouding of the glassy slag. Accordingly, the formation of very small crystal nuclei cannot be excluded, completely. Nonetheless, since no quantitative evidence of crystallisation could be made, the ST-D-2 slag is seen to be non-crystalline after 7 hours of holding time at 1225 °C.

As a next slag, SOM-1 will be described in the following. The corresponding figure is also settled in the appendix (Fig. A.7). Based on the stepwise measurements, the experimental parameters were set to 1225 °C and 3 hours of holding time. Similar to the ST-D-2 slag, several looped measurements were applied. The viscosity data also display a non-linear correlation, as previously mentioned for ST-D-2. A slight viscosity increase of SOM-1 aligns with an increase of the holding time (Fig. A.7). The viscosities of the last measurement series (150-180 min) are approx. 6-12% higher, compared to the ones of the first loop (0-30 min). Though, such viscosity increase might be reasoned by crystallisation, the overall dimension of the isothermal measurement is significantly lower, compared with the data

of the stepwise measurement that initially led to the hypothesis of occurred crystallisation.

The analysis of the prepared cross section of the SOM-1 crucible revealed a blackish, but glassy slag (Fig. A.7). Some particles were observed in the slag that have a negligibly low fraction. SEM-EDX analysis determined that the particles are based on Mo-particles, as well. As mentioned before for ST-D-2, some particles show signs of oxidation, some formed alloys with iron. Accordingly, no crystallised phases could be found in the slag. Also, the microscope image does not reveal any signs of crystallisation, which potentially grew below the cross section surface (Fig. A.7). It can be summarised that SOM-1 slag does not show any evidence of crystallisation at 1225 °C for 3 hours of holding time. The slight viscosity increase is not substantially enough to indicate crystallisation. However, during the stepwise measurement, the higher viscosity of 327 Pa·s could not be reproduced by the isothermal measurement. It can be argued that crystallisation occurred in the stepwise measurement, but not in the single isothermal one. As already mentioned in chapter 2.4.2, crystallisation (i.e. nucleation) underlies probabilities, which could be accounted for the seemingly mismatch of the viscosity measurements.

The slag behaviour of the HKT sample will be described in the following. The main results are concluded in Fig. 4.10, including viscosity data, microscopic and SEM-EDX analysis. The viscosity measurement was not looped, but it was constantly proceeded with one measurement (Fig. 4.10).

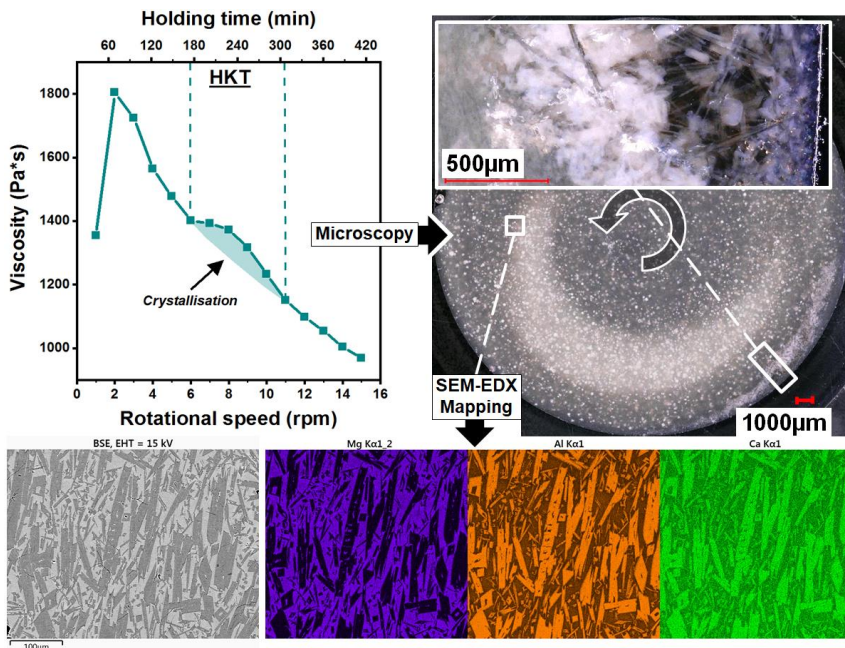


Fig. 4.10: HKT viscosity data of the isothermal measurement at 1250 °C (top left). Microscopic image of the prepared cross section of the crucible (top right). SEM-EDX mapping of crystallised anorthite: purple = Mg, orange = Al, green = Ca (bottom).

The viscosity plot follows the typical non-linear, declining tendency, as higher rpm are reached in the slag. However, it can be observed that the graph formed a hilly structure between approx. 175 min and 305 min of holding time (Fig. 4.10). It was expected that crystallisation occurred in the slag, leading to a lesser decline of the viscosity with respect to the higher rpm. Above 11 rpm, the viscosity aligned again with the regular trend of the graph. It was concluded that the crystals did not disappear, but orientated parallel to the applied shear stress, resulting in a relative decline of the viscosity. The slag would have therefore shown shear-thinning behaviour.

As the seven hour measurement campaign was finished, the furnace heating was switched off, the sample cooled down and it solidified eventually. Due to the comparable high viscosity, crystallisation structure was trapped as it was present during the very last measurement. A cross section of the crucible was prepared and analysed via digital microscopy, revealing a distinct presence of crystals in the sample (Fig. 4.10). Microscope images show a turbid-whitish discoloration of the slag, which is supposed to be glassy and dark green in an amorphous state. At the crucible walls, large crystals with length of several hundred μm were observed (Fig. 4.10). It is concluded that the aforementioned hilly structure of the viscosity data is truly based on slag crystallisation.

Some areas of the slag sample were additionally investigated via SEM(-EDX) to further characterise the crystal phase. As can be seen in the BSE image, the slag contains elongated crystals with a vertical orientation (Fig. 4.10). Based on the location in the sample, the orientation is parallel to spindle's applied shear stress. The assumption of shear-thinning behaviour is also confirmed by the orientated crystallisation structure. In Fig. 4.10, an element mapping was selected to visualise the crystal phase characteristics. Based on its composition, the phase was identified as anorthite. Its depletion of Mg, but enrichment of Al and Ca are characteristic for anorthite, as will be seen furthermore in the following chapters of this study. The crystal content was also determined via SEM in the range between 48-51% and so is comparably high. As already described in chapter 2.3.3, studies suggest an already significantly increased consistency for a liquid with such high amounts of non-spherical particles (Fig. 2.12). The documented viscosity behaviour can therefore only be explained, if anorthite crystallisation modifies the slag composition towards a less acidic composition with lesser amounts of network formers. For the rheological behaviour, it can be summarised that the remaining lower viscous modified slag composition compensates the influence of the high anorthite fractions.

Finally, the HKR slag system will be described. To avoid a further extension of this section, the displayed viscosity data and the microscopic image of the HKR slag are settled in the appendix of this study (Fig. A.8). The viscosity graph of the HKR slag displays a similar behaviour, compared to the previous HKT slag. The expected non-linear decline with respect to the increase of the spindle rpm is disturbed by a distinct hilly structure (Fig. A.8). Also for the HKR slag, crystallisation is expected to be reasonable for that phenomenon. The crystallisation occurred after approx. 45 min (30 rpm) and the end of the rheological influence was observed after 190 min (150 rpm). Since the hilly structure is very pronounced and comparably high rpm were required until shear-thinning behaviour was reached, intense crystallisation was expected in the slag sample.

The viscosimetry crucible was prepared and the slag surface was investigated via microscopy (Fig. A.8). The slag surface is dominated by crystallisation products, glassy regions could not be identified. On the slag surface, crystal morphologies could already be observed via digital microscopy. The crystals display a surprisingly symmetric quadrangular ground face (Fig. 4.11).

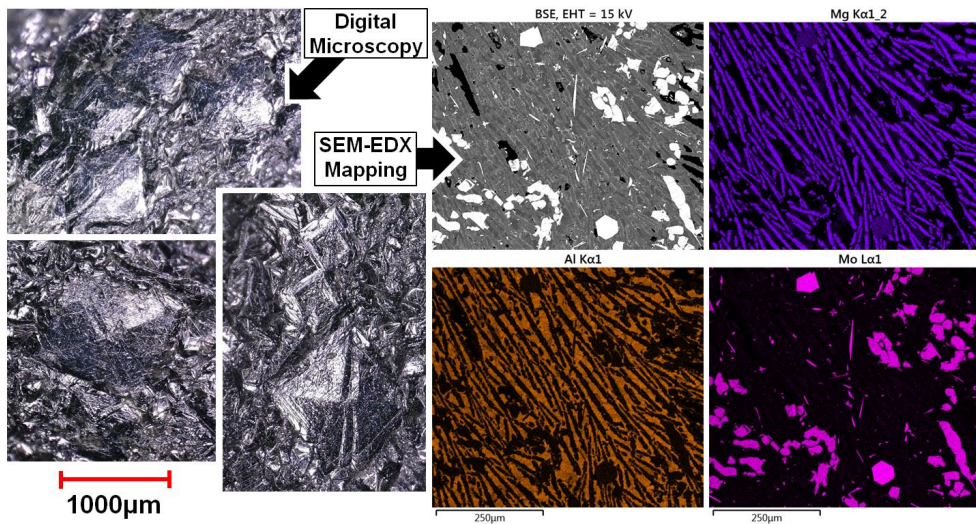


Fig. 4.11: Digital microscopic images of crystals on the slag surface after isothermal high temperature viscosimetry at 1150 °C (left). SEM-EDX mapping of a cross section: purple = Mg, orange = Al, pink = Mo (right).

Regarding the angle of the microscopic light source, it can furthermore be seen that the crystals have a topography, giving the outlook of a quadrangular pyramid (Fig. 4.11). With an edge length of up to 1 mm, those pyramids are relatively large and clearly identifiable. However, as a cross section of the same crucible (below the slag surface) was analysed, the crystallisation structure appears to be differently. The BSE image displays high contrast particles in the slag, surrounded by well orientated, elongated crystals. The whitish particles are fragments of Mo (and MoO_x), as indicated by the Mo mapping (Fig. 4.11). They derived from the crucible and seemingly fell into the slag. The other crystals however, seem to be either enriched in Mg or in Al. SEM-EDX measurements revealed that the Mg-enriched phase shows an olivine composition (i.e. forsterite (Mg_2SiO_4)) and the Al-enriched regions show a melilite composition (favour towards gehlenite ($\text{Ca}_2\text{Al}(\text{Al},\text{Si})\text{O}_7$)). Neither the quadrangular crystal shapes of the slag surface could be found inside the slag, nor the elongated crystals on the slag surface. The reason for that finding is unclear, but two scenarios can be discussed. Firstly, the crystals have a different density and the quadrangular crystals float on the slag (low density), while the elongated ones sink into the slag (high density). Due to the spindles rotation (least rpm before the final cool down: 400), turbulence was expected in the slag and an isostatic fractioning does not seem likely. The second and more probable reason might be found in the measurement procedure itself. While the crystallisation on the slag surface was not affected by the rotating spindle, crystals were able to grow idiomorphic. The crystals in the slag however, might got ripped apart by the high rpm of the spindle. Furthermore, it might be possible that crystal growth occurred during intense slag shearing, allowing crystals only to grow parallel towards the shear direction, since “edgy” parts of the crystals would have been dragged apart by the surrounding slag. Based on the intense crystallisation of HKR slag, crystal growth could potentially be causal for the viscosity data gap at the lower temperatures, occurred during the stepwise measurements. Accordingly, HKR slag showed the most significant crystallisation behaviour of all investigated slags. HKT and HKR crystals displayed elongated crystals inside the slag (anorthite, as well as olivine and melilite), but HKR also displayed quadrangular crystals on the slag surface. Both slags clearly displayed an influence on the viscosity due to crystallisation. ST-D-2 and SOM-1 slag however, did not crystallise during the examined time frames and solidified glassy.

4.3 Crystallisation Characteristics

Since the slag viscosities were vastly described and the potentially occurring crystallisation was explained, this section refers to results of the next two main experiments: quenching and CLSM. To investigate the crystallisation characteristics and kinetics of the four slag systems, the quenching experiment was conducted. The slags were also supercooled below their liquidus and subsequently quenched with respect to the passed time. For the high viscous slags, longer incubation times were expected, resulting in longer holding times. Vice versa, for SOM-1 and HKR slag, the holding times were reduced. The chosen parameters are listed in Table 4.2.

In contrast to the previous results, crystallisation was found in all four slag samples during the quenching experiments. The samples were prepared and analysed via digital microscopy, XRD and SEM. Firstly, the slag crystallisation will be described from a macroscopic point of view, using microscopic and CLSM images, since they already contain many useful results. When an overall consciousness of the crystallisation is provided, the crystal phases were determined via XRD. The crystallisation analysis via SEM follows subsequently, including a further chemical determination of the crystal phases, as well as high resolution images of the crystallised phases. Lastly, the crystallisation kinetics of the slag systems will be presented to complete the slag crystallisation characterisation. It must be noted that the SOM-1 slag will only be described very briefly in this section, as the results were generated in the study of Saar (2019) [124]. Since the ST-D-2 and HKT slag have roughly comparable compositions (Table 3.1), shall display similar crystallisation products (Fig. 4.4 and Fig. 4.5), and are both representatives of high viscous slags (Fig. 4.7), their description will temporarily be closely associated with each other.

Table 4.2: Temperature and holding time parameters chosen for the quenching experiments of the analysed slag systems.

Slag systems	Temperatures	Holding time
ST-D-2	900-1300 °C (steps of 50 °C)	0, 1, 4, 7, 24 h
HKT	850-1300 °C (steps of 50 °C)	0, 1, 4, 7, 24 h
SOM-1	1000-1250 °C (steps of 50 °C)	0, 1, 1.5, 3, 4, 5, 7, 24 h
HKR	1100-1350 °C (steps of 50 °C)	0, 10, 30 min, 1, 4, 7, 24 h

4.3.1 Macroscopic Investigations

To start with the high viscous slags, ST-D-2 macroscopic crystallisation will be described firstly. In total, 45 quenched samples were considered for the following observations. ST-D-2 crystallisation displayed basically two different crystallisation behaviours, as can be seen in Fig. 4.12: separated elongated crystals at high temperatures and fine-grained, cloudish to turbid crystallisation at intermediate and low temperatures, respectively. The example of Fig. 4.12a displays the first observed crystallisation at 1250 °C after 24 h of holding time. The slag appears greenish with a slight tendency to a brownish colour and seems to be glassy at first glance (ring-light mode). Yet, the grayscale coaxial-light mode enables the ability to emphasize the cross section surface topography. Since the hardness of the crystals deviates from the glassy slag, the crystals create a relief on the cross section surface. The crystals have an elongated shape and a hopper inner structure. These crystals are seemingly almost vitreous, leading to the relatively glassy look of the slag under ring light-mode. The majority of the crystals consist out of hopper segments that are barely connected with each other.

At 1200 °C and 7 h of holding time, the slag displays a more visible crystallisation (Fig. 4.12b)). Ring light-mode again reveals that a significant part of the slag remained glassy, but at the slag surface, crystallisation can be identified. The crystallisation zone is characterised by a cloudish i.e. turbid appearance. As the utilization of the coaxial light-mode reveals, these areas consist of a fine

topography, which can barely be recognised by the microscopic magnification (Fig. 4.12b)). The fact that crystallisation started at the slag surface points out that the transition from the liquid slag to the gas phase is an energetically preferred location for crystallisation to start. Though, the transition from the liquid slag to the Mo-crucible walls does not function as an incubation spot. This observation is representative and was observed for all slag samples. Accordingly, the usage of Mo-crucibles did not influence the crystallisation, as well as the results.

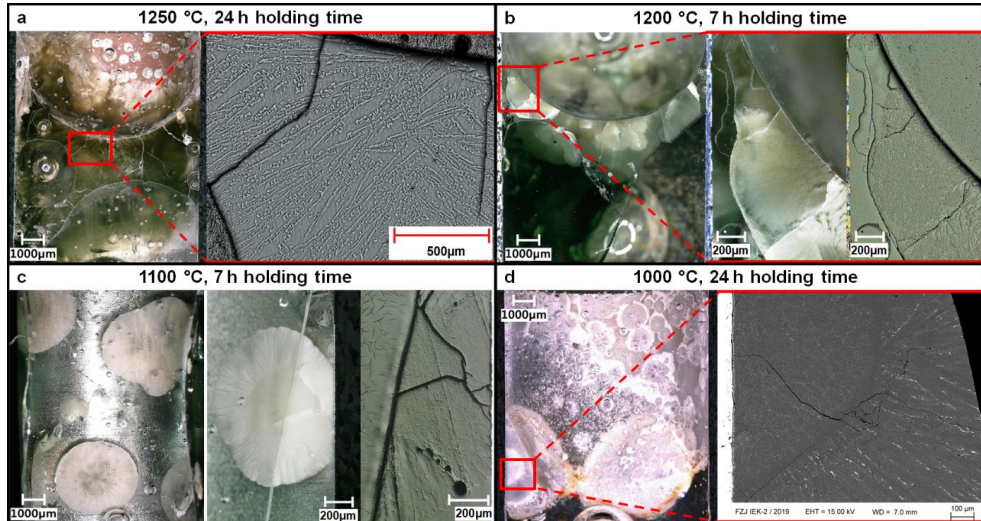


Fig. 4.12: Microscopic view of four representative ST-D-2 quenching samples, quenched at 1250, 1200, 1100, and 1000 °C after a holding time of 24 h, respectively 7 h each. The sample at 1000 °C is also characterised by a SEM-BSE image.

At lower temperatures of 1100 °C and 1000 °C, crystallisation displays a comparable macroscopic behaviour (Fig. 4.12c, d)). The crystals grew in the form of whitish concentric clouds, especially the sample at 1100 °C and 7 h of holding time faces such pattern. Regarding the viscosity data of ST-D-2 slag (Fig. 4.9), it can be argued that the very high viscosities at intermediate and low temperatures disable the growth of long single crystals, but support the growth of many crystal nuclei. Consequently, the slag behaviour is in agreement with the fundamentals of the crystallisation theory, as mentioned in chapter Fig. 2.19 of this study [86, 87]. At the lowest temperatures of 1000 °C, the SEM-BSE image indicates the presence of a phase with a higher contrast (higher atom mass) at the outer margins of the crystallisation cloud (Fig. 4.12d)). Since the magnification of the corresponding microscopic image is not sufficient (Fig. 4.12d)), it must be mentioned that this phase appears to be dark coloured, probably blackish in this and other low temperature ST-D-2 samples. Accordingly, at least two different phases seemingly grow inside the ST-D-2 slag.

The macroscopic crystallisation characteristics of HKT slag will be described, next. A total amount of 50 samples passed the quenching experiment to determine the crystallisation of HKT. Crystallisation was found in more than half of the samples that indicated diverse growth characteristics. The synthetic slag melt occasionally crept up the crucible walls and contained trapped gas bubbles. Whereas highest temperatures (1250 °C and 1300 °C) led to the growth of few but large elongated crystals, slightly lower temperatures caused smaller crystals to grow (1200 °C and 1150 °C, Fig. 4.13). Intermediate investigated temperatures (1100 °C and 1050 °C) generated cloudish, clearly distinguishable crystallisation fronts (Fig. 4.13). At low temperature regimes between 1000 °C and 900 °C, both cloudish crystallisation fronts and distinct single crystals formed as well.

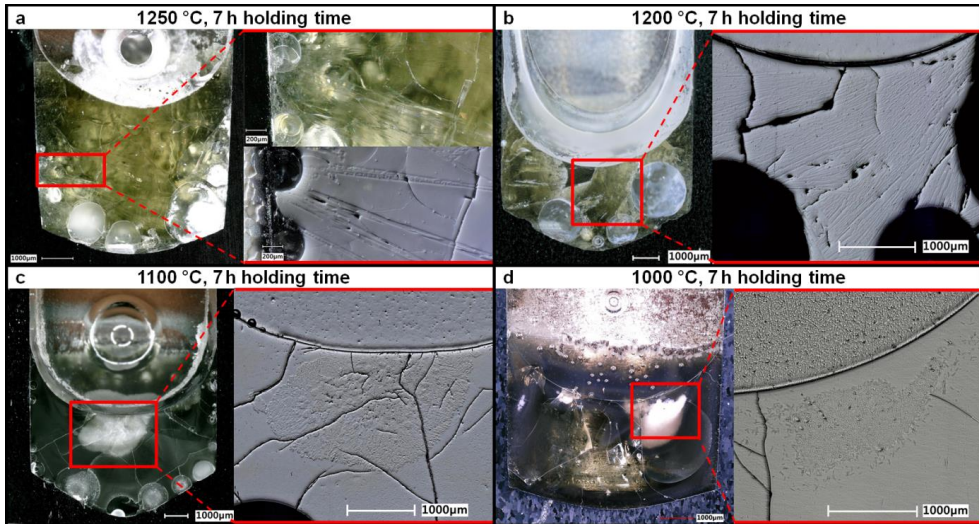


Fig. 4.13: Microscopic view of four representative HKT quenching samples, quenched at 1250, 1200, 1100, and 1000 °C after a holding time of 7 h each.

Microscopic investigations of the large crystals at 1250 °C and 1300 °C showed crystal lengths from a higher double-digit micrometre scale to a few millimetres (Fig. 4.13a). The growth of these crystals was partly limited by the crucible inner dimensions. So, the formation of even longer crystals could have been possible. Initially, the crystals started their growth from the crucible inner walls or the slag surface and grew towards the slag centre. The crystals appeared vitreous, showing no natural colour. The crystals which formed at 1200 °C and 1150 °C display elongated shapes and a vitreous look as well. Due to their relatively small crystal size (double- to triple-digit micrometre), these crystals grew in a threadlike crystallisation front.

The crystals forming in cloudish crystallisation fronts at 1100 °C and 1050 °C could not be individually distinguished by microscopic investigations due to their very small crystal sizes (few micrometres Fig. 4.17b). The crystallisation fronts had a whitish appearance and, therefore, could be identified easily from the surrounding greenish to brownish amorphous solidified slag. These fronts began to grow majorly from the slag surface and evolved in the direction of the slag centre as well, forming an indistinctly spherical shape. Though Fig. 4.13d indicates a similar cloudish crystal growth as shown in Fig. 4.13c, crystal nucleation showed a random spatial distribution. Instead of a propagating growth from one initial nucleus, several cloudish areas as well as single crystals appeared. As a result, low temperatures (900-1000 °C) led to heterogeneously spatial distributed crystallisation. At the temperature of 850 °C, a fully amorphous slag was obtained in the quenched samples, indicating that the slag already solidified as glass and no crystals could precipitate. Therefore, samples quenched at 850 °C are not further described.

Ultimately, the macroscopic crystallisation characteristics of the low viscous HKR slag will be described in the following. Crystallisation of HKR slag system was investigated by samples of the quenching and the CLSM experiments, also. A total amount of 30 samples were quenched after certain holding times in the supercooling regime. Fig. 4.14 displays a microscopic view of two representative samples, which experienced the same holding time of one hour at temperatures of 1250 °C (a) and 1150 °C (b). HKR slag showed a brownish to blackish colour in the Mo crucibles (left column, Fig. 4.14) and is interspersed with several cracks originated from the quenching procedure. Furthermore, both images indicate rectangular, prismatic macro crystals with a millimetre scale size that formed in the slag. This three-dimensional view was enabled due to the utilisation of transparent epoxy resin and ring-light observations with the digital microscope.

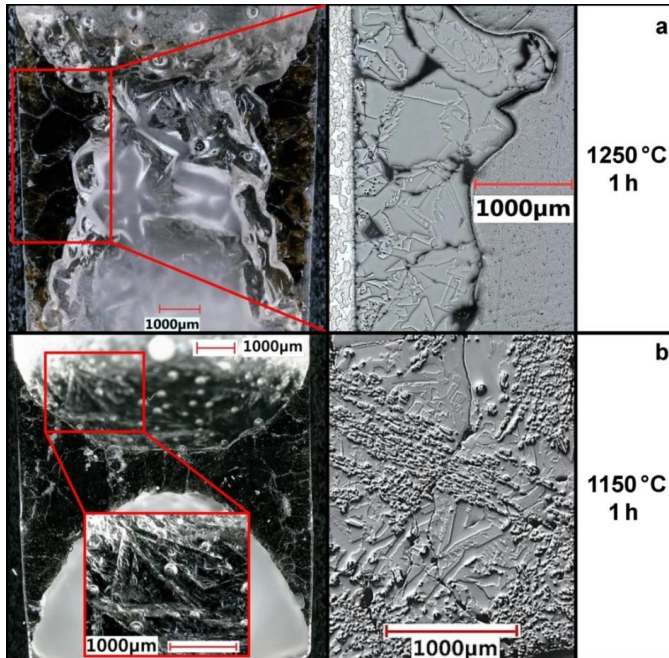


Fig. 4.14: Microscopic view of two representative HKR samples quenched at 1250 °C and 1150 °C after a holding time of 1 h each. Microscope images in the left column are made by ring light-mode and images in the right column are taken by coaxial-light mode.

However, the images made by coaxial light-mode reveal divergent symmetries. At 1250 °C, a selection of macro crystals is present, which are partially in a dendritic or skeletal shape. Additionally, at least one more crystalline phase can be identified, especially at Fig. 4.14b (1150 °C). Coaxial-light mode revealed the presence of a smaller granular fraction with spatial distribution that sometimes showed an aligned arrangement. In contrast, at 1250 °C (Fig. 4.14a) only very few granular particles could be identified close to the crucible walls. To enhance the understanding of the crystal growth evolution, two samples investigated by CLSM are displayed in Fig. 4.15. In-situ imaging indicated the growth of quadrangular crystals, floating on the liquid slag (Fig. 4.15a). The microscopic image indicates that several quadrangular crystals with sizes up to a millimetre scale were present in the slag after 30 minutes of holding time. However, as the in-situ CLSM image shows, holding times of 750 s already enabled such growth. Fig. 4.15b documents that also at approx. 1150 °C (applied cooling slope: -200 K/min) quadrangular crystals formed in the slag. By taking the digital microscope image into account, the quadrangular, prismatic crystals can be described as four-sided pyramids. The overall crystal dimensions and morphologies are of a comparable matter with the morphologies revealed under ring-light mode of quenched samples (Fig. 4.14, Fig. 4.15).

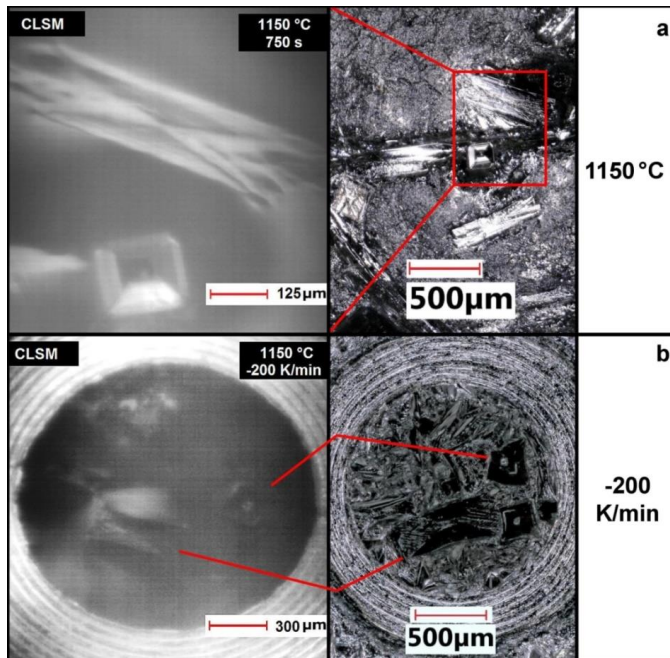


Fig. 4.15: CLSM in-situ view (left column) and microscopic view (right column) of two representative CLSM samples. Microscopic images were taken with ring-light mode after the experiment. a) was supercooled to 1150 °C and hold for 30 minutes, ultimately. b) was constantly supercooled with a slope of -200 K/min.

Lastly, the crystallisation characteristics of SOM-1 slag will be described briefly, a deeper description can be found in the originating study [124]. The slag structure of the SOM-1 slag is displayed in the appendix in Fig. A.9. It can be seen that the slag is glassy at 1250 °C. At 1200 °C, some elongated crystals can be identified in the slag with length of several millimetres. At 1200 °C and below, crystallisation in the slag intensifies until 1100 °C. From 1100 °C to 1000 °C the slag crystallisation appears to be uniformly whitish, cloudy (Fig. A.9). However, at 1000 °C, some blackish spots in between the cloudish areas can be identified.

It can be summarised that ST-D-2 and HKT slag display similar macroscopic crystallisation behaviour. Elongated single crystals grow at higher temperatures, followed by a fine grained crystallisation zone at intermediate and low temperatures. Regarding the analysed viscosimetry crucible (Fig. 4.10) and Equilib predictions (Fig. 4.4, Fig. 4.5), elongated crystals were ascertained to be anorthite. Simply based on the macroscopic observations, it can be assumed that anorthite also grew in ST-D-2 and HKT at the higher temperatures. Conclusions about the cloudish crystallisation cannot be made, since the crystals are too small. SOM-1 slag displays comparable crystallisation behaviour. Regarding the Equilib predictions (Fig. A.5) and the previously described elongated shape, it is also possible that anorthite is the high temperature crystal phase in the SOM-1 slag. HKR slag in contrast, displayed a completely different behaviour. Distinct quadrangular crystals, partly with a pyramidal shape were observed on the slag surface. These crystals clearly refer to the observations made by the viscosimetry crucible analysis of HKR slag (Fig. 4.11), indicating that it is the same crystal phase. The cross sections however, contain large skeletal crystals and a fine grained crystal phase.

4.3.2 Structural Phase Determination

To determine the crystalline phases by their structural (crystallographic) properties, XRD measurements of representative samples were carried out for all four slag systems. As described in the previous chapter, ST-D-2 and HKT slag seemed to show highly comparable crystallisation behaviour. Due to the fact that HKT slag is a five component system and its comparability towards the real slag systems is therefore improved, a stronger focus is set on HKT to the disadvantage of ST-D-2. XRD spectra of the slags were compared with reference datasets of the ICSD database.

To determine the crystallised phases of ST-D-2 slag, XRD measurements on slag samples with 24 h of holding time were applied. The longest time frame was chosen, as these samples shall be closest to equilibrium conditions and can therefore be preferably compared with the equilibrium calculations (Fig. 4.4). The results are shown in Table 4.3. The sample quenched at 1250 °C indicates the solely presence of anorthite. The overall crystallinity of the sample was assessed to be 18%. No further peaks were determined at this high temperature. As will be seen in the following chapter, SiO₂ was also determined based on the SEM-EDX results. Probably, the amount of sample was not representative for the XRD measurements. However, both phases were determined in the slag sample at 1150 °C (Table 4.3). In contrast to the 1250 °C, cristobalite was clearly identified at these intermediate temperatures. Both, anorthite and cristobalite (SiO₂) are the only documented phases, though the overall crystallinity was ascertained to be very high (Table 4.3). Approx. ¾ of the crystal phases are based on anorthite, the remaining quarter accounts from cristobalite. At the lower temperatures, anorthite and cristobalite are still present in the slag and can be clearly identified by XRD measurements. As the slag was fully crystallised, the fractions of anorthite and cristobalite rise to more than 90% (Table 4.3). Thus, some minor peaks were also detected: fayalite (olivine) and hercynite (spinel). Due to the fact that both, anorthite and cristobalite do not incorporate iron, it seems reasonable that fayalite (Fe₂SiO₄), the Fe-rich endmember of Fe-olivine is forming in the slag. In the previous slags (at higher temperatures), the Fe-content of the remaining slag must have been enriched as well. Thus, the lack of olivine or another Fe-containing phase could be rooted in a still insufficient enrichment of Fe afforded for crystallisation to occur.

Table 4.3: XRD results of three ST-D-2 samples.

	detected phases	phase fractions	crystallinity
1250 °C +24 h	anorthite	100%	18%
1150 °C +24 h	anorthite cristobalite	73% 27%	almost 100%
950 °C +24 h	anorthite cristobalite fayalite hercynite	57% 35% 6% 2%	100%

For the HKT slag, deeper structural investigations were conducted that will be described in the following. The selection of HKT samples represents temperature steps 1200 °C and 1100 °C with an associated holding time of 4 h (Fig. 4.16). The spectra were compared with several datasets, and two phases were identified to be present in the crystallised slags: anorthite and cristobalite. Sample spectra below 31° 2θ show a satisfactory accordance with the dataset peaks. Since the analysed samples were embedded into epoxy resin for subsequent SEM investigations, only a two-dimensional planar surface of the crystallised slag was analysed, to determine the spatial distribution of the grown crystals in the cross section area. The crystallographic orientation (hkl) was determined by XRD and then compared with the crystal orientations observed in the microscopic analysis. At a higher temperature of 1200 °C, peak analysis revealed that anorthite crystallised preferably in orientations (130), (131) and (240) (Fig. 4.16). According to (130) and (240), anorthite crystal surfaces show orientations perpendicular to the c-axis of the crystal lattice. Anorthite peaks of the 1100 °C spectrum indicate further hkl such as (222), (20 $\bar{2}$) and (244).

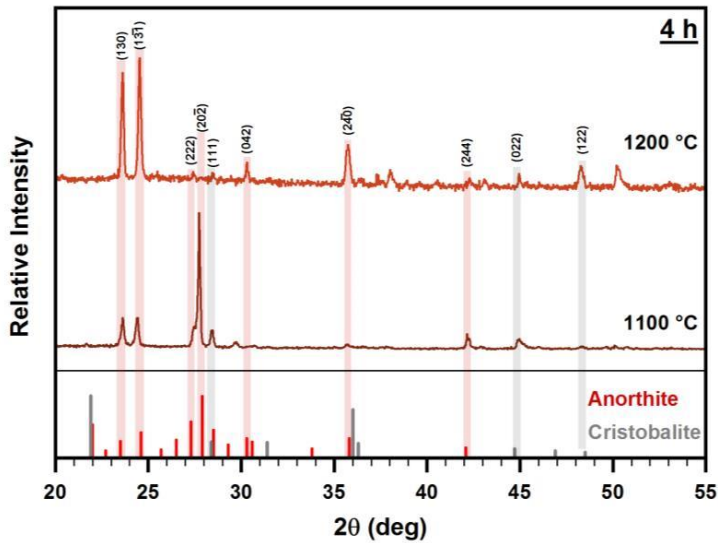


Fig. 4.16: XRD spectra of two representative samples quenched at 1200 °C and 1100 °C after a holding time of 4 h each

The crystallographic orientation was correlated with the crystal morphologies and their spatial orientation by microscopic images. The associated samples are displayed in Fig. 4.17. The microscopic image of the sample cross section (1200 °C, 4 h holding time), for example, indicates that crystallisation is dominated by elongated crystals in an overall threadlike structure and oriented parallel to the cross section (Fig. 4.17a). XRD peaks show similarities of anorthite lattice orientations (perpendicular to c-axis, Fig. 4.16) and microscopic images display a preferred crystal orientation in the same sample. Thus, an overall conclusion of both results is legitimised. Therefore, it can be concluded that anorthite crystals show an elongated growth in direction of the crystals c-axis. Similar observations were made by Wang et al., 2012 [142].

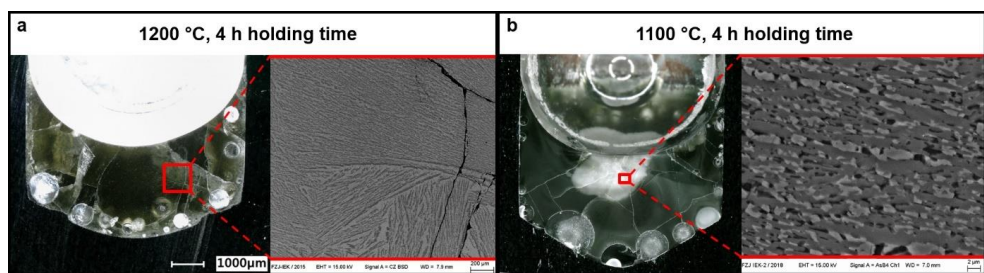


Fig. 4.17: Microscopic view of the cross sections of quenched HKT slag samples at 1200 °C and 1100 °C. The corresponding holding time was four hours each.

As XRD spectra were further compared with ICSD datasets, a vague accordance with cristobalite was found. Regarding both spectra (Fig. 4.16), only few peaks can be correlated unambiguously. Therefore, the overall presence of cristobalite cannot be concluded undoubtedly. Indeed, other phases such as clinopyroxene and cordierite (Fig. 4.5) are not considered in the XRD spectra. Quenched samples show intensified crystallisation as the holding time is increased. Therefore, four representative samples with the maximum holding time of 24 h were chosen to represent equilibrium conditions in the HKT slag. Slag powder was preferably used to enhance the spectra

quality compared with the embedded samples mentioned before. As displayed in Fig. 4.18, all four spectra show a comparable course, indicating similar crystalline phases. At 1150 °C, anorthite is the dominant phase as already stated at shorter holding times. However, other phases such as SiO₂ (including cristobalite, high quartz and low quartz), clinoenstatite and augite (both belong to the Clinopyroxene group) can be correlated with the spectrum (Fig. 4.18). Regarding the lower temperatures, the peak correlation of SiO₂, augite and clinoenstatite becomes more trustworthy, likewise their peak intensity increases. These three phases preferably crystallise at lower temperatures, while anorthite is always present. The comparison of Fig. 4.16 and Fig. 4.18 clearly indicates that the evolution of crystallised phases is strongly influenced by the sample holding time and therefore kinetics. Accordingly, an extended period of time is necessary for the synthetic HKT slag system to reach a (quasi-)equilibrium state.

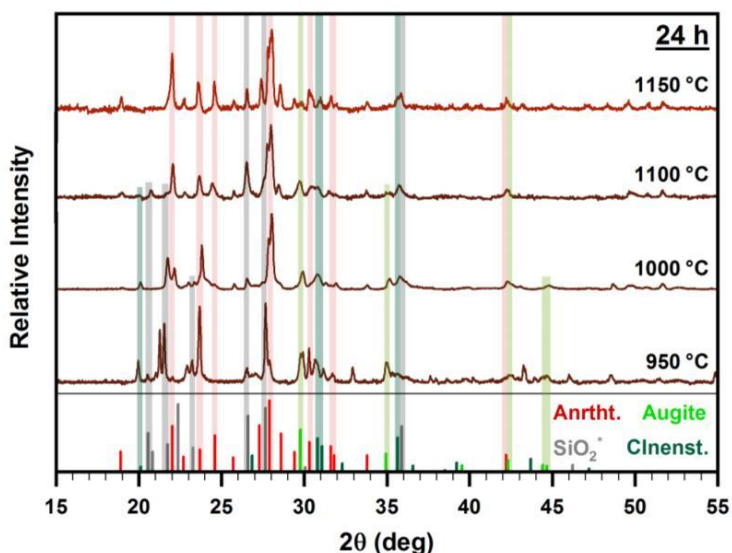


Fig. 4.18: XRD spectra of four representative samples quenched at 1150 °C, 1100 °C, 1000 °C and 950 °C after a holding time of 24 h each. The correlated datasets are: anorthite (red), SiO₂* (including cristobalite, quartz and quartz low, grey), augite (light green), clinoenstatite (dark green). Datasets derive from ICSD database.

As will be seen later on in chapter 4.3, the crystallisation kinetics of the HKR slag significantly varies from the ones of ST-D-2 and HKT. Therefore, XRD analysis was applied to samples with a lower holding time. A selection of three samples was chosen and is displayed in Fig. 4.19, representing 1250, 1150 and 1100 °C. The holding times of the samples are in a range of 0 minutes (instant quench) up to 60 minutes. As the comparison of the analysed spectra indicates, all samples are in a very well agreement with each other. Major peaks are present in all samples, also displaying similar peak intensities. However, the sample quenched at 1250 °C contains a slightly higher background signal between 25 and 35 2 θ , which represents the amorphous slag that was still present in the sample. Compared with the instant quenched sample at 1100 °C, the noticeable presence of amorphous slag at 1250 °C (60 min holding time) is an indicator for an overall lower crystallisation content and therefore slower crystallisation kinetics (Fig. 4.19). Melilite was undoubtedly identified as the main phase in all spectra. Peak positions and also peak intensities are in coincidence with ICSD dataset 187934 for melilite phase (Ca₂(Mg_{0.495}Fe_{0.202}Al_{0.303})(Fe_{0.248}Al_{0.216})Si_{1.536}O₇). As a second phase, forsterite was identified in the XRD spectra. Though, the overall accordance with ICSD dataset is less plain, compared with melilite. Quantitative analysis of the XRD spectra indicated degrees of

crystallinity for melilite and forsterite of 98:2 (1250 °C), 95:5 (1150 °C) and 83:17 (1100 °C), respectively. Ultimately, it can be concluded that forsterite is preferably crystallising at lower temperatures compared with the melilite phase. The overall crystallinity was determined in the range of 70- 80 wt%.

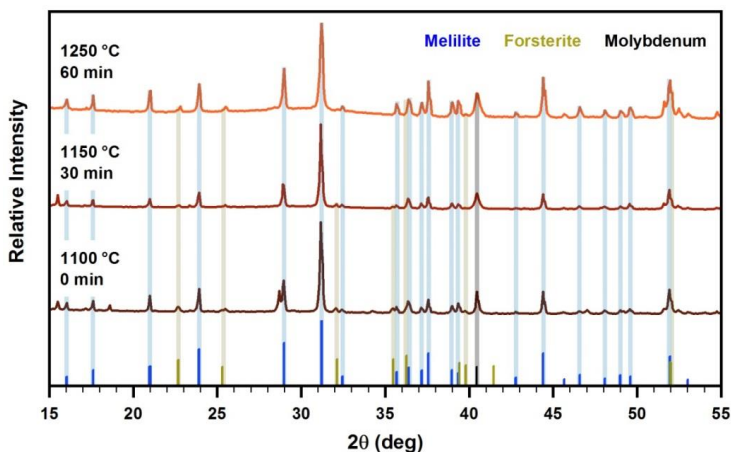


Fig. 4.19: XRD spectra of three representative samples quenched at 1250 °C, 1150 °C, and 1100 °C after holding times of 0, 30 and 60 minutes. The correlated datasets are: melilite (blue), forsterite (green) and molybdenum (black). Datasets derive from ICSD database.

Ultimately, some brief descriptions on the SOM-1 crystallisation will be given. The phases: anorthite, clinopyroxene, and olivine were identified in the slags (Fig. A.10) [124]. The peak intensity of anorthite is always the highest, indicating that SOM-1 slag is also dominated by that phase. However, at lower temperatures, the peak intensities of clinopyroxene become also significant. The peak intensity of olivine is the weakest of all crystallised phases. With respect to the contrary holding times of 0 h (instant quench) and 24 h, no trend could be identified, indicating that the crystal fractions grew uniformly with respect to time (Fig. A.10).

Finally, it can be summarised that ST-D-2 and HKT slag show (some) accordance on the crystallised phases with initially performed equilibrium calculations, as well as HKT and SOM-1. Anorthite is noticeably the dominant phase in these slag systems. Due to the high SiO₂ fractions in the bulk ST-D-2 and HKT slags (Table 3.1), cristobalite crystallisation occurs, which on the other hand did not crystallise in SOM-1 slag. However, the formation of clinopyroxene is based on the enrichment of Fe and Mg in the remaining liquid slag, since both cannot be incorporated in anorthite and cristobalite. HKR slag in contrast, displays a dominance of melilite, but forsterite (Mg-olivine) can also be clearly identified. The spectra also include very few, minor peaks that could not be correlated with certain datasets.

4.3.3 Chemical Phase Determination

Utilising the widely used XRD analysis, crystal phases were identified based on the crystallographic structure. However, sometimes minor phases cannot be identified by XRD due to weak peak intensities. To support the previously mentioned crystal phase determination, SEM-EDX analysis was performed to identify crystal phases by their chemical composition. Since SEM provides also high resolution images, the crystal phases can also be determined by their crystal shape.

Once again, ST-D-2 slag crystallisation will be described firstly in this section. A selection of three representative samples was chosen and compared in Fig. 4.20. As a representative sample for

crystallisation at higher temperatures, Fig. 4.20a with a holding time of 24 h at 1250 °C was chosen. Digital microscopic image reveals that the slag has a greenish to brownish colour and is seemingly vitreous (ring-light mode). Thus, the relief of the cross section shows the presence of elongated crystal structures. Those crystals consist of single hopper segments, which aligned in an elongated arrangement, or the crystals potentially fall apart into segments (Fig. 4.20a). SEM-EDX mappings indicate an enrichment of Al and Ca as well as a slight depletion of Si and no contents of Fe in this phase. Further SEM-EDX point measurements confirmed an anorthite composition of that phase. As already described in chapter 4.2.2, anorthite phase is characteristically depleted in Fe and enriched in Al and Ca, also in other anorthite bearing slags (HKT, SOM-1), as will be seen later on in this study.

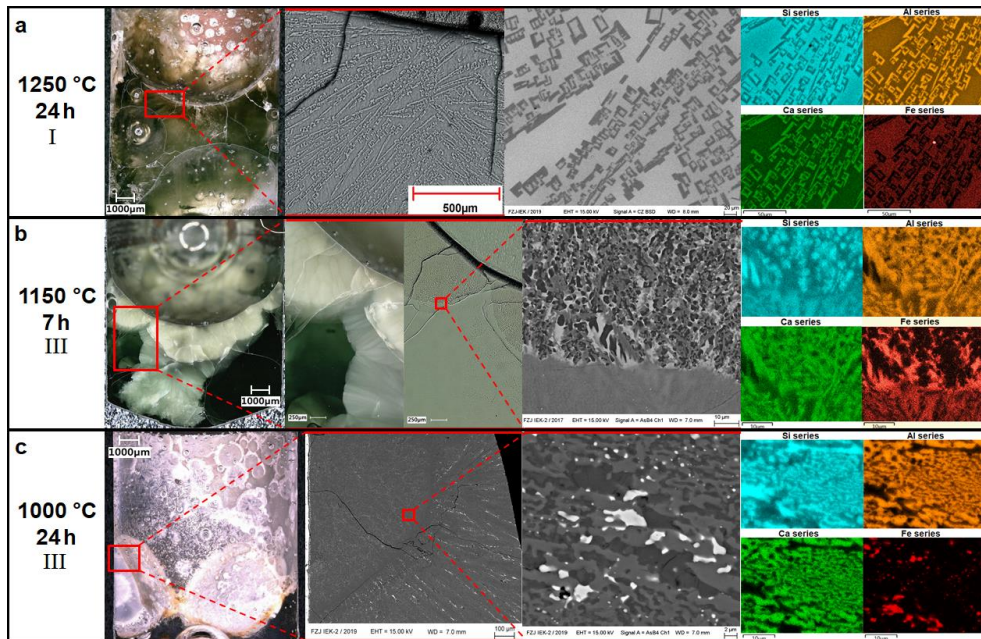


Fig. 4.20: ST-D-2 crystallisation documented by SEM and SEM-EDX mapping in representative samples, quenched at 1250 °C, 1150 °C, and 1000 °C, with holding times of 24 and 7 h. Colours of element mappings: cyan = Si, orange = Al, green = Ca, red = Fe.

At intermediate temperatures of 1150 °C, Fig. 4.20b consists of a typical example of the turbid, cloudish crystallisation of ST-D-2 slag. The crystallisation is very fine grained and single crystals cannot be observed with the microscope. However, the microscope and SEM images indicate, that the cloudish regions consist of an outer crystallisation margin, surrounding the inner crystallisation zone (Fig. 4.20b). SEM images reveal that the inner zone contains a second phase that is not present in the outer margin. By applying element mappings on these zones, it can be seen that anorthite is widely present (Ca and Al signal). The crystal shape is still elongated, but segments cannot longer be identified. In the inner regions, the second phase stands out due to a strong enrichment of Si and a remarkable depletion of Ca and Al and no fractions of Fe (Fig. 4.20b). Additional SEM-EDX point measurements confirmed this phase to be SiO_2 . SiO_2 did not crystallise in a remarkable crystal morphology. Mostly, the crystals fill existing gaps between anorthite crystals and appear granular. The Fe mapping clearly displays that the slag in the inner regions is highly enriched in Fe, since both, anorthite and SiO_2 due not incorporate Fe.

A representative sample for the lower temperatures was chosen (1000 °C, 24 h, Fig. 4.20c). Microscopic images indicate that the slag is seemingly fully crystallised in form of whitish, turbid spots. SEM images firstly show the presence of a phase or areas with a high contrast (white

appearance, indicating elements with high atomic number, Fig. 4.20c). Element mappings indicate a strong enrichment in Fe, fractions of Si and a clear depletion of Ca and Al. Due to the previously mentioned fact that Fe is not incorporated in anorthite and SiO_2 a further concentration was not surprising. However, clear crystal shapes cannot be identified in these regions, assuming that it is Fe-enriched slag and not a crystal phase (Fig. 4.20c). Nonetheless, SEM-EDX point measurements proved that this high-contrast phase has a perfect fayalite composition. The possibility that these areas simply display remaining glassy Fe-enriched slag can therefore be neglected. Thus, it is concluded that an olivine phase (fayalite) is the third and also the last crystallising phase in the ST-D-2 slag. Due to the last remaining gaps between anorthite and SiO_2 , fayalite lacks of space to crystallise in a specific shape and appears fully xenomorphic.

For the ST-D-2 slag, it can be summarised that anorthite (all temperatures), SiO_2 (intermediate and low temperatures) and olivine with fayalite composition (low temperatures) crystallise. While anorthite crystals appear as distinct, segmented (hopper shaped) crystals with an overall elongated appearance at high temperatures of 1250 °C, temperatures of 1200 °C and below generated cloudish crystallisation with small crystal sizes. SiO_2 appears as granular crystals and fayalite grew xenomorphic, regarding the left over empty space between the other two phases. These observations can be used to achieve kinetic information on ST-D-2 crystallisation properties. Anorthite crystallises firstly, followed by SiO_2 , indicated by the outer margin (containing only anorthite) surrounding the inner crystallisation zone (anorthite + SiO_2). Since fayalite crystallises completely xenomorphic, it crystallises lastly and fills the inter-crystalline gaps.

The crystallisation of the HKT slag, displays similarities with the ST-D-2 slag. In consensus with the crystallisation theory [86], larger crystals (but less in number) formed at higher temperatures, while lower temperatures allowed numerous crystals to form (but with a limited size, Fig. 4.21). The sample quenched at 1250 °C contains few crystals with lengths varying from several hundred micrometres up to a few millimetres. The corresponding SEM images in Fig. 4.21a display a detailed view on their elongated, hopper shapes. These crystals also show partial disintegration into single quadrangular fragments. It can also be seen that the fragments consist of a crystalline frame, while the inner region still contains amorphous slag. Furthermore, EDX mapping reveals an enrichment of Al and Ca in that phase, while Si is depleted compared with the surrounding slag. Mg and Fe are absent in the phase (Fig. 4.21a). At a slightly reduced temperature (1200 °C), quenched slags show a higher number of crystals in a threadlike pattern. They are elongated as well, and their inner structure is jagged. By taking occasional crystal shape deviations into account, the crystal morphologies are comparable between 1250 °C and 1200 °C. Element mapping also indicates the enrichment of Al and Ca, as well as the depletion of Si and the abundance of Fe and Mg. Thus, the crystallised phases at both temperatures are likely identical. Large grown, fragmented crystals were also found at 1300 °C (24 h of holding time) and threadlike crystal arrangements were observed as well at 1150 °C (1, 4, 7 and 24 h of holding time). Thus, this elongated phase is dominant between 1150 °C and 1300 °C, showing also comparable morphologies.

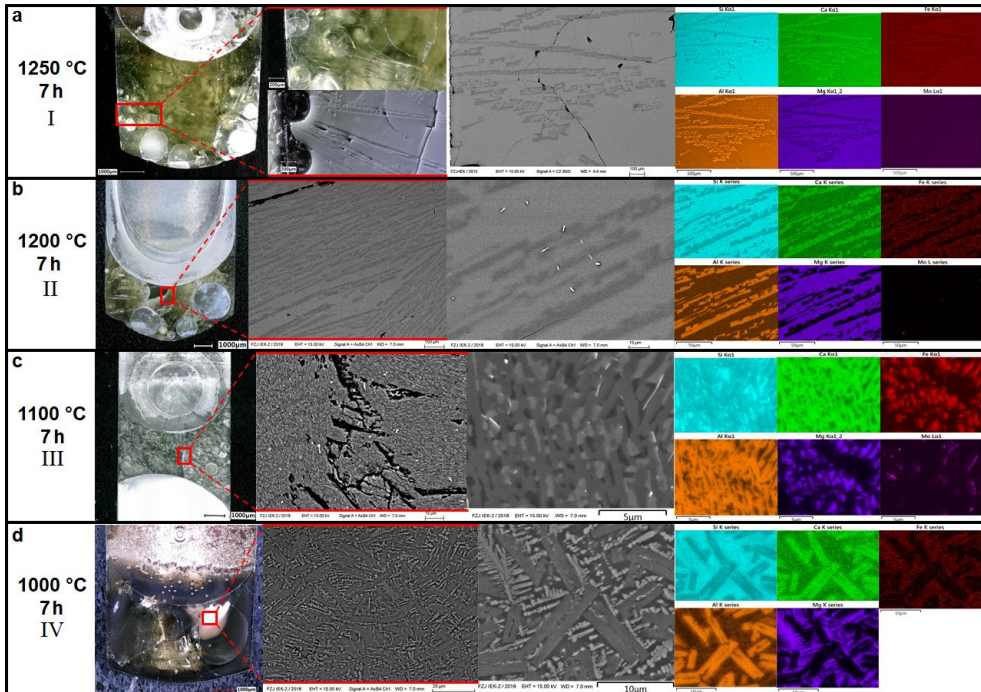


Fig. 4.21: HKT crystallisation documented by SEM and SEM-EDX mapping in representative samples, quenched at 1250 °C, 1200 °C, 1100 °C, and 1000 °C, with a holding time of 7 h each. Additional colours of element mappings: violet = Mg

However, from 1100 °C downwards, crystallisation shows alternate characteristics. The microscopic image indicates that the complete slag has a turbid appearance and is no longer vitreous (Fig. 4.21c). Therefore, detailed SEM images display the appearance of two different crystalline phases. The first phase has an elongated shape with lengths of a maximum of approx. 20 μm . The second phase formed with xenomorphic shapes in the gaps between the elongated phase. The xenomorphic crystals seem not to disrupt the growth of the elongated crystals, indicating that elongated phase growth was finished before the xenomorphic phases nucleated. By taking chemical information from the EDX-mapping into account, the elongated phase shows the same element distribution as the higher temperature elongated phases. Therefore, it is likely that both phases are identical in spite of a reduction in crystal sizes. The xenomorphic phase displays an intense Si signal but lacks of other elements. The lowest temperature of 1000 °C led to the forming of a cloudish crystallisation zone that has a different inner structure (Fig. 4.21d) compared to that at 1100 °C. This zone consists of H-shaped, rectangular crystals with lengths of 10-35 μm , perpendicular orientated dendrites (5-35 μm length), and some xenomorphic crystals (<15 μm diameter) that formed in the gaps between the other two phases. Regarding the EDX-mappings, the H-shaped phase indicates the same chemical distribution as the elongated phase described before, though its shape seems different. The xenomorphic phase shows strong similarities in terms of growth characteristics and chemistry with the xenomorphic phase described at 1100 °C. The dendritic-phase was firstly documented at 1000 °C. EDX-mapping indicates a significant enrichment of Mg, as well as a depletion of Al and Ca. The dendrite phase growth characteristics clearly indicate that they also evolved in the gaps between the H-shaped crystals. Thus, dendrites formed after the H-shaped crystals. The dendrites growth is only limited by the presence of the H-shaped phase and not by the xenomorphic phase. In terms of the growth order, the dendrite- grew after the H-shaped- and seemingly before the xenomorphic-phase.

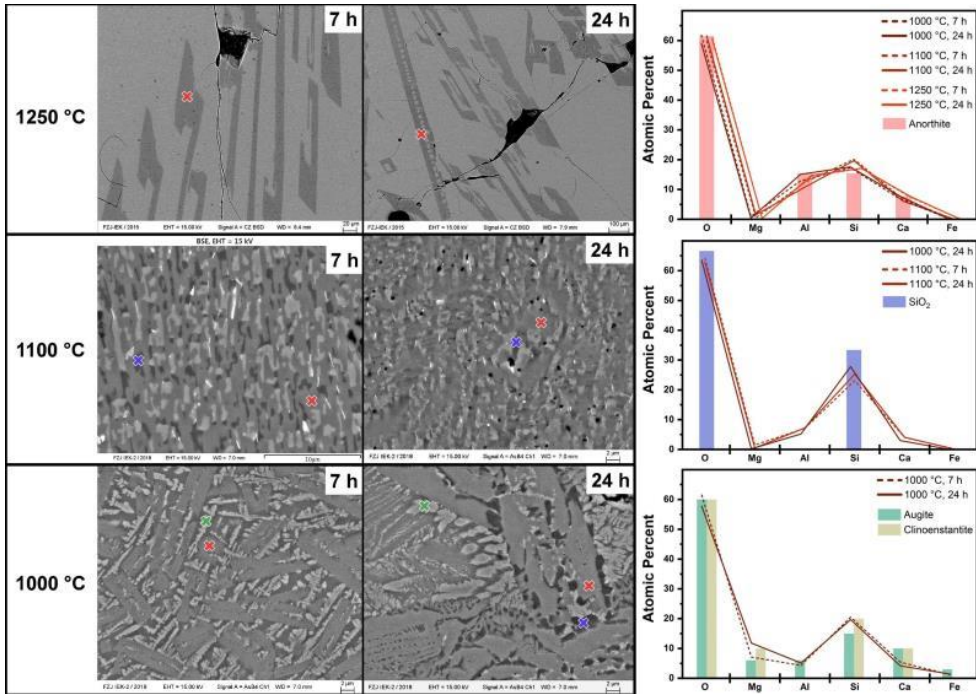


Fig. 4.22: Representative SEM images of HKT slag samples at 1000, 1100 and 1250 °C with holding times of 7 and 24 h. Anorthite, SiO₂ and clinopyroxene phases are determined by SEM-EDX measurements.

The before mentioned phases were identified using single SEM-EDX point measurements, as displayed in Fig. 4.22. The first elongated Al- and Ca- enriched phase displays anorthite composition. EDX measurements of crystal compositions are consistent in all displayed samples. It follows that anorthite, in combination with the XRD measurements, is clearly identified as the Al- and Ca- rich, elongated phase. Fig. 4.22 reveals that the xenomorphic crystal phase consists of Si and O. Therefore, the xenomorphic phase was determined to be SiO₂, though SEM-EDX measurements also indicate Al and Ca to be present in that phase. This divergence can be explained by the tiny size of the analysed crystals (Fig. 4.22). Surrounding areas are prompted by the electron beam as well, leading to a slight distortion of the backscattered electron signal. The third phase described is the Mg-rich dendrite phase, documented at 1000 °C. A comparison of the slag augite and clinoenstatite indicates that the overall fit is satisfactory. As can be seen in Fig. 4.22, the dendritic phase in both samples (7 h and 24 h) shows minor deviations in its Mg content. By also taking diopside (CaMgSi₂O₆) and pigeonite ((Mg,Fe,Ca)₂Si₂O₆) into account, clinopyroxenes face a miscibility of Ca, Mg, Fe and Al. Accordingly, a clear match with one of these members is unlikely. However, the phase composition is still well represented in a miscible clinopyroxene. Another visible finding in Fig. 4.22 is the fact that in terms of the crystal size, the clinopyroxene phase grew slightly as the holding time increased. Furthermore, its crystal shape partially transformed from a dendritic shape to a polygonal shape, indicating that a crystallographic preferred structure was about to form out of the dendrite shape.

The low viscous HKR slag system will be described in the following. Novel results will be shown on the crystallised phases, due to different crystallised phases. A representative sample, quenched at 1250 °C after 4 h of holding time, was chosen to display the crystallised phases: melilite, olivine and spinel (Fig. 4.23). Those three phases crystallised in distinctly different shapes and sizes. While melilite grew in the form of dendritic to skeletal macro-crystals, olivine crystallised in hyp-, idiomorphic, angular crystals with intermediate lengths of maximum 300 µm. Lastly, a spinel phase

with limited crystal sizes and idiomorphic appearance was found as well (Fig. 4.23c). Regarding EDX point measurements of the crystallised phases, melilite composition is in a very good agreement with a melilite solid solution of 75% åkermanite and 25% gehlenite (Fig. 4.23c,d). Referring to all analysed slag samples, the melilite phase is always dominated by åkermanite with contents between 50% and 85% compared to the corresponding endmember gehlenite. As already described by XRD results (Fig. 4.19), the amount of olivine crystals is significantly lower compared to the melilite phase, which is also indicated by the SEM results (Fig. 4.23b). EDX point measurements reveal that the olivine phase consists almost completely of forsterite, the Mg-rich endmember of olivine. SEM analysis of further samples proved that also fayalite (Fe-rich) and monticellite (Ca-rich) contribute to the olivine phase, though forsterite remains as the dominant endmember. In contrast to the XRD data, very low portions of MgAl_2O_4 -spinel (Fig. 4.23d) were identified in several slag samples. The spinel phase also incorporated amounts of iron, resulting in a solid solution of spinel and hercynite. The apparent mismatch between XRD and SEM results concerning the presence of spinel can be explained, regarding the minor fractions of spinel crystals, not generate enough reflection signals.

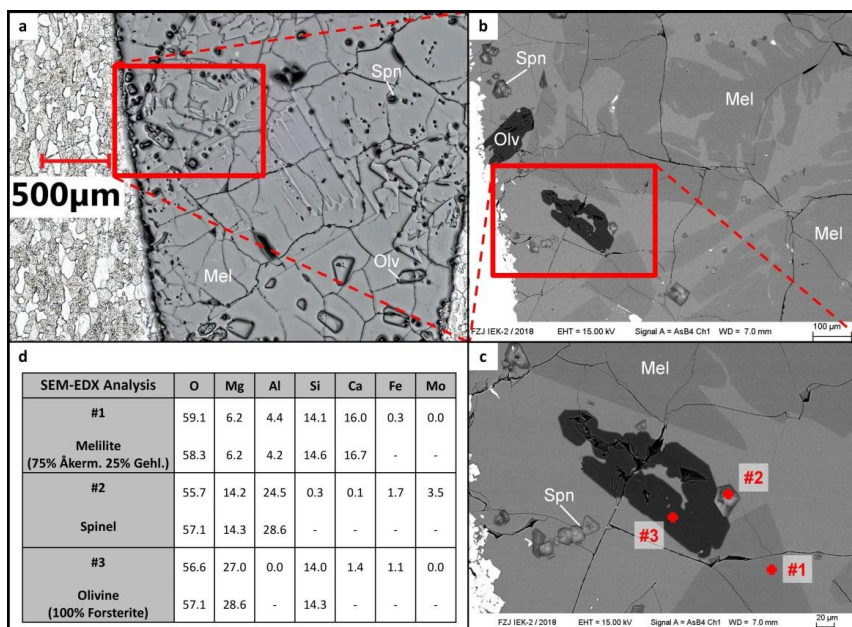


Fig. 4.23: Representative crystallised phases in a HKR sample, quenched at 1250 °C after 4 h of holding time. a) The microscopic view of the quenched sample. b, c) SEM BSE images of the same area as seen in a, including locations of EDX point measurements. d) Data of the EDX point measurements seen in c, in the unit of atom%.

The determined crystallised phases were also found in the CLSM samples. A SEM EDX elemental mapping is shown in Fig. 4.24 that contained the aforementioned phases as well. CLSM data also indicated that melilite is the major phase in synthetic HKR slag. As melilite has a comparably high content of Ca and shows non-incorporation of Fe, it can be clearly identified in the mapping (Fig. 4.24). The already displayed crystal shape of olivine (Fig. 4.23) can be added by an elongated macro crystal shape (Fig. 4.24). Regarding Fig. 4.24, it needs to be noted that the olivine macro crystal growth was enabled because of the free space in the intercrystalline gap between the melilite crystals. Due to the high content of Mg and the lack of Ca and Al, the olivine phase can be clearly distinguished from the remaining sample (Fig. 4.24).

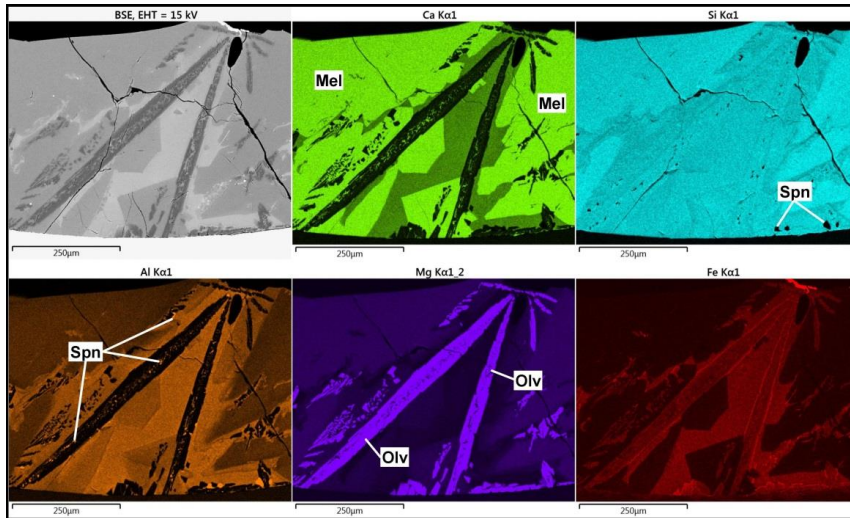


Fig. 4.24: SEM EDX elemental mapping of a HKR sample investigated by the CLSM experimental set up. The sample was constantly supercooled with a slope of -6 K/min.

Ultimately, the SEM EDX mappings further revealed that the spinel phase faces a strong association with the olivine phase. Spinel even crystallised in the hollow olivine macro crystal (Fig. 4.24, Al mapping). The association of crystal phases is not of a random nature, thus it is based on the fluctuations of the slag chemical composition, that is induced by the initial crystallisation. The melilite phase is expected to grow firstly, based on its dominant portion in the slag and the fact that melilite crystal growth shows principally no sign of growth restriction by other crystal phases. The SEM EDX data (Fig. 4.23, Fig. 4.24) give evidence that melilite formation leads to an enrichment of Fe and a depletion of Ca in the remaining liquid slag, which in turn favors the growth of Mg-, Fe- olivine. Subsequently, olivine formation leads to a significant enrichment of Al in the slag, as it can not be incorporated by the olivine structure. Eventually, the Al-rich spinel phase grows in a very close arrangement with the olivine crystals.

Lastly, SOM-1 slag analysis will be described, comprehensively. An example of the crystallised phases and their appearance is given in the appendix (Fig. A.11). Anorthite formed large elongated crystals in the slag at higher and intermediate temperatures and smaller crystallites at lower temperatures [124]. On the margins of the anorthite crystals, zones of fine grained olivine and clinopyroxene growth was observed in the slag samples. The olivine phase shows miscibilities of Mg-rich forsterite and Fe-rich fayalite endmembers (Fig. A.11). The clinopyroxene phase displays variations on the chemical composition, based on the Mg-, Fe-, and Ca-enrichment of the slag at the respective areas in the sample [124]. Olivine and clinopyroxene appear mostly with xenomorphic shapes in the fine-grained crystallisation areas, yet olivine sometimes displays polygonal hypidiomorphic crystals, as well (Fig. A.11).

For all analysed slag systems, it can be summarised that ST-D-2, HKT and SOM-1 are clearly dominated by the growth of anorthite phase. It appears as elongated crystals and growths smaller with a reduction of time. SiO_2 is the second growing phase for the ST-D-2 slag and relevant for the HKT slag, as well. While ST-D-2 slag displays additional growth of olivine (Fe-rich, fayalite), clinopyroxene formed in the HKT slag parallel with SiO_2 . SOM-1 slag in contrast, showed simultaneous growth of olivine and clinopyroxene as the 2nd and 3rd phase. For SiO_2 , clinopyroxene and olivine, no characteristic crystal shape was documented. It was assumed that the nucleation was the dominant force, when the fine grained crystallisation zones of these phases occurred. Based on that, the crystals lack of space to evolve in a characteristic shape. It can also be argued that the present viscosity was too high to enable sufficient diffusion for crystal growth. For the HKR slag,

melilite is the dominant crystals phase, followed by olivine and spinel. Melilite crystallised in the form of mainly skeletal crystals in the sample cross sections. Olivine showed (hyp-)idiomorphic crystallisation with an intermediate crystal size. Spinel occurred in very slight fractions in the slag, but appears idiomorphic.

4.3.1 Crystallisation Kinetics

In this section, the section of crystallisation characteristics will be completed by explaining the crystallisation kinetics of the investigated slag systems. The high viscous slag systems could be characterised solely by the quenching experiment, due to comparable slow kinetics. In contrast, the HKR slag crystallised almost instantly, for which reason extensive CLSM investigations were performed as well. As already concluded for the viscosity, SOM-1 slag lies in between the high and the low viscous slags. Therefore, quenching and CLSM investigations were conducted to determine the kinetic data. Since the samples were quenched in specific time steps, the precise incubation time cannot be defined. The following TTT diagrams include the crystallisation zone, at which crystallisation was documented in the samples. Nonetheless, the initial crystallisation potentially could have been occurred between the neighbouring amorphous and the first crystalline sample. Whenever an incubation time is mentioned in this section, it represents the time frame of the first prove of crystallisation, yet not a precise, quantitative incubation time. Accordingly, the crystallisation zones shall be treated wisely for further considerations.

Familiarly, it will be started with the ST-D-2 slag system, based on the generated samples from the quenching experimental setup. Since every sample was analysed via microscopy and crystallised samples additionally via SEM and XRD, a crystallisation zone, formerly known as “crystallisation nose” was identified (Table 4.4). Other studies using i.e. SHTT experiments to gain kinetic data deliver a higher time resolution, especially for slag systems with short incubation times [89, 108, 109, 117]. However, these studies do not characterise the crystallised phases at all, since they cannot be specifically quenched.

As the TTT diagram for the ST-D-2 slag indicates, the overall incubation time for crystallisation varies between 1 h and 24 h (Fig. 4.25). At 1300 °C (25 °C below T_{liq}), no crystallisation was observed in the slag, not even after 24 h of holding time. At 1250 °C, initial crystallisation was observed after 4 h, with appearing anorthite crystals (blue zone). After 24 h however, SiO₂ additionally, crystallised. Below 1250 °C, both anorthite and SiO₂ were always present, whenever crystallisation was documented (Fig. 4.25). The lowest incubation time was observed at 1150 °C, with 1 h of holding time. The incubation times above 1150 °C (at 1200 °C, 1250 °C) and below (1100-950 °C) were verified after 4 h of supercooled holding time. Until 1000 °C and a holding time of 7 h, only anorthite and SiO₂ were observed in the slag. However, between 7 h and 24 h, olivine (i.e. fayalite) started to grow in supercooled ST-D-2 slag, as the Fe-enrichment of slag seemingly became significant. At the lowest, investigated temperatures, 950 °C and 900 °C, anorthite, SiO₂ and olivine (fayalite) were present simultaneously. At 900 °C, the incubation time increased again and lay between 7-24 h (Fig. 4.25).

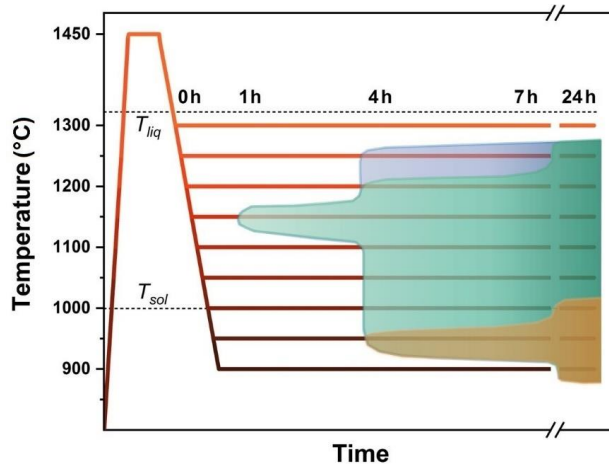


Fig. 4.25: Time temperature transformation (TTT) diagram of the ST-D-2 slag based on the quenching experiments. The crystallisation zones were determined based on the crystallised phases. Blue = anorthite, green = anorthite + SiO₂, orange = anorthite + SiO₂ + olivine (fayalite).

It can be summarised that the shortest incubation time was observed at 1150 °C, between the liquidus and the solidus of ST-D-2 slag, as predicted via FactSage Equilib calculations (Fig. 4.4). Furthermore, it can be seen that ST-D-2 slag could be supercooled up to 100 °C below the solidus, while still showing crystallisation. The slag must have been “liquid” at this degree of supercooling. If the longest holding time of 24 h is considered to be (close to) “equilibrium conditions”, a comparison with the thermodynamic calculations of chapter 4.1.2 can be made. The phase occurrences align very well with the equilibrium calculations. The kinetic data are also listed in Table 4.4.

As a next step, kinetic data of HKT slag will be explained. The overall crystallisation kinetics and incubation time are considered to be as slow as the one of ST-D-2 slag. As Fig. 4.26 displays, the shortest incubation time of 1 h or less was determined at 1150 °C (Fig. 4.26). At higher temperatures, the incubation times were ascertained to be 4 h (1250 °C) and 24 h (1300 °C). Accordingly, HKT slag crystallised at the predicted liquidus temperature of 1300 °C (Fig. 4.5). As the coloured crystallisation zones indicate, HKT slag produces solely anorthite until 24 h at 1150 °C and at temperatures above. Equilibrium calculations predicted a solidus temperature of 1060 °C (Fig. 4.5). However, quenching experiments documented that crystallisation in supercooled HKT slag at 900 °C still occurred after a holding time of 24 h (Fig. 4.26). Thus, it was possible to supercool HKT slag to 850 °C (200 °C below T_{sol}) in a “liquid” state.

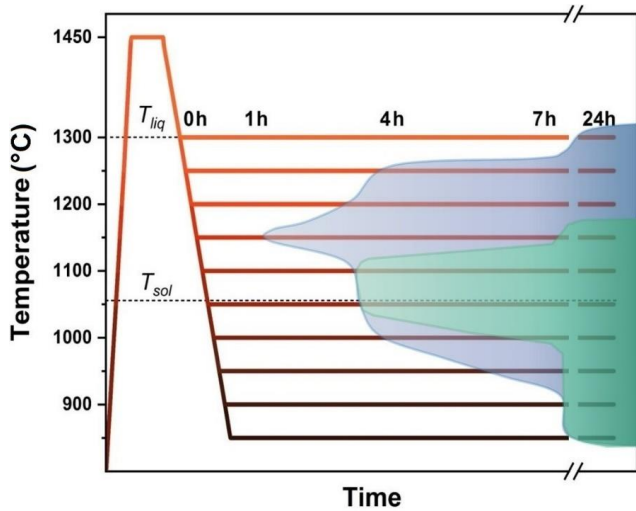


Fig. 4.26: Time temperature transformation (TTT) diagram of the HKT slag based on the quenching experiments. The crystallisation zones were determined based on the crystallised phases. Blue = anorthite, green = anorthite + SiO₂ + clinopyroxene.

Anorthite was documented as the dominant phase in terms of the incubation time. Since every crystallised sample contains anorthite crystals, anorthite has the highest crystallisation kinetics among all crystallised phases. SiO₂ and clinopyroxene were firstly observed at 1150 °C (24 h holding time) and the lower temperatures, respectively. Since two crystallisation zones, regarding the corresponding phases, could be identified, two “nose tips” exist (Fig. 4.26). The shortest incubation time of the whole slag is settled at 1150 °C and 1 h, represented by the growth of anorthite, only (blue zone). The nose tip of all three crystallised phases occurred after 4 h at 1100 and 1050 °C (green zone, Fig. 4.26). Previous results on the crystallisation characteristics indicate that the clinopyroxene phase may have crystallised slightly before the SiO₂ phase (Fig. 4.22). However, on the above mentioned larger time frame, both phases are always present simultaneously (Table 4.4). Since ST-D-2 and HKT slag show comparable crystallising phases, both kinetic data can be compared as seen in Table 4.4. The similarities of the observed incubation times are substantial. Since both slags were chosen as high viscous representatives, a similar behaviour may have been expected, beforehand. However, while ST-D-2 slag shows additionally a great accordance with equilibrium calculations, HKT slag data converge with the calculation results (Fig. 4.5). Especially the missing cordierite phase represents a huge difference between the results. Furthermore, the overall growth of SiO₂ is shifted to lower temperatures and is therefore simultaneous with the clinopyroxene.

Table 4.4: Occurrence of crystallised phases in HKT and ST-D-2 slag. HKT data are written with bold letters (upper row in a cell), ST-D-2 data are written *italic + underlined* (bottom row in a cell). ST-D-2 slag was not investigated at 850 °C. A = anorthite, C = clinopyroxene, S = SiO₂, O = olivine (fayalite).

TTT-data	0 h	1 h	4 h	7 h	24 h
1300 °C	-	-	-	-	A -
1250 °C	-	-	A <i><u>A</u></i>	A <i><u>A</u></i>	A <i><u>A, S</u></i>
1200 °C	-	-	A <i><u>A, S</u></i>	A <i><u>A, S</u></i>	A <i><u>A, S</u></i>
1150 °C	-	A <i><u>A, S</u></i>	A <i><u>A, S</u></i>	A <i><u>A, S</u></i>	A, S, C <i><u>A, S</u></i>
1100 °C	-	-	A, S, C <i><u>A, S</u></i>	A, S, C <i><u>A, S</u></i>	A, S, C <i><u>A, S</u></i>
1050 °C	-	-	A, S, C <i><u>A, S</u></i>	A, S, C <i><u>A, S</u></i>	A, S, C <i><u>A, S</u></i>
1000 °C	-	-	A <i><u>A, S</u></i>	A, S, C <i><u>A, S</u></i>	A, S, C <i><u>A, S, O</u></i>
950 °C	-	-	- <i><u>A, S, O</u></i>	A <i><u>A, S, O</u></i>	A, S, C <i><u>A, S, O</u></i>
900 °C	-	-	-	-	A, S, C <i><u>A, S, O</u></i>
850 °C	-	-	-	-	A, S, C

Since ST-D-2 and HKT slag showed comparable crystallisation kinetics, HKR kinetic data are expected to provide deviant results, based on two recently made findings: varying equilibrium calculation results on the crystallised phases and a significantly lower viscosity. Following the previous approach, crystallisation kinetics of synthetic HKR slag were determined based on the results of the quenching experiments. As will be seen in this section, additional CLSM investigations were required to suitably cover the rapid incubation times of HKR slag. As can be seen in Fig. 4.28, the slag showed no crystallisation at the highest temperatures of about 1300-1350 °C, though the liquidus shall be reached at 1330 °C as seen in the equilibrium calculations (Fig. 4.27). As the temperature is reduced to at least 1250 °C an extensive crystallisation zone was documented. Crystallisation kinetics were high enough to initiate crystallisation below 1300 °C during the cooling slope segment of -7 K/min. Accordingly, all samples below 1300 °C are expected to be influenced by crystallisation, already occurring during the applied cooling slope and thus at higher temperatures. Due to the fact that the crystallisation zone could not be bypassed by a sufficient cooling slope, the zone of glassy solidification below the crystallisation zone could not be determined by this experimental approach. The analysis of the samples revealed that in all crystallised samples (1100-1300 °C and 0-24 h), melilite, olivine and spinel were present. Therefore, the blue crystallisation zone represents melilite and olivine. Spinel crystallisation requested slightly longer holding times, but due to the minor fractions, spinel could not always be identified reliably. The performance of further investigations at lower temperatures was stopped, since every sample would have been influenced by cooling slope related crystallisation. Due to the limited heat release from the furnace chamber, higher cooling slopes could not be applied, unfortunately. To possibly find the margins of the crystallisation nose, CLSM experiments were conducted, as the setup provides significantly higher cooling rates.

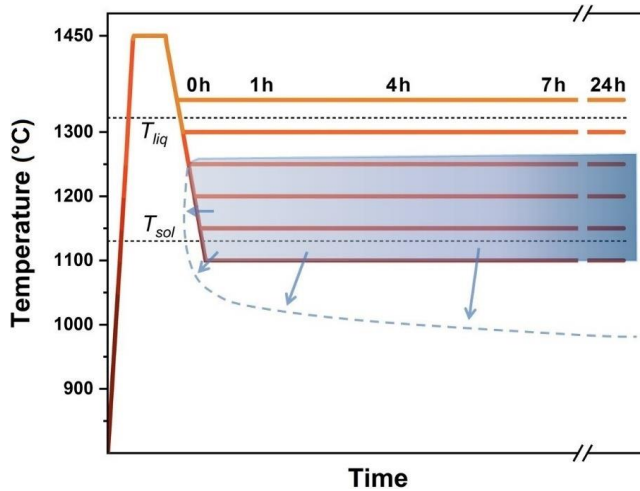


Fig. 4.27: Time temperature transformation (TTT) diagram of the HKR slag based on the quenched samples. The borderlines of the crystallization zone could not be fully determined by the quenched samples as suggested by the dotted line.

CLSM experiments were applied to document the crystallisation kinetics in more detail and to determine, if a glassy solidification of HKR slag can be achieved. Therefore, measurements with high supercooling slopes were applied: -7, -15, -30, -60, -100, -150, and -200 K/min. For every cooling slope, the measurement was looped three times to improve the certainty of the kinetic data. Based on that, maximum, minimum, and an average temperature of initial crystallisation could be ascertained. Crystallisation phenomena were observed for each cooling conditions as displayed in Fig. 4.28. It must be noted that a TTT analysis in the CLSM experiment could not be completed successfully, since HKR already crystallised during the cooling procedure, even as high cooling slopes of -300 K/min were applied. Therefore, it was decided to determine the kinetics based on constant cooling conditions.

The initial crystallisation temperatures were determined at approx. 1270 °C for low supercooling slopes (-7, -15, and -30 K/min). For the high supercooling slopes (-100, -150, and -200 K/min), initial crystallisation temperatures are settled at approx. 1150 °C. The fact that two “plateaus” of incubation temperatures formed, could be explained by the following reasons. Firstly, a certain degree of supercooling is required until the crystallisation initiates, so no higher incubation temperatures were reached (high-temperature plateau for low cooling slopes). Secondly, the initial crystallisation cannot be kinetically shifted to lower temperatures without crystallising (low temperature plateau for higher cooling slopes). In contrast, the temperatures, at which no further crystallisation progress was observed i.e. completed, are constantly declining from 1150 °C (-7 K/min) to 975 °C (-200 K/min). Between the average initial crystallisation temperatures and the average temperatures of crystallisation completion, a crystallisation zone was defined (Fig. 4.28). CLSM results further indicated that HKR slag could not be sufficiently supercooled to bypass the crystallisation zone and to solidify completely amorphous. However, quenched samples from the quenching experiment (e.g. 1300 °C), displayed a completely glassy solidification (Fig. 4.27). For the case of a gasifier application, HKR crystallisation kinetics undoubtedly prove that slag crystallisation is a serious issue that occurs with a high degree of certainty during real operation conditions for low viscous slags.

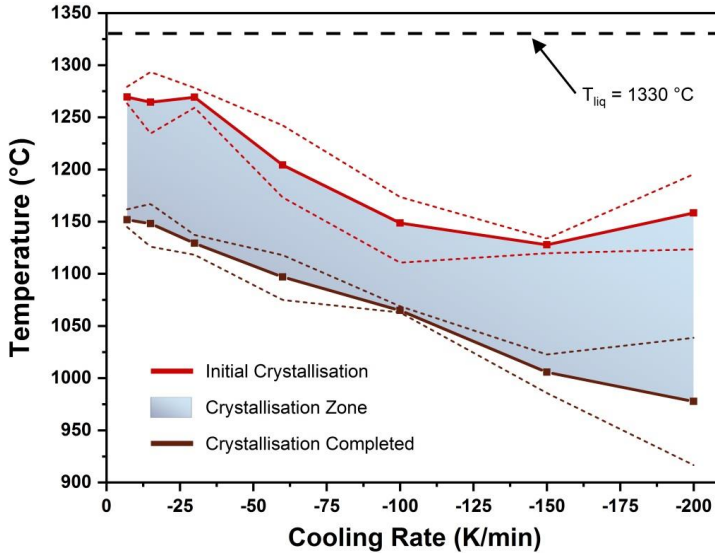


Fig. 4.28: Synthetic HKR crystallisation zone defined by the average initial crystallisation temperatures and the average temperatures of crystallisation completion as determined via CLSM slope experiments. The dotted lines represent the maximum and minimum temperatures for the respective slag crystallisation behaviour. Each slope measurement was repeated three times.

Repeatedly, a brief summary of the findings of the SOM-1 slag will be presented in the following. Kinetic information on the incubation time of SOM-1 slag is given in Table 4.5. At 1250 °C, which is slightly below the liquidus, a comparably long incubation time was observed. In the intermediate temperature range of 1150 °C and 1200 °C, the quenching experiment was yet sufficient to supercool the slag fully liquid. However, at 1100 °C and below, CLSM experiments were also necessarily applied. The incubation time shortened until 1000 °C, indicating that the slag was still above the crystallisation nose tip. Overall, the SOM-1 slag is settled once again in between the high and low viscous slags, now in terms of the crystallisation kinetics.

Table 4.5: Overview of the kinetic data of SOM-1 investigations. * Kinetic data that were expected to be influenced by slag impurities were excluded. Table based on the data of Saar (2019) [124].

TTT-data	fully liquid slag until	crystallisation starting at	experiment
1250 °C	180 min	300 min	quenching
1200 °C	0 min	60 min	quenching
1150 °C	0 min	60 min	quenching
1100 °C	52 min	53 min	CLSM
1050 °C	38 min	39 min	CLSM
*1000 °C	29 min	30 min	CLSM

To summarise the kinetic results, it can be concluded that ST-D-2 and HKT slag not only show similar crystallised phases, but also have similar crystallisation kinetics. Incubation time is settled between 1 h and 4 h for a vast temperature regime. While ST-D-2 kinetic data are in good agreement with the equilibrium calculations, HKT kinetic data diverge from the calculation results. Cordierite was not

found and the crystallisation of SiO_2 is shifted to lower temperatures. Yet, it must be noticed that the kinetic crystallisation data and the evolution over time (for a constant temperature) provide beneficial information, which equilibrium calculations do not provide. HKR slag displays rapid crystallisation that could not be covered by TTT investigations. Constant cooling measurements revealed a crystallisation channel that is constantly shifted to lower temperatures, as the cooling rates are increased. The incubation times of SOM-1 slags were determined in a double-digit minute to 5 h scale. Therefore, SOM-1 slag is once again in an intermediate state between ST-D-2, HKT as well as HKR.

4.4 Crystal Phase Quantification

The main scope of this study is the providing of crystal morphology data that can be implemented in a future viscosity model for partially crystallised slags. In previous sections, the role of crystal morphologies was explained and the crystallisation characteristics of the investigated slag systems were described. In this chapter, the morphologies of relevant crystal phases will be quantified: anorthite, spinel, olivine, and melilite. The most morphology datasets were gathered for anorthite, as the phase was documented in ST-D-2, HKT, and SOM-1 slag, resulting in a total number of 626 single crystal morphology datasets. The remaining three phases were quantified based on the HKR slag investigations by the quenching and the CLSM experiments. Some quantifications of the SOM-1 slag were performed again in this study, to uniform the applied methodology and to exclude crystal morphology measurement errors. The absolute amount of individual crystals measured is 1027. The quality of the results based on the quantity of datasets is seen as trustworthy (Table 4.6). However, in the case of melilite, the total amount of datasets is lower, compared to the other phases.

In the following, the crystal morphology quantifications will be treated one by one, starting with the anorthite phase, as it covers three of the slag systems. The morphology data of HKR slag follow subsequently, starting with spinel, followed by olivine and ending with melilite [143]. As this chapter contains the most valuable results of this study, the presented content is vast.

Table 4.6: Overview of the crystallised phases and their quantified morphology datasets. In total, 1022 individual crystals were quantified. *Crystal morphology data of the SOM-1 slag were taken from [124]. Yet, the quantification for 1200 °C and 1250 °C was performed again to uniform the measuring procedure.

phases	slag systems	experiments	number of datasets
anorthite	ST-D-2	quenching	150
	HKT	quenching	213
	SOM-1*	quenching	263
spinel	HKR	quenching, CLSM	194
olivine	HKR	quenching, CLSM	119
melilite	HKR	CLSM, quenching	83

4.4.1 Anorthite – ST-D-2, HKT, and SOM-1 Slag Systems

As announced before, this section will treat the anorthite morphology quantification. Due to the various datasets and three involved slag systems, the characteristics of the individual slag system will be described only briefly. Although, ST-D-2, HKT, and SOM-1 slags also produced SiO_2 , clinopyroxene, and olivine, anorthite is the only phase that will be quantified in this study. In the case of SiO_2 , its permanent xenomorphic appearance Fig. 4.22 hinders the definition of a representative single crystal morphology. Furthermore, the appearance is strongly influenced by the remaining space in-between

the anorthite crystals. The same justification is valid for clinopyroxene and olivine as well. Also, clinopyroxene indicates a certain evolution with an increasing holding time: dendrites are substituted by polygonal crystal forms, which might reach an idiomorphic state at a certain holding time (only observed in HKT slag, Fig. 4.22). Since these three phases obviously did not form a characteristic morphology, but were influenced by remaining space, a parametrisation is not meaningful. An overview of anorthite morphology data for the HKT slag is given in Table A3.

The elongated crystal morphology of anorthite described in this study is in very good agreement with anorthite morphology described in the literature. Fig. 4.29 includes several examples of anorthite morphology, which will be used to define a generalised anorthite morphology. In chapter 4.2.2, isothermal viscosity measurements of HKT slag led to non-Newtonian behaviour due to the presence of anorthite crystals (Fig. 4.29a,c). The crystals appear with an elongated shape. Such morphology was additionally observed in samples from the quenching experiment (Fig. 4.29b). As mentioned before, the crystals shrink in their size at lower temperatures, so does the anorthite phase. Anorthite crystals with a comparable morphology as the one shown in Fig. 4.29a,b,c were also observed in the ST-D-2 and SOM-1 slag (Fig. 4.12, Fig. A.11). In a study by Sato (2005) [144], plagioclase crystals grew during a viscosity measurement of a subliquidus magma. Since anorthite is part of the solid solution of plagioclase (Fig. 2.14), the morphology of plagioclase and anorthite can be treated as similar. The observed crystals are elongated as well, as can be seen in Fig. 4.29d. In the recent study of Seebold (2017), real ST-D-2 slag was investigated on the viscosity and large anorthite crystals were found in the slag (Fig. 4.29e) [58]. The comparison of both anorthite morphologies from synthetic HKT and real ST-D-2 slag (Fig. 4.29c,e) clearly display that the elongated morphology is identical, even though the slags have different compositions (and real ST-D-2 contains also alkalis). Further experimental studies on high-pressurised H₂O-, H₂O-CO₂-saturated magmas and coal ash slags, additionally revealed the elongated shape of anorthite crystals (Fig. 4.29f,g) [142, 145]. Furthermore, other studies observed the crystallisation of elongated anorthite or plagioclase crystals in systems with various slag or magma compositions [122, 144, 146-148]. A century ago, Goldschmidt (1922) collected early findings on crystal morphologies [84] and also defined an elongated shape with an asymmetric crystal tracht (Fig. 4.29h) based on the triclinic crystallographic system (Fig. A.2). However, it must be mentioned that anorthite not only forms elongated shapes as displayed in the figure by Goldschmidt, but also forms tabular crystals with a very weak elongated characteristic. Yet, tabular crystals are not represented in comparable studies, as previously described. These overarching coincidences prove firstly that the abundance of anorthite in slag and natural systems gives high relevance to its quantification. Secondly, anorthite morphology is not influenced by the composition of the investigated systems (different slags and magmas) or the experimental procedure and can therefore be seen as characteristic for the anorthite phase.

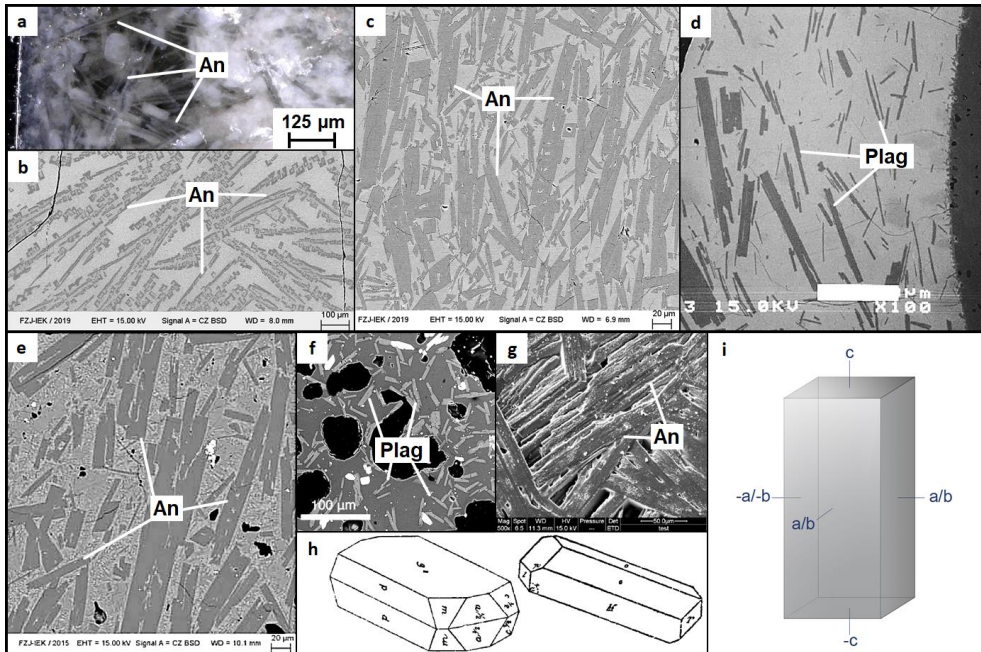


Fig. 4.29: Selection of documented anorthite morphologies. a) microscopic image of anorthite crystals on the wall of the previously investigated viscosimetry crucible, b) crystallised anorthite from the quenching experiment (1250 °C, 24 h), c) SEM image of orientated anorthite crystals due to spindle rotation (same sample like a)), d) crystallised anorthite during viscosity measurement of subliquidus magma [144], e) crystallised anorthite in real HKT slag [32], f) crystallised plagioclase in H₂O and H₂O-CO₂-saturated magmas [145], g) crystallised anorthite in quenched coal ash slag [142], h) anorthite morphologies as described by Goldschmidt (1922) [84], i) generalised tetragonal prism morphology for the anorthite crystal quantification.

As a result of the uniformity of anorthite (or plagioclase) crystals, a generalised anorthite morphology was created as a basis for the quantification (Fig. 4.29i). The idealised crystal was defined as a tetragonal prism (see also Fig. A.3) with a varying prism length. Since the XRD investigations revealed that the elongated axis must be represented by the c-axis, crystallographic spatial axis could be identified (Fig. 4.29i). Theoretically, a tetragonal prism morphology stands in conflict with the asymmetric triclinic crystallographic system of anorthite, as it presumes equal lengths of the a- and b- axis, as well as an rectangular orientation towards each other. The defined morphology would therefore represent the tetragonal crystallographic system, which is not applicable for anorthite. Thus, the quality of data requires such generalisation: SEM images of slag cross sections only reveal a two-dimensional view on anorthite crystals. A classification based on the longest axis (c-axis) can be performed, but the differentiation between the a- and b-axis is impossible due to the two-dimensional nature of the data. As a result, all crystals widths (a- and b-axis) were treated equally, resulting in a tetragonal prism. Since the morphology of an anorthite crystal was described, the quantification was performed by measuring the crystal length and the aspect ratio (length/width). As the a- and b-axis are treated equally, the whole crystal morphology can be ascertained by the generalised width. Even the volume and the surface area could potentially be determined based on those two values. Accordingly, in the following paragraphs, anorthite “length” means the length of the c-axis and anorthite “width” symbolises the width of the tetragonal prism (a- and b-axis). To

simplify the understanding if the anorthite morphology changed, the elongation of the crystals defined by the aspect ratio (length/width) will be described as a metric of morphology uniformity.

Fig. 4.21 indicated that the anorthite aspect ratio can be classified in four different crystallisation regimes: H-shaped (I), cloudish (II), featherlike (III), and macro (IV) for the HKT slag. As can be seen in the appendix (Table A.3, A.4, A.5), also ST-D-2 and SOM-1 slag can be categorised in that way. Though, the transitions from the individual crystallisation regimes differ slightly in terms of the temperature. Nonetheless, the overall paragenesis of all three slag samples is seen to be relatively similar: macro-crystals at high temperatures, followed by a featherlike crystallisation and cloudish fronts at intermediate and low temperatures. The H-shaped anorthite paragenesis as described for the HKT slag however, could not be found in the other two slag systems (Table A.3, A.4, A.5). ST-D-2 and SOM-1 slag in contrast displayed further fine grained, cloudish crystallisation with the tendency to form polysynthetic twins with quartz, comparable with the growth of myrmekite in geological settings [66, 81]. Due to that twin-formation, no ST-D-2 morphology data could be generated for 900 °C and 950 °C.

The anorthite morphology data for the generalised tetragonal prism shape are displayed in the following figures. Fig. 4.30 contains anorthite length and Fig. 4.32 includes aspect ratio (AR) data. Besides the mean value of the length, the 90th and 10th quantile were added to display the bandwidth of anorthite crystallisation. These quantiles were chosen as the maximum and minimum representative values. Otherwise, if solely the highest and lowest value would have been chosen, rarely present crystals with extraordinary sizes would have distorted the overall morphology data.

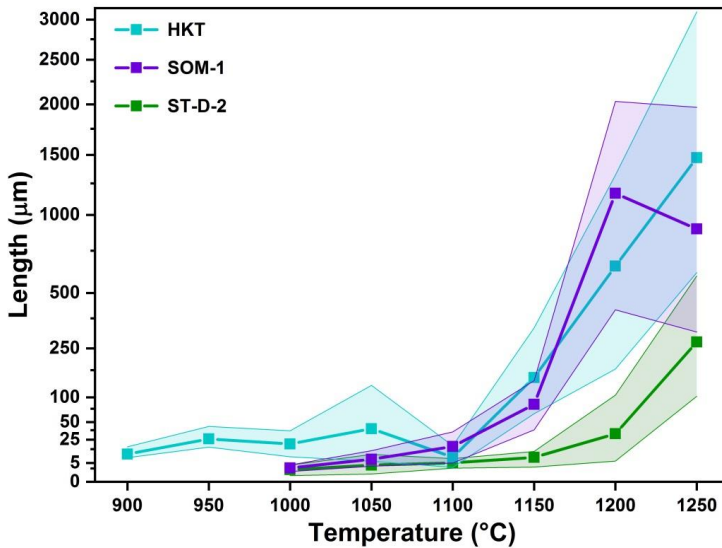


Fig. 4.30: 90th/10th quantile and mean anorthite crystal length with respect to the quenching temperature of ST-D-2, HKT, and SOM-1 slag.

By comparing anorthite tetragonal prism length data, a clear tendency can be seen to form large crystals at higher temperatures and smaller ones at intermediate and low temperatures (Fig. 4.30). As already mentioned several times in this study, crystallisation theory specifies crystal growth to be dominant at high temperatures and nucleation at low temperatures, which accounts for the anorthite phase [87, 149]. In general, anorthite crystals grew comparably large in the HKT and SOM-1 slag. Especially the sharp decline in anorthite mean length until 1100 °C is similar. ST-D-2 slag in contrast, generally displays lower anorthite lengths (Fig. 4.30). Below 1100 °C, anorthite mean length in HKT slags displays fluctuations on a low double-digit μm-scale, while SOM-1 and ST-D-2 length constantly decline further. The corresponding quantile data can be seen as channel margins in which

anorthite crystals highly likely form in the slags.

To uniform anorthite length data, it was decided to define average anorthite length data. Therefore, the individual slag mean lengths and quantiles were condensed by averaging between the three slag systems. The precise data can be found in the appendix (Table A.6). Fig. 4.31 displays that the average anorthite length can be divided into two major regimes: 1250 °C to 1100 °C and 1100 °C to 900 °C. At 1250 °C, anorthite mean length was determined to 1471 μm with a bandwidth of 344-1888 μm. The margin of the high temperature regime at 1100 °C is marked by an averaged anorthite mean length of 8 μm and quantiles of 20.3 μm and 3.5 μm, respectively. The intermediate to low temperature regimes display anorthite length fluctuations and are strongly influenced by the HKT slag, since it was the only slag providing data for 900 °C and 950 °C (Fig. 4.30). As mentioned earlier in chapter 4.3.3, anorthite crystallises cloudish and the crystals are in close spatial distance to each other (also with other phases: SiO₂, clinopyroxene, olivine). Accordingly, there is an external influence on the anorthite length, which might not be characteristic for the pure anorthite phase.

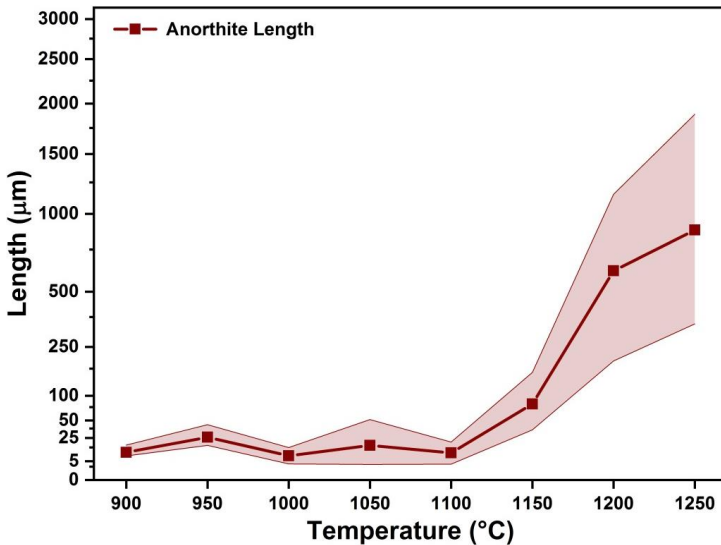


Fig. 4.31: Averaged 90th/10th quantile and mean anorthite crystal length in dependency of the temperature, based on the ST-D-2, HKT, and SOM-1 slags.

Anorthite tetragonal prism is furthermore described by the width (a-, b-axis) of the crystal. The deviation of the length and the width results in the crystal aspect ratio. The precise AR data are listed in the appendix (Table A.3, A.4, A.5, A.6). The AR data of the three analysed slag systems are displayed in Fig. 4.32. The overall AR graphs follow a general trend: higher temperatures lead to more elongated anorthite crystals. HKT slag produced anorthite crystals with the highest mean AR of 29.6 (1200 °C). SOM-1 slag reaches a maximum AR of 19.2 (1200 °C) and ST-D-2 of 16.2 (1250 °C). HKT slag also produced a high variability of anorthite elongations, as indicated by the bandwidth of 52.6 to 12.0 for 1200 °C. While anorthite AR of SOM-1 slag also produced fluctuating data, anorthite crystals in ST-D-2 slag display a smooth decline of crystal AR to lower temperatures (Fig. 4.32). Similar to the mean anorthite length, ST-D-2 anorthite crystals have the lowest AR, compared to the other slag systems. As can be seen at low temperatures (1000 °C), the AR deviation between ST-D-2, HKT, and SOM-1 slag narrows and anorthite crystals face a similar elongation (Fig. 4.32). Accordingly, the AR of anorthite crystals in all three slags have a better overlap, compared with the crystal length data, shown before (Fig. 4.32).

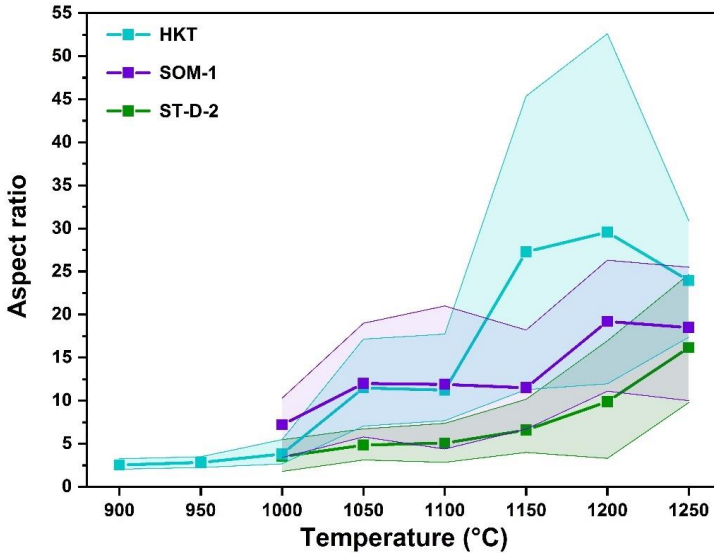


Fig. 4.32: 90th/10th quantile and mean anorthite aspect ratio (length/width) with respect to the quenching temperature of ST-D-2, HKT, and SOM-1 slag.

According to the averaged anorthite length, anorthite AR was also averaged based on the three slag systems. The averaged mean AR, as well as the 90th and 10th quantiles can be seen in Fig. 4.33. The fundamental trend of larger AR at higher temperatures is present for the averaged AR data, likewise. At the lowest temperature of 900 °C, the averaged mean AR is approx. 2.5 (only HKT data). Above 950 °C, anorthite AR begins to rise almost perfectly constant until the maximum investigated temperature of 1250 °C. The bandwidth of the maximum and minimum AR values is comparably narrow, indicating a higher homogeneity of anorthite crystals AR, compared with the absolute lengths. Surprisingly, the fine-grained, cloudish crystallisation did not have an influence on anorthite AR, in contrast to the crystal length (below and above 1100 °C, Fig. 4.31).

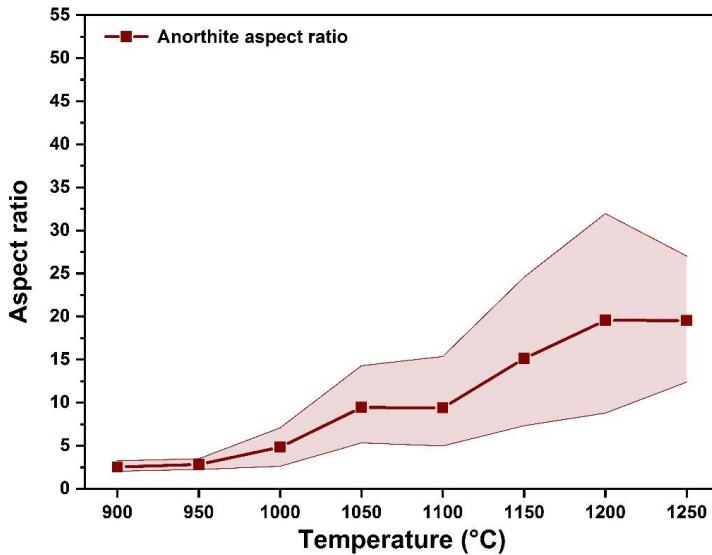


Fig. 4.33: Averaged 90th/10th quantile and mean anorthite crystal aspect ratio in dependency of the temperature, based on the ST-D-2, HKT, and SOM-1 slags.

Finally, it can be concluded that anorthite crystallises with an elongated shape. The findings presented in this study are in good agreement with various examples from the field of slag investigations or natural magma analysis. The elongated shape is therefore seen as characteristic. Based on the observations, anorthite crystals were generalised as tetragonal prisms. Anorthite crystals can be described spatially by measuring the length and the width of the crystals. With respect to the defined morphology, anorthite crystals can be defined as 3D objects. Such quality of spatial data is supposed to be beneficial for a future viscosity model for partially liquid slags. Anorthite length increases above 1100 °C up to single millimetres, but fluctuates below 1100 °C in a double digit μm -range. In contrast, anorthite aspect ratio almost perfectly increases, if higher temperatures are applied to the slag systems. As a conclusion, anorthite crystals grow asymmetric and become (constantly) more elongated, with an increase of the crystallisation temperature.

4.4.2 Spinel – HKR Slag System

As a next phase, crystal morphology of spinel will be described in this section. It is the first out of three phases that were quantified based on the HKR slag system. The variation of the crystallisation products from the ST-D-2, HKT, and SOM-1 slag system, are reasonable for such crystal phase variety (chapter 4.1.2). As already indicated by the slag characterisation results, spinel is only present in minor fractions in the HKR slag. Therefore, this section will be held as condensed as possible to leave sufficient space for the subsequently following olivine and melilite phase quantification.

The spinel crystals appear in the HKR slag mostly as hypidiomorphic to idiomorphic crystals. In the appendix, Fig. A.12 displays a typical hypidiomorphic spinel crystal in HKR slag. As previously mentioned, the spinel crystals tend to grow in the surrounding area of olivine crystals (Fig. 4.24). Due to its edgy shape, undistorted crystal faces, and its relief in microscopic and SEM images, spinel can be distinguished effortlessly from the olivine and melilite phase (Fig. A.12). As it is not a silicate mineral, SEM-EDX element mappings reveal even small portions of anorthite in the HKR slag. As Fig. A.12 displays, spinels incorporate Al and Mg, but also minor fractions of Fe in the HKR slag (not displayed). The intense Al-signal is a reliable indicator for the spinel phase, as the other crystals are

silicate-based. The term spinel describes a whole group of minerals (solid solution), with varying composition but similar crystal structure. As can be seen further on in Fig. A.12, spinel crystal displays a zoned structure. Zoning occurs in solid solution phases, when crystallisation conditions changed (temperature, pressure, composition, etc.) [66, 67]. Due to the controlled experimental parameters, the displayed zoning (also in Fig. 4.34), is solely based on a change in the composition. The fundamental spinel (MgAl_2O_4) becomes partly substituted by hercynite (FeAl_2O_4), as no other potentially substituting 2-valent cation is present in the slag. Due to the higher atomic number of Fe, (compared to Mg) the brighter zones of spinel crystals in the SEM images contain some fractions of Fe, accordingly.

Similar to the previously quantified anorthite, spinel morphology will be defined firstly. Fig. 4.34 includes a selection of spinel phases from this study and other works. Fig. 4.34a,b shows crystallised spinels in the HKR slag deriving from the quenching experiment. They also display intense zoning of Fe-rich hercynite phase and are associated with olivine, as previously mentioned (Fig. 4.34b). For further comparison, spinels of three metallurgic studies were chosen as additional examples of spinel shapes (Fig. 4.34c,d,e). Though, different slag systems were analysed, spinels also crystallised hyp- to idiomorphic. In the field of geology, spinels are also known for their comparably ideal crystal shapes [80, 150].

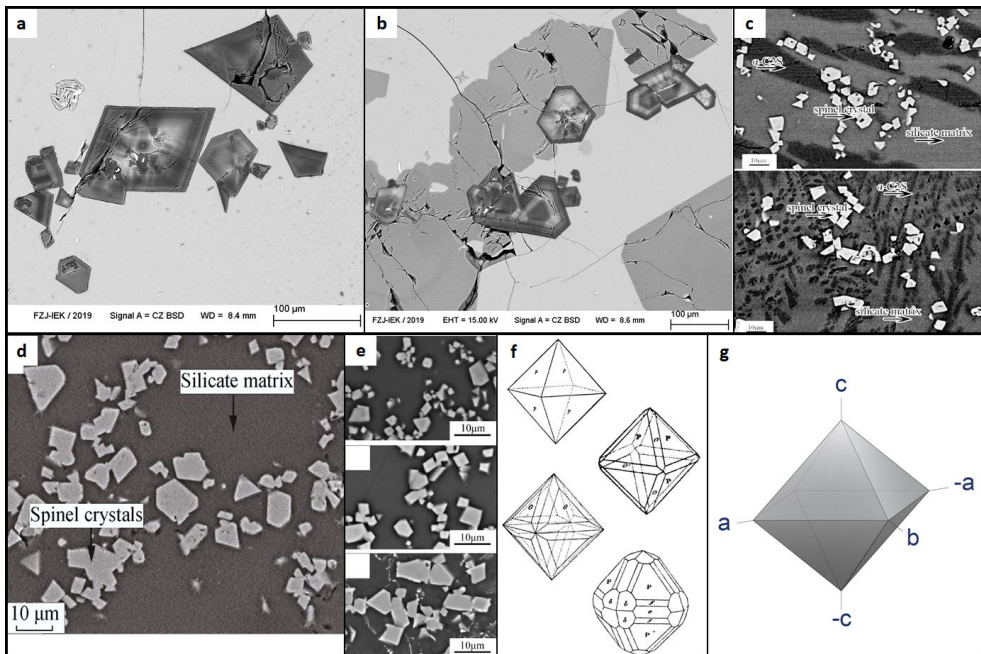


Fig. 4.34: Spinel shapes/morphologies by different studies: a,b) hyp- to idiomorphic spinel crystals with inner zoning (quenching experiment, 1250 °C, 24 h), c) Cr-containing spinels precipitating in an experimental study of steel-making-slags [151], d) Mg-Fe-Cr spinels growing during an experimental study on metallurgic slags [152], e) Mg-Fe-Cr containing spinels crystallised in a stainless steel-making-slag [153], f) typical cubic spinel morphologies described by Goldschmidt (1922) [84], g) generalised octahedron morphology applied in this study.

Once again, idealised morphologies of Goldschmidt (1922) were used as three-dimensional examples of cubic spinel crystallisation (Fig. 4.34f). Spinel habit is described as an octahedron (see also Fig. A.3). Due to different crystal face growth rates, the tracht of spinel octahedrons can potentially

become more complex (Fig. 4.34f, from top to bottom). However, as described in chapter 2.4.1, the crystal habit is the important property, when it comes to crystal quantification. Accordingly, a generalised morphology of an octahedron was defined for the spinel phase (Fig. 4.34g).

The spinel crystals were quantified on their diameter. As spinel crystallises in a cubic crystallographic system, a highly symmetric octahedron can sufficiently be characterised by the crystal diameter (from the tip to the bottom). Therefore, the longest distance from corresponding edges were measured. The morphology results are displayed in Fig. 4.35. As described in a previous section (chapter 4.3.1), crystallisation was only documented at 1150 °C, 1200 °C and 1250 °C in the quenching experiment due to the very short incubation times. Therefore, any observable trend has a limited significance and shall be treated carefully. An overall trend for spinel crystallisation can be concluded only with a degree of uncertainty (Fig. 4.35). Between 1150 °C and 1200 °C, a small decline in the spinel diameter was determined, but above 1200 °C, the crystal diameter increase clearly. The last tendency is assumed to be attributed to the crystallisation theory [87, 149], but the minor diameter increase towards 1150 °C cannot be accounted by that theory. In addition to the graph, diameter quantification data can be found in the appendix (Table A.7)

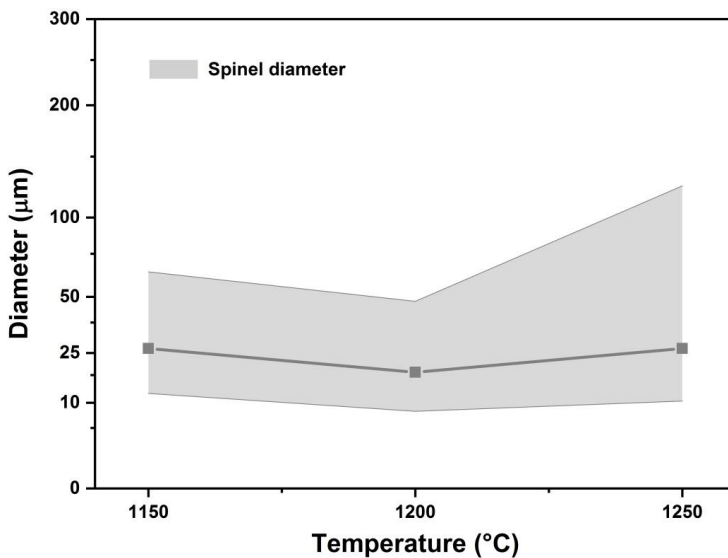


Fig. 4.35: Spinel morphology quantification based on quenching results of the HKR slag. The crystal diameter was measured from the most distant edges.

It can be summarised that spinel is a minor phase in the HKR slag system due to its low fractions and small crystal sizes (compared to the following olivine and melilite phases). Nonetheless, since spinel crystallised in hyp- to idiomorphic shapes, a morphology quantification could be conducted, successfully. Based on the highly symmetric cubic crystallographic system, spinel was defined as an octahedron. The morphology was quantified by the inner diameter of the crystal. It could be observed that spinel growth did not follow a certain trend. Octahedron diameters increased from 1200 °C to 1250 °C clearly, though a further decrease at 1150 °C, as expected by the crystallisation theory, was not observed.

4.4.3 Olivine – HKR Slag System

As the second most abandoned phase in HKR slag, olivine will be described and quantified in the following section. It will be shown, that olivine also faces a characteristic morphology based on the crystallographic properties. As olivine was predicted i.e. determined several times in slag studies, a certain importance is given to that phase (Table 2.5, Table 2.6). A total number of 119 individual crystals have been measured to gather the morphology data.

Olivine crystallised as individual, highly symmetric crystals. However, they sometimes form elongated macro crystals, which are build up on the single crystals. As Fig. 4.36a indicates, the olivine macro crystals incorporated Ca and Fe, representing a solid solution from forsterite (Mg_2SiO_4), fayalite (Fe_2SiO_4) and monticellite ($Ca,MgSiO_4$). That solid solution composition represents the average olivine composition of all micro and macro crystals quiet well. A detailed spatial view on the olivine crystals is displayed in Fig. 4.36c. Olivine crystals appeared in parallel aligned elongated macro crystals that consisted of single rhomboid crystals. As shown in Fig. 4.36b, olivine crystal shapes show a high accordance with an ideal type rhomboid shape. Some crystals appeared to be hollow. Hence it can be concluded that the individual growth was not fully completed as the sample was quenched. Due to the hollow appearance of olivine crystals, it can be assumed that olivine crystallisation did not reach an equilibrium state with slag system.

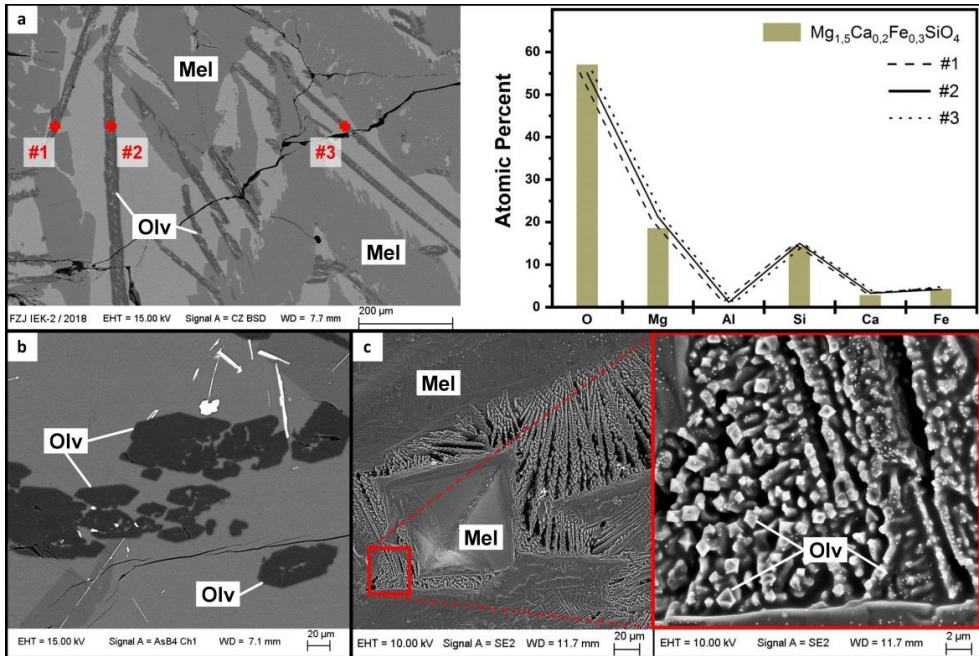


Fig. 4.36: Representative samples of olivine crystallization of the synthetic HKR slag system. a) SEM BSE image of a sample immediately quenched at 1150 °C. Three olivine macro crystals were investigated via EDX measurements and compared with an olivine (Mg-Ca-Fe) solid solution, b) SEM BSE image of a sample quenched at 1150 °C after 30 min of holding time, c) SEM image of the sample surface, investigated via CLSM and an applied cooling rate of -100 K/min.

CLSM samples displayed in Fig. 4.37a,b give additional evidence of olivine rhomboid crystal shape based on samples cross section analysis. The presence of rhomboid olivine crystals in various

samples, investigated in both of the experiments, suggests that the experimental results are absolutely comparable and that olivine shape formation underlies an overall characteristic. Rhomboid olivine crystals are also found in magmatic rocks, as shown in Fig. 4.37c [150]. Compared with the analysed synthetic slag system, it can be stated that olivine crystallisation shape is characteristic and independent of the analysed supercooled liquid system. Based on that conclusion, fundamental findings in the field of mineralogy and crystallography can be used to define a valid spatial morphology of olivine crystals. The typical olivine morphology (Fig. 4.37d, e, f) was already described several decades, respectively a century ago [83, 129] and coincides with the results described in this study very well. Accordingly, a single olivine crystal is described as a rhomboid-bipyramid (Fig. 4.37f), which is elongated in the direction of the c-axis. To define a three-dimensional morphology based on the two-dimensional information from the samples cross sections, generalisations on the crystal morphology were made. Firstly, olivine crystal surface arrangement was defined as an equiaxed rhombic-bipyramid with a variable elongation in the c-axis direction (Fig. 4.37g). Secondly, the main morphology was described by the length and the aspect ratio of the bipyramid, determined by length and width measurements of single olivine crystals. Since the bipyramid is defined as equiaxed, the crystal width is identical with the crystal depth (Fig. 10 g).

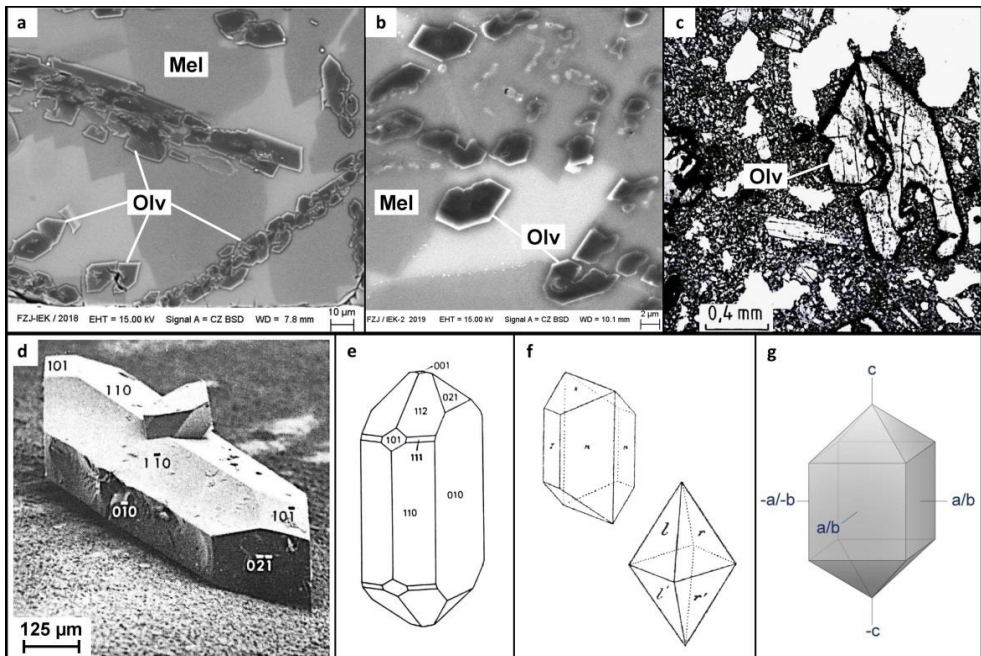


Fig. 4.37: Comparison of investigated olivine crystals (a,b) with typical olivine morphologies (c-g). CLSM samples crystallised at an applied cooling slope of -6 K/min (a) and at isothermal treatment of 1100 °C (b). Cross section of an altered hypidiomorphic olivine crystal in an alkaliolivinebasalt, modified after Pichler & Schmitt-Riegraf (1982) [150]. d Forsterite crystal derived from crystal growth experiment and calculated growth form of an olivine type mineral [154]. f) Early description of olivine crystal morphologies by Goldschmidt (1920) [83]. f) Generalized elongated, equiaxed bipyramidal morphology, generalized for the olivine crystal quantification.

Olivine morphology data were quantified (Fig. 4.38) by the analysis of 119 single crystals in a variety of samples. Samples from both, the quenching and the CLSM experiments were used therefor. As the

investigated target temperature is raised, the average olivine crystal length is increasing from 21.8 μm (1100 $^{\circ}\text{C}$) to 70.2 μm (1200 $^{\circ}\text{C}$), as well. Concurrently, the range between the maximum and minimum crystal length also increased at higher temperatures. However, olivine crystals with a triple digit micrometre length were seldom, indicated by an overall moderate increase in the average crystal length. The fundamental characteristic of growing larger crystals at higher temperatures is in agreement with the general crystallisation theory [87, 149]. A smaller degree of supercooling (i.e. higher temperatures) led to the growth of few, but larger crystals, as the growth was the dominating driving force. These mechanisms did not impact the overall olivine crystal shape due to its constant aspect ratio (Fig. 4.38). Regarding the fact that data from the two experiments with completely different set ups, including various holding times and sample amounts, were incorporated in the quantification, it is notable that the crystal aspect ratio subjected only minor fluctuations between 2.13 and 2.25 (1150 $^{\circ}\text{C}$, 1100 $^{\circ}\text{C}$). As a consequence, it can be concluded that olivine crystallises with an isometric morphology. However, it must be noted that the elongated macro crystal shape of olivine is not represented by the single crystal morphology described above. Its macro dimensions are strongly impacted by the available space in the intercrystalline gaps of the slags crystallised texture and therefore cannot be predicted.

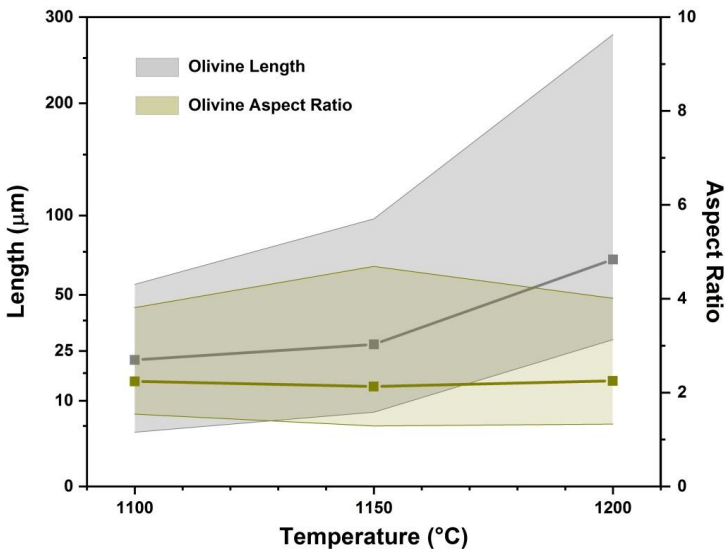


Fig. 4.38: Olivine crystal morphology quantification based on samples from the quenching and the CLSM experiments. Maximum, minimum, and average crystal length as well as crystal aspect ratio in dependency of the temperature. The x-axis is in logarithmic scale.

It can be summarised that olivine crystals are the second most abundant phase in HKR slag. The observed crystals may form elongated macro crystals, but mostly precipitate as individual crystals. Olivine crystals are highly symmetric and similar to olivines documented in other slag and magmatic studies. Based on the orthorhombic crystallographic system, an elongated, equiaxed bipyramid was chosen as the generalised morphology. Olivine morphology quantification revealed an increasing average length with an increase of temperature. In contrast, the olivine aspect ratio remains constantly. It was therefore concluded that olivine crystals grow isometric, resulting in an always constant morphology.

4.4.4 Melilite – HKR Slag System

Melilite is the dominant phase in the synthetic HKR slag system. Therefore, the quantification of its crystal morphology is essential to understand the impact of crystallisation on the viscosity of the HKR system. The melilite phase is also abundantly present in analysed slag systems (Table 2.5, Table 2.6). As will be seen in the following section, the morphology quantification of melilite is more complex compared to the previous anorthite, spinel, and olivine phases. The overall amount of measured crystals is the lowest towards all quantified phases (Table 4.6).

The melilite phase was identified to form comparable large dendritic, skeletal crystals (Fig. 4.23). Those crystal morphologies were also displayed in cross sections (Fig. 4.14), indicating recurring melilite morphology. However, CLSM images of the samples surface (Fig. 4.15) indicated large crystals with a pyramidal and an hour-glass shape but no dendritic or skeletal crystals. Nonetheless of this apparent discrepancy in the crystal structure, SEM EDX measurements indicated a uniform melilite solid solution with dominance of åkermanite in all of the aforementioned morphologies.

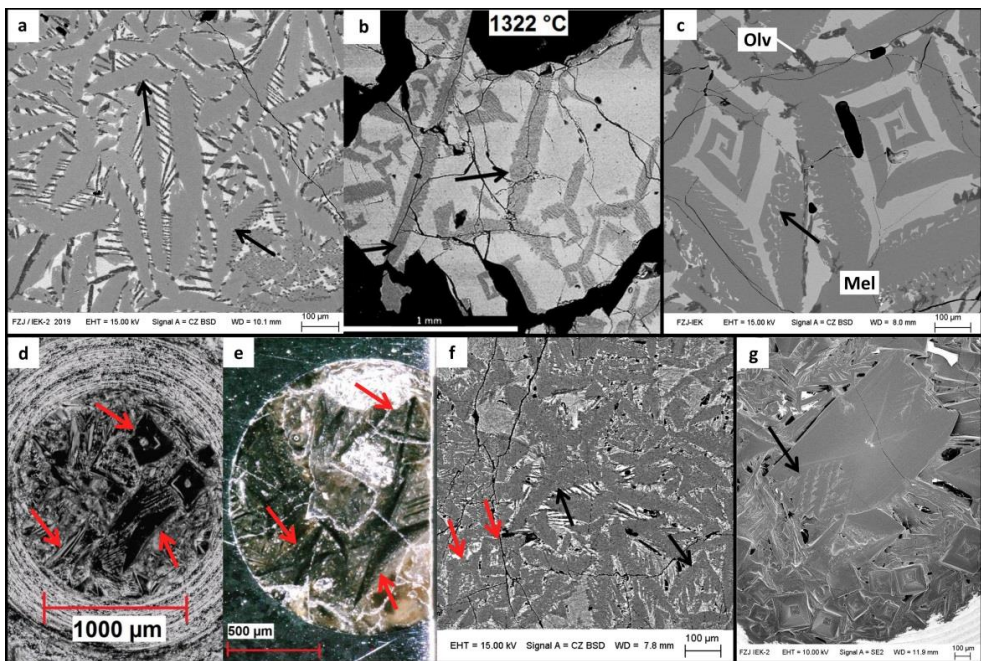


Fig. 4.39: Selection of melilite crystal shapes and morphologies. a) SEM BSE image of a CLSM sample supercooled to 1100 °C and hold for 7 minutes. **b)** SEM BSE image of a slag system quenched under air at 1322 °C, modified after Schwitalla et al., 2017 [103]. **c)** Sample quenched instantly from 1150 °C in the quenching experiment. **d)** Microscope image of sample surface, **e)** surface cross section, and **f)** SEM BSE image of the vertical cross section of a sample supercooled with -200 K/min in the CLSM experiment. **g)** SEM image of the sample surface, supercooled with -60 K/min in the CLSM experiment.

Hence, a selection of samples treated in the quenching and the CLSM experiments were chosen to validate the systematic of the melilite morphology (Fig. 4.39, Fig. 4.40). Melilite crystals displayed in Fig. 4.39a, indicated Y- to skeletal crystal shapes. A similar shape was observed in a coal slag after viscosity measurements by Schwitalla et al., 2017 [103] (Fig. 4.39b) for a melilite solid solution, also dominated by åkermanite. Due to the similar shapes, it can be suspected that there is an overall

mechanism responsible for the melilite crystal shape formation. To complete the observed variations of melilite shapes, a quadrangular spiral shell structure was also observed (Fig. 4.39c). To comprehend the connection of all described shapes, a representative CLSM sample was intensively analysed (Fig. 4.39d-f). Microscopic analysis of the samples surface revealed elongated square pyramidal shaped melilite crystals, as indicated by the red arrows (Fig. 4.39d). After sample preparation, those crystals appear in an hour-glass shape in sample cross sections (Fig. 4.39e). Thus, a prepared perpendicular cross section of the same sample showed the Y- shaped skeletal crystals again (Fig. 4.39f, black arrows), while they were arranged with hollow melilite square crystals (red arrows). Based on these observations, it can be confirmed that pyramidal melilite crystals and skeletal ones coexist next to each other. Furthermore, the inner structure of melilite pyramids is not completely filled, as the hour-glass shape of melilite cross section pyramids indicate.

The aforementioned observations can be enhanced by the analysis of the chosen slag samples, displayed in Fig. 4.40. A mm-scale, elongated melilite pyramid, which grew in the CLSM experiment at 1100 °C, was investigated (Fig. 4.40a, b). Its outer morphology is a distinctive pyramidal structure, with mainly smooth crystal surfaces that show signs of horizontal growth lamella. The analysed cross section of the pyramid revealed instead that it is partly hollow on the inside (Fig. 4.40b, black arrow). Furthermore, the inner structure has a skeletal appearance, built up of an oblique main axis and smaller teeth-like outgrowths. Those structures align well with previous skeletal melilite structures (Fig. 4.14a, Fig. 4.23a, b, and Fig. 4.39a, b, f). The frequent occurrence of the inner skeletal structures can be further legitimized by the åkermanite crystal displayed in Fig. 13c. The shown åkermanite crystal has a rectangular elongated shape and is hollow on the inside accompanied by teeth-like outgrowths (Fig. 4.40c). The combination of its hollow nature with the internal outgrowths is described as the “peg-structure” [150] and represents a special property of the melilite phase. Finally, it can be summarised that the presence of skeletal melilite crystals in the cross sections coincides with the rectangular pyramid structure as they are describing the same crystal from different point of views (Fig. 4.14, Fig. 4.15, Fig. 4.23, and Fig. 4.39). Additionally, there is further evidence for the hollow characteristic of melilite pyramid crystals. As already visible in Fig. 4.39f (red arrows) the cross section included some rectangular melilite crystals with a portion of remaining slag in its centre. Similar structure of melilite pyramids is given in Fig. 4.39d, e, and f. Supercooled HKR slag with an applied supercooling rate of -150 K/min led to the formation of large melilite pyramids, whose upper external morphology was not completed by crystal growth (Fig. 4.39d, e). The inner space of the pyramid showed additional crystallisation of small rectangular melilite crystals and olivine macro crystals, which crystallised out of the remaining inner liquid slag. Furthermore, another CLSM sample also displayed such crystallisation in the inner space of melilite pyramids (Fig. 4.39f, red arrows). It can be summarised, that the inner structure of melilite crystals has a complex growth systematic, while its outer morphology displayed highly symmetric pyramids.

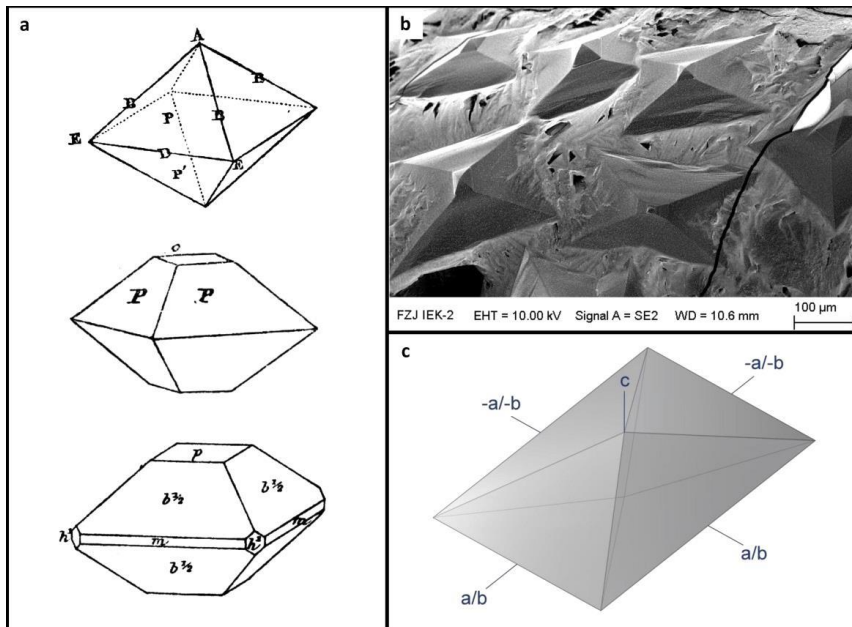


Fig. 4.40: a) Selection of melilite morphologies as already described by Goldschmidt (1920) [83]. b) SEM image of sample morphology, sample treated in the CLSM experiment at 1200 °C for 60 minutes. c) Generalized rectangular bipyramid. The dimensions of the ground surface are described by the aspect ratio and its elevation in c-axis by a 35° angle of the face diagonal above the ground surface

Since the characteristics of melilite pyramidal growth was intensively discussed, an individual morphology was determined for its quantification. Fig. 4.40a displayed a selection of pyramidal melilite crystal morphologies [83], considering the restrictions of melilite tetragonal crystallographic system. As the tetragonal crystallographic system has a high degree of symmetries, the pyramidal habits are formed as bipyramids. Due to the performed CLSM experiments, melilite pyramids could only be investigated from the top view (Fig. 4.40b). It could not be validated, if the pyramidal morphology turned out to be a bipyramidal one, since the bottom of the crystals was submerged in the slag. However, as the symmetric restrictions of the tetragonal crystallographic system could not be ignored, a bipyramidal melilite morphology is the only reasonable generalisation, as seen in Fig. 4.40b.

Since the melilite crystal morphology was described, its dimensions were quantified. A selection of 10 samples was chosen for the quantification, including two samples from the quenching and eight samples from the CLSM experiments. Melilite pyramids were measured based on digital microscopy and SEM images. In total, 83 melilite pyramids were quantified on their length and on their aspect ratio, respectively. The melilite quantification results are shown in Fig. 4.41. The average pyramid length is increasing, as the degree of supercooling is reduced, a finding that was already concluded for olivine (Fig. 4.38) and that is in agreement with the fundamentals of the crystallisation theory [87]. To describe the span width of melilite length growth, the 10th and 90th quantile was chosen, since some individual large pyramids, e.g. the one seen in Fig. 4.39a and b, strongly impacted the maximum and minimum length value. In contrast to the crystal length, the aspect ratio of melilite pyramids did not display a specific trend. The highest average aspect ratio (2.4) of melilite pyramids was detected at 1150 °C, all remaining temperature regimes led melilite crystals to grow in aspect ratios between 1.37 (1200 °C) and 1.68 (1100 °C). A noteworthy finding is the fact that the lowest determined aspect ratios were settled at around the value of 1 (Fig. 4.41), which means that the

melilite bipyramidal crystals had a square ground surface. In fact, approx. 40% of the quantified pyramids were in a square ground shape. Since no systematic of elongated and square pyramids was found, the generalised elongated bipyramidal structure was set to be ideal.

Based on this melilite morphology conclusion, the initially documented crystals on the HKR slag surface after the viscosity measurement can be identified as melilite (Fig. 4.11). As Fig. 4.11 displayed, HKR slag seemingly formed pyramidal crystals on the slag surface with several hundred μm of edge lengths that is in general agreement with the morphology quantification data (Fig. 4.41).

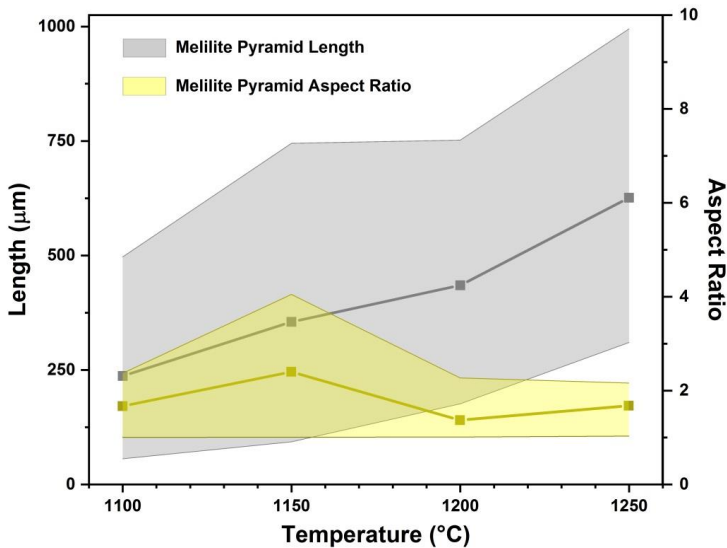


Fig. 4.41: Melilite crystal morphology quantification based on samples from the quenching and the CLSM experiments. 90th, 10th quantile, and average crystal length as well as melilite aspect ratio in dependency of the temperature.

Lastly, a brief conclusion on the melilite morphology can be ascertained. Melilite shape was identified as skeletal to dendritic macro crystals in the sample cross sections. However, slag surface investigations via CLSM revealed pyramidal shapes of melilite crystals. Due to customised preparation methods it was revealed that melilite pyramids display an internal, hollow structure with skeletal outgrowths. As a result, it could be focused on the external melilite shape, which was generalised as a rectangular bipyramid. Melilite pyramid length increases with an increase of temperature, following the laws of crystallisation theory [87, 149]. In contrast, the pyramid aspect ratio did not display a specific trend and fluctuates.

4.5 Crystallisation in PiTER Slags

The following last chapter of the results section shall give a different insight into the previously gathered results of this study. As mentioned in the very beginning, this study was performed as part of the German national HotVeGas project. During the previous project phases, a pressurised high-temperature entrained flow reactor (PiTER) was constructed at the department of Energy Systems of the Technical University of Munich [123]. In this reactor, numerous real coal and biomass fuels were analysed under varying gasification conditions. Since this study focussed on synthetic systems, a slag sample based on real coal ash was provided from the project partner in Munich. To create a transition from the basic research on synthetic slag systems of this study to real coal ash slags, the provided samples were analysed to validate if crystallisation occurred in the PiTER reactor.

4.5.1 PiTER setup and Slag Origin

The PiTER reactor is vertically installed and consists of several individual units, as can be seen in Fig. 4.42a. The applied gases are N_2 , O_2 , H_2 , CO_2 , and H_2O and the flow capacities lie in the range of 10 to $100 \text{ Nm}^3/\text{h}$ [155]. The gases are mixed and preheated in an external gas unit. Afterwards, they are injected at the very top of the setup and additionally preheated. In the second preheater, the gas mixture is heated up to maximum temperatures of $1800 \text{ }^\circ\text{C}$ [155, 156]. The diameter of the preheater is larger compared to the nozzle of the preheating unit to achieve additional gas acceleration.

The fuel dosing system is installed parallel to the gas treating system and pre-treats the applied fuel (Fig. 4.42a). The feed rate can be controlled from 0.2 kg/h to 5 kg/h [155]. As the reactor is designed for high-pressure applications, the fuel dosing unit is already pressurised. At the top of the reaction zone, the injected fuel and the gas firstly get in contact with each other [35, 155]. The fuel is injected by a water-cooled probe at an angle of 40° , as can be seen in Fig. 4.42b. The inner walls of the reaction zone consist of high-grade alumina tubes, with an inner diameter of 70 mm (Fig. 4.42b,c) [155]. For further information on the experimental setup and applied experiments, it is referred to the works of Tremel (2012), Steibel (2017), and DeYoung (2019) [35, 155, 156].

As can be seen in Fig. 4.42b,c, the provided sample consists of a fragment of the upper reaction tube, still including the fuel injection probe. An overhang of two overlapping Al_2O_3 tubes is visible (Fig. 4.42c). The whole length of the provided reaction tube was approx. 60 cm . The reaction tube fragment was disintegrated into single peaces to enable a microscopic and SEM analysis. The slag-on-tube samples represent a distance of 40 cm below the fuel dosing tube and are therefore located closely to the initial reaction. Accordingly, the experienced temperatures of the slag were expected to be equal with the applied temperatures due to the limited distance.

The sample material was taken after an apparatus failure. Small cracks in the Al_2O_3 tubes resulted in a leakage of the gas mixture, resulting in a subsequently disintegration of the graphite heating elements. According to an immediate (and not a controlled) shut-down of the setup, the slag probably cooled down rapidly and the potential influence of crystallisation phenomena during the cooling procedure is expected to be minor.

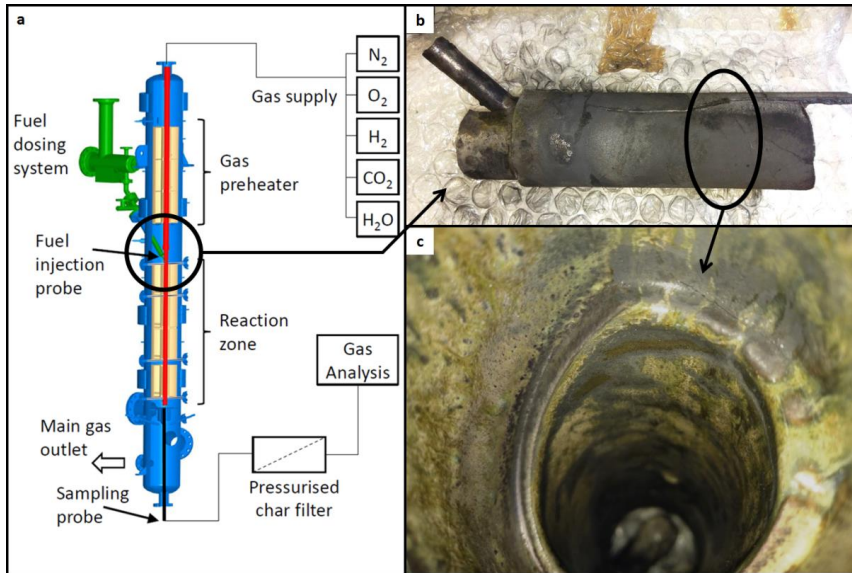


Fig. 4.42: a) Schematic setup of the PiTER experiment, b) extracted part of the fuel injection probe unit, c) image of the inner walls of the Al₂O₃ reaction tube covered with yellowish-greenish-greyish slag residues.

The provided reaction tube experienced several fuel compositions, as can be seen in Table 4.7. KOL2 coal was blended with HKN, GMS, and a torrefied biomass, resulting in various compositions of injected fuels. Since some slag residues may have been attached to the generally rough Al₂O₃ tube surface, a precise composition of the slag producing fuel cannot be reconstructed, afterwards. However, the last applied mixture was KOL2/torrefied biomass, yet with different blendings. Due to the unpredictable fuel composition, a characterisation of potentially crystallised phases would serve as a beneficial addition to the assessment of abundant crystallising phases, performed earlier in this study (Table 2.6). The gasification temperatures varied between 1200 °C and 1400 °C, during the measurement campaign.

Table 4.7: Composition of the applied fuels in the measurement campaign of PiTER experiments. The last applied blending consisted of KOL2/torrefied biomass.

Samples	SiO ₂	Al ₂ O ₃	CaO	Fe ₂ O ₃	SO ₃	MgO	NaO	K ₂ O	other
KOL2	54.8	18.8	1.6	8.6	1.3	1.4	0.8	1.9	10.8
HKN	2.8	1.6	27.1	9.3	21.3	14.0	4.2	2.7	17.0
GMS	41.5	0.7	22.0	5.2	8.7	4.9	0.0	0.1	16.9
torrefied biomass	34.0	5.1	28.5	4.1	2.6	4.7	0.8	14.5	5.7

4.5.2 Crystallisation Characterisation and Comparison

Similar to the investigated samples in this study, few fragments of the reaction tube were prepared by embedding into resin, grinding, and polishing. As a first analysis, digital microscopy was applied on the individual fragments (Fig. 4.43). Three images representatively display the surface of the reaction tube with the attached slag. Firstly, it can be concluded that the slag layer seemingly has a thickness

of less than 1mm. Accordingly, the downwards slag flow proceeded during the experiments and no blockage obviously occurred. Secondly, it is clearly visible, that the Al_2O_3 tube does not display distinct face edges, but has a rough surface instead (whitish-purplish areas, Fig. 4.43a). It can be assumed that the oxidic slag was able to dissolve parts of the Al_2O_3 tube, probably resulting in the reactor failure.

Two regions of the slag were further investigated with higher magnification (Fig. 4.43b,c). In Fig. 4.43b several elongated crystals can be seen in the slag. While the slag facing towards the inner reaction zone (right) faces a whitish to yellowish colour, the elongated crystals appear vitreous or whitish (left and mid). The segregated Al_2O_3 tube with the attached slag can clearly be distinguished from each other (Fig. 4.43c). Yet, it can be seen that the slag crystallised at the tubes surface as well as in between the segregated particles. Already by the microscopic analysis, distinct and vastly spread crystallisation was found in the PiTER samples.

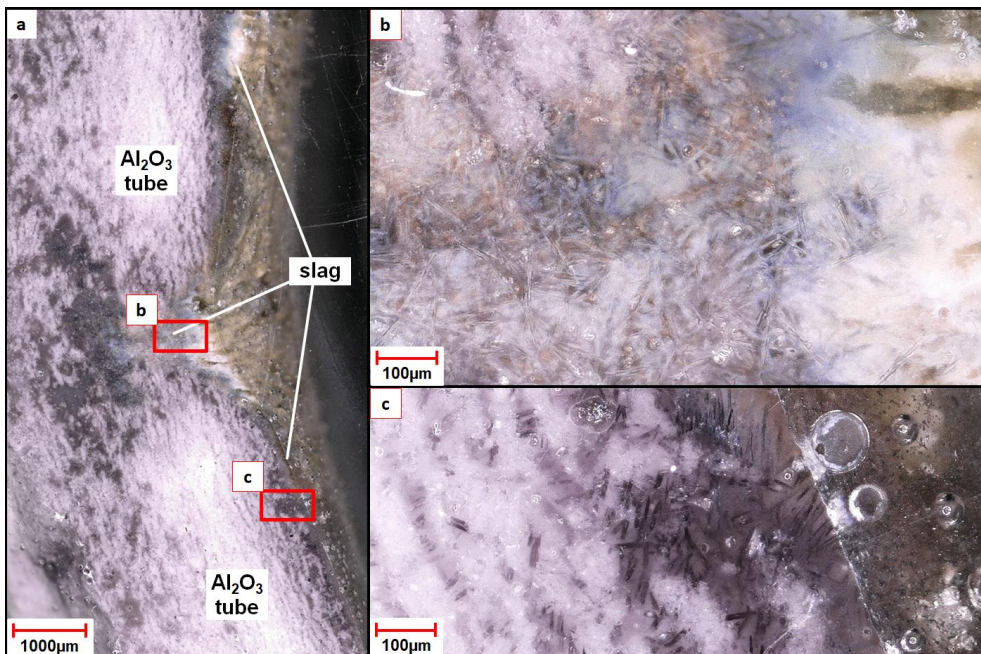


Fig. 4.43: Microscopic images of PiTER slag. a) Fragment of the Al_2O_3 reaction tube with attached slag on the inner surface, b) and c) indicate the presence of elongated crystals in the slag on the segregated Al_2O_3 tube surface.

To additionally increase the magnification and to determine the crystallised phase by their composition, SEM i.e. SEM-EDX analyses were performed. A selection of representative fragments was chosen, as can be seen in Fig. 4.44. The elongated shape of the abovementioned crystals is also revealed by the SEM images. As Fig. 4.44a indicates, the elongated phases appear at the outer slag margins with smaller grain sizes, compared to the inner regions, marked by the tube particles. While these inner crystals appear solid, the outer ones appear segmented and feathered. SEM-EDX point measurements at several fragments proved this elongated phase to have an anorthite composition. Since XRD measurements could not be conducted on the samples, an additional confirmation by the crystal structures was not achieved. However, as previously quantified, the shapes of the crystals align very well with the anorthite crystals observed in the synthetic slags, allowing the conclusion that the elongated phase is anorthite. Fig. 4.44b displays a gap between the inner reaction tube and an overlapping connection-tube segment that is filled with partly crystallised slag. Also in this area, well-shaped anorthite crystals were observed. The slag probably crept into this gap and was not

influenced by the reactor operation. Due to no disturbance, anorthite growth shall be representative. Also, small spinel crystals were found in this gap. Fig. 4.44c shows a comparable area to Fig. 4.44a, at the segregated margin of the Al_2O_3 tube. Anorthite crystals can be found once again with the characteristic shape. Idiomorphic spinel crystals with small crystal sizes also appeared in the slag. Several SiO_2 (or probably: quartz) grains were found in the slag layer. Due to the inner structure, it was concluded that these grains are fuel residues, originating from the coal fuel. This hypothesis is supported by the fact that no smaller SiO_2 crystals precipitated at the grains margins.

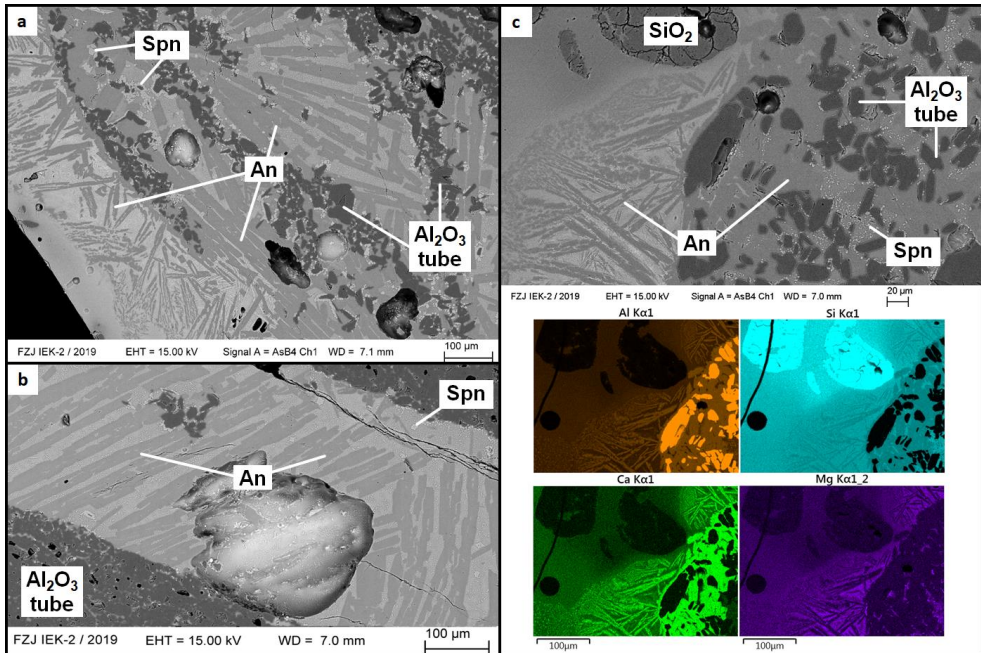


Fig. 4.44: SEM and SEM-EDX images of the PiTER slag. a) partly crystallised slag in between segregated Al_2O_3 tube particles of the reaction tube, b) partly crystallised slag between the inner reaction tube (bottom left) and overlapping connecting-tube segment (top right), c) SEM and SEM-EDX analysis of partly crystallised slag between Al_2O_3 tube particles. An = anorthite, Spn = spinel.

SEM-EDX mapping were applied on the area of Fig. 4.44c. It is obvious that the segregated Al_2O_3 tube particles have a positive signal on the Al mapping and the SiO_2 grains a strong signal on the Si mapping. As presented for the synthetic slags, anorthite crystals can be recognised by enrichments in Al and Ca and depletions in Si and Mg, compared to the slag composition.

A last comparison was made between the crystallisation in PiTER slags and the previous results on the synthetic slag samples (Fig. 4.45). Typical anorthite morphologies are displayed in Fig. 4.45a,b. Anorthite crystals in the PiTER slags clearly formed the elongated shape, as seen e.g. in the HKT viscosimetry crucible. The uniformity of the crystal dimensions for the PiTER slags surpasses the one of the stirred HKT slag (Fig. 4.45b). This finding is surprising for several reasons: Firstly, the synthetic slag has a limited oxide variability, allowing pure anorthite growth, while the PiTER slags also contained sodium and potassium and therefore could have formed other feldspars (albite or orthoclase). However, they did not crystallise. Secondly, due to the more diverse composition and so, availability of additional elements in the PiTER slag, more phases could have potentially crystallised. However, anorthite still remained as the dominant phase. The spinel crystals seen in Fig. 4.45c,d are also in very good agreement with each other concerning the crystal shape. As the SEM images

indicate, spinels in PiTER slags do not show any zoning, indicating a very homogeneous composition (SEM-EDX point measurements indicated a pure spinel composition (MgAl_2O_4)). Due to the already mentioned diverse composition of PiTER slags, these findings are seen as unexpected. Since the spinel crystals are mostly associated with the Al_2O_3 tube fragments, it is conceivable that Al_2O_3 dissolution enriched the slag in Al and therefore supported the spinel growth. Spinel growth would therefore rely on heterogeneous nucleation, which is not supposed to be representative. Real gasifiers have other refractory materials, which would not serve as a nucleation source, such as SiC [17]. Nonetheless, there are gasifiers with spinel-phase containing refractory materials [17] existing that could support spinel growth as well.

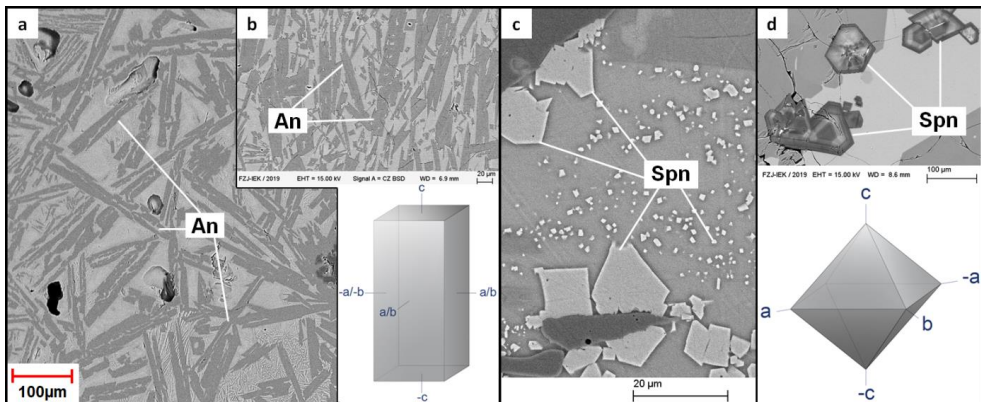


Fig. 4.45: Comparison of crystal shapes in PiTER and synthetic slags for anorthite and spinel by SEM images. a) anorthite crystals in PiTER slag, b) orientated anorthite crystals in synthetic HKT viscosimetry sample and generalised anorthite morphology, c) idiomorphic spinels in PiTER slags, d) idiomorphic spinel crystals in quenched HKR slag and generalised spinel morphology. An = anorthite, Spn = spinel.

Finally, it can be summarised that real-coal-based PiTER slags, crystallised during the experimental campaigns of the project partner in Munich. Anorthite was defined as the main phase and minor fractions of spinel were detected. The segregated surface of the Al_2O_3 reaction tube clearly indicated its dissolution by the present slag. Anorthite crystals grew in every part of the slag and formed elongated shapes that are very similar to the previously investigated anorthite crystals. Even the more diverse composition of PiTER slags resulted in anorthite and not in other plagioclase growth, stating the significance of the anorthite phase formation even in real coal slags. Spinel crystallised idiomorphic, similar to the ones in the synthetic HKR slag. It is assumed that dissolution of the Al_2O_3 tube material supported spinel growth, leading to initial heterogeneous nucleation. The shapes of anorthite and spinel are in absolute agreement with the generalised morphologies made in this study. These findings undoubtedly legitimise the approach of investigating crystal morphologies performed in this study.

5 General Discussion

Even though the results were described, explained and already discussed in the previous chapter, some additional discussions on the results are required. Therefore, this section focusses on the discussion of more general conclusions made in this study. Firstly, the quality of the performed approach will be judged, based on the applied experiments, to validate if the results can be seen as representative and reproducible. Secondly, the significance and applicability of results will be evaluated. Since crystallisation is a very complex phenomenon, several factors must be considered to assess the potential impact of the results.

5.1.1 Accordance of the Applied Methods and Experiments

To validate the representativeness of the findings in this study, the individual results of the experiments will be compared with the equilibrium results firstly. Since the experiments are potentially influenced by kinetics and since equilibrium calculations are vastly used for model approaches, potential deviations are of great interest. Equilibrium calculation results can be found in chapter 4.1.2 and the experimental results on slag crystallisation in chapters 4.2, 4.3, 4.4, and 4.5.

ST-D-2 slag displayed the most generalised composition with 4 oxidic compounds $\text{SiO}_2\text{-Al}_2\text{O}_3\text{-CaO-Fe}_2\text{O}_3$. The predicted phases anorthite, cristobalite and olivine (FactSage Equilib) were found in the slag. However, the cristobalite phase did not occur in any sample. Also for SOM-1 slag, cordierite was predicted as the second phase to crystallise, but it was also not determined in the samples. HKT was the third cordierite bearing slag system, predicted via Equilib. Likewise to ST-D-2 and SOM-1, cordierite was also not observed in HKT slag (Fig. 5.1). As summarised in Fig. 5.1, cordierite crystallisation was predicted from 1260 °C until the solidus temperature of 1050 °C, but only anorthite, SiO_2 , and clinopyroxene were found in the slag. The mismatch of the predicted cordierite with the experimental results cannot be fully explained. It can be argued that the cordierite datasets of the GTox database are not correct. However, further investigations on the cordierite phase are required to give a trustworthy explanation.

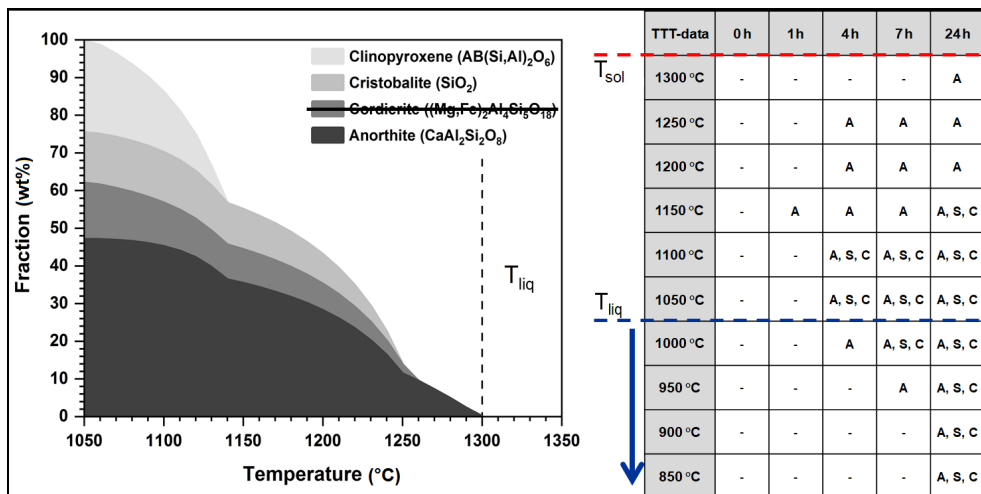


Fig. 5.1: Example of the comparison between equilibrium calculations via FactSage Equilib (left) and experimentally determined phases during the quenching experiment (right) of the HKT slag. A = anorthite, S = SiO_2 , C = clinopyroxene.

Also, the crystallisation temperature of cristobalite i.e. SiO_2 is shifted to lower temperatures in the experiments (Fig. 5.1). For the HKR slag, the predicted anorthite phase did not occur during the experiments, while melilite, olivine, and spinel were found. The major crystallising phase was melilite and not olivine, as it was predicted.

While HKR slag could not be supercooled below the solidus (due to immediate crystallisation), ST-D-2, HKT and SOM-1 slag displayed crystallisation below the solidus. Accordingly, higher viscous slags could be supercooled more sufficiently. In glas studies, the glas transition temperature is defined as the temperature where a glas melt can be described as “solid” [157, 158]. The “solid” state shall be reached at 2/3 of the glas melting temperature, non-regarding the actual solidus temperature. Due to the high silica content, ST-D-2, HKT, and SOM-1 slag behave comparable to a glas, resulting in the high supercooling degrees (Fig. 5.1). The comparison expresses that equilibrium calculations may serve as a rough estimate on the crystallising phases, but a fully correct prediction of the crystallised phases is unlikely. Accordingly, many studies on the crystallisation of slag [90, 108, 115-117] in which the crystal phases are only determined by equilibrium calculations and not by additional chemical and/or structural analysis shall be treated with serious concern. While the prediction of the liquidus temperature aligns well with the experiments, high viscous slags can be supercooled below the solidus due to the high silica contents (and the slow diffusion).

The fact that equilibrium calculations did not align satisfactorily with experimental data was expected to some extent. Yet, the reproducibility of results between several experimental setups is also an important issue that needs to be assessed. Since ST-D-2, HKT and SOM-1 slags were analysed in the quenching experiment and by high temperature viscosimetry, both experimental approaches will be described firstly. Table 5.1 summarises the crystallisation results of the viscosimetry and the quenching experiment. ST-D-2, HKT, and SOM-1 slag displayed non-Newtonian behaviour, which is why isothermal measurements were performed at temperatures where crystallisation shall be present in the slags. Several hours were chosen to enable sufficient incubation time for crystals to grow. However, only HKT and HKR slag contained crystals during the measurement (Table 5.1).

Table 5.1: Comparison of the crystallised phases determined in the viscosity experiment during isothermal measurements with the corresponding samples from the quenching experiment.

Slags	non-Newtonian	parameters of isotherm. visco. measurement	crystallised phases (viscosimetry)	parameters of quenching experiment	crystallised phases (quenching)
ST-D-2	$\leq 1250\text{ }^\circ\text{C}$	$1225\text{ }^\circ\text{C} + 7\text{ h}$	-	$1250\text{ }^\circ\text{C} + 7\text{ h}$ $1200\text{ }^\circ\text{C} + 7\text{ h}$	anorthite anorthite + SiO_2
HKT	$\leq 1275\text{ }^\circ\text{C}$	$1250\text{ }^\circ\text{C} + 7\text{ h}$	anorthite	$1250\text{ }^\circ\text{C} + 7\text{ h}$	anorthite
SOM-1	$\leq 1250\text{ }^\circ\text{C}$	$1225\text{ }^\circ\text{C} + 3\text{ h}$	-	$1250\text{ }^\circ\text{C} + 4\text{ h}$ $1200\text{ }^\circ\text{C} + 4\text{ h}$	anorthite anorthite + SiO_2 + olivine
HKR	-	$1150\text{ }^\circ\text{C} + 4.5\text{ h}$	olivine + melilite	$1150\text{ }^\circ\text{C} + 4\text{ h}$	melilite + olivine + spinel

ST-D-2 slag produced anorthite, as well as anorthite + SiO_2 phases, while during viscosimetry no crystals formed at all (Table 5.1). In contrast, crystallised phases of HKT slag are identical. Comparably to the ST-D-2 slag, SOM-1 slag did not crystallise during viscosimetry, but formed anorthite (+ SiO_2 + olivine) in the quenching experiment, instead. Lastly, HKR slag showed good agreement between both experiments. The lack of determined spinels in the viscosimetry sample could be based on the generally minor fractions of spinel, which were possibly overseen.

It can be concluded that the crystallisation characteristics of stirred slag in the viscosimetry setup partly vary from the quenching experiment at similar time and temperature parameters. Variations in the factual temperatures of the samples could be accounted for that phenomenon, despite accurate temperature calibrations of each experiment. As a rule of a thumb, one percent of temperature

deviation shall always be considered for high temperature experimental studies. Also, thermocouples with long operation times can suffer from alteration (e.g. alkali condensation, hydrogen embrittlement). If a temperature shift of 50 °C would be assumed, the experimental results would align well with each other. Since HKR slag was also analysed via CLSM, a third experimental setup can be taken into account, as well. The crystallised phases: melilite, olivine and spinel were documented in both experiments. The CLSM results were gathered at several measurement campaigns. In between, sample holders and thermocouples have been replaced. As a result, a minor temperature shift of the initial incubation time was also observed in CLSM experiments.

Accordingly, it must be noted that the initially assumed weak correlation of the experimental results (Table 5.1) can be tolerated, since a precise accordance of experimentally applied temperatures cannot be ensured. The fact that slag samples got stirred in the viscosimetry setup, but not in the quenching experiments may also be influential. However, the determination of the stirring impact is hard to quantify. Nonetheless, some evidence was gathered that is mentioned in the following.

The potential impact of slag stirring on the crystallisation will be exemplarily shown by a selection of representative samples from each performed experiment, assembled in Fig. 5.2. In all performed experiments, pyramidal shaped crystals (or symmetric macro crystals in Fig. 5.2b) were observed on the slag surface. As explained during the crystal morphology quantification, crystal phases require sufficient space in the slag to crystallise according to their crystallographic nature. At the slag surface, it is seemingly effortless for melilite to crystallise in the typical bipyramidal morphology. As already explained in chapter 4.4.4, melilite crystals appear as skeletal macro crystals in two-dimensional cross sections (Fig. 5.2b,c). The fact that both shapes represent the same morphology was adequately evidenced (chapter 4.4.4). If the shape of melilite crystals is investigated in the two-dimensional cross section of the stirred viscosimetry sample, skeletal melilites are not present (Fig. 5.2a). Instead, melilite is present in the form of elongated crystals, very similar to the olivine phase. Since the experimental parameters were set alike, the experimental properties must be responsible for the crystallisation shape of melilite. As can be imagined, large bipyramids do not behave fluid dynamically and generate a certain resistance in the slag. As a specific shear rate was exceeded, melilite bipyramids got disrupted into elongated particles and aligned well with the shear direction. In contrast, crystallising melilite on the slag surface floated on the underlying sheared slag and was able to form the typical bipyramidal morphology (Fig. 5.2a). The crystal morphologies of melilite were therefore influenced by the experimental procedure and should not be compared with results of “untouched” slag samples.

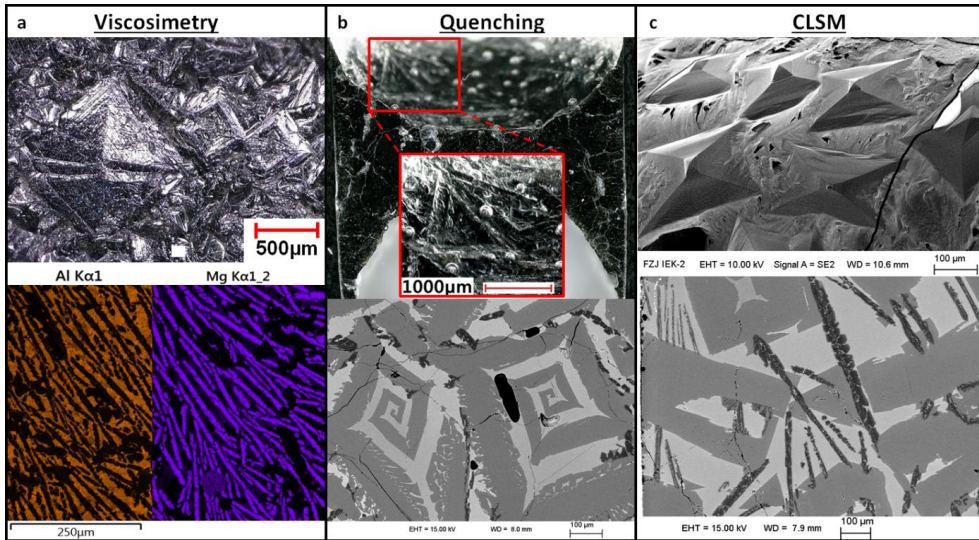


Fig. 5.2: Comparison of crystallised HKR slag. a) Viscosimetry – microscopic image of pyramidal crystals on the slag surface and SEM-EDX mapping of elongated melilite and olivine crystals in the cross section, b) quenching – microscopic image of symmetric crystals on the slag surface and SEM image of melilite skeletal macro crystals in the cross section, c) CLSM – SEM images of crystallised melilite pyramids on the slag surface and skeletal to pliers-like melilite crystals.

All in all, an impact of the experimental procedure on the crystallisation characteristics could be proven. Several consequences result from these findings. Firstly, crystallisation characteristics of viscosimetry samples cannot be compared with quenching and CLSM samples, if the crystallised phases occupy non-fluid-dynamic morphologies. Secondly, crystal morphology studies of crystallised slags simply based on viscosity measurement must be accompanied by additional experiments to truly determine the crystal morphologies. Thirdly, viscosity measurements of non-fluid-dynamic bearing crystals cannot represent the real viscosity of slags. High shear rates destroy the crystals, resulting lastly in a shear thinning behaviour.

5.1.2 Application of Crystallisation Results

Since the accordance of the applied experiments and methods was discussed and the representativeness of crystal morphologies was confirmed, the applicability of the results will be discussed in the following. Firstly, the significance of the analysed crystal phases will be classified. Secondly, an understanding of the kinetic concept of crystallisation shall be provided. Lastly, some additional application-relevant aspects will be discussed.

In chapter 2.4.4 of this study, a literature assessment of recent studies was made that investigated slag crystallisation. It was concluded that there is a deviation between equilibrium calculations and experimental results. Additionally, it was ascertained that the number of crystallising phases is not numerous but follows repeating patterns: some phases are highly abundant in typical coal slags, others are only minorly present. The assessment was restructured and listed, based on the crystallising phases. Additionally, the analysed and quantified crystal phases of this study were added in Table 5.2.

Table 5.2: Comparison of literature assessment findings (equilibrium calculations + experimental data) on slag crystallisation (Table 2.6) with results of this study. Underlined phases were quantified in this study; phases in brackets were documented, but could not be quantified due to xenomorphic appearance.

crystal phases	abundance by calculations	abundance in experiments	phase crystallised in analysed slags	generalised morphology
anorthite	6	5	ST-D-2, HKT, SOM-1	tetragonal prism
melilite	6	5	HKR	rectangular bipyramid
quartz/SiO ₂	2	2	(ST-D-2, HKT, SOM-1)	xenomorphic
spinel	5	2	HKR	octahedron
clinopyroxene	3	2	(HKT)	xenomorphic
wollastonite	2	1	-	-
hematite/wustite/Fe _x O _x	1	1	-	-
“iron silicon oxide”	-	1	-	-
olivine	2	-	HKR, (ST-D-2, SOM-1)	elongated, equiaxed bipyramid
mullite	2	-	-	-
cordierite	2	-	-	-
nepheline	1	-	-	-
merwinite	1	-	-	-
andradite	1	-	-	-

Firstly, it can be seen that the deviation between the calculation results and experimental ones deviate quite strongly (Table 5.2). By taking the prevalence of crystallised phases into account, anorthite and melilite seem to be the most important phases by far, with an occurrence in 5 out of 9 compared studies. Additional relevance with verification in 2 out of 9 studies can be accounted to quartz/SiO₂, spinel, and clinopyroxene. Other phases such as mullite, cordierite and nepheline are seemingly not relevant under experimental conditions (Table 5.2).

The comparison clearly indicates that the crystallised phases, quantified in this study, cover the relevant phases very well. Vastly present anorthite and melilite morphologies were defined and could be quantified in this study. The spinel phases could also be generalised and quantified, though it is not as common. The generalised and quantified olivine phase was documented in three slags, but could only be quantified in the HKR slag as olivine crystals formed idiomorphic shapes. Surprisingly, no other study documented olivine after the experiments. The quartz/SiO₂ and the clinopyroxene phase are also quite common in slags and were identified in this study. However, they crystallised xenomorphic, resulting in no morphology definition and quantification.

It can be summarised that the selection of slag systems performed in this study was chosen wisely. The most abundant phases were covered and could be quantified. In combination with the previous conclusion, that the defined morphologies are more accurate than the simple geometries defined by other studies [32, 60, 77], the significance of the gathered results is additionally stated. All in all, it can be summarised that the performed methodological approach was concise and generated reproducible data. Accordingly, the applicability of the results is seen as high.

As mentioned above, SiO₂, clinopyroxene, and olivine (in ST-D-2 and SOM-1 slag) phase could not be defined and quantified due to their xenomorphic appearance. Since olivine formed idiomorphic in the HKR slag, it cannot be explained yet why some phases crystallised idiomorphic and some did not. In geological systems, there are also examples of more idiomorphic (e.g. spinel) and more xenomorphic phases (quartz), e.g. due to twin formation [66, 150]. But generally, every mineral can

potentially crystallise idiomorphic. So, there must be one (or several) driving force(s) involved. In the following, some aspects will be discussed to improve the understanding of slag crystallisation.

It is assumed that the composition of the slag has a significant influence on the characteristic growth of certain crystal phases. Two examples of crystallised phases and crystallisation zones of the HKR and ST-D-2 slag are provided in Fig. 5.3. The example of typical HKR slag crystallisation shows the composition of melilite, the (bulk) slag and olivine (Fig. 5.3a). It can be seen that the composition of melilite is comparable to the one of the slag, while olivine faces a strong enrichment in Mg and depletion in Ca and Al (Fig. 5.3a). The majority of HKR samples indicated an initial growth of melilite, before olivine started to grow. In other words, the saturation of required elements for melilite growth is higher, compared to the one of olivine, resulting in a preferred growth of melilite. In case of the ST-D-2, HKT and SOM-1 slag, anorthite is the major crystallising phase. Compared with the other phases SiO_2 , clinopyroxene, and olivine, anorthite composition aligns best with the slag compositions.

Accordingly, the crystallisation of the first phase can be explained, yet it must be discussed how the other phases form in the slag, afterwards. In case of the low viscous HKR slag, a significant delay of olivine growth (the 2nd phase) could not be observed, but it seems that spinel crystallised noticeably later. In the results section, it was mentioned several times that spinel is strikingly often associated with olivine. The example of Fig. 5.3a shows that olivine crystals are surrounded with a margin of slag with modified composition. Based on olivine composition, the slag is enriched in Al, Ca and depleted in Mg. It can be discussed that intense olivine crystallisation enriches the slag sufficiently enough in Al that the energetic barrier for spinel crystallisation is reduced and spinel crystals form close to olivine. In some cases, olivine crystals were also observed in the surrounding area of melilite crystals. The typical slag enrichment and depletion behaviour of melilite indicates that the composition is slightly modified in favour of an olivine composition, which could also support olivine growth (Fig. 5.3a). A further example is given in Fig. 5.3b for the case of fayalite growth in ST-D-2 slag. As mentioned in the results section (chapter 4.3.3), fayalite crystallised as a last phase at low temperatures in the gaps between anorthite and SiO_2 . The crystallisation of both phases results in a strong enrichment of Fe in the remaining slag, as the higher contrast of the surrounding slag also indicates in the SEM image (Fig. 5.3b). Based on the modification of slag composition, fayalite grew in between anorthite and SiO_2 . Additionally, it can be seen that the cloudish crystallisation of anorthite and SiO_2 strongly depletes the slag in Si, Ca, and Al, which highly likely hampers further growth of those phases. Crystal growth can therefore not be seen as a constant parameter. The growth order and the growth speed strongly rely on the already present crystallisation structure with the resulting degree of slag depletion and respectively enrichment in the surrounding slag margins. This phenomenon can be accounted for the comparable low anorthite lengths, documented in the HKT slag at 1100 °C (Fig. 4.30).

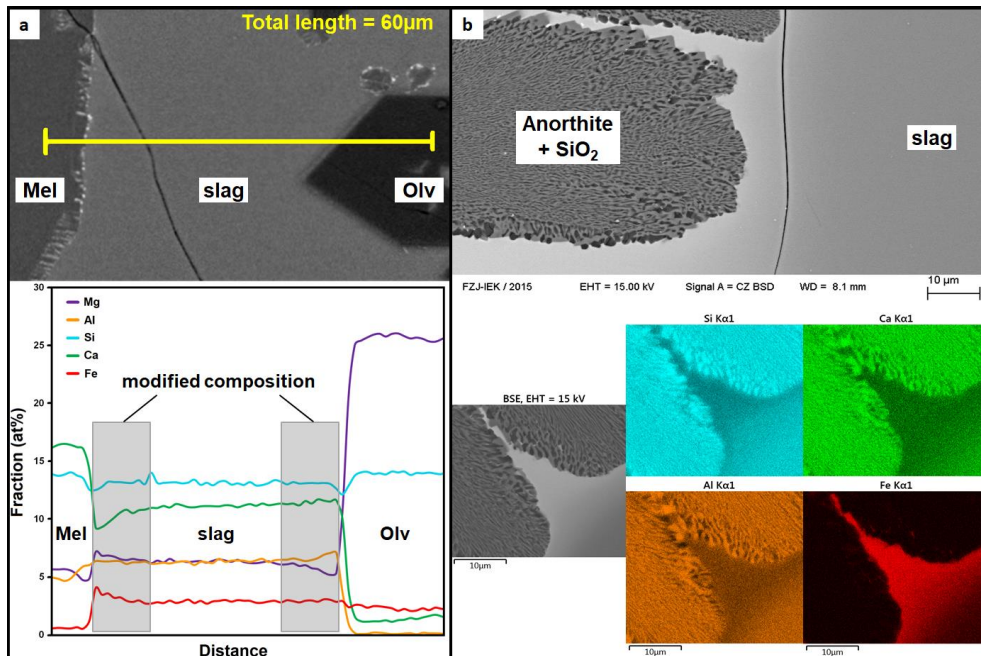


Fig. 5.3: a) SEM-EDX line scan through melilite-slag-olivine in the HKR slag with the determined corresponding composition, b) SEM and SEM-EDX mapping of cloudish crystallisation zone including anorthite + SiO_2 in the ST-D-2 slag. Mel = melilite, Oliv = olivine. Mapping colours: cyan = Si, green = Ca, orange = Al, red = Fe.

Regarding the fundamentals of magmatic multicrystalline systems, mentioned in chapter 2.4.3, these aforementioned observations seem reasonable [98, 99, 159]. The Bowen series represents a distinct growth order for magmatic systems, starting with olivine, pyroxene, and kalifeldspar, which was developed on natural crystallisation phenomena (Fig. 2.21) [98, 99, 159]. In contrast, many studies on slag crystallisation apply the JMAK-equations to determine crystallisation kinetics, while not identifying the crystallised phases and the possible amount of phases [88, 108, 160]. These studies determine the kinetics by condensing all crystallised phases together as one. As natural examples and the findings of this study indicate, the growth of each phase has influence on the kinetics of the following phases [98, 99]. The imagination that all possibly crystallising phases (e.g. defined by equilibrium calculations) follow internal kinetics that shall be applied as soon as the slag is supercooled below the liquidus is not correct. A more reasonable concept of crystallisation kinetics would correspond to the individual crystal growth order, starting with the initial phase, followed by slag composition modification and the crystallisation of the second phase and so forth.

It can be concluded that the slag bulk composition determines the growth of the initial crystalline phases. Based on the modification of slag composition, the growth of other phases is supported or hampered. As a result, slag crystallisation faces a dependency related to time (kinetics) and space (slag composition modification, margin of other crystals). While low viscous slags more likely enable simultaneous growth due to improved diffusion, high viscous systems more strongly rely on the ordered growth of crystallised phases based on slag composition modification.

A recent study by Seebold (2017) [32] developed a viscosity model that includes a physical and chemical viscosity of partly crystallised slag and JMAK equations for the crystallisation kinetics. The provided morphology data can be implemented in such a model to increase the accuracy. The fact that slag crystallisation modifies the slag chemistry, resulting in an influence of the slag viscosity, is a

reasonable approach that can be confirmed by the observations made in this study. However, since crystallisation relies on the growth order and the resulting kinetics, a more complex approach would be required to satisfactorily model the viscosity of partly crystallised slags.

5.1.3 Approach of model implementation

The following section is based on a publication by Schupsky et al., (2020) [143] and includes a potential structure of a viscosity model for partly crystallised slags, including the crystal morphology data. The modifications made in this section are minor, compared to the publication. Therefore, the reference accounts for any following content [143].

The viscosity of partially crystalline slags is contributed from two parts: the viscosity of remaining liquid slag (η_l) and the relative viscosity (η_r) due to the crystallised phases. A flowsheet is proposed to determine the viscosity of partially crystalline slags, as shown in Fig. 5.4. The first part is sufficiently calculated, using a structure-based viscosity model [54, 73, 140, 141]. It was recently developed for molten fuel slags and is described by the function of temperature and the slag composition. In contrast, the second part is much more complex, which is not only related to the volume fraction of crystallised phases, but also to the crystal morphology, the crystal size and the crystal size distribution. Furthermore, the shear rate is also taken into account, if the volume fraction of crystallised phases reaches a critical value that causes the transition from Newtonian to Non-Newtonian fluid behaviour. Therefore, the simple correlation of the relative viscosity only with the volume fraction of crystallised phases fails. However, it remains an ongoing challenge to consider all aforementioned parameters influencing the relative viscosity. There are numerous existing viscosity models for suspension systems, such as the Einstein-Roscoe model [161] and the Krieger-Dougherty model [162]. In this study, a modified Einstein-Roscoe model is proposed as a first step with consideration of the volume fraction and crystal morphology. The volume fraction in the original Einstein-Roscoe model is replaced by an effective volume fraction (see Eq. 14). The contribution of each kind of crystals to the relative viscosity varies due to different crystal morphologies. Because of that, the quantitative description of the crystal morphology, especially for major crystallised phases, is performed in the previous chapters. The volume fraction of each crystallised phase is calculated from the corresponding mass fraction, predicted by FactSage using GTox database considering their individual crystal morphology. This calculation requires density models for both, crystals and remaining liquid slag. Sometimes, the volume fraction is directly estimated by the mass fraction, if the required density models lack.

It is noted that the influence of crystallisation kinetics on the volume fraction of crystallised phases is ignored in this flowsheet, which needs to be further considered in the future. As mentioned in the previous chapter, a kinetic approach with respect to the modified slag composition is required. Also the fact that the initially crystallising phases (anorthite and melilite) displayed the dominant crystal fractions shall be considered.

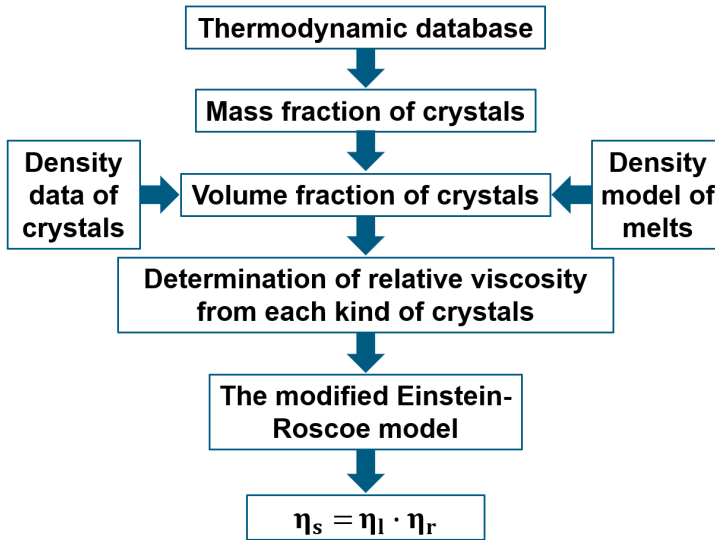


Fig. 5.4: The flowsheet to modelling the viscosity of partial crystalline slags

$$\eta_r = (1 - \sum_i \alpha_i \cdot V_i)^{-2.5} \quad (14)$$

where V_i is the volume fraction of crystallised phase i ; α_i is the weighting factor to determining the contribution of the crystallised phase i to the relative viscosity. The factor α_i is strongly dependent on the aspect ratio and increases generally with increasing aspect ratio.

As a result, the investigation of crystal morphology and its size quantification marks the reasonable next step in the research field of viscosity modelling of partly crystallized gasifier slags. The distinct crystal morphologies and the repeatability of their appearance presented in this study and in recent publications, clearly support the significance of the gathered data [125, 137, 143, 163]. As a next step, these data shall be used to enhance existing model approaches, as described above.

6 Summary and Outlook

The global energy demand is constantly rising and fossil fuels play a major role for the energy supply industries of many countries. The use of efficient techniques such as gasification can serve as a key technology. Gasification can flexibly fill gaps in the power network, and so harmonise supply fluctuations of the renewable energy sources. During the gasification process, a residue is produced that is named as slag. Slag is in a liquid state and consists of oxidic compounds, which are incorporated in coal or biomass and are not converted into syngas. The production of slag is a continuous process and its properties affect the operation of a gasifier. If the slag becomes too highly viscous, a slag blockage may occur and the facility must be shut down for required maintenance work. The phenomenon of crystallisation is accounted for a viscosity increase, as the presence of a solid phase in the liquid slag increases the viscosity drastically. Such a partly crystallised slag cannot be modelled sufficiently, as the implementation of a solid phase into a liquid slag is very challenging and since no crystal morphology data are available in the literature.

This study marks a novel approach of analysing the crystallisation behaviour of four synthetic gasifier slags and to define and quantify the morphologies of individual crystal phases. Initially, the slag systems were characterised by HSM and DTA measurements, subsequently followed by equilibrium calculations using FactSage Equilib programme. Afterwards, high temperature viscosimetry, quenching, and CLSM experiments were applied on the four slag systems to determine the crystallisation behaviour of the slags. The viscosimetry measurements revealed that ST-D-2 and HKT are highly viscous slags. SOM-1 slag has an intermediate viscosity and HKR slag a low viscosity. Isothermal viscosity measurements were conducted to prove if non-Newtonian behaviour was caused by crystallisation. HKT and HKR slag displayed crystallisation, while a non-Newtonian behaviour of ST-D-2 and SOM-1 could not be reproduced. Since crystallisation was partly detected, the slags were further investigated in a quenching experimental setup. It was used to analyse the crystallisation evolution by quenching supercooled samples isothermally with variations of time. The slag samples were prepared to enable the analysis of two-dimensional cross sections, subsequently afterwards. Microscopic analysis revealed a greenish to blueish colour for ST-D-2, HKT and SOM-1 slag and a blackish colour for the HKR slag. ST-D-2, HKT and SOM-1 displayed crystallisation of large elongated crystals at higher temperatures, turning into fine grained whitish clouds of crystallisation at temperatures of about 1100-1150 °C and below. While ST-D-2 and HKT slag required at least 1 h but mostly 4-7 h of holding time until incubation of crystals appeared, SOM-1 slag crystallised during the scheduled cooling slope of the utilised quenching furnace. HKR slag displayed an even shorter incubation time. Most of the investigated temperatures displayed instant crystallisation. Therefore, SOM-1 and HKR slag were additionally investigated in the CLSM setup. For the SOM-1 slag, shortest incubation times of a double-digit minute scale were reached, while HKR slag still crystallised during the cooling slope. As a result, HKR slag crystallisation nose could not be bypassed. The crystallisation nose represents the kinetically retarded crystallisation zone of a slag with respect to time and temperature.

The crystallised phases were determined via XRD and SEM analysis. XRD analysis revealed high fractions of anorthite in the ST-D-2, HKT and SOM-1 slags. It was also measured that anorthite crystals display elongation in direction of their c-axis. Additional detected phases are: cristobalite (SiO₂), fayalite and spinel (ST-D-2); cristobalite and clinopyroxene (HKT); olivine and clinopyroxene (SOM-1). For the HKR slag, melilite and forsterite (olivine) were detected in the crystallised slag samples.

SEM and SEM-EDX analysis were vastly used to further identify crystallised phases and to determine the crystal morphologies of the individual phases. Thus, spinel could be identified in the HKR slag, which was not detected in previous XRD analysis, probably due to small fractions. The variety of analysed samples revealed characteristic shapes of crystal phases. Based on the crystallographic properties, generalised crystal morphologies could be defined for anorthite, spinel, olivine, and melilite (Fig. 6.1).

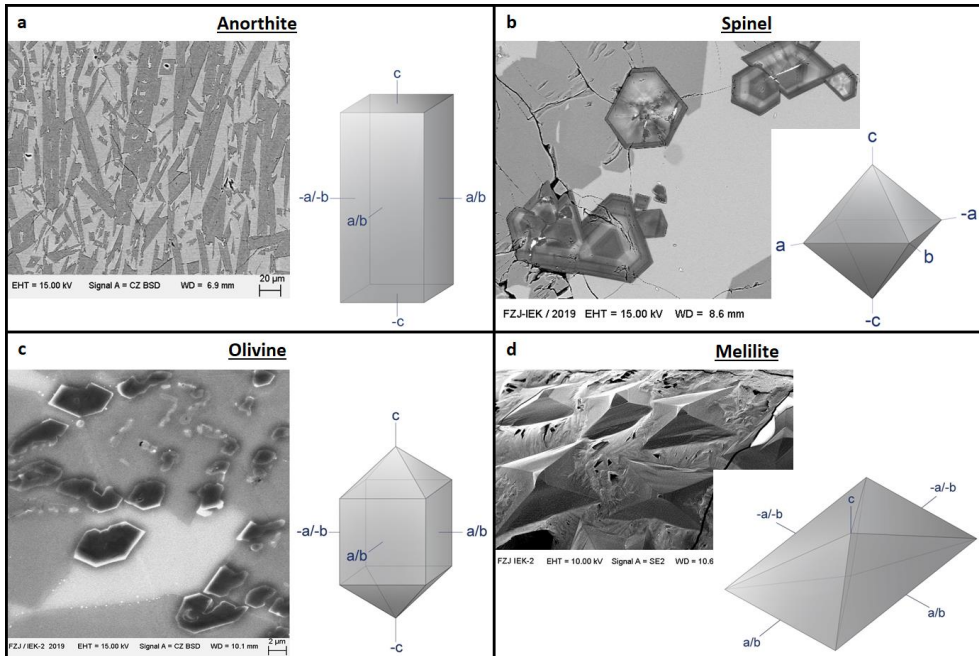


Fig. 6.1: Defined and quantified crystal morphologies with SEM images of the crystallised phases. a) anorthite = tetragonal prism, b) spinel = octahedron, c) olivine = elongated, equiaxed bipyramid, d) melilite = rectangular bipyramid.

Anorthite could be defined as a tetragonal prism with variations of the prism elongation. Spinel forms idiomorphic octahedron morphologies. Olivine crystallised also idiomorphic as elongated, equiaxed bipyramids and melilite formed symmetric rectangular bipyramids (Fig. 6.1). The defined crystal phases were quantified on their dimensions by measuring more than 1000 individual crystals to generate morphology data that can be used for viscosity modelling. It was documented that all crystal phases grew larger in size with an increase of the applied temperature, yet this trend was not as clear for the spinel phase. Regarding the crystallisation theory, higher temperatures favour crystal growth and lower temperatures support nucleation. Therefore, findings are generally in agreement with this theory. By also measuring the width, crystals aspect ratio was quantified as well. Due to the defined symmetric morphologies, any additional morphological properties can be assessed based on the provided datasets. Lastly, a small comparison with real slags from PiTER reactor was made. In the facility, slags with various compositions were converted. However, well-known anorthite majorly crystallised, accompanied by small fractions of spinel crystals. Anorthite and spinel morphologies were identical compared to the results of the synthetic slags. This consensus is seen as a confirmation that the novel approach and the defined crystal morphologies of this study are reasonable, trustworthy, and provide beneficial data for a viscosity model of partly crystallised slags.

It is highly recommended to follow the novel approach made in this study to further investigate crystal morphologies. Anorthite and melilite are probably the most relevant phases of slag crystallisation. The example of melilite clearly shows that crystallisation is very complex when it comes to identifying the morphologies, as the cross sections reveal different shapes than observations of the slag surface. SiO_2 and clinopyroxene could not be quantified due to the xenomorphic appearance. It is therefore recommended to firstly investigate more slag systems, including the already described phases to further strengthen the provided data statistics. Secondly, additional quantifications of crystallising phases such as wollastonite would extend the present

datasets by additional relevant phases.

Furthermore, the influence of viscosity measurements on the crystal morphology and the agreement of viscosimetry with quenching experiments must be investigated. As this study proved for melilite crystals, their morphology got disrupted by viscosity measurements, resulting in a non-representative impact on the slag viscosity. Also, a reasonable concept of crystallisation kinetics must be provided. Based on the findings of crystallisation in low viscous (HKR) and high viscous (ST-D-2, HKT) slags, crystallisation order may have a significant influence on the following crystallisation (kinetics). Simple JMAK equations shall not simply be applied as they cannot deal with growth characteristics of individual phases.

Literature

1. UNFCCC, *ADOPTION OF THE PARIS AGREEMENT*, in *Report No. FCCC/CP/2015/L.9/Rev.1*, U. Nations, Editor. 2015, Framework Convention on Climate Change: Paris.
2. The White House, *Statement by President Trump on the Paris Climate Accord*. 2017, The White House: Washington.
3. Presse- und Informationsamt der Bundesregierung *Speech of Chancellor Merkel at the Symposium "10 Jahre Elektromobilität - Zukunft wird Gegenwart"* by Mennekes GmbH & Co. KG. 2018 September 27, 2018 [cited 2019 11-10-2019]; Available from: www.bundesregierung.de/breg-de/suche/rede-von-bundeskanzlerin-merkel-beim-symposium-10-jahre-elektromobilitaet-zukunft-wird-gegenwart-der-mennekes-gmbh-co-kg-am-27-september-2018-1533260.
4. International Energy Agency. *Statistics data browser - Energy supply*. 2019 [cited 2019 10-10-2019]; Available from: <https://www.iea.org/statistics/>.
5. Warner, K.J. and Jones, G.A., *The 21st Century Coal Question: China, India, Development, and Climate Change*. Atmosphere, 2019. **10(8)**: p. 476.
6. BP p.l.c, *Statistical Review of World Energy, 2018*. British Petroleum, 2018. **67th edition**: p. 61.
7. Khadse, A.N., *Resources and economic analyses of underground coal gasification in India*. Fuel, 2015. **142**: p. 121-128.
8. Kumar, A., Kumar, K., Kaushik, N., et al., *Renewable energy in India: Current status and future potentials*. Renewable and Sustainable Energy Reviews, 2010. **14(8)**: p. 2434-2442.
9. Wang, W., Li, Z., Lyu, J., et al., *An overview of the development history and technical progress of China's coal-fired power industry*. Frontiers in Energy, 2019. **13(3)**: p. 417-426.
10. Huang, L., Hu, J., Chen, M., et al., *Impacts of power generation on air quality in China—part I: An overview*. Resources Conservation and Recycling, 2017. **121**: p. 103-114.
11. Hansen, L.D., *Coal: Typology, Physics, Chemistry, Constitution. Third Edition*. By D. W. van Krevelen. Journal - American Chemical Society, 1994. **116(21)**: p. 9813.
12. Grotzinger, J. and Jordan, T., *Press/Siever Allgemeine Geologie*. Vol. 7. Auflage. 2017, Berlin Heidelberg: Springer Spektrum.
13. Van Krevelen, D.W., *Coal : typology, physics, chemistry, constitution*. 1993.
14. Vassilev, S.V., Vassileva, C., Baxter, D., et al., *Relationships between chemical and mineral composition of coal and their potential applications as genetic indicators. Part 1. Chemical characteristics*. Geol Balcanica, 2010. **39**: p. 21-41.
15. Higman, C. and van der Burgt, M., *Gasification*. 2008: Gulf Professional Publishing.
16. Dohrn, M., *Ansatzverhalten von Aschen in Kohledampferzeugern bei brennstoff- und lastflexiblem Betrieb*, in *Fakultät für Maschinenwesen (Fak. 4)*. 2018, RWTH Aachen University: Aachen. p. 121.
17. Spliethoff, H., *Power Generation from Solid Fuels*. 2010, Dordrecht London New York: Springer-Verlag Berlin Heidelberg.
18. McCann, V., *Geologie im Gelände : das Outdoor-Handbuch*. Springer Spektrum, 2015.
19. Adrian, F., *Fossil beheizte Dampfkraftwerke*. Handbuchreihe Energie. 6, 1986.
20. UNFCCC, *Clarifications on Definition of Biomass and Consideration of Changes in Carbon Pools to a CDM Project Activity*. 2005, EB 20, Report, Annex 8.
21. Basu, P., *Biomass Gasification, Pyrolysis and Torrefaction : Practical Design and Theory*. Vol. 2nd edition. 2013, London, San Diego: Academic Press.
22. Kaltschmitt, M., Hartmann, H., Hofbauer, H., *Energie aus Biomasse: Grundlagen, Techniken und Verfahren*. 2016, Berlin Heidelberg: Springer Vieweg.
23. Vassilev, S.V., Vassileva, C.G., Song, Y.C., et al., *Ash contents and ash-forming elements of biomass and their significance for solid biofuel combustion*. Fuel, 2017. **208**: p. 377-409.
24. Vassilev, S.V., Kitano, K., Vassileva C.G., *Some relationships between coal rank and chemical and mineral composition*. Fuel, 1996. **75(13)**: p. 1537-1542.
25. Speight, J.G., *The chemistry and technology of coal, third edition*. 2012. 1-808.

26. Van Krevelen, D.W., *Graphical-statistical method for the study of structure and reaction processes of coal*. Fuel, 1950. **29**: p. 269-284.
27. Van Krevelen, D.W. and Schuyer, J., *Coal Science: Aspects of Coal Constitution*. 1957: Elsevier Applied Science.
28. Jones, J.M., et al., *Towards biomass classification for energy applications*. Science in Thermal and Chemical Biomass Conversion, 2006. **1 CPL Press**: p. 9.
29. Council, N.C., *Coal = Reliable Energy?* 2015, National Coal Council: Washington DC.
30. EIA, *International Energy Outlook 2016*. 2016. p. 290.
31. Dohrn, M. and Müller, M., *Influence of Load Changes on the Deposit Behavior during Combustion of Five Different Hard Coals*. Energy and Fuels, 2018. **32**(3): p. 3985-3994.
32. Seebold, S., *Über den Einfluss der Kristallisation auf das Fließverhalten oxidischer Schmelzen*, in *Fakultät für Maschinenwesen*. 2017, Rheinisch-Westfälische Technische Hochschule Aachen: Aachen. p. 168.
33. Brünger-Weilandt, S. *Kohlevergasung mit CO₂-Abtrennung*. 2013 [cited 2019 23rd October]; Available from: <https://kraftwerkforschung.info/kohlevergasung-mit-co2-abtrennung-igcc/>.
34. Lorson, H., Schingnitz, M., Leipnitz, Y., *The thermal treatment of wastes and sludges with the Noell entrained-flow gasifier*, IChemE Conference - Gasification: An Alternative to Natural Gas. 1995: London.
35. DeYoung, S., *Numerical Simulation of Entrained Flow Gasification with Focus on Char Reaction Kinetics*, in *Fakultät für Maschinenwesen*. 2019, Technische Universität München: München. p. 214.
36. Hannemann, M.F. and Hui, W.d., *Siemens Fuel Gasification Technology Status and New Developments*, in *Coal Conversion and Syngas*, T.I.F.I.M.C.o.I.X. Technologies, Editor. 2015, Technische Universität Bergakademie Freiberg.
37. Hannemann, F., Schingnitz, M., Zimmermann, G., *Siemens IGCC and gasification technology: today's solution and developments*, in *2nd Freiberg International Conference on IGCC and Xtl Technologies*. 2007: Freiberg.
38. Halama, S. and Spliethoff, H., *Numerical simulation of entrained flow gasification: Reaction kinetics and char structure evolution*. Fuel Processing Technology, 2015. **138**: p. 314-324.
39. Fletcher, T.H., *6 - Gasification fundamentals*, in *Integrated Gasification Combined Cycle (IGCC) Technologies*, T. Wang and G. Stiegel, Editors. 2017, Woodhead Publishing. p. 223-256.
40. Brünger-Weilandt, S. *IGCC: Vergasungsprozesse verstehen*. 2013 25th February 2013 [cited 2019 23rd October]; Available from: <https://kraftwerkforschung.info/igcc-vergasungsprozesse-verstehen/>.
41. The U.S. Department of Energy, *Tampa Electric Integrated Gasification Combined-Cycle Project*. 2000. p. 24.
42. Company, T.E., *Tampa Electric Polk Power Station, Integrated Gasification Combined Cycle Project*, J.M. Hornick, Editor. 2002: Tampa. p. 260.
43. Eurling, J. and Ploeg, J. *Process Performance of the SCGP at Buggenum IGCC*. in *Gasification Technologies Conference*. 1999. San Francisco, California.
44. Heymann, A., Batista Grau, P., Forster, E., et al. *Chemical Stability of Ceramic Dual-Phase Membrane Materials for H₂-Separation in Water-Gas Shift Reactors*. in *15th Conference & Exhibition of the European Ceramic Society*. 2017. Budapest.
45. Forster, E., van Holt, D., Ivanova, M.E., et al., *Stability of ceramic materials for H₂ transport membranes in gasification environment under the influence of gas contaminants*. Journal of the European Ceramic Society, 2016. **36**(14): p. 3457-3464.
46. Gude, U., Baumann, S., Meulenber, W.A., et al., *Towards the development of materials for chemically stable carbonate-ceramic membranes to be used for CO₂ separation in water-gas-shift reactor*. Separation and purification technology, 2019. **215**: p. 6.
47. Doležal, R., *Dampferzeugung: Verbrennung, Feuerung, Dampferzeuger*. Hochschultext. 1990: Springer.
48. Heek, K.H.v. and Mühlen, H.-J., *Heterogene Reaktionen bei der Verbrennung von Kohle*. Vol. Band 37. 1985: BWK.

49. Żelkowski, J., *Kohlecharakterisierung und Kohleverbrennung : Kohle als Brennstoff, Physik und Theorie der Kohleverbrennung, Technik*. Vol. Band 8. 2004: VGB.
50. Klose, E., *Pyrolyse - Wissenschaftsgebiet und technische Anwendung*. Energieanwendung + Energietechnik, 1992. **41 (12)**: p. 488-496.
51. Solomon, P.R. and Colket, M.B. *Coal devolatilization*. in *Proceedings of the 17th International Symposium on Combustion*. 1979. Pittsburg: The Combustion Institute.
52. Holmgren, P., Broström, M., Backman, R., *Slag Formation during Entrained Flow Gasification: Silicon-Rich Grass Fuel with a KHCO₃ Additive*. Energy & Fuels, 2018. **32(10)**: p. 10720-10726.
53. Vargas, S., Frandsen, F.J., Dam-Johansen, K., *Rheological properties of high-temperature melts of coal ashes and other silicates*. Progress in Energy and Combustion Science, 2001. **27(3)**: p. 237-429.
54. Wu, G., *Modelling and Experimental Validation of the Viscosity of Liquid Phases in Oxide Systems Relevant to Fuel Slags*, in *Fakultät für Maschinenwesen*. 2015, Rheinisch-Westfälische Technische Hochschule Aachen: Aachen.
55. Benson, S.A., Sondreal, E.A., Hurley, J.P., *Status of coal ash behavior research*. Fuel Processing Technology, 1995. **44(1-3)**: p. 1-12.
56. BBP (Babcock Borsing Power) Power Plants, *Gasification Technology*. Company Brochure, 2001.
57. Kong, L., Bai, J., Li, W., et al., *The internal and external factor on coal ash slag viscosity at high temperatures, Part 1: Effect of cooling rate on slag viscosity, measured continuously*. Fuel, 2015. **158**: p. 968-975.
58. Seebold, S., Wu, G., Müller, M., *The influence of crystallization on the flow of coal ash-slags*. Fuel, 2017. **187**: p. 376-387.
59. Liu, Z., Malfliet, A., Blanpain, B., et al., *Rheological Transitions of the Solid-Bearing Slag During Cooling Process*. Metallurgical and Materials Transactions B-Process Metallurgy and Materials Processing Science, 2018. **49(5)**: p. 2649-2657.
60. Liu, Z., Blanpain, B., Guo, M., *Viscosity of Heterogeneous Silicate Melts: A Review*. Metallurgical and Materials Transactions B, 2018. **49(5)**: p. 2469-2486.
61. Mader, H.M., Llewellyn, E.W., Mueller, S.P., *The rheology of two-phase magmas: A review and analysis*. Journal of Volcanology and Geothermal Research, 2013. **257**: p. 135-158.
62. Mueller, S., Llewellyn, E.W., Mader, H.M., *The rheology of suspensions of solid particles*. Proceedings of the Royal Society A: Mathematical, Physical and Engineering Science, 2010. **466(2116)**: p. 1201-1228.
63. Farges, F. and Brown Jr Calas, G.E., *X-Ray Scattering and X-Ray Spectroscopy Studies of Silicate Melts*. 2005. p. 317-410.
64. Zachariasen, W.H., *The Atomic Arrangement In Glass*. Journal of the American Chemical Society, 1932. **54(10)**: p. 3841-3851.
65. Bockris, J., Mackenzie, J.D., Kitchener, J.A., *Viscous flow in silica and binary liquid silicates*. Transactions of the Faraday Society, 1955. **51(0)**: p. 1734-1748.
66. Matthes, S. and Okrusch, M., *Mineralogie: Eine Einführung in die spezielle Mineralogie, Petrologie und Lagerstättenkunde*. Vol. 6. 2001, Heidelberg: Springer-Verlag Berlin. 507.
67. Putnis, A., *Introduction to mineral sciences*. 1992: Cambridge University Press. 457.
68. Jiang, Y., Ideta, K., Kim, J., et al., *The crystalline and microstructural transformations of two coal ashes and their quenched slags with similar chemical compositions during heat treatment*. Journal of Industrial and Engineering Chemistry, 2015. **22**: p. 110-119.
69. Greaves, G.N., *EXAFS and the structure of glass*. Journal of Non-Crystalline Solids, 1985. **71(1)**: p. 203-217.
70. Chartrand, P. and Pelton, A.D., *Modeling the charge compensation effect in silica-rich Na₂O-K₂O-Al₂O₃-SiO₂ melts*. Calphad, 1999. **23(2)**: p. 219-230.
71. Nowok, J.W., *Viscosity and Phase-Transformation in Coal Ash Slags near and below the Temperature of Critical Viscosity*. Energy & Fuels, 1994. **8(6)**: p. 1324-1336.
72. Senior, C.L. and Srinivasachar, S., *Viscosity of Ash Particles in Combustion Systems for Prediction of Particle Sticking*. Energy & Fuels, 1995. **9(2)**: p. 277-283.

73. Wu, G., Seebold, S., Yazhenskikh, E., et al., *Slag mobility in entrained flow gasifiers optimized using a new reliable viscosity model of iron oxide-containing multicomponent melts*. Applied Energy, 2019. **236**: p. 837-849.
74. Yazhenskikh, E., Hack, K., Müller, M., *Critical thermodynamic evaluation of oxide systems relevant to fuel ashes and slags, Part 5: Potassium oxide–alumina–silica*. Calphad, 2011. **35**(1): p. 6-19.
75. Yazhenskikh, E., Hack, K., Müller, M., *Critical thermodynamic evaluation of oxide systems relevant to fuel ashes and slags, Part 4: Sodium oxide–potassium oxide–silica*. Calphad, 2008. **32**(3): p. 506-513.
76. Jantzen, T., Hack, K., Yazhenskikh, E., *Addition of TiO_2 and Ti_2O_3 to the Al_2O_3 -FeO- Fe_2O_3 -MgO system*. Calphad, 2018. **62**: p. 187-200.
77. Mueller, S., Llewelin, E.W., Mader, H.M., *The effect of particle shape on suspension viscosity and implications for magmatic flows*. Geophysical Research Letters - Geophys Res Lett, 2011. **38**: p. 5.
78. Maron, S.H. and Pierce, P.E., *Application of ree-eyring generalized flow theory to suspensions of spherical particles*. Journal of Colloid Science, 1956. **11**(1): p. 80-95.
79. Klein, C. and Dutrow, B., *The 23rd edition of the manual of mineral science : (after James D. Dana)*. 2008: John Wiley & Sons, Inc. 675.
80. Markl, G., *Minerale und Gesteine: Mineralogie - Petrologie - Geochemie*. 2008: Spektrum Akademischer Verlag.
81. Nesse, W.D., *Introduction to optical mineralogy*. 2009: Oxford University Press.
82. Borhardt-Ott, W., *Kristallographie - Eine Einführung für Naturwissenschaftler*. Vol. 7th. 2009: Springer-Verlag Berlin Heidelberg. 360.
83. Goldschmidt, V., *Atlas der Krystallformen*. Markasit - Pyrit; Band 6: Tafeln. 1920, Heidelberg: Winter.
84. Goldschmidt, V., *Atlas der Krystallformen*. Safflorit - Topas; Band 8: Tafeln. 1922, Heidelberg: Winter.
85. Goldschmidt, V., *Atlas der Krystallformen*. Danalith - Feldspat-Gruppe; Band 3: Tafeln. 1916, Heidelberg: Winter. 247.
86. Tammann, G. and Hesse, W., *Die Abhängigkeit der Viscosität von der Temperatur bei unterkühlten Flüssigkeiten*. Zeitschrift für anorganische und allgemeine Chemie, 1926. **156**(1): p. 245-257.
87. Liebertz, J., *Crystal growth from melts of high viscosity*. Progress in Crystal Growth and Characterization, 1983. **6**(4): p. 361-369.
88. Yang, J., Cui, Y., Wang, L., et al., *In-Situ Study of Crystallization Behavior of a Mold Flux Using Single and Double Hot Thermocouple Technique*. Steel Research International, 2015. **86**(6): p. 636-643.
89. Wen, G.-H., Liu, H., Tang, P., *CCT and TTT Diagrams to Characterize Crystallization Behavior of Mold Fluxes*. Journal of Iron and Steel Research, International, 2008. **15**(4): p. 32-37.
90. Xuan, W., Whitty, K.J., Guan, Q., et al., *Influence of CaO on Crystallization Characteristics of Synthetic Coal Slags*. Energy & Fuels, 2014. **28**(10): p. 6627-6634.
91. Klug, J.L., Hagemann, R., Heck, N.C., et al., *Solidification Behaviour of Slags: The Single Hot Thermocouple Technique*. Journal for Manufacturing Science and Production, 2013. **13**(1-2): p. 91-102.
92. Semykina, A., Nakano, J., Sridhar, S., et al., *Confocal Scanning Laser Microscopy Studies of Crystal Growth During Oxidation of a Liquid FeO-CaO-SiO₂ Slag*. Metallurgical and Materials Transactions B-Process Metallurgy and Materials Processing Science, 2011. **42**(3): p. 471-476.
93. Zhang, Z., *Crystallization Behaviors of Slags through a Heat Flux Simulator*. isij International, 2010. **50**(8): p. 1142-1150.
94. Seebold, S., Eberhard, M., Wu, G., et al., *Thermophysical and chemical properties of bioliq slags*. Fuel, 2017. **197**: p. 596-604.
95. Jung, S.S. and Sohn, I., *Crystallization Control for Remediation of an FetO-Rich CaO-SiO₂-Al₂O₃-MgO EAF Waste Slag*. Environmental Science & Technology, 2014. **48**(3): p. 1886-1892.

96. Song, W., Tang, L., Zhu X., et al., *Fusibility and flow properties of coal ash and slag*. Fuel, 2009. **88**(2): p. 297-304.
97. Hurst, H., *Phase diagram approach to the fluxing effect of additions of CaCO₃ on Australian coal ashes*. Energy & Fuels, 1996. **10**(6): p. 1215-1219.
98. Bowen, N.L., *The evolution of the igneous rocks*. The evolution of the igneous rocks. 1956: New York: Dover Publications. 332.
99. Raymond, L.A., *Petrology, the study of igneous, sedimentary, metamorphic rocks*. 1995: Dubuque, IA : W.C. Brown Pub. 742.
100. Sunagawa, I., *Natural crystallization*. Journal of Crystal Growth, 1977. **42**(Supplement C): p. 214-223.
101. Melchior, T., *Untersuchungen zur Oberflächenspannung von Kohleschlacken unter Vergaserbedingungen*, in *Fakultät für Maschinenwesen*. 2010, Rheinisch-Westfälische Technische Hochschule: Aachen. p. 270.
102. Melchior, T., Bläsing, M., Pütz, G., et al., *Surface tension measurements of coal ash slags under reducing conditions at elevated pressures*. Fuel, 2011. **90**(1): p. 280-287.
103. Schwitalla, D.H., Bronsch, A.M., Klinger, M., et al., *Analysis of solid phase formation and its impact on slag rheology*. Fuel, 2017. **203**(C): p. 932-941.
104. Yuan, H.P., Liang, Q., Gong, X., *Crystallization of Coal Ash Slags at High Temperatures and Effects on the Viscosity*. Energy & Fuels, 2012. **26**(6): p. 3717-3722.
105. Zhou, J., Shen, Z., Liang, Q., et al., *A new prediction method for the viscosity of the molten coal slag. Part 1: The effect of particle morphology on the suspension viscosity*. Fuel, 2018. **220**: p. 296-302.
106. Bowen, N.L. and Schairer, J.F., *The evolution of the igneous rocks*. 1956: New York (N.Y.) : Dover publications. 332.
107. Shen, Z., Hua, X., Liang, Q., et al., *Reaction, crystallization and element migration in coal slag melt during isothermal molten process*. Fuel, 2017. **191**: p. 221-229.
108. Xuan, W., Whitty, K.J., Guan, Q., et al., *Influence of isothermal temperature and cooling rates on crystallization characteristics of a synthetic coal slag*. Fuel, 2014. **137**: p. 193-199.
109. Esfahani, S. and Barati, M., *Effect of slag composition on the crystallization of synthetic CaO–SiO₂–Al₂O₃–MgO slags: Part I- Crystallization behavior*. Journal of Non-Crystalline Solids, 2016. **436**: p. 35-43.
110. Xuan, W., Whitty, K.J., Guan, Q., et al., *Influence of SiO₂/Al₂O₃ on crystallization characteristics of synthetic coal slags*. Fuel, 2015. **144**: p. 103-110.
111. Ren, Q., Zhang, Y., Long, Y., et al., *Crystallisation behaviour of blast furnace slag modified by adding fly ash*. Ceramics International, 2018. **44**(10): p. 11628-11634.
112. Liu, J.-J., Chen G., Yan, P., et al., *In-situ observation of isothermal CaSiO₃ crystallization in CaO–Al₂O₃–SiO₂ melts: A study of the effects of temperature and composition*. Journal of Crystal Growth, 2014. **402**: p. 1-8.
113. Kashiwaya, Y., Nakauchi, T., SOn Pham, K., et al., *Crystallization Behaviors Concerned with TTT and CCT Diagrams of Blast Furnace Slag Using Hot Thermocouple Technique*. ISIJ International, 2007. **47**(1): p. 44-52.
114. Park, J., Wook Ryu, J., Sohn, I., *In-situ Crystallization of Highly Volatile Commercial Mold Flux Using an Isolated Observation System in the Confocal Laser Scanning Microscope*. Metallurgical and Materials Transactions B-Process Metallurgy and Materials Processing Science, 2014. **45**(4): p. 1186-1191.
115. Xuan, W., Whitty, K.J., Guan, Q., et al., *Influence of Fe₂O₃ and Atmosphere on Crystallization Characteristics of Synthetic Coal Slags*. Energy & Fuels, 2015. **29**(1): p. 405-412.
116. Xuan, W., Zhang, J., Xia, D., *The influence of MgO on the crystallization characteristics of synthetic coal slags*. Fuel, 2018. **222**: p. 523-528.
117. Xuan, W.W., Whitty, K.J., Guan, Q., et al., *Influence of Fe₂O₃ and Atmosphere on Crystallization Characteristics of Synthetic Coal Slags*. Energy & Fuels, 2015. **29**(1): p. 405-412.
118. Xuan, W., Zhang, J., Xia, D., *Crystallization characteristics of a coal slag and influence of crystals on the sharp increase of viscosity*. Fuel, 2016. **176**: p. 102-109.

119. Kong, L., Bai, J., Bai, Z., et al., *Improvement of ash flow properties of low-rank coal for entrained flow gasifier*. Fuel, 2014. **120**: p. 122-129.
120. Shen, Z., Li, R., Liang, Q., et al., *Effect of Cooling Process on the Generation and Growth of Crystals in Coal Slag*. Energy & Fuels, 2016. **30**(6): p. 5167-5173.
121. Xuan, W., Wang, Q., Zhang, J., et al., *Influence of silica and alumina ($\text{SiO}_2+\text{Al}_2\text{O}_3$) on crystallization characteristics of synthetic coal slags*. Fuel, 2017. **189**: p. 39-45.
122. Xuan, W., Wang, H., Xia, D., *In-situ observation of crystallization inside coal slags and influence of crystals on flow behavior*. Fuel, 2019. **251**: p. 242-248.
123. Halama, S., Kerscher, F., Geißler, A., et al., *Verbundvorhaben HotVeGas III - FLEX 1. Zwischenbericht 2017*. 2017: München.
124. Saar, O., *Kinetische Untersuchung zum Kristallisationsverhalten einer synthetischen Oxidschlacke*, in Steinmann - Institut für Geowissenschaften. 2019, Rheinische-Friedrich-Wilhelms Universität Bonn: Bonn. p. 104.
125. Schupsky, J.P., Guo, M., Blanpain, B., et al., *Investigations on Crystallization Processes of Three Oxidic Gasifier Slag Systems*. Journal of Energy Resources Technology, 2020. **142**: p. 9.
126. Stabile, F.M., Piccio, M., Serra, M.F., et al., *Viscosity and Thermal Evolution of Density and Wetting Angle of a Commercial Glaze by Means of Hot Stage Microscopy*. Procedia Materials Science, 2015. **9**: p. 563-570.
127. Duarte, I. and Ferreira, J.M.F., *Evolution of Metallic Foams Using Hot-stage Microscopy*. Procedia Materials Science, 2014. **4**: p. 251-256.
128. Schwedt, G., Schmidt, T.C., Schmitz, O.J., *Analytische Chemie - Grundlagen, Methoden und Praxis*. Vol. 3. Auflage. 2016, Weinheim: WILEY-VCH Verlag GmbH & Co. KGaA. 544.
129. Bale, C.W., Bélisle, E., Chartrand, P., et al., *FactSage thermochemical software and databases, 2010–2016*. Calphad, 2016. **54**: p. 35-53.
130. Hack, K., Jantzen, T., Müller, M., et al. *A novel thermodynamic database for slag systems and refractory materials*. in *Proceedings of the 5th International Congress on the Science and Technology of Steelmaking*. 2012. Dresden, Germany.
131. Nentwig, T., *Experimentelle Bestimmung und numerische Simulation von Viskositäten in Schlackesystemen unter Vergasungsbedingungen*, in Fakultät für Maschinenwesen. 2011, Rheinisch-Westfälische Technische Hochschule Aachen: Aachen.
132. Mielke, K., *Über das Verhalten und die Kontrolle von Schlacken des bioliq®-Vergasers*, in Fakultät für Maschinenwesen. 2020, Rheinisch-Westfälische Technische Hochschule Aachen: Aachen.
133. Nakano, J., Duchesne, M., Bennett, J., et al., *Thermodynamic effects of calcium and iron oxides on crystal phase formation in synthetic gasifier slags containing from 0 to 27 wt.% V_2O_5* . Fuel, 2015. **161**: p. 364-375.
134. Brugger, C.R. and Hammer, J.E., *Crystal size distribution analysis of plagioclase in experimentally decompressed hydrous rhyodacite magma*. Earth and Planetary Science Letters, 2010. **300**(3): p. 246-254.
135. Jones, P.T., Desmet, D., Guo, M., et al., *Using confocal scanning laser microscopy for the in situ study of high-temperature behaviour of complex ceramic materials*. Journal of the European Ceramic Society, 2007. **27**(12): p. 3497-3507.
136. Liu, Z., Chen, L., Blanpain, B., et al., *Effect of Crystallization on the Abrupt Viscosity Increase during the Slag Cooling Process*. Isij International, 2018. **58**(11): p. 1972-1978.
137. Schupsky, J.P., Guo, M., Blanpain, B., et al., *The Impact of Sample Homogeneity, Crucible Material, and Oxygen Partial Pressure on the Crystallization of Fe-Rich Oxidic Slag in CLSM Experiments*. Journal of Sustainable Metallurgy, 2020 (Slag Valorisation).
138. Schmidt, P.F., *Praxis der Rasterelektronenmikroskopie und Mikrobereichsanalyse*. Vol. 444. 1994, Renningen-Malmsheim: Technische Akademie Esslingen. 810.
139. Erdman, N., Bell, D.C., Reichelt, R., *Scanning electron microscopy*, in *Springer Handbooks*. 2019, Springer. p. 229-318.

140. Wu, G., Yazhenskikh, E., Hack, K., et al., *Viscosity model for oxide melts relevant to fuel slags. Part 1: Pure oxides and binary systems in the system $\text{SiO}_2\text{-Al}_2\text{O}_3\text{-CaO-MgO-Na}_2\text{O-K}_2\text{O}$* . Fuel Processing Technology, 2015. **137**: p. 93-103.
141. Wu, G., Yazhenskikh, E., Müller, M., *Viscosity model for oxide melts relevant to fuel slags. Part 2: The system $\text{SiO}_2\text{-Al}_2\text{O}_3\text{-CaO-MgO-Na}_2\text{O-K}_2\text{O}$* . Fuel Processing Technology, 2015. **138**: p. 520-533.
142. Wang, H., Qiu, P., Li, Yaoqiang L., et al., *Effect of quenching temperatures on melting characteristics of coal ash in a reducing atmosphere*. Energy and Fuels, 2012. **26**(4): p. 2204-2219.
143. Schupsky, J.P., Wu G., Guo, M., Müller, M., *Crystallisation characteristics and crystal phase quantification of a synthetic lignite gasifier slag system*. Fuel Processing Technology, 2020. **201**.
144. Sato, H., *Viscosity measurement of subliquidus magmas: 1707 basalt of Fuji volcano*. Journal of Mineralogical and Petrological Sciences, 2005. **100**(4): p. 133-142.
145. Riker, J., Cashman, K.C., Rust, A.C., et al., *Experimental Constraints on Plagioclase Crystallization during H_2O - and $\text{H}_2\text{O-CO}_2$ -Saturated Magma Decompression*. Journal of Petrology, 2015. **56**: p. 32.
146. Vetere, F., Sato, H., Ishibashi, H., et al., *Viscosity changes during crystallization of a shoshonitic magma: new insights on lava flow emplacement*. Journal of Mineralogical and Petrological Sciences, 2013. **108**(3): p. 144-160.
147. He, C., Bai, J., Kong, L., et al., *Effects of atmosphere on the oxidation state of iron and viscosity behavior of coal ash slag*. Fuel, 2019. **243**: p. 41-51.
148. Cashman, K.V., Thornber, C., Kauahikaua, J.P., *Cooling and crystallization of lava in open channels, and the transition of Pāhoehoe Lava to 'A'ā*. Bulletin of Volcanology, 1999. **61**(5): p. 306-323.
149. Tammann, G., *Kristallisieren und Schmelzen: ein Beitrag zur Lehre der Änderungen des Aggregatzustandes*. Barth, 1903.
150. Pichler, H. and Schmitt-Riegraf, C., *Gesteinsbildende Minerale im Dünnschliff : 22 Tab.* 1987, Stuttgart: Ferdinand Enke Verlag. 230.
151. Li, J., Mou, Q., Zeng, Q., et al., *Experimental Study on Precipitation Behavior of Spinels in Stainless Steel-Making Slag under Heating Treatment*. Processes, 2019. **7**(8): p. 487.
152. Mou, Q.Q., Li, J.-L., Zeng, Q., et al., *Effect of Fe_2O_3 on the size and components of spinel crystals in the $\text{CaO-SiO}_2\text{-MgO-Al}_2\text{O}_3\text{-Cr}_2\text{O}_3$ system*. International Journal of Minerals, Metallurgy, and Materials, 2019. **26**(9): p. 1113-1119.
153. Zeng, Q., Li, J., Mou, Q., et al., *Effect of FeO on Spinel Crystallization and Chromium Stability in Stainless Steel-Making Slag*. JOM, 2019. **71**(7): p. 2331-2337.
154. Hart, J.t., *The structural morphology of olivine-type minerals: a qualitative and quantitative approach, and a comparison of theoretical morphologies with habits of natural and synthetic crystals*. 1978, Rijksuniversiteit te Leiden: Leiden. p. 139.
155. Tremel, A., *Reaction Kinetics of Solid Fuels during Entrained Flow Gasification*, in *Fakultät für Maschinenwesen*. 2012, Technische Universität München: München. p. 260.
156. Steibel, M., *Experimentelle Untersuchung der Flugstromvergasung von Festbrennstoffen bei hohen Drücken und hohen Temperaturen*, in *Fakultät für Maschinenwesen*. 2018, Technische Universität München: München. p. 266.
157. Kauzmann, W., *The Nature of the Glassy State and the Behavior of Liquids at Low Temperatures*. Chemical Reviews, 1948. **43**(2): p. 219-256.
158. Beaman, R.G., *Relation between (apparent) second-order transition temperature and melting point*. Journal of Polymer Science, 1952. **9**(5): p. 3.
159. Klein, E.M., 3.13 - *Geochemistry of the Igneous Oceanic Crust*, in *Treatise on Geochemistry*, H.D. Holland and K.K. Turekian, Editors. 2003, Pergamon: Oxford. p. 433-463.
160. Esfahani, S., Mostaghel S., Barati, M., *Effect of slag composition on the crystallization of synthetic $\text{CaO-SiO}_2\text{-Al}_2\text{O}_3\text{-MgO}$ slags: Part II- Measurement and prediction of critical cooling rate*. Journal of Non-Crystalline Solids, 2016. **436**: p. 29-34.

-
161. Roscoe, R., *The viscosity of suspensions of rigid spheres*. Br. J. Appl. Phys., 1952. **3**: p. 267–269.
 162. Krieger, I.M. and Dougherty, T.J., *A Mechanism for Non-Newtonian Flow in Suspensions of Rigid Spheres*. Trans. Soc. Rheol., 1959. **3**: p. 137–152.
 163. Schupsky, J.P., Saar, O., Wu, G., Dohrn, M., Müller, M., Viscosity and Crystal Morphology Data of Anorthite Bearing Synthetic Coal Slag Systems, Fuel, 2020. 280 (118663)

Index of Figures

Fig. 1.1	Electric generation by source of the European-28. Data provided by the International Energy Agency [4].	2
Fig. 1.2	Electric generation by coal of the countries China, the USA and India in TWh (left Y-axis) and the global energy consumption in PWh (right Y-axis). Data provided by the International Energy Agency [4]	2
Fig. 2.1	Classification of coal-based and biomass fuels, regarding the H/C and O/C ratio. Data provided by [28], as seen in [21].	6
Fig. 2.2	Sketch of the Siemens SFG Gasifier with cooling screen, as shown in [15].	8
Fig. 2.3	Simplified flow diagram of the Polk Power Station process (Tampa Electric, USA) [41], as an example for an IGCC plant.	9
Fig. 2.4	Schematic drawing of the gasification process in entrained flow gasification, modified after [17].	10
Fig. 2.5	Sketch of refractory lining (left) and membrane walls (right) covered with slag, as shown in [15], source [56].	11
Fig. 2.6	Conceptual illustration of the viscosity. A represents the surface area of the plates; Y the distance between both plates; v represents the upper plates velocity and F the applied force on the upper plates.	12
Fig. 2.7	Rheological characteristics of liquids and materials with shear thickening and shear thinning behaviour, compared with a Newtonian behaviour. Modified after [60].	13
Fig. 2.8	Two suggested structural ions in silicate melts, modified after [65].	14
Fig. 2.9	Sketch of a two-dimensional modified random network of an oxide glass. White circles = network former, black dots = network modifiers, solid lines = covalent bonds, connecting dashed lines = ionic bonds. Modified after [69]	15
Fig. 2.10	Rheological behaviour of a partial liquid with increasing amount of solid particles (left). Concept of the relative viscosity η_r , (right). Modified after Seebold (2017) [32].	17
Fig. 2.11	Investigated particle shapes by Mueller et al. (2009, 2011). An oblate polyacrilic glitter, b spherical glass beads (both scale bars = 1 mm), c angular silicon carbide grit (scale bar = 500 μm), d high aspect ratio wollastonite (scale bar = 1 mm). Modified after [62, 77].	18
Fig. 2.12	Relative consistency Kr versus the particle volume fraction ϕ of oblate particles. Bt = biotite, Gl1,2 = glitter, modified after [62].	19

Fig. 2.13	Crystallographic systems and their parameters, modified after Markl (2008) [80].	20
Fig. 2.14	Systematic of the plagioclase and the alkali feldspar series in natural systems, as shown in Klein & Dutrow (2008) [79].	21
Fig. 2.15	a) Sketches of crystals occupying the similar crystal habit and crystal "tracht". b) Examples of four three-dimensional crystal shapes that have similar habit and similar tracht. Modified after Markl (2008) [80].	22
Fig. 2.16	Examples of idiomorphic crystals: (a) cubic goldish pyrite (FeS ₂) crystals on silicate bedrock, Ardino, Bulgaria, personal collection; (b) cubic greenish fluorite (CaF ₂) and hexagonal blackish foitite (Na _{0.5} (Fe ²⁺ ,Al,Mn ²⁺ ,Li) _{3Al6} [(OH) ₄ (BO ₃) ₃ Si ₆ O ₁₈]) on tabular beige alkali feldspar ((Na,K)AlSi ₃ O ₈), Erongo mountains, Namibia, terra mineralia (Freiberg).	23
Fig. 2.17	Free energy of formation of crystal nuclei from a melt as a function of size. (a) Abundance of different size crystal embryos in melt. (b) Gibbs free energy of formation ΔG of crystal nuclei for isothermal conditions. (c) Critical growth radius for different degrees of undercooling. As seen in Nesse (2009) [81].	25
Fig. 2.18	Growth on a crystal face for a cubic nucleus. (a) Adding a crystal unit on a planar crystal face. (b) Adding a crystal unit on the edges or partially completed crystal layer. (c) Growth of a unit on a screw dislocation. Modified after Nesse (2009) [81].	25
Fig. 2.19	Sketch of the relationship of nucleation and growth for a supercooled liquid. T_s is the solidus temperature, T_{liq} is the liquidus temperature. Modified after [32].	26
Fig. 2.20	Schematic drawing of a TTT curve and the determined crystallisation zone. T_{liq} is the liquidus temperature of the investigated system.	27
Fig. 2.21	Example of magmatic mafic differentiation based on the Bowen's reaction series [98]. (a) Stable magma bulk above T_{liq} . (b) Slightly supercooled magma with crystallising olivine (green). (c) Moderate supercooled magma with crystallising pyroxene (brown) and precipitated olivine. (d) Intense supercooled magma with crystallising kalifeldspar (pink) and precipitated olivine and pyroxene	28
Fig. 2.22	Crystallization images of the SHTT experiment for different temperatures. SEM BSE images of the sample surfaces displaying crystal morphologies. Modified after [118].	31
Fig. 3.1	Schematic sketch of the hot stage microscope setup used in this study. Including modified content of Dohrn (2018) [16].	35

Fig. 3.2	Schematic sketch of the sample holder architecture with relevant components of a DTA device, modified after Seebold (2017) [32].	36
Fig. 3.3	Experimental setup of the high temperature viscosimetry experiment, modified after Seebold (2017) [32].	39
Fig. 3.4	Schematic drawing of the quenching experimental set up and the custom-made sample holder.	41
Fig. 3.5	Example of the HKT temperature profile applied in the quenching experimental setup. The number of isothermal steps, as well as the temperature range varies for other slag systems.	42
Fig. 3.6	Sketch of the CLSM high temperature furnace, as shown in [135] (left). Image of the ocular lenses on top of the quartz window containing cover by operation (right).	43
Fig. 3.7	The CLSM high temperature furnace, loaded with synthetic oxide powder in a Pt-crucible (left) and an annealed slag particle in a Mo-crucible (right), as shown in Schupsky et al., (2020) [137].	45
Fig. 3.8	Diffraction from parallel planes of atoms. X-ray 1 and 2 display constructive interference, due to no phase shift of their wavelengths, as seen in	48
Fig. 3.9	Example of an XRD measurement of a powdered sample. Modified after Nesse (2009) [81]	48
Fig. 3.10	Schematical drawings of a regular SEM setup (left), as well as of the generated signals by impinging electrons on a thin sample. Modified after Erdman et al. (2019) [139].	50
Fig. 4.1	Evolution of the synthetic HKT slag during hot stage microscopy documented by binary images.	53
Fig. 4.2	DTA heating (top) and cooling (bottom) graph of the HKR slag. Softening (ST), hemispherical (HT) and flow temperature (FT) were added to the heating graph.	54
Fig. 4.3	DTA signals of cyclic HKT measurements and curves are shifted on the y-axis to improve the visibility of signals.	55
Fig. 4.4	FactSage Equilib prediction of ST-D-2 slag phase formation at an oxygen partial pressure of $p(\text{O}_2) = 10\text{-}12$ bar.	56
Fig. 4.5	FactSage Equilib prediction of HKT slag phase formation at an oxygen partial pressure of $p(\text{O}_2) = 10\text{-}12$ bar.	57
Fig. 4.6	FactSage Equilib prediction of HKR slag phase formation at an oxygen partial pressure of $p(\text{O}_2) = 10\text{-}12$ bar.	58

Fig. 4.7	Viscosity data of the high viscous ST-D-2 and HKT slag measured isothermally in steps of 25 °C. The y-axis is logarithmic scaled.	59
Fig. 4.8	Viscosity data of the intermediate viscous SOM-1 and low viscous HKR slag measured isothermally in steps of 25 °C. The y-axis is logarithmic scaled. The lower measuring tolerance of 4 Pa·s is marked with the red dotted line.	60
Fig. 4.9	Comparison of the viscosity data of the four slag systems, with the viscosity modelling results executed with the model of Wu et al., (2015, 2015, 2019) [73, 140, 141].	61
Fig. 4.10	HKT viscosity data of the isothermal measurement at 1250 °C (top left). Microscopic image of the prepared cross section of the crucible (top right). SEM-EDX mapping of crystallised anorthite: purple = Mg, orange = Al, green = Ca (bottom).	63
Fig. 4.11	Digital microscopic images of crystals on the slag surface after isothermal high temperature viscosimetry at 1150 °C (left). SEM-EDX mapping of a cross section: purple = Mg, orange = Al, pink = Mo (right).	65
Fig. 4.12	Microscopic view of four representative ST-D-2 quenching samples, quenched at 1250, 1200, 1100, and 1000 °C after a holding time of 24 h, respectively 7 h each. The sample at 1000 °C is also characterised by a SEM-BSE image.	67
Fig. 4.13	Microscopic view of four representative HKT quenching samples, quenched at 1250, 1200, 1100, and 1000 °C after a holding time of 7 h each.	68
Fig. 4.14	Microscopic view of two representative HKR samples quenched at 1250 °C and 1150 °C after a holding time of 1 h each. Microscope images in the left column are made by ring light-mode and images in the right column are taken by coaxial-light mode.	69
Fig. 4.15	CLSM in-situ view (left column) and microscopic view (right column) of two representative CLSM samples. Microscopic images were taken with ring-light mode after the experiment. a) was supercooled to 1150 °C and hold for 30 minutes, ultimately. b) was constantly supercooled with a slope of -200 K/min.	70
Fig. 4.16	XRD spectra of two representative samples quenched at 1200 °C and 1100 °C after a holding time of 4 h each	72
Fig. 4.17	Microscopic view of the cross sections of quenched HKT slag samples at 1200 °C and 1100 °C. The corresponding holding time was four hours each.	72

- Fig. 4.18** XRD spectra of four representative samples quenched at 1150 °C, 1100 °C, 1000 °C and 950 °C after a holding time of 24 h each. The correlated datasets are: anorthite (red), SiO₂* (including cristobalite, quartz and quartz low, grey), augite (light green), clinoenstatite (dark green). Datasets derive from ICSD database. 73
- Fig. 4.19** XRD spectra of three representative samples quenched at 1250 °C, 1150 °C, and 1100 °C after holding times of 0, 30 and 60 minutes. The correlated datasets are: melilite (blue), forsterite (green) and molybdenum (black). Datasets derive from ICSD database. 74
- Fig. 4.20** ST-D-2 crystallisation documented by SEM and SEM-EDX mapping in representative samples, quenched at 1250 °C, 1150 °C, and 1000 °C, with holding times of 24 and 7 h. Colours of element mappings: cyan = Si, orange = Al, green = Ca, red = Fe. 75
- Fig. 4.21** HKT crystallisation documented by SEM and SEM-EDX mapping in representative samples, quenched at 1250 °C, 1200 °C, 1100 °C, and 1000 °C, with a holding time of 7 h each. Additional colours of element mappings: violet = Mg 77
- Fig. 4.22** Representative SEM images of HKT slag samples at 1000, 1100 and 1250 °C with holding times of 7 and 24 h. Anorthite, SiO₂ and clinopyroxene phases are determined by SEM-EDX measurements. 78
- Fig. 4.23** Representative crystallised phases in a HKR sample, quenched at 1250 °C after 4 h of holding time. a) The microscopic view of the quenched sample. b, c) SEM BSE images of the same area as seen in a, including locations of EDX point measurements. d) Data of the EDX point measurements seen in c, in the unit of atom%. 79
- Fig. 4.24** SEM EDX elemental mapping of a HKR sample investigated by the CLSM experimental set up. The sample was constantly supercooled with a slope of -6 K/min. 80
- Fig. 4.25** Time temperature transformation (TTT) diagram of the ST-D-2 slag based on the quenching experiments. The crystallisation zones were determined based on the crystallised phases. Blue = anorthite, green = anorthite + SiO₂, orange = anorthite + SiO₂ + olivine (fayalite). 82
- Fig. 4.26** Time temperature transformation (TTT) diagram of the HKT slag based on the quenching experiments. The crystallisation zones were determined based on the crystallised phases. Blue = anorthite, green = anorthite + SiO₂ + clinopyroxene. 83

- Fig. 4.27** Time temperature transformation (TTT) diagram of the HKR slag based on the quenched samples. The borderlines of the crystallization zone could not be fully determined by the quenched samples as suggested by the dotted line. 85
- Fig. 4.28** Synthetic HKR crystallisation zone defined by the average initial crystallisation temperatures and the average temperatures of crystallisation completion as determined via CLSM slope experiments. The dotted lines represent the maximum and minimum temperatures for the respective slag crystallisation behaviour. Each slope measurement was repeated three times. 86
- Fig. 4.29** Selection of documented anorthite morphologies. a) microscopic image of anorthite crystals on the wall of the previously investigated viscosimetry crucible, b) crystallised anorthite from the quenching experiment (1250 °C, 24 h), c) SEM image of orientated anorthite crystals due to spindle rotation (same sample like a)), d) crystallised anorthite during viscosity measurement of subliquidus magma [144], e) crystallised anorthite in real HKT slag [32], f) crystallised plagioclase in H₂O and H₂O-CO₂-saturated magmas [145], g) crystallised anorthite in quenched coal ash slag [142], h) anorthite morphologies as described by Goldschmidt (1922) [84], i) generalised tetragonal prism morphology for the anorthite crystal quantification. 89
- Fig. 4.30** 90th/10th quantile and mean anorthite crystal length with respect to the quenching temperature of ST-D-2, HKT, and SOM-1 slag. 90
- Fig. 4.31** Averaged 90th/10th quantile and mean anorthite crystal length in dependency of the temperature, based on the ST-D-2, HKT, and SOM-1 slags. 91
- Fig. 4.32** 90th/10th quantile and mean anorthite aspect ratio (length/width) with respect to the quenching temperature of ST-D-2, HKT, and SOM-1 slag. 92
- Fig. 4.33** Averaged 90th/10th quantile and mean anorthite crystal aspect ratio in dependency of the temperature, based on the ST-D-2, HKT, and SOM-1 slags. 93
- Fig. 4.34** Spinel shapes/morphologies by different studies: a,b) hyp- to idiomorphic spinel crystals with inner zoning (quenching experiment, 1250 °C, 24 h), c) Cr-containing spinels precipitating in an experimental study of steel-making-slags [151], d) Mg-Fe-Cr spinels growing during an experimental study on metallurgic slags [152], e) Mg-Fe-Cr containing spinels crystallised in a stainless steel-making-slag [153], f) typical cubic spinel morphologies described by Goldschmidt (1922) [84], g) generalised octahedron morphology applied in this study. 94

- Fig. 4.35** Spinel morphology quantification based on quenching results of the HKR slag. The crystal diameter was measured from the most distant edges. 95
- Fig. 4.36** Representative samples of olivine crystallization of the synthetic HKR slag system. a) SEM BSE image of a sample immediately quenched at 1150 °C. Three olivine macro crystals were investigated via EDX measurements and compared with an olivine (Mg-Ca-Fe) solid solution, b) SEM BSE image of a sample quenched at 1150 °C after 30 min of holding time, c) SEM image of the sample surface, investigated via CLSM and an applied cooling rate of -100 K/min. 96
- Fig. 4.37** Comparison of investigated olivine crystals (a,b) with typical olivine morphologies (c-g). CLSM samples crystallised at an applied cooling slope of -6 K/min (a) and at isothermal treatment of 1100 °C (b). Cross section of an altered hypidiomorphic olivine crystal in an alkaliolivinebasalt, modified after Pichler & Schmitt-Riegraf (1982) [150]. d Forsterite crystal derived from crystal growth experiment and calculated growth form of an olivine type mineral [154]. f) Early description of olivine crystal morphologies by Goldschmidt (1920) [83]. f) Generalized elongated, equiaxed bipyramidal morphology, generalized for the olivine crystal quantification. 97
- Fig. 4.38** Olivine crystal morphology quantification based on samples from the quenching and the CLSM experiments. Maximum, minimum, and average crystal length as well as crystal aspect ratio in dependency of the temperature. The x-axis is in logarithmic scale. 98
- Fig. 4.39** Selection of melilite crystal shapes and morphologies. a) SEM BSE image of a CLSM sample supercooled to 1100 °C and hold for 7 minutes. b) SEM BSE image of a slag system quenched under air at 1322 °C, modified after Schwitalla et al., 2017 [103]. c) Sample quenched instantly from 1150 °C in the quenching experiment. d) Microscope image of sample surface, e) surface cross section, and f) SEM BSE image of the vertical cross section of a sample supercooled with -200 K/min in the CLSM experiment. g) SEM image of the sample surface, supercooled with -60 K/min in the CLSM experiment. 99
- Fig. 4.40** a) Selection of melilite morphologies as already described by Goldschmidt (1920) [83]. b) SEM image of sample morphology, sample treated in the CLSM experiment at 1200 °C for 60 minutes. c) Generalized rectangular bipyramid. The dimensions of the ground surface are described by the aspect ratio and its elevation in c-axis by a 35° angle of the face diagonal above the ground surface 101

- Fig. 4.41** Melilite crystal morphology quantification based on samples from the quenching and the CLSM experiments. 90th, 10th quantile, and average crystal length as well as melilite aspect ratio in dependency of the temperature. 102
- Fig. 4.42** a) Schematic setup of the PiTER experiment, b) extracted part of the fuel injection probe unit, c) image of the inner walls of the Al₂O₃ reaction tube covered with yellowish-greenish-greyish slag residues. 104
- Fig. 4.43** Microscopic images of PiTER slag. a) Fragment of the Al₂O₃ reaction tube with attached slag on the inner surface, b) and c) indicate the presence of elongated crystals in the slag on the segregated Al₂O₃ tube surface. 105
- Fig. 4.44** SEM and SEM-EDX images of the PiTER slag. a) partly crystallised slag in between segregated Al₂O₃ tube particles of the reaction tube, b) partly crystallised slag between the inner reaction tube (bottom left) and overlapping connecting-tube segment (top right), c) SEM and SEM-EDX analysis of partly crystallised slag between Al₂O₃ tube particles. An = anorthite, Spn = spinel. 106
- Fig. 4.45** Comparison of crystal shapes in PiTER and synthetic slags for anorthite and spinel by SEM images. a) anorthite crystals in PiTER slag, b) orientated anorthite crystals in synthetic HKT viscosimetry sample and generalised anorthite morphology, c) idiomorphic spinels in PiTER slags, d) idiomorphic spinel crystals in quenched HKR slag and generalised spinel morphology. An = anorthite, Spn = spinel. 107
- Fig. 5.1** Example of the comparison between equilibrium calculations via FactSage Equilib (left) and experimentally determined phases during the quenching experiment (right) of the HKT slag. A = anorthite, S = SiO₂, C = clinopyroxene. 108
- Fig. 5.2** Comparison of crystallised HKR slag. a) Viscosimetry – microscopic image of pyramidal crystals on the slag surface and SEM-EDX mapping of elongated melilite and olivine crystals in the cross section, b) quenching – microscopic image of symmetric crystals on the slag surface and SEM image of melilite skeletal macro crystals in the cross section, c) CLSM – SEM images of crystallised melilite pyramids on the slag surface and skeletal to pliers-like melilite crystals. 111
- Fig. 5.3** a) SEM-EDX line scan through melilite-slag-olivine in the HKR slag with the determined corresponding composition, b) SEM and SEM-EDX mapping of cloudish crystallisation zone including anorthite + SiO₂ in the ST-D-2 slag. Mel = melilite, Olv = olivine. Mapping colours: cyan = Si, green = Ca, orange = Al, red = Fe. 114

- Fig. 5.4** The flowsheet to modelling the viscosity of partial crystalline slags 116
- Fig. 6.1** Defined and quantified crystal morphologies with SEM images of the crystallised phases. a) anorthite = tetragonal prism, b) spinel = octahedron, c) olivine = elongated, equiaxed bipyramid, d) melilite = rectangular bipyramid. 118

Index of Tables

Table 2.1	Generalised mineral phases included in coal. Data based on [19], modified after [17].	5
Table 2.2	Ten most abundant elements in a generalised dried plant biomass. Data provided by Kaltschmitt et al., 2016 [22].	5
Table 2.3	Network forming, amphoteric, and modifying cations in silicate melts [53].	15
Table 2.4	Selection of some associate species, relevant for this study [54].	17
Table 2.5	Crystallising phases of ten ash or slag samples as predicted by FactSage Equilib (v7.2 with GTox database). The applied atmosphere was set to $p(O_2) = 10\text{-}12$ atm. The basicity was calculated using Eq (4).	29
Table 2.6	Overview of investigated crystal bearing slag systems as presented by different authors.	32
Table 3.1	The compositions of the investigated slag samples (wt%). Samples were synthetically produced, based on real coal ash samples. SOM-1 slag was partly investigated in the originating study by Saar (2019) [124].	34
Table 4.1	Softening, hemispherical and flow temperature of the four synthetic oxidic slag systems as determined by HSM. SOM-1 data derive from Saar (2019) [124].	54
Table 4.2	Temperature and holding time parameters chosen for the quenching experiments of the analysed slag systems.	66
Table 4.3	XRD results of three ST-D-2 samples.	71
Table 4.4	Occurrence of crystallised phases in HKT and ST-D-2 slag. HKT data are written with bold letters (upper row in a cell), ST-D-2 data are written <i><u>italic + underlined</u></i> (bottom row in a cell). ST-D-2 slag was not investigated at 850 °C. A = anorthite, C = clinopyroxene, S = SiO ₂ , O = olivine (fayalite).	84
Table 4.5	Overview of the kinetic data of SOM-1 investigations. * Kinetic data that were expected to be influenced by slag impurities were excluded. Table based on the data of Saar (2019) [124].	86
Table 4.6	Overview of the crystallised phases and their quantified morphology datasets. In total, 1022 individual crystals were quantified. *Crystal morphology data of the SOM-1 slag were taken from [124]. Yet, the quantification for 1200 °C and 1250 °C was performed again to uniform the measuring procedure.	87

- Table 4.7** Composition of the applied fuels in the measurement campaign of PiTER 104 experiments. The last applied blending consisted of KOL2/torrefied biomass.
- Table 5.1** Comparison of the crystallised phases determined in the viscosity 109 experiment during isothermal measurements with the corresponding samples from the quenching experiment.
- Table 5.2** Comparison of literature assessment findings (equilibrium calculations + 112 experimental data) on slag crystallisation (Table 2.6) with results of this study. Underlined phases were quantified in this study; phases in brackets were documented, but could not be quantified due to xenomorphic appearance.

Appendix

Table A.1: Composition of a selection of ten ash or slag samples investigated in previous studies (wt%). The fractions were normalised, based on the analysis from [32] and [102]. Increased values of other compounds for ST-ZAF-2 and HTC originate from the species P_2O_5 and SO_3 , respectively.

ID	Sample	Reference	SiO ₂	Al ₂ O ₃	CaO	Fe ₂ O ₃	MgO	K ₂ O	Na ₂ O	TiO ₂	Other	Basicity
S1-3	Gasifier slag	Melchior (2011) [102]	53.42	25.40	3.32	13.41	1.14	0.96	1.39	0.76	0.19	0.07
ST-ZAF-2	Hard coal ash	Seebold (2017) [32]	46.49	26.48	7.23	15.75	0.00	0.00	0.00	0.00	4.04	0.08
ST-D-6	Hard coal ash	Melchior (2011) [102]	39.76	29.74	3.55	20.76	1.55	1.71	2.05	0.54	0.32	0.10
K3-1	Lignite ash	Melchior (2011) [102]	68.22	3.72	8.47	15.67	2.70	0.66	0.09	0.28	0.19	0.14
ST-D-1	Hard coal ash	Seebold (2017) [32]	59.79	21.10	4.29	5.50	4.72	2.20	1.37	1.03	0.00	0.14
ST-D-2	Hard coal ash	Seebold (2017) [32]	56.18	16.40	10.42	5.01	8.25	1.93	1.81	0.00	0.00	0.29
ST-N-1	Hard coal ash	Melchior (2011) [102]	46.22	16.66	13.73	11.89	4.74	1.80	3.52	1.06	0.39	0.31
BK-D-1	Lignite ash	Seebold (2017) [32]	56.55	12.73	16.38	1.03	9.43	0.00	2.82	1.06	0.00	0.40
HTC	Biomass ash	Seebold (2017) [32]	37.74	4.73	41.96	3.34	1.17	2.44	1.09	0.00	7.53	1.02
HKS	Lignite ash	Melchior (2011) [102]	25.56	3.72	32.70	11.26	14.37	0.44	11.15	0.28	0.50	1.44

Table A.2: Summary of the selected species for the FactSage Equilib calculations (v7.2), performed in this study.

Base-Phase	Full Name	Configuration
GTOX-C12A	C12A7	regular
GTOX-C1A2	C1A2	regular
GTOX-C1A6	C1A6	regular
GTOX-C2F	C2F	regular
GTOX-C2SA	C2SA	regular
GTOX-C2SP	C2S_PRIME	regular
GTOX-C3A1	C3A1	regular
GTOX-CAF2	CAF2	regular
GTOX-CAO1	CAO1	regular
GTOX-CAO2	CAO2	regular
GTOX-C12A	C12A	regular
GTOX-WOLL	WOLLASTONITE	regular
GTOX-BCC	BCC_A2	regular
GTOX-CLIN	CLINO_PYROXENE	regular
GTOX-CORD	CORDIERITE	regular
GTOX-CORU	CORUNDUM	immiscible
GTOX-LEUC	Leucite	regular
GTOX-KALL	Kaliophilite-LT	regular
GTOX-FSPA	FSPA	immiscible
GTOX-MULL	MULLITE	regular
GTOX-CAO2	CaO(Al,Cr,Fe)2O3-beta	regular
GTOX-CAO1	CaO(Al,Cr,Fe)2O3-alfa	regular
GTOX-CGKS	Carnegieite	regular
GTOX-LOWC	Lowclinopyroxene	regular
GTOX-MELM	MELLILITE	Regular
GTOX-MEO	MeO	immiscible
GTOX-ORTH	Orthopyroxene	regular
GTOX-PROT	Protopyroxene	regular
GTOX-SAPP	SAPPHIRINE	regular
GTOX-LIOS	Slag	immiscible
GTOX-C2SA	C2S_C3P	regular
GTOX-CORD	Cordierite	regular
GTOX-OLIV	OLIVINE	regular
GTOX-HCP	HCP_3	regular
GTOX-FCC	FCC_A1	regular
GTOX-SPIN	SPINEL	regular

Table A.3: HKT anorthite morphology data from quenching samples. The unit of length is μm .

Temperature	category	paragenesis	mean length	90 th /10 th quantile length	mean aspect ratio	90 th /10 th quantile asp. rat.
1250 °C	IV	macro-crystals, separated, sharded, hollow, hopper shaped	1474.2	3100.4 614.2	23.9	30.9 17.4
1200 °C	III	featherlike arrangement, sharded, hollow, hopper shaped	652.7	1320.6 178.6	29.6	52.6 12.0
1150 °C	III	featherlike arrangement, hopper shaped	152.6	332.7 65.2	27.3	45.4 11.3
1100 °C	II	cloudish fronts, connected arrangement, elongate hoppers	8.6	18.4 3.0	11.2	17.7 7.7
1050 °C	II	cloudish fronts, connected arrangement	39.6	130.4 5.9	11.5	17.1 7.1
1000 °C	I	H-shaped, separated, hopper shaped	20.1	36.6 8.8	3.8	5.5 2.7
950 °C	I	H-shaped, separated, hopper shaped	25.9	43.1 16.9	2.8	3.5 2.2
900 °C	I	H-,X-shaped, separated, hopper shaped	10.8	17.2 8.2	2.5	3.3 2.1

Table A.4: ST-D-2 anorthite morphology data from quenching samples. Due to intense twin-formation of anorthite with quartz at the lowest temperatures, no individual anorthite morphology data could be gathered. The unit of length is μm .

Temperature	category	paragenesis	mean length	90 th /10 th quantile length	mean aspect ratio	90 th /10 th quantile asp. rat.
1250 °C	IV	macro-crystals, separated, sharded, hollow, hopper shaped	274.2	594.3 102.4	16.2	24.7 9.8
1200 °C	IV	separated, sharded, hollow, hopper shaped	32.4	105.2 6.0	9.9	17.0 3.3
1150 °C	III	featherlike arrangement, hopper shaped	8.4	12.9 3.0	6.6	10.2 4.0
1100 °C	II	cloudish fronts, connected arrangement, elongate hoppers	5.1	7.5 2.6	5.1	7.4 2.8
1050 °C	II	cloudish fronts, connected arrangement	3.9	10.5 0.9	4.9	6.7 3.1
1000 °C	II	cloudish fronts, connected arrangement	2.1	3.9 0.5	3.5	5.5 1.8
950 °C	-	xenomorphic, polysynthetic twin-formation	-	-	-	-
900 °C	-	xenomorphic, polysynthetic twin-formation	-	-	-	-

Table A.5: SOM-1 anorthite morphology data from quenching samples. Morphology data below 1200 °C were gathered by Saar (2019) [124]. The unit of length is μm .

Temperature	category	paragenesis	mean length	90 th /10 th quantile length	mean aspect ratio	90 th /10 th quantile asp. rat.
1250 °C	IV	macro-crystals, partly hopper, not sharded	897.3	1969 315	18.5	25.5 10
1200 °C	IV	macro-crystals, not sharded, toothed	1168.1	2030.9 415.3	19.2	26.3 11.1
1150 °C	III	featherlike arrangement, parallel aligned	84.2	143.8 38	11.5	18.2 6.7
1100 °C	III/II	featherlike arrangement, cloudish fronts,	17.5	35 5	11.9	21 4.4
1050 °C	II/III	cloudish fronts, featherlike arrangement	7.2	13.6 3.4	12	19 5.8
1000 °C	II	cloudish fronts, polysynthetic twin-formation	2.7	4 1.5	7.2	10.3 3.4

Table A.6: Averaged anorthite morphology data from ST-D-2, HKT, and SOM-1 slag system. The unit of length is μm .

Temperature	mean length	90 th quantile length	10 th quantile length	mean aspect ratio	90 th quantile aspect ratio	10 th quantile aspect ratio
1250 °C	1474.2	1887.9	343.9	23.9	27.0	12.4
1200 °C	652.7	1152.3	200.0	29.6	32.0	8.8
1150 °C	152.6	163.1	35.4	27.3	24.6	7.3
1100 °C	8.6	20.3	3.5	11.2	15.4	5.0
1050 °C	39.6	51.5	3.4	11.5	14.3	5.3
1000 °C	20.1	14.8	3.6	3.8	7.1	2.6
950 °C	25.9	43.1	16.9	2.8	3.5	2.2
900 °C	10.8	17.2	8.2	2.5	3.3	2.1

Table A.7: Spinel diameter data from HKR slag system. In total, 199 spinel crystals were measured. The unit of length is μm .

Temperature	mean diameter	90 th quantile diameter	10 th quantile diameter
1250 °C	44.6	98	16.3
1200 °C	18.4	29.3	10.3
1150 °C	26.7	37.2	14.4

Table A.8: Olivine length and aspect ratio data from HKR slag system. In total, 119 olivine crystals were measured. The unit of length is μm .

Temperature	mean length	90 th quantile length	10 th quantile length	mean aspect ratio	90 th quantile aspect ratio	10 th quantile aspect ratio
1200 °C	70.2	191	10.4	2.24	3.2	1.7
1150 °C	27.5	49.7	5.6	2.13	2.7	1.5
1100 °C	21.8	46.5	5.0	2.25	3.1	1.6

Table A.9: Melilite length and aspect ratio data from HKR slag system. In total, 119 melilite crystals were measured. The unit of length is μm .

Temperature	mean length	90 th quantile length	10 th quantile length	mean aspect ratio	90 th quantile aspect ratio	10 th quantile aspect ratio
1250 °C	625.9	994.8	310.2	1.68	2.2	1.0
1200 °C	435.2	752.6	167	1.37	2.3	1.0
1150 °C	359.1	690.0	92.4	2.40	4.1	1.1
1100 °C	239.1	500.8	55.6	1.67	2.4	1.0

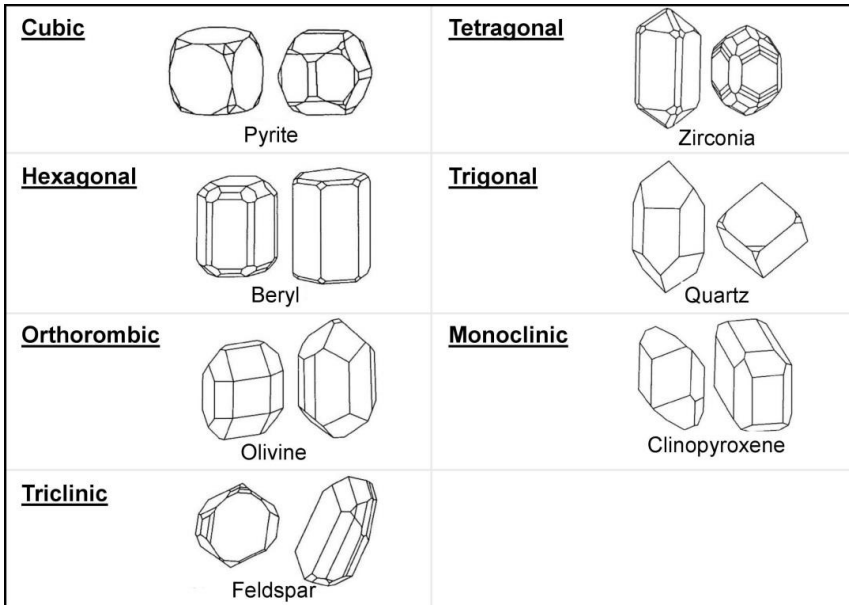


Fig. A.1: Examples of natural crystals for the different crystallographic systems, modified after Markl (2008) [80].

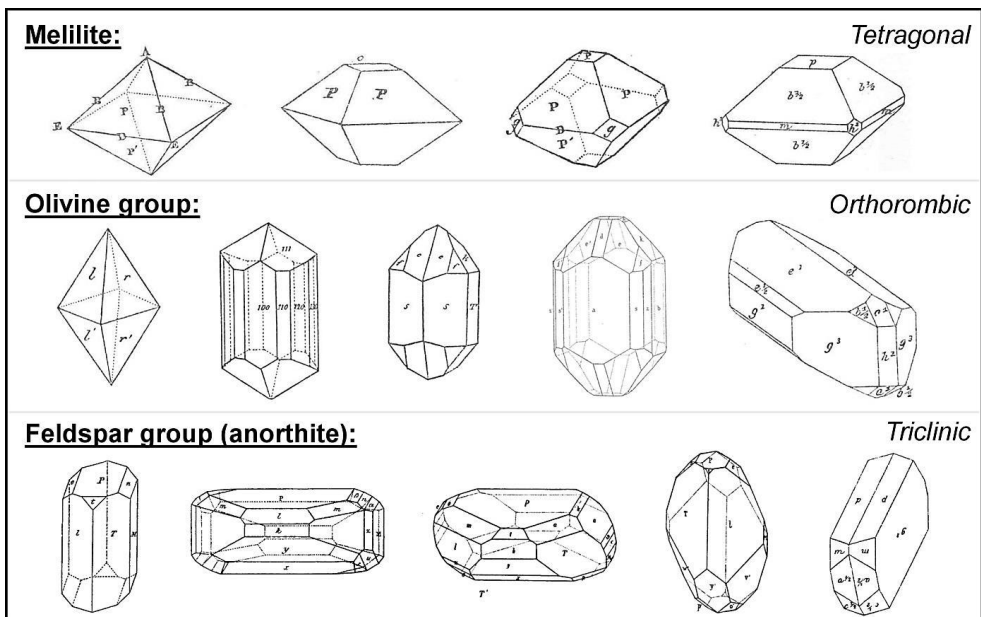


Fig. A.2: A representative selection of crystal morphologies for: melielite, the olivine group and the feldspar group. Modified after Goldschmidt (1916, 1920) [83, 85].

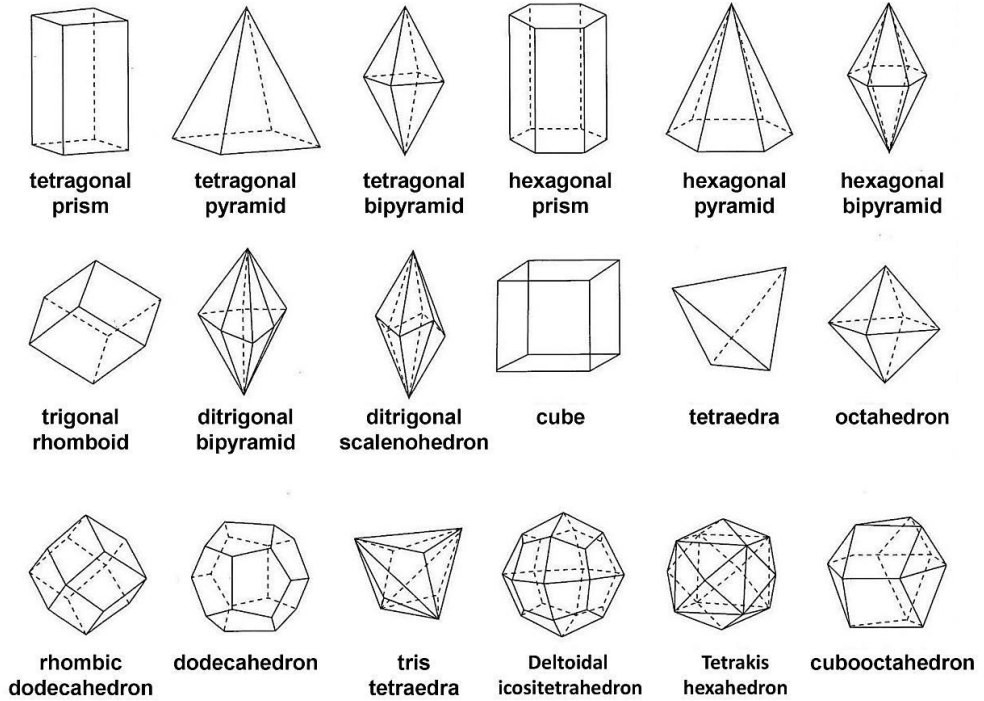


Fig. A.3: Systematic of high symmetric crystal habits, modified after Markl (2008) [80].

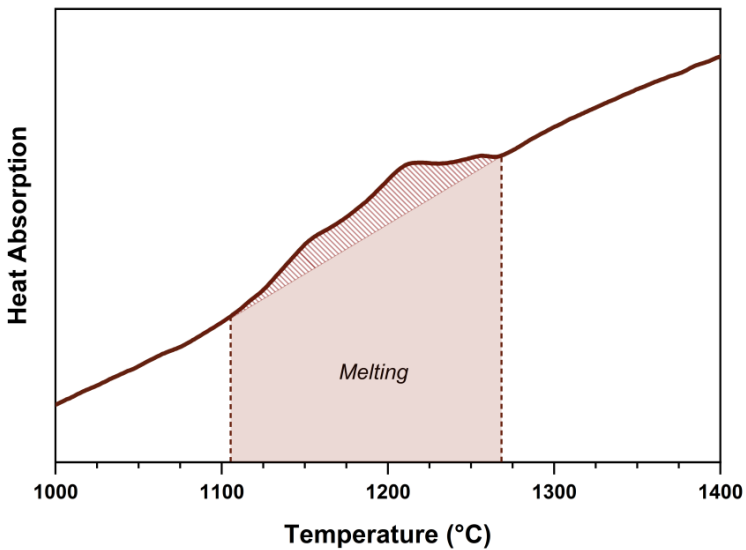


Fig. A.4: DTA initial heating graph of the HKT slag.

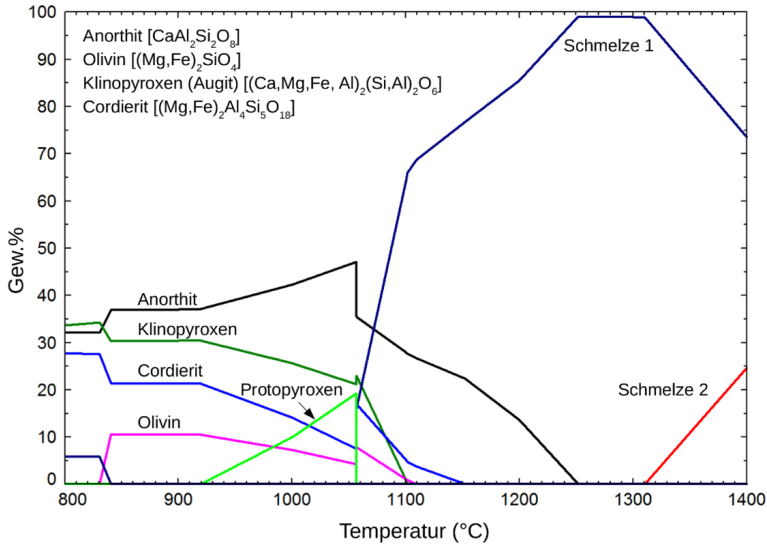


Fig. A.5: FactSage Equilib prediction of SOM-1 slag phase formation under $p(\text{O}_2) = 10^{-12}$ bar, as shown in Saar (2019) [124].

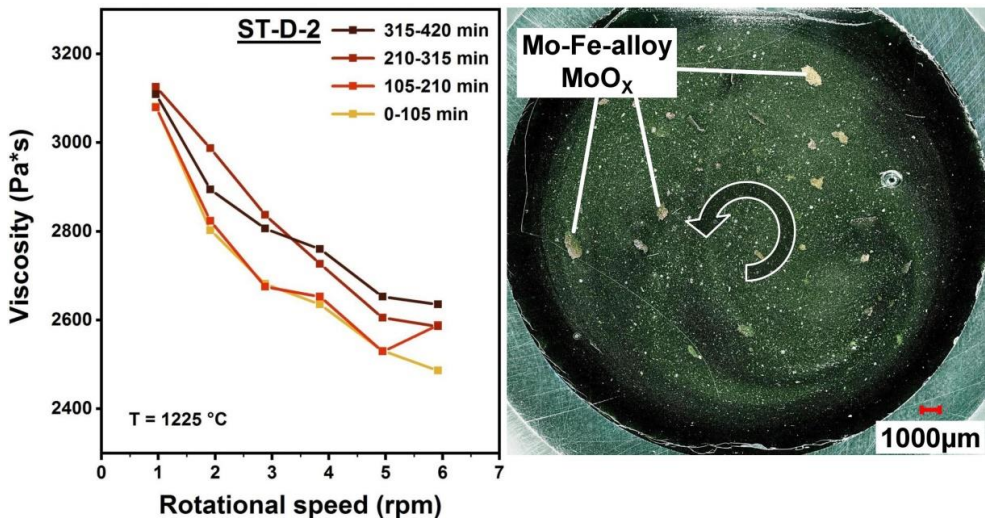


Fig. A.6: Isothermal viscosity data of ST-D-2 slag, measured for 7 hs (left). Microscopic image of the prepared cross section of the ST-D-2 sample (right). The spindle rotated counter-clockwise as indicated by the black arrow.

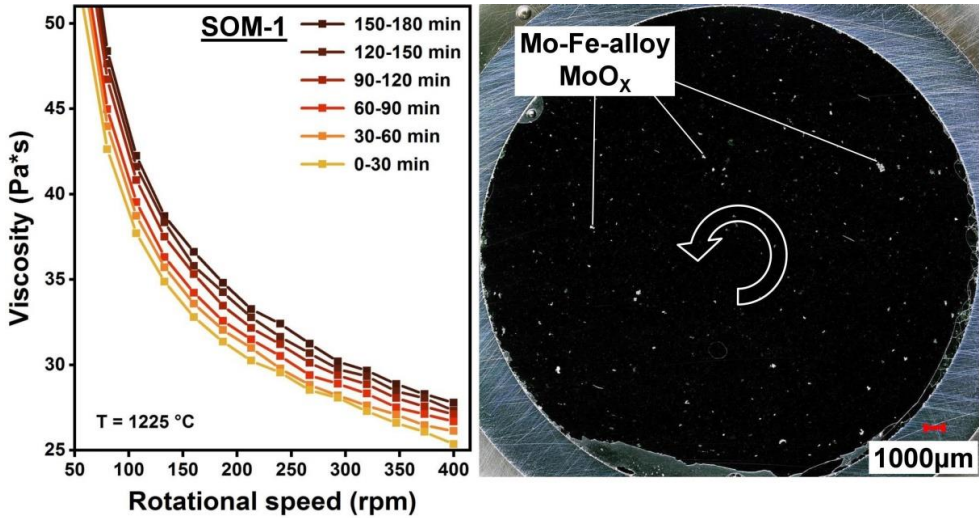


Fig. A.7: Isothermal viscosity data of SOM-1 slag, measured for 3 h (left). Microscopic image of the prepared cross section of the SOM-1 sample (right). The spindle rotated counter-clockwise as indicated by the black arrow.

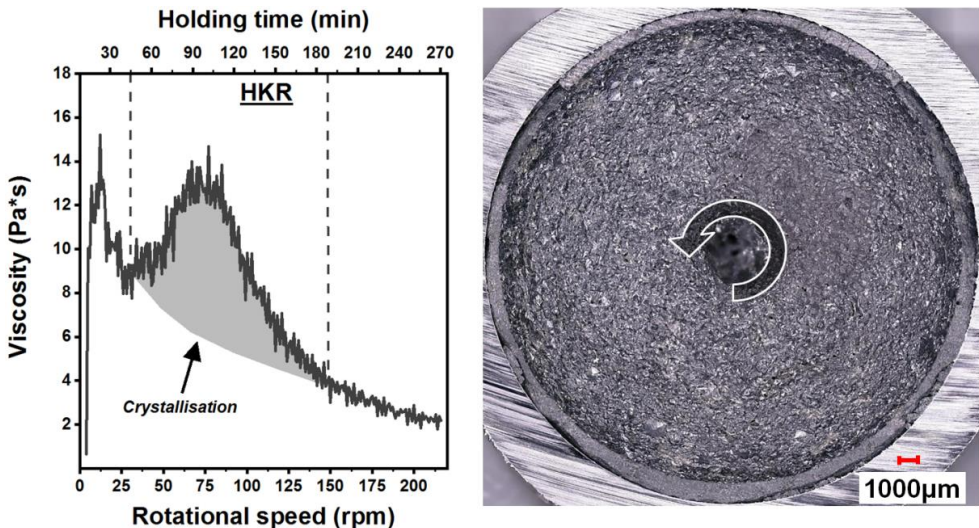


Fig. A.8: Isothermal viscosity data of HKR slag, measured for 4.5 h (left). Microscopic image of the unprepared SOM-1 slag surface (right). Crystallisation can clearly be identified of the slag surface. The spindle rotated counter-clockwise as indicated by the black arrow.

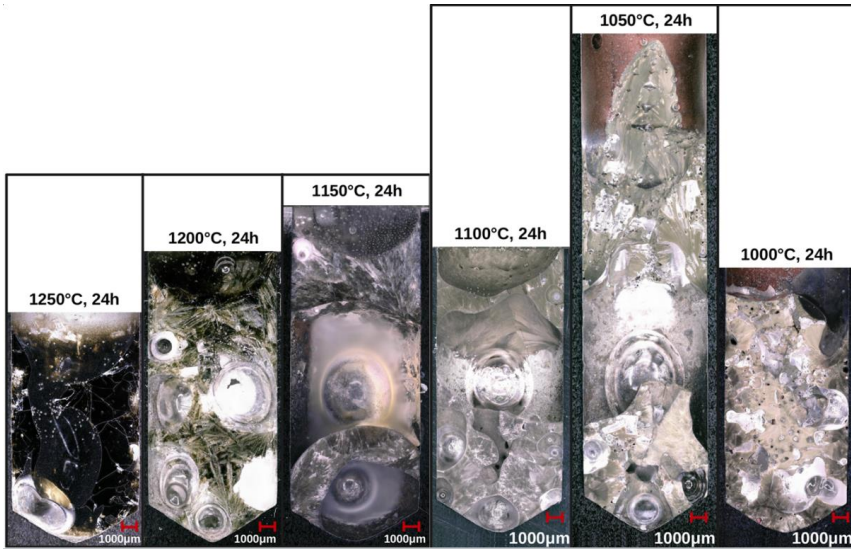


Fig. A.9: SOM-1 samples quenched after 24 h at various holding temperatures, as shown in Saar (2019) [124].

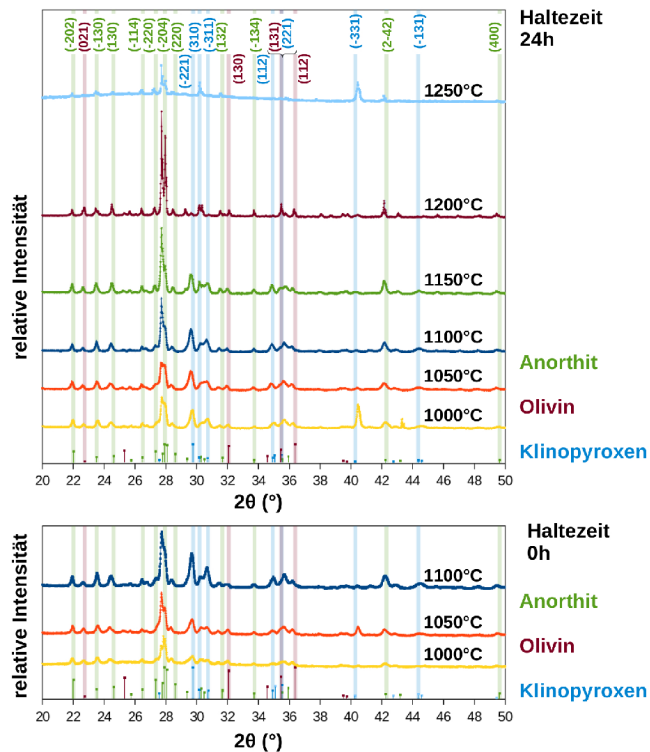


Fig. A.10: Comparison of SOM-1 XRD results, quenched at different temperatures for 0 h and 24 h of holding time, as shown in Saar (2019) [124].

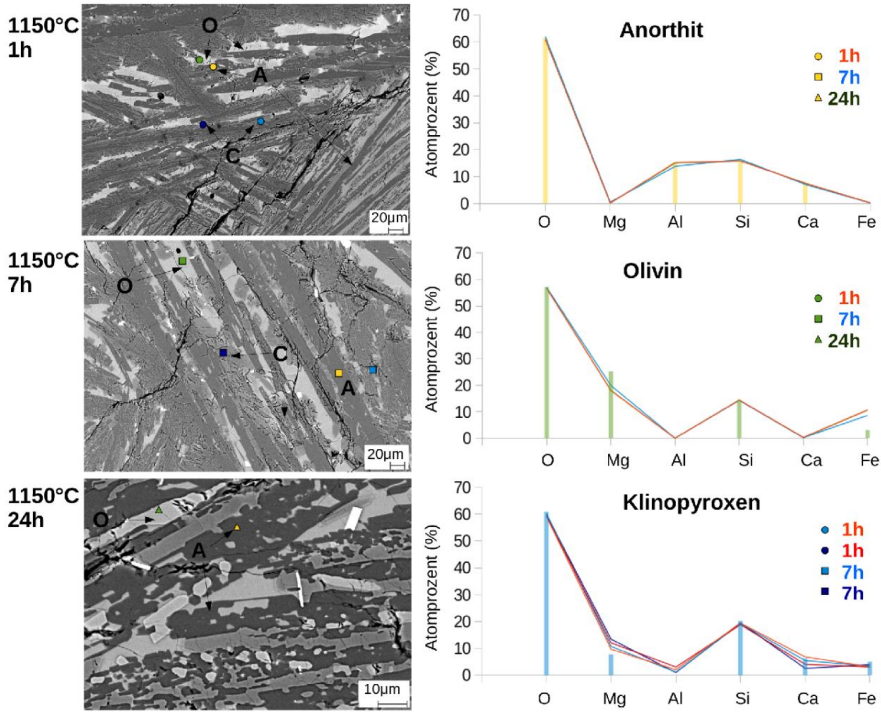


Fig. A.11: SEM-EDX results of SOM-1 slag, quenched at 1150 °C at various holding times. A = anorthite, O = olivine, C = clinopyroxene, as seen in Saar (2019) [124].

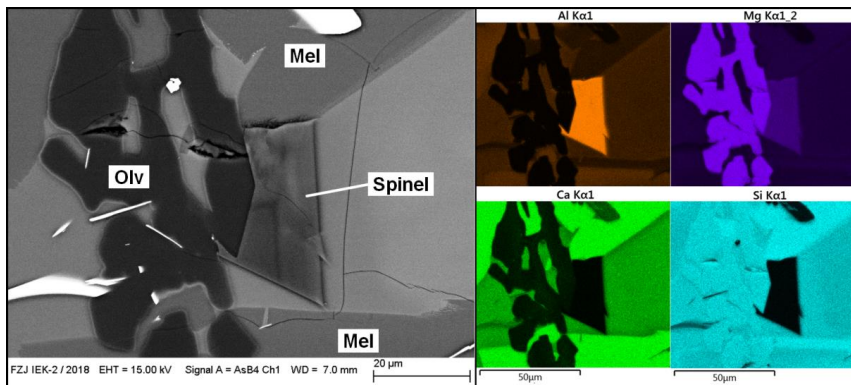


Fig. A.12: SEM image of crystallised spinel in HKR slag at 1200 °C after 24 h. Spinel crystallised in close arrangement of skeletal olivine. SEM-EDX mapping display characteristic enrichment of Al, but no presence of Si and Ca in the crystal. Many spinel crystals also contain minor fractions of Fe.

Appreciation

Firstly, I want to express my sincerest thanks to PD Dr. Michael Müller, who recognized my inner slumbering creativity from the first day we met and who gave me the opportunity to perform my PhD study in the institute of energy and climate research (IEK-2) at Forschungszentrum Jülich GmbH. Also, I want to thank PD Dr. Michael Müller for the trust and the vast degree of freedom I could experience during my PhD.

I want to thank deeply my (former) colleagues of the Thermochemistry group: Dr. Matthias Dohrn, Dr. Sören Seebold, Dr. Marc Bläsing, Dr. Dmitry Sergeev, Dr. Elena Yazhenskikh, Alexandra Heymann, Konrad Mielke, Urusula Gude, Xin Zhao, Jia Qi, Florian Lebendig, Shivani Gonde, Ralf Küppers and Inge Dreger, who heartily welcomed me at IEK-2, supported my work and who made my time absolutely enjoyable. I also want to thank Dr. Egbert Wessel, Dr. Daniel Grüner, Jörg Bartsch, Volker Gutzeit, Mirko Ziegner, Manuel Hucko, Christoph Bütow and Max Borzikov for the scientific and technical support of my study. My additional thanks belong to my team mates of FC Mikro 02. I was proud to win three trophies in the past three tournaments with you for the glory of IEK-2.

For the possibility of performing CLSM experiments at MTM institute of KU Leuven, I want to thank Prof. Bart Blanpain and Dr. Muxing Guo. I also want to thank Dr. Zhuangzhuang Liu, Dr. Amy van den Bulck and Joris van Dyck, who helped me by the performance of experiments and who made my stays always substantial.

I thank Tobias Netter and Sebastian Miebling for the delightful moments we spent in Clearwater (Florida, US) during the 44th International Technical Conference on Clean Energy, as well as the research progress I was able to gather out of our resulting cooperation.

Special thanks belong to Dr. Matthias Dohrn who encouraged me to dare the step of performing a PhD and for giving me numerous scientific advices in the past years. I also want to thank him and Dr. Florian Thaler for forming the most entertaining carpool I could ever imagine.

Lastly, I want to thank my wife Fé Marlen Aengenvoort from the bottom of my heart for supporting and encouraging me in the past years and for giving me the confidence to be on the right track. A special thanks goes to my family, who always believed in me and my determination.

The work and results of this thesis have been performed in the framework of the HotVeGas Project supported by Bundesministerium für Wirtschaft und Energie (FKZ 0327773).

Band / Volume 500

**Mechanical Behavior of Solid Electrolyte Materials
for Lithium-ion Batteries**

G. Yan (2020), x, 139 pp

ISBN: 978-3-95806-484-3

Band / Volume 501

**Retrieval of atmospheric quantities from remote sensing measurements of
nightglow emissions in the MLT region**

Q. Chen (2020), 208 pp

ISBN: 978-3-95806-485-0

Band / Volume 502

Auswirkungen der Energiewende auf das deutsche Gastransportsystem

B. Gillessen (2020), XVII, 186

ISBN: 978-3-95806-487-4

Band / Volume 503

**Lagrangian Simulation of Stratospheric Water Vapour: Impact of Large-
Scale Circulation and Small-Scale Transport Processes**

L. Poshyvailo (2020), 124 pp

ISBN: 978-3-95806-488-1

Band / Volume 504

**Water Management in Automotive Polymer-Electrolyte-Membrane
Fuel Cell Stacks**

S. Asanin (2020), XVIII, 172 pp

ISBN: 978-3-95806-491-1

Band / Volume 505

**Towards a new real-time irrigation scheduling method: observation,
modelling and their integration by data assimilation**

D. Li (2020), viii, 94 pp

ISBN: 978-3-95806-492-8

Band / Volume 506

Modellgestützte Analyse kosteneffizienter CO₂-Reduktionsstrategien

P. M. Lopion (2020), XIV, 269 pp

ISBN: 978-3-95806-493-5

Band / Volume 507

**Integration of Renewable Energy Sources into the Future
European Power System Using a Verified Dispatch Model
with High Spatiotemporal Resolution**

C. Syranidou (2020), VIII, 242 pp

ISBN: 978-3-95806-494-2

Band / Volume 508

Solar driven water electrolysis based on silicon solar cells and earth-abundant catalysts

K. Welter (2020), iv, 165 pp

ISBN: 978-3-95806-495-9

Band / Volume 509

Electric Field Assisted Sintering of Gadolinium-doped Ceria

T. P. Mishra (2020), x, 195 pp

ISBN: 978-3-95806-496-6

Band / Volume 510

Effect of electric field on the sintering of ceria

C. Cao (2020), xix, 143 pp

ISBN: 978-3-95806-497-3

Band / Volume 511

Techno-ökonomische Bewertung von Verfahren zur Herstellung von Kraftstoffen aus H₂ und CO₂

S. Schemme (2020), 360 pp

ISBN: 978-3-95806-499-7

Band / Volume 512

Enhanced crosshole GPR full-waveform inversion to improve aquifer characterization

Z. Zhou (2020), VIII, 136 pp

ISBN: 978-3-95806-500-0

Band / Volume 513

Time-Resolved Photoluminescence on Perovskite Absorber Materials for Photovoltaic Applications

F. Staub (2020), viii, 198 pp

ISBN: 978-3-95806-503-1

Band / Volume 514

Crystallisation of Oxidic Gasifier Slags

J. P. Schupsky (2020), III, 127, XXII pp

ISBN: 978-3-95806-506-2

Weitere **Schriften des Verlags im Forschungszentrum Jülich** unter
<http://wwwzb1.fz-juelich.de/verlagextern1/index.asp>

Energie & Umwelt / Energy & Environment
Band / Volume 514
ISBN 978-3-95806-506-2

Mitglied der Helmholtz-Gemeinschaft

